Earthquake cycle and continental deformation along the Peruvian subduction zone

Juan Carlos Villegas Lanza

UNIVERSITE DE NICE SOPHIA ANTIPOLIS - UFR SCIENCES
Ecole Doctorale des Sciences Fondamentales et Appliquées

T H E S E

pour obtenir le titre de

Docteur en Sciences

de l'UNIVERSITE de Nice-Sophia Antipolis

Spécialité: Sciences de la Terre et de l'Univers - Géophysique

Présentée et soutenue par
Juan Carlos VILLEGAS LANZA

Earthquake cycle and continental deformation along the Peruvian subduction zone

Cycle sismique et déformation continentale le long de la subduction Péruvienne

Thèse dirigée par **Jean-Mathieu NOCQUET** et **Mohamed CHLIEH**

Soutenue le 05 Novembre 2014

Jury :

VIGNY Christophe	Directeur de Recherche	Rapporteur
AUDIN Laurence	Chargée de Recherche	Rapporteur
M. DELOUIS Bertrand	Professeur	Examinateur
SOCQUET Anne	Physicien Adjoint	Examinatrice
NOCQUET, Jean-Mathieu	Directeur de Recherche	Directeur de thèse
CHLIEH Mohamed	Chargé de Recherche	Co-directeur de thèse

Abstract

The Nazca/South American subduction zone is one of the most active regions on Earth. Large earthquakes and associated tsunamis occur recurrently almost all along its margin. Nevertheless, the ~1000 km long (from lat.2ºS to 9ºS) segment in northern Peru and southern Ecuador subduction has remained in relative seismic silence for at least the past five centuries. Before the work presented in this thesis, no information about the processes accommodating the convergence was available for this region and it was impossible to answer whether it could host a great Mw>8.5 earthquake in future or not. Nowadays, spatial geodesy, and more specifically GPS/GNSS enable us to quantify the surface displacement on the overriding plate with a millimeter accuracy. Geodetic measurements together with the use of elastic models allow us to determine the amount of interseismic coupling at the plate interface. My thesis focuses on the seismic cycle and the continental deformation along the Peruvian subduction margin, with particular interest along its northern and central segments. We use GPS measurements acquired since 2008 in the frame of an international French-Peruvian-Ecuadorian project (the Andes Du Nord project, ADN). Our GPS velocity field covers the entire Peruvian subduction margin, with measurements in the Andean cordillera and part of the sub-Andean region. Modeling of GPS velocity field show the existence of a new tectonic microplate that we baptized as the Inca Sliver, which is in southeastward translation a rate of 4-5 mm/yr with respect to stable South America. The Inca sliver encompasses the entire Peruvian subduction margin from southern Ecuador to northern Bolivia including the coastal areas and the Western cordillera of Peru. We find that the Inca sliver diverges from the North Andean Sliver in Ecuador and Colombia, contributing to the opening of the Gulf of Guayaquil. In its southern part, the Inca sliver possibly contributes to the lateral holding of the Altiplano plateau. We propose that the primary driving process that induces the motion of the slivers observed all along the Andes is partitioning of the oblique Nazca/South America convergence. However, our results show that the level of partitioning is partial in Peru (~25%). Inland the Inca sliver motion appears to be accommodated by complex fault systems and internal deformation within its eastern part. In terms of interseismic coupling (ISC), we demonstrate important variations both along-strike and along-dip. We find that the subduction segments of northern Peru and southern Ecuador (from lat.2ºS to 9ºS) shows in general a low to weak ISC, with possibly shallow partial coupling confined near the trench. Our results therefore explain the absence of large earthquakes in this region and correlate with the occurrence of moderate magnitude tsunami-earthquakes that occurred in the last decades. Contrasting with this behavior, the central Peru segment (lat. 10ºS a 14ºS) shows a high ISC that spatially correlates with the rupture area of past large earthquakes (M>8) and in particular with the Mw~8.8 1746 devastating earthquake. The present-day interseismic moment deficit suggests a recurrence time of 266-347 to reproduce a similar event. In southern Peru, our models show two areas with high ISC near Nazca (lat. 15ºS) and near the boundary with Chile (lat. 18ºS). We also find evidence for ongoing postseismic deformation in the area of the 2001 Mw=8.4 Arequipa earthquake. Finally, we document a Slow Slip Event (SSE) synchronous to seismicity swarms that took place in northern Peru in 2009. This sequence lasted 7 months and released a total moment equivalent to an earthquake of Mw=6.7. We analyze the relationship between seismic and aseismic processes. Finally based on all these results, we propose inferences about the anatomy of the plate interface in terms of its frictional properties at the scale of the Peruvian subduction. In overall, our results contribute to better quantify the hazard posed by subduction and continental earthquakes in Peru. They also shed light on the active tectonics and the long-term deformation of the Peruvian Andes.

Résumé

La zone de subduction entre les plaques Nazca et Amérique du Sud est une des régions les plus actives de notre planète. De grands tremblements de terre et tsunamis associés se produisent de façon récurrente presque tout au long de sa marge. Néanmoins, le segment de subduction au nord du Pérou (de lat.3ºS à 9ºS) est resté le seul segment sismiquement silencieux depuis les premières informations historiques sur les séismes qui remontent au XVème siècle. Avant le travaux présentés dans ce manuscrit, aucune information sur les processus accommodant la convergence de la plaque Nazca vers le continent Sud-Américain n'était disponible le long du segment de 1000km au nord Pérou et sud Equateur. Les techniques de géodésie spatiale, en particulier le GPS/GNSS, nous permettent de quantifier les mouvements à la surface de la plaque supérieure avec une précision millimétrique. Ces mesures, couplées à l'utilisation de modèles élastiques, nous permettent de déterminer le niveau du couplage intersismique le long de l'interface entre les plaques. Le but de ma thèse est d'étudier le cycle sismique et la déformation continentale le long de la zone de subduction du Pérou, avec un intérêt particulier pour son segment nord. Nous utilisons des mesures GPS acquises depuis 2008 dans le cadre d'un projet international (le projet Andes Du Nord, ANR-ADN). Le champ de vitesse GPS obtenu couvre l'ensemble de la marge de subduction péruvienne, avec des mesures dans la cordillère et dans une moindre mesure dans la région sub-Andine. L'analyse et la modélisation du champ de vitesse GPS ont permis d'obtenir les résultats suivants: Premièrement: nous mettons en évidence l'existence d'un nouveau domaine continental, que nous avons baptisé comme le sliver Inca et qui est en translation a une vitesse de 4-5 mm/an en direction sud-est par rapport au craton Sud Américain. Le sliver Inca s'étend tout le long de la marge péruvienne. Le sliver Inca diverge du sliver Nord-Andin en Equateur et en Colombie, contribuant ainsi à l'ouverture du golfe de Guayaquil. Dans sa partie sud, le sliver Inca contribue probablement à maintenir latéralement l'Altiplano. Nous proposons que le processus responsable du mouvement des slivers est le partitionnement de la convergence oblique de la plaque Nazca vers le continent Sud-Américain. Cependant, nos résultats montrent que ce partitionnement est partiel (~25%). A l'intérieur du continent, le mouvement de ces slivers semble être accommodé par des systèmes de failles complexes dans la partie orientale des Andes. En terme de couplage intersismique (ISC) le long de l'interface de subduction, nous démontrons d'importantes variations latérales et en profondeur. Nos résultats indiquent que le segment de subduction du nord du Pérou et du sud de l'Equateur (de lat.2ºS à 9ºS, 1000 km long) sont faiblement couplés, avec éventuellement un couplage partiel superficiel proche de la fosse. Ces résultats expliquent l'absence de grands séismes dans cette région. Au contraire, le segment central du Pérou (lat. 10ºS un 14ºS) montre une fort couplage intersismique qui corrèle avec les zones de rupture des grands séismes (M>8.0) dans du siècle passé. Le déficit actuel de moment intersismique suggère un temps de récurrence de 266 à 347 années pour reproduire un séisme similaire à celui de 1746 (~M8.8). Dans le sud du Pérou, nos modèles montrent deux zones fortement couplées près de Nazca (lat. 15ºS) et près de la frontière avec le Chili (lat. 18ºS). Nous mettons de plus en évidence que le région du séisme du 2001 Mw8.4 2001 d'Arequipa subit actuellement une déformation postsismique significative. Enfin, nous documentons un épisode de glissement transitoire asismique simultané à un essaim de sismicité dans le nord du Pérou en 2009. Cette séquence a duré 7 mois et libéré un moment total équivalent à un séisme de Mw6.7. Nous analysons la relation entre les processus sismiques et asismiques. Enfin sur la base de ces résultats, nous proposons des inférences sur l'anatomie de l'interface de subduction et en particulier de ses propriétés frictionnelles, à l'échelle de la subduction péruvienne. Nos résultats contribuent à quantifier l'aléa associé aux séismes de subduction et continentaux. Ils contribuent aussi à mieux comprendre la tectonique active et la déformation long terme de la Cordillère des Andes.

Resumen

La zona de subducción de Sudamérica es una de las regiones más activas de la Tierra. A lo largo de casi todo este margen ocurren grandes terremotos y tsunamis de manera cíclica. Sin embargo, el segmento de la subducción entre el norte de Perú y sur de Ecuador (from lat.2ºS to 9ºS, de aprox. ~1000 km de largo), ha permanecido relativamente en silencio sísmico desde hace al menos 5 siglos, desde los primeros reportes históricos, sin conocer si en esta región se han producido grandes sismos en el pasado. Hasta antes de los resultados presentados en esta tesis, no existía información disponible acerca de los procesos que acomodan la convergencia de placas en esta región, por lo cual resultaba imposible saber si en el futuro podría ocurrir o no un sismo de gran magnitud Mw>8.5 en dicha región. Las técnicas de geodesia espacial, en particular el GPS/GNSS, permiten cuantificar con precisión milimétrica la deformación de la placa superior en zonas de subducción. Las mediciones geodésicas junto con el uso de modelos de dislocación elástica permiten determinar el grado de acoplamiento intersísmico en la interfaz de placas. Mi tesis tiene por objetivo central estudiar el ciclo sísmico y la deformación continental el la zona de subducción de Perú, con interés particular en la región centro y norte de Perú. Para ello, hago uso de mediciones GPS adquiridas desde el año 2008 en el marco de un proyecto internacional (Andes del Norte, ANR-ADN). El campo de velocidad GPS obtenido cubre todo el margen de subducción de Perú con algunas mediciones en la cordillera de los Andes y parte de la región sub-Andina. El modelamiento del campo de velocidad muestra la existencia de una nueva microplaca a la cual hemos denominado el sliver Inca, que se encuentra en traslación hacia el Sur-Este a una velocidad de 4-5 mm/yr con respecto a la parte estable de Sudamérica. Este sliver abarca todo el margen de subducción peruano desde el sur de Ecuador hasta el norte de Bolivia, incluyendo el margen costero y la cordillera occidental de Perú. Los resultados muestran que el sliver Inca junto con el sliver nor-Andino se encuentran en movimiento divergente, contribuyendo a la apertura del Golfo de Guayaquil. En el extremo sur el sliver Inca posiblemente contribuye a sostenimiento lateral del Altiplano. Proponemos que el principal proceso que induce el movimiento de los slivers a lo largo de toda Sudamérica es el particionamiento de la convergencia oblicua de las placas Nazca/Sudamericana. Sin embargo, nuestros resultados muestran que el particionamiento es solo parcial en el Perú (25%). En el interior del continente el movimiento del sliver Inca parece ser acomodado por complejos sistemas de fallas con deformación activa hacia el Este en la cordillera Oriental y zona sub-Andina. En términos de acoplamiento intersísmico (ISC), nuestros resultados muestran importantes variaciones tanto de manera lateral como en profundidad a lo largo de toda la interfaz. El segmento de subducción del norte de Perú y sur de Ecuador (lat. 2ºS a 9ºS) muestra en general un bajo a débil ISC, con posible acoplamiento parcial confinado en la parte superficial de la zona de contacto (<30km). Estos resultados permiten explicar la ausencia de grandes terremotos en el pasado reciente y se correlacionan con la ocurrencia de eventos tipo tsunami-earthquakes como los ocurridos en las décadas anteriores (i.e 1960 & 1996). La región central de Perú (lat. 10ºS a 14ºS) muestra un alto ISC que se correlaciona espacialmente con las áreas de ruptura de grandes terremotos (M≥8.0) ocurrido en el pasado, en particular con el área de ruptura del devastador terremoto de 1746 (Mw~8.6-8.8). Los cálculos actuales del déficit de momento intersísmico sugieren un tiempo de recurrencia de 266-347 años para reproducir un evento de características similares. En el sur del Perú los modelos muestran dos áreas con alto ISC cerca de la ciudad de Nazca (lat. 15ºS) y cerca a la frontera con Chile (lat. 18ºS). Estas zonas representan son de alto peligro en términos del potencial sísmico. Los resultados también muestran evidencia del efecto post-sísmico del sismo de 2001 (Mw 8.4) aún perdura. Finalmente, es esta tesis se documenta un sismo lento (Slow Slip Event) sincronizado con una secuencia de sismicidad en el año 2009. Esta secuencia duró 7 meses y liberó un momento equivalente a un sismo de Mw=6.7. Estudiamos la evolución espacio temporal de la secuencia y analizamos la relación entre los procesos sísmicos y asísmicos. Finalmente, en base a todos estos resultados obtenidos en esta tesis planteamos inferencias sobre la anatomía de la interfaz de placas en términos de las propiedades friccionales a escala de toda la zona de subducción de Perú. Los resultados obtenidos en esta tesis contribuyen en general, a cuantificar mejor el riesgo tanto en la zona de subducción como en el interior del continente, además que permiten comprender mejor los procesos de la tectónica activa así como la deformación de los Andes Peruanos.

Remerciements

Cette thèse a été réalisée avec le soutien de l'Institut de Recherche pour le Développement (IRD-DSF), le projet ANR-ADN (Andes du Nord), le laboratoire Géoazur UMR7329 UR082 et l'Instituto Geofísico del Perú (IGP).

Je tiens tout d'abord à remercier mon directeur et co-directeur de thèse, Jean-Mathieu Nocquet et Mohamed Chlieh. Ce fut un grand privilège d'avoir travaillé sous leurs encadrements. Je les remercie de m'avoir transmis de leur expérience, esprit de synthèse, et recul sur les résultats obtenus. Enfin je les remercie pour leurs conseils et encouragement.

J'adresse mes remerciements aux membres du jury qui ont accepté de prendre de leur temps pour évaluer ce travail: Pr. Christophe Vigny et Dr. Laurence Audin d'avoir accepté d'être rapporteurs, Pr. Betrand Delouis et Dr. Anne Socquet d'avoir accepté d'être examinateurs.

Je tiens à remercier Pr. Emmanuel Tric, directeur du laboratoire Géoazur, pour m'avoir accueilli au sein du laboratoire, ainsi que Jenny Trevisan directrice adjointe, ainsi que l'ensemble de l'équipe administrative, informatique et bibliothèque pour leur aide précieuse.

Je remercie l'Instituto Geofísico del Perú et plus particulièrement son Président, ses directeurs et chefs d'équipes: Pr. Dr. R. Woodman, Dr. J. Macharé, Dr. H. Tavera, Dr. J. Chau et Dr. E. Norabuena, pour leur confiance, conseils et les facilites pour mener cette thèse à son terme.

Je tiens à remercier la représentation de l' IRD de Lima, ses directeurs G. Hérail et J. L. Guyot, ainsi que toute l'équipe administrative, notamment L. Lalonde, M. Soto, et A. Corde pour leur aide précieuse.

J'adresse aussi mon remerciement aux chercheurs de Géoazur et de l'IRD en particulier: O. Cavalier, A. Sladen, J. Salichon, L. Rolland, M. Vergnolle, F. Courboulex, T. Monfret, B. Delouis, G. Nolet, P. Charvis, T. Sempere, et P. Baby avec qui j'ai pu discuter et échanger. Un grand merci à F. Rolandone de l'ISTeP et M. Vallée de l'IPGP pour les discussions et ses conseils. Je remercie aussi les membres des équipes 'Failles' et 'Astrogeo' de Géoazur pour m'avoir accueilli en leur sein.

Un grand merci aux ingénieurs et techniciens avec qui j'ai eu l'opportunité de faire des missions de terrain et voyager a travers le Pérou pour installer et mesurer des stations GPS. Un grand Merci à toi Francis, Xavier, José, Jimmy, Gudner, Manuel et autres. Merci également aux institutions, autorités et personnes des différentes villes et pueblitos qui nous ont aidé ces six dernières années.

A tous le thésards, collègues et amis avec qui j'ai partagée des agréables moments, pendants mes séjours à Nice et Lima: Amina, Clarita, Marianne, Flore, Luisa, Elodie, Huyen, Zahida, Imane, Yevgeniya, Nestor, Tran, Dung, Benoit, Swann, Alain, Vincent, Clément, Eddy, Pedro, Quentin, Sadrac, Battulga, Aurélien, Kuan-Chuan, Jérémi, Maurin, Liliana, Isabel, Marita Cristobal, Christian, Rocio et John. Un grand merci à mon ami David Cisneros de l'IGM Equateur ainsi que Paul Jarrin, Patty Mothes Victor Naya de l'IG-EPN.

Enfin, je remercie a ma famille pour leur soutien constant et pour partager mes espoirs, je pense à mes parents Serapio y Grimalda et mes frères Lincoln, Tonny, Jésus y Jimmy.

A Sheilita pour son amour et sa patience.

GRACIAS !!!

Juan Carlos Villegas Lanza
05-11-2014

A mis Padres y Hermanos.

A Sheila.

Contents

Chapter 1

1. Introduction

Subduction zones are converging plate boundaries where an oceanic plate moves beneath another and sinks into the mantle. The subduction process gives raise to the most active and dynamic phenomena on the Earth's surface, including crustal deformation, earthquakes, tsunamis, volcanism, mountain building, among others. My thesis focuses on the surface deformations associated with the subduction zone in Peru and its relation with the processes leading to continental deformation and the occurrence of large subduction earthquakes.

The largest earthquakes recorded on Earth usually happen at subduction zones. Among the 19 largest earthquakes (M>8.5) recorded by seismometers since 1900. 17 occurred at subduction megathrust (Figure 1.1). Indeed, only during the last decade 6 great subduction earthquakes occurred and were followed by large tsunamis leading to dramatic consequences for human societies. For the two most devastating events, the 2004 Sumatra-Andaman Islands (Mw 9.2) and the Tohoku-Oki 2011 Japan (Mw 9.0), the seismic potential had not been correctly assessed prior to their occurrence, because several assumptions were incorrect [*Stein et al.*, 2012]. First, because of a correlation found between the age of subducting ocean floor and convergence rate with the occurrence of past M>8.5 earthquakes, it was thought that the old oceanic subduction in Sumatra and Japan would not be able to generate M~9 earthquakes [*Ruff and Kanamori*, 1980]. Second, seismic hazard assessment in Japan relied on the earthquake catalog spanning roughly 4 centuries, which was thought to be all-inclusive of earthquake types along the Honshu subduction zone. Finally, the large amount of slip along the shallowest part of the plate interface that lead to the generation of the huge tsunami challenged the view that significant stress could not accumulate in the shallowest portion of the subduction interface.

Currently, several hundreds of million of people live under the direct threat of large earthquakes and potentially associated tsunamis all along coastal regions of the

circum-Pacific subduction. According to official estimates more than a third of the world population will be living in seismically active areas by 2040 [*UNAVCO Science Report*, 1994; *United Nations*, 2004]. It is therefore essential and urgent to better understand the processes and parameters controlling the occurrence of great subduction earthquakes to identify which areas are prone to produce them and provide reliable assessment of their location and potential size.

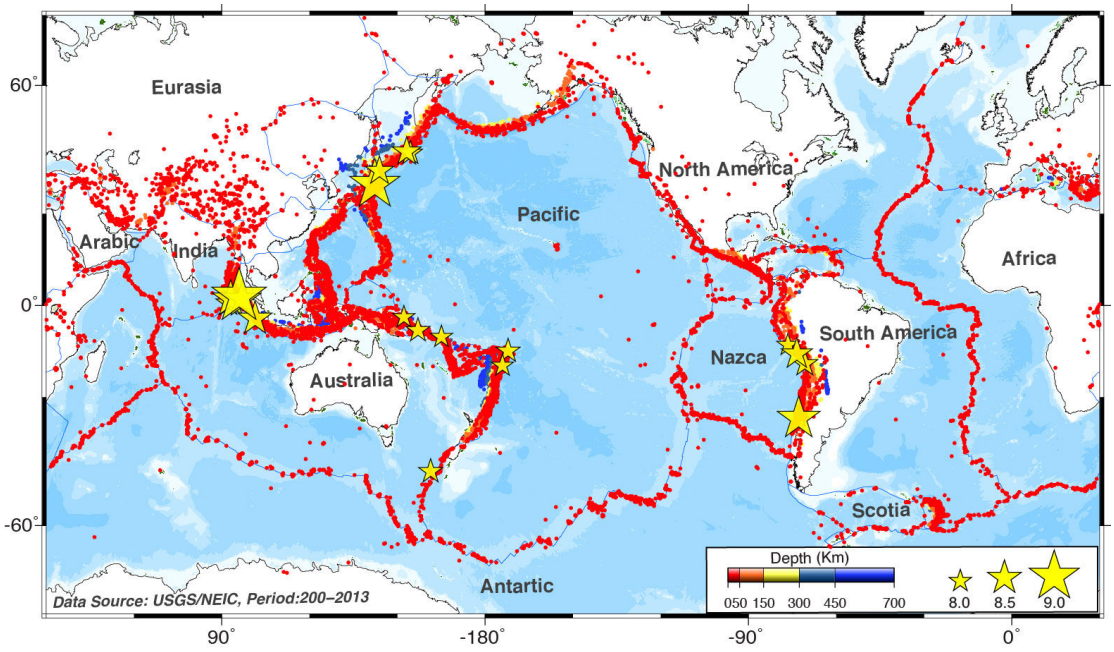

Figure 1.1: Global distribution of earthquakes for the period 2000–2013 of magnitudes M≥5.0 extracted from the NEIC catalog (http://earthquake.usgs.gov/earthquakes). Earthquakes are represented by dots and plotted in function of depth according to the color bar. Shallow events (<50km) delineate the plate boundaries. During this period up to 17 events of M>8.0 occurred in various subduction zones. The scaled stars indicate their location and magnitude.

In the following paragraphs, I present the main concepts of the earthquake cycle in subduction zones, describing the principal phases of the cycle with its associated crustal deformation. I briefly present recent discoveries of transient slip events that add-up more insights to the complexities of the seismic cycle. Then, I introduce the main aspects of the geological and seismotectonic setting of the Peruvian subduction zone and present a state of the art of previous geodetic studies carried out in Peru. Finally, I state the main questions that this thesis tries to answer and present the contents of this manuscript.

2. Earthquake cycle

2.1. The birth of the concept of the earthquake cycle

Probably the first observations that describes and quantifies the characteristics and effects of a great subduction earthquake and tsunami relating them to a cyclic behavior were done by Charles Darwin during the *Voyage of the Beagle* (1831 - 1836). During that expedition, in 1835 he was onshore near Valdivia in Chile, when a great earthquake occurred near the Concepcion city (~300 km to the north). Darwin's description indicates that the shaking lasted about 2 minutes with a trend motion in an eastward direction. He also found that rocks lined with recent marine shells were elevated above the tide after the earthquake. Uplifts measurements along the coast were of ~1 m with a maximum of ~3 m at the Santa Maria island [*Darwin et al.*, 1846]. During expedition into the pre-Cordillera he discovered a series of remaining marine shells at 2000 m of altitude, proof that the shifting that had uplifted the coast during the earthquake may have occurred over and over to bring shells to that altitude. The eyewitness testimony of Darwin suggested that the Andes of South America were very slowly rising and its growth was linked to the earthquakes occurrence.

We know today that earthquakes result of a sudden slip at the interface of two plates boundary moving relatively one to each other in the long term. In the simplest concept of the seismic cycle, a fault remains locked and accumulates stress during the interseismic period, which is totally or partially released by seismic slip. In this view, the amount of seismic slip equals the cumulated plate convergence of the plates during the interseismic period. This concept known as the elastic rebound model was introduced by *Reid*, [1910] after the M7.8 San Francisco 1906 earthquake that ruptured a segment of the San Andreas Fault (Figure 2). He hypothesized that the Earth's crust behaves like an elastic solid driven by forces at a constant rate, rupturing in earthquakes at periodic intervals. Under this concept, if the date of the last great earthquake is known, using the rate of relative motion determined by geodesy, it is possible then to make some prediction about the slip deficit to be caught up in the next earthquake.

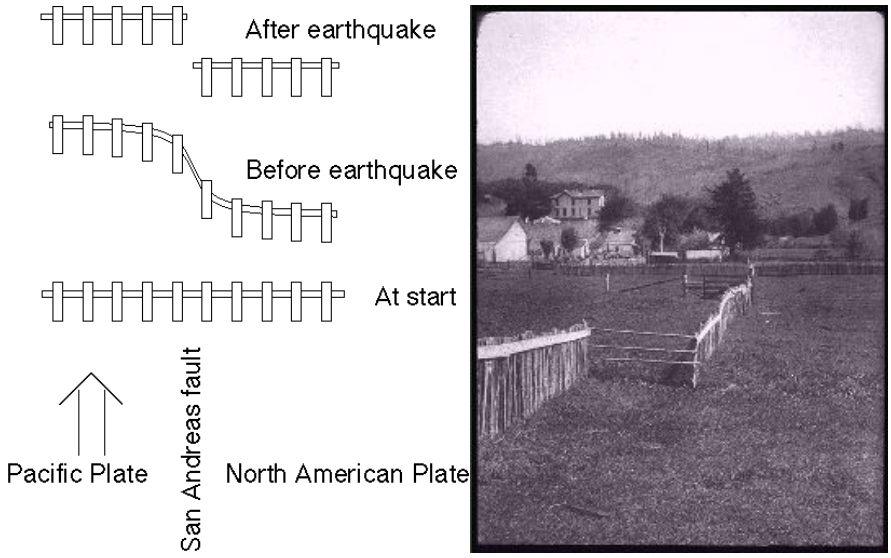

Figure 1.2: Left: Schematic representation of the elastic rebound model after Reid, [1910]. Right: picture showing a fence that was offset due to the fault slip during 1906 San Francisco earthquake. USGS image: (http://earthquake.usgs.gov/regional/nca/1906/18april/reid.php).

Reid went a step further. He also showed that the static displacement observed after the San Francisco 1906 earthquake followed the prediction of a rupture dislocation in an elastic medium. Since the sum of the interseismic and co-seismic slip should be equal to the long-term relative displacement of plates, the interseismic strain should reflect the stress accumulation along the fault. During the interseismic period, the ground deforms smoothly in a manner that depends on the relative plate velocities, the elastic plate rigidity and the thickness of the elastic plate. The size of an earthquake on a fault would depend on the length and depth of the locked fault zone, and the recurrence time suspected on that fault would depend on how much strain had built up since the last one.

2.2. Earthquake cycle in subduction zone

2.2.1. Phases of the earthquake cycle

The concept of the earthquake cycle was initially applied for the case of continental faults (i.e. strike-slip type), and then adapted to the subduction zone context. *Fedotov*, [1967] introduced the 'seismic cycle' expression to describe the

cycle of elastic deformation during and between large (Mw>8.0) megathrust earthquakes. In this model, the seismic cycle was characterized by two principal phases of deformation: A permanent interseismic phase and a transient coseismic phase

2.2.1.1 The interseismic phase

This phase corresponds to the period where seismic asperities on the megathrust are locked during decades to hundreds of years. The plate convergence induces a slip deficit in the locked fault zone that accumulates stress on the plate interface and deforms the overriding plate. The horizontal surface deformation is characterized by GPS gradients of the order of mm/yr to cm/yr, which decrease as the distance from the trench increases. The vertical deformation pattern is characterized by a subsiding area linked to the updip limit of the locked fault zone followed by an uplifted area linked to the downdip limit of the locked fault zone (Figure 1.3B). The width of the locked fault zone controls the wavelengths and the level of locking controls the amplitudes of the displacements.

2.2.1.2. The coseismic phase

The coseismic phase corresponds to the seismic rupture when sudden slip occur on the megathrust interface. The moment deficit accumulated during the interseismic phase was supposed in the first models to be totally released during the tens of second to minutes of rupture. For large earthquake in 0-50km depths, the surface displacements are typically of the order of decimeters to meters. The pattern of deformation observed during this phase is opposite in sign of the pattern observed during the interseismic period.

This is only later, that a third major phase of the seismic cycle called the postseismic period has been introduced to explain the relaxation processes that follow large earthquakes [*Brown et al.*, 1977; *Bürgmann et al.*, 1997; *Heki et al.*, 1997]. Each phase of the seismic cycle is well characterized by a specific signature of the Earth crust deformation with amplitudes and wavelengths varying in order of magnitude.

Figure 1.3 shows a simplified schematic representation of the three main phases of the seismic cycle together with the associated predicted horizontal and vertical displacements produced with forward elastic dislocation models.

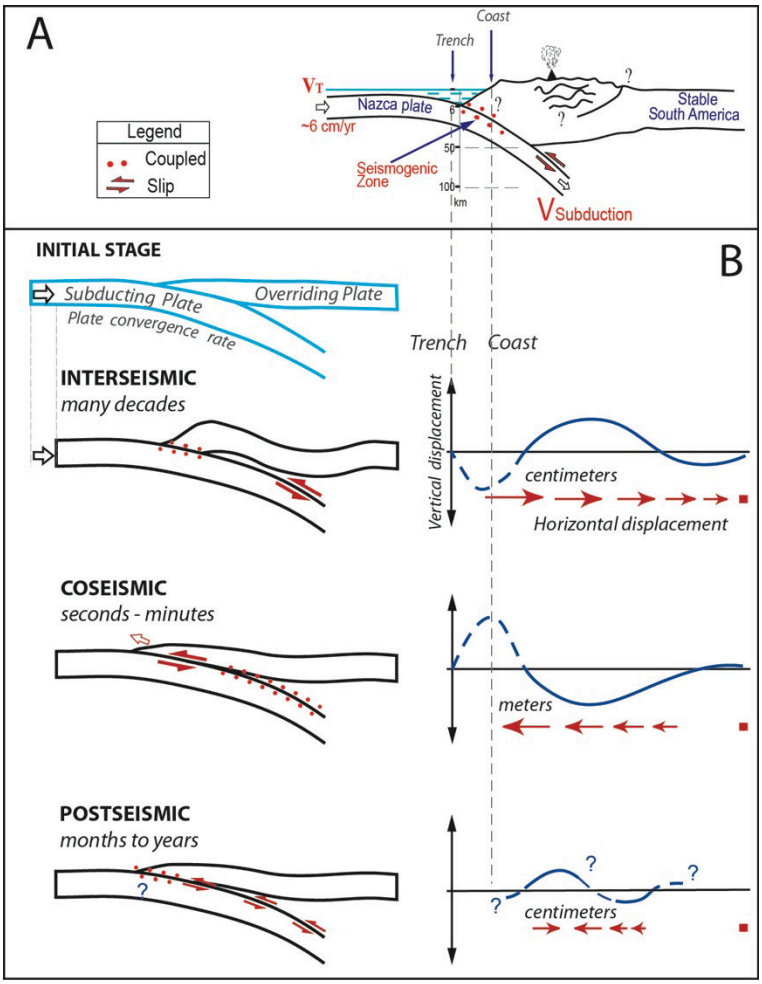

Figure 1.3: A: Schematic cross-section of the South American subduction zone. B: Schema showing the main phases of the seismic cycle and its associated horizontal (red arrows) and vertical patterns of deformation (blue line). We consider a stable South America reference frame.

Using an elastic rheology for the earth Lithosphere, we can relate the locking at a specific elementary fault with respect to the displacement components at any site on the surface. A widely used approach to mimic the inter-seismic behavior of a locked fault segment is the back-slip model introduced by *Savage*, [1983]. In this model, the interseismic pattern of deformation is the sum of two terms, the first being a rigid plate motion where an oceanic plate subducts beneath the overriding plate at a fixed plate velocity, plus a slip in the opposite plate convergence direction (back-slip) in the

region supposed to be locked (Figure 1.4). The back-slip rate equals the plate convergence rate when it is fully locked but can be a fraction of it for partial locking. Using the analytical equations of Okada that link the 3D surface displacements with elementary source points embedded in an elastic half-space, we can retrieve the characteristics of the source from surface displacement measurements [*Okada*, 1985, 1992].

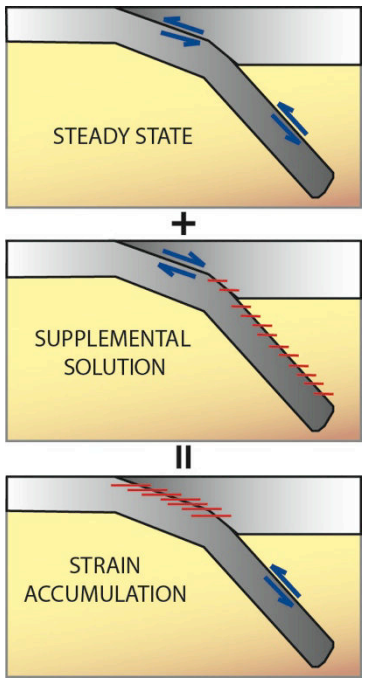

Figure 1.4: Schematic representation of the back-slip model showing the superposition of a stable steady state at plate convergence rate and a supplemental solution that is slip normal to the plate convergence at the same rate, resulting in locking and strain accumulation at the subduction interface during the interseismic period. Gray areas correspond to the tectonic plates and colored area to the asthenosphere. Figure modified after Savage, [1983].

Dislocations solutions, either analytical for a semi-infinite homogeneous elastic half-space or numeric for an heterogeneous elastic half-space, can then be used to predict the 3-D displacement at GPS sites. An inverse problem, relating the GPS displacement to the amount of normal slip at each elementary sub-fault of the interface can then be setup to derive a model of the back-slip rate. The ratio of the back-slip rate divided by the plate convergence defines the interseismic coupling coefficient.

2.2.2. Transient phases of the earthquake cycle

Numerous transient deformations have been observed during the seismic cycle. After large earthquakes, a postseismic deformation takes place in the form of rapid afterslip at the plate interface that generate aftershocks and visco-elastic relaxation of the Lithosphere that can spend decades for the greater Mw9-type earthquakes. Similarly, slow slip events lasting from days to several years and releasing energy comparable to moderate magnitude earthquakes are reported frequently since the beginning of the XXIth century in most subduction zones.

2.2.2.1. Postseismic deformation

The postseismic deformation refers to the deformation that occurs in the months to decades after an earthquake (Figure 1.5), and is attributed to three different processes: *i) Afterslip*, that is the frictional response of the plate interface propagating around the rupture area stressed by the coseismic slip; this process is usually thought to occur during the first stage of the post-seismic phase (days to years). *ii) Viscoelastic relaxation,* which is the viscous response of the upper mantle and lower crust to the rapid stress increment induced by the coseismic rupture; this process can last up to more than 50 decades as observed for the 1960 M9.5 Chile earthquake [*Wang et al.*, 2012]. *iii) Poro-elastic effect,* that is deformation induced by fluids flow in response to the coseismic stress change [*Jonsson et al.*, 2003]. The slip during this period can release as much moment as the earthquake itself [*Bürgmann et al.*, 2001]. Permanent measurements of the postseismic deformation help to constraint the principal characteristics of the frictional parameters of the plate interface and the rheology of the surrounding medium [*Perfettini and Avouac*, 2004; *Perfettini et al.*, 2010].

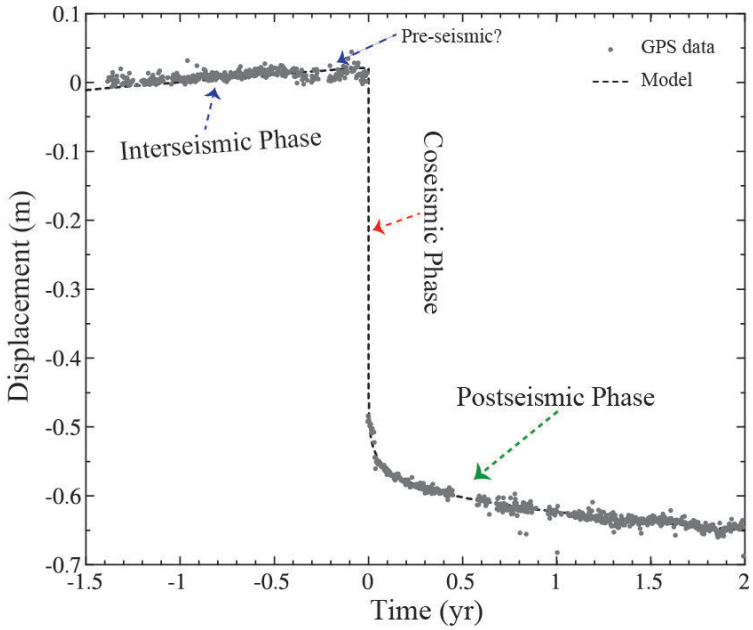

Figure 1.5: Displacement in a N55ºE direction of the GPS station AREQ showing the displacement associated with the 2001 Mw=8.4 Arequipa earthquake. The tree main phases of the seismic cycle are evidenced here (Figure adapted after [*Perfettini et al.*, 2005]).

2.2.2.2. Slow Slip Events (SSE)

Slow Slip Events (called also silent or slow earthquakes) are slip episodes that occur during the interseismic period and are characterized by long-lasting slips with duration typically ranging from days to years (Figure 1.6). Slip occurs without radiating detectable seismic energy and induces surface displacements of several millimeters to centimeters [*Schwartz and Rokosky*, 2007]. This type of events has started to be detected since the deployment of continuous GPS networks in subduction zones, principally in Cascadia and Japan, where they are observed to occur in the downdip portion of the seismogenic zone [*Dragert et al.*, 2001; *Ozawa et al.*, 2001]. The progressive deployment of GPS together with sensitive seismic networks in various subduction zones has evidenced that SSE would be a common process including a series of episodic transient. Some slip events are synchronous to tremor or low frequency earthquakes emitting low seismic radiation [*Ide et al.*, 2007; *Peng and Gomberg*, 2010]. Recent observations of SSE suggest that these events can also occur in the shallow part of the of the seismogenic zone [*Walter et al.*, 2011]. The modeled sources are consistent with slip on the plate interface, accommodating the relative plate motion and contributing to release the accrued stresses. The geodetic moment released by SSEs is equivalent to earthquakes of magnitude from ~6.0 to 7.6

Mw, as the observed in Cascadia, Japan, New Zealand, Ecuador and Mexico [*Dragert et al.*, 2001; *Douglas et al.*, 2005; *Vallée et al.*, 2013].

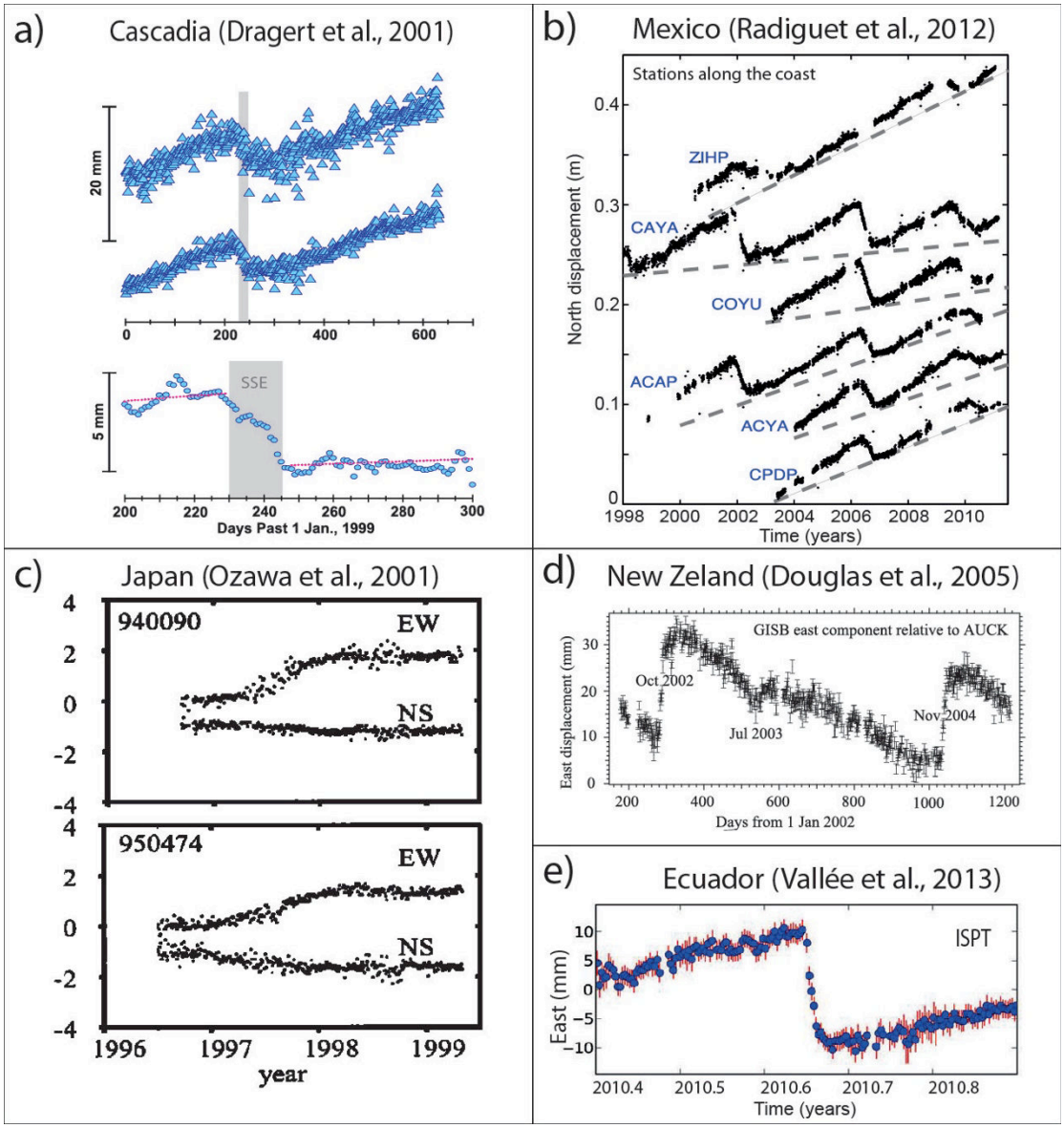

Figure 1.6: GPS time series showing Slow Slip Events recorded in different subduction zones of the world. One of the most classical examples of SSE occur in Cascadia where they use to last several weeks and recur with a periodicity of around 14 months, releasing stress equivalent to Mw=6.7 earthquakes [*Dragert et al.*, 2001]. In Mexico in 2006 occurred the largest SSE recorded so far, it was equivalent to an earthquake Mw=7.6Mw [*Radiguet et al.*, 2012]. Similarly, SSEs reported in Japan and New Zealand last various months to years and as the previous regions they occur in the downdip of the seismogenic zone [*Obara*, 2002; *Douglas et al.*, 2005]. A different type of SSEs occurring in the shallow portion of the seismogenic zone are characterized by short durations and associated microseismicity. This new type of events have been documented in the Northern Hikurangui [*Wallace and Beavan*, 2010], the Boso Peninsula and recently in Ecuador [*Vallée et al.*, 2013].

Another type of transient deformation, termed as Preseismic deformation, has also been reported in few particular cases during the weeks to days before large earthquakes [*Ruegg et al.*, 2001; *Melbourne and Webb*, 2002; *Ruiz et al.*, 2014]. This deformation is believed to act as an acceleration of the slip in the bounds of the locked fault portion. This process is sometimes associated to an increase in the rate of seismicity (Figure 1.5).

All these features add more complexities to the anatomy of the subduction interface and the mode of stress accumulation and release that vary in space and time, thus a diversity of deformation processes are expected during the earthquake cycle.

2.3. Nature of the subduction interface

The seismogenic zone is the portion of the plate interface where earthquakes nucleate via stick-slip sliding [*Brace and Byerlee*, 1966]. A current view, is that the anatomy of the plate interface is made of an inter-fingering of areas that are locked accumulating stress and strain during the interseismic period –named asperities- that will rupture during an earthquake. They are surrounded by areas that are partially or weakly locked, that either could facilitate post-seismic slip and/or either arrest the coseismic rupture, those areas that arrest laterally the rupture are named barriers [*Schwartz and Rokosky*, 2007; *Kaneko et al.*, 2010]. According to the frictional properties of the materials the asperities that undergo unstable regime are characterized by a velocity weakening behavior, while weakly locked areas and barriers that undergo conditionally stable and stable regime are characterized by a velocity strengthening behavior [*Scholz*, 1998] (Figure 1.7).

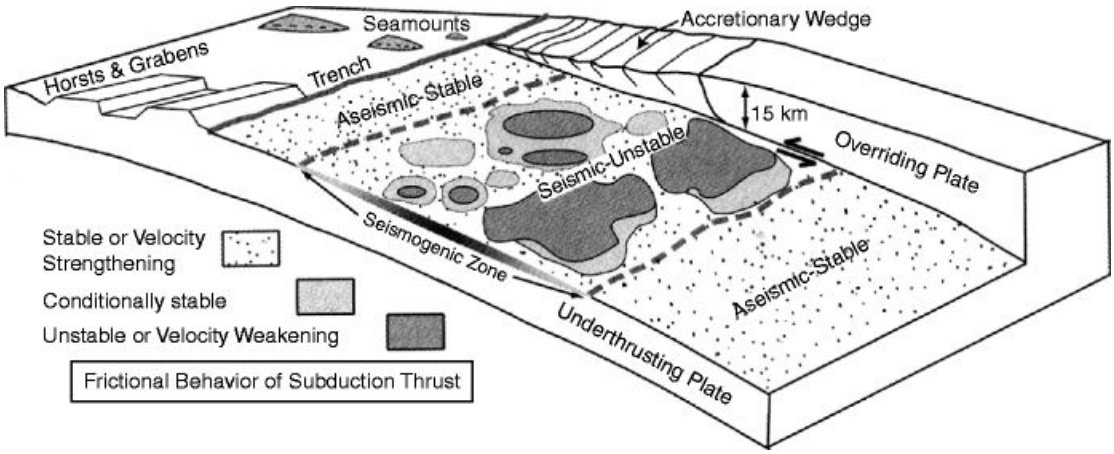

Figure 1.7: Simplified illustration of the subduction interface environment showing the heterogeneous distribution of asperities (velocity weakening material) surrounded by areas that undergo a conditionally stable regime both embedded in a stable or velocity strengthening material. Figure from: Bilek, [2010] and Hasegawa, [2014].

3. The Subduction zone in Peru

Along the Colombia-Ecuador-Peru-Chile trench the oceanic Nazca plate subducts beneath the South American continent at a rate of 5.3 cm/yr in Colombia (lat. 6ºN) increasing gradually southward up to 6.3 cm/yr in south central Chile (lat. 30ºS) in a N78ºE average direction [*Kendrick et al.*, 2003]. The South America subduction zone is one of the most seismically active areas in the world. This rapid convergence has generated three among the seven greatest subduction earthquakes (M≥8.8) ever recorded (Colombia-Ecuador 1906, Chile 1960 and 2010) and almost its entire length has ruptured through several large (M≥8.0) earthquakes [*Bilek*, 2010]. The Peruvian subduction zone, where I focus my study, is located in the central part of the Andean subduction (from 3ºS to 19ºS), extending over ~2300 km long that constitutes about a third of the total length of the Nazca/South America subduction. In the next paragraphs I present a brief description of the geological and seismotectonic context of the Peruvian subduction margin.

3.1. Geological context of the Peruvian subduction zone

The subduction in Peru is believed to have been ongoing since the early Jurassic (~200Ma) [*Mégard*, 1978]. The current tectonic configuration of the Andes is attributed to compressional and transpressional episodes during the Cenozoic

evolution of the plate boundary. The main tectonic characteristics vary both parallel and perpendicular to the strike of the trench (Figure 1.8).

Among the along-strike variations, there are remarkable bathymetric features on the subducting Nazca plate entering the trench that are believed to play a role in the segmentation and seismotectonics of the Peruvian subduction margin. From north to south these structures are: the Grijalva (GR), Alvarado (AR), and Sarmiento (SR) ridges, the Virú (VFZ) and Mendaña fracture zones (MFZ), the Nazca ridge (NR), and the Nazca fracture zone (NFZ). At the trench, the age of the oceanic plate increases gradually from ~30 Myr (Oligocene-age) in front of the Gulf of Guayaquil, to 54 Myr (Eocene-age) offshore the Arica bend. The MFZ, NR and NFZ correlate with rapid positive changes in the age of the plate (Figure 1.5).

The presence of these structures together with the occurrence of large earthquakes led authors to divide the Peruvian subduction zone into three segments: the north, the central and the south segments, being the MFZ (Lat. 9ºS) and the NR (Lat. 14ºS) the structures delimiting the central segment from the north and south segments [*Kelleher*, 1972; *Beck and Ruff*, 1989; *Dorbath et al.*, 1990]. Moreover, seismological studies have evidenced two distinct modes of subduction in Peru. In the southern segment (south of 15ºS) the slab is steeply dipping with an angle 20-30º diving into the mantle, while in central and northern Peru the slab dips gently with an angle of 10º to 20º up to a depth of about 100 km where it becomes flat over an extension of about 300 km width and 1500 km along-strike long [*Barazangi and Isacks*, 1976; *Cahill and Isacks*, 1992]. Active volcanism is only present in southern Peru where steeply dipping subduction exits.

Perpendicular to the strike of the trench the structural style of the Andean subduction margin is characterized by five main tectonic regions [*Dalmayrac*, 1978]

3.1.1 The Trench and Coastal zone

This zone extends from the trench up to the western boundary of the Andean Cordillera. This region is the primary target to study most of the processes related to the plate convergence (interplate coupling, deformation of the overriding plate, seismic and aseismic slip, etc.). The offshore portion shows lower rates of sediment

deposition, and a small or restricted presence of the accretionary prism [*von Huene and Lallemand*, 1990; *Krabbenhöft et al.*, 2004; *Heuret et al.*, 2012]. The onshore portion in northern Peru consists of gently folded Mesozoic volcanic and sedimentary rocks [*Suarez et al.*, 1983; *Megard*, 1984], in central and southern Peru the intense deformation lead to outcrops of strongly folded crystalline basement and extensional and compressional faulting around the Altiplano [*Megard*, 1984; *Machare and Ortlieb*, 1992; *Sempere et al.*, 2004].

3.1.2. The Occidental Cordillera

It is a high mountain range of about 150km width and elevations from 3500 to 5000 m being bounded by trench-coastal zone and the Altiplano. This region is dominated by the coastal batholith consisting in multiple intrusions, although intense volcanism since the late Eocene masks part of the central and the southern region. The older units show effects of compressive deformation presumably occurred during the late Eocene to Miocene [*Mégard*, 1978; *Wipf*, 2006].

3.1.3. The Altiplano

It is a high plateau at a mean elevation of 4000 m and a maximum width of 450 km that is bounded by the oriental and occidental cordilleras. It is composed of thick deposits of Paleozoic and Mesozoic marine and continental sedimentary rocks that were compressed and folded during the early Cenozoic [*Mégard*, 1978]. In Peru, there is evidence for quaternary normal and strike-slip faulting over the last 1 Myr but with negligible submetric displacements [*Suarez et al.*, 1983].

3.1.4. The Oriental Cordillera

It is a mountain range that reaches elevations of ~4000 m and a width that increases from north to south from ~100 to 150 km width. It is composed of crystalline and plutonic rocks overlain by Paleozoic shallow marine and continental deposits [*Dalmayrac*, 1978]. The main structures in the region include open folds and steep thrust faults. Seismic and geologic data indicate that tectonics in the eastern

edge is predominantly thrust with components of strike slip and normal faulting [*Suarez et al.*, 1983; *Barke and Lamb*, 2006].

3.1.5. The Sub-Andean Fold and Thrust Belt

This is the region of present day most active deformation occurring in the Andes. It is characterized by active thin-skinned thrusting since at least the Pleistocene [*Mégard*, 1978; *Suarez et al.*, 1983]. Focal mechanisms analysis of recent shallow crustal earthquakes (< 60 km) in this region are consistent with thrust faults steeply dipping (30-60º) to the west becoming shallower toward the south [*Suarez et al.*, 1983; *Devlin et al.*, 2012]. Post-Oligocene crustal shortening is probably the dominant process for thickening the Andean crust, although shortening has migrated Eastward with time from the Altiplano in the Miocene to its present position to the East in the Sub-Andean zone [*Suarez et al.*, 1983; *Isacks*, 1988].

Geologic shortening rates averaged over the past 10 Ma to present in the Andes exceed 10 mm/yr, contrasting with the shortening estimated from GPS 5-10 mm/yr [*Norabuena et al.*, 1998; *Bevis et al.*, 2001; *Brooks et al.*, 2011; *Chlieh et al.*, 2011], and shortening rates estimated from the seismic energy released by major crustal earthquakes range between 2 to 3.8 mm/yr [*Suarez et al.*, 1983; *Dorbath et al.*, 1991].

Recent compilations of quaternary faults [Macharé et al., 2003; Veloza et al., 2011, and http://neotec-opendata.com] evidence reverse active faulting all along the sub-andean domain through thrust and folds belts, while within the Andes the deformation shows a complex pattern with reverse, normal and strike-slip faults.

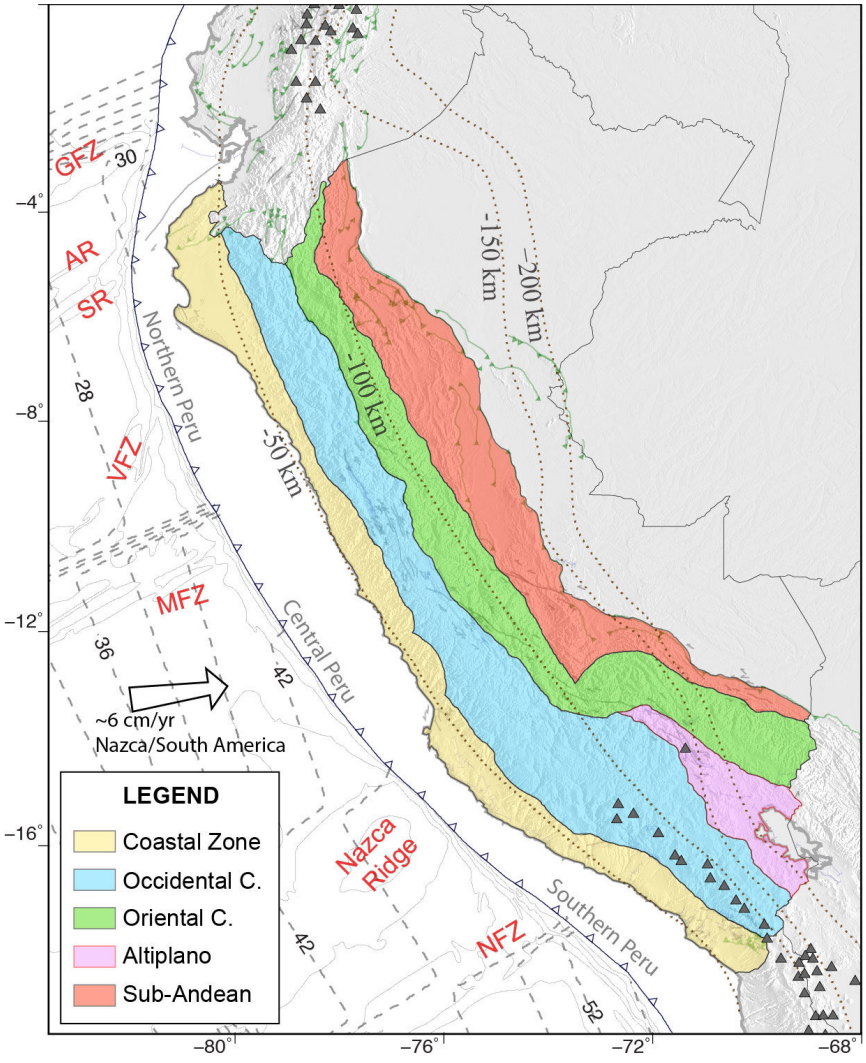

Figure 1.8: Main elements of the geotectonic context of the Peruvian subduction zone. The structures on the Nazca plate subducting into the trench are: the Grijalva Fracture Zone (GFZ), the Alvarado (AR) and Sarmiento ridges (SR), the Virú (VFZ) and Mendaña Fracture Zones (MFZ), the Nazca Ridge (NR) and the Nazca Fracture Zone (NFZ). The NR and the MFZ delimit the central subduction segment from the north and south segments, respectively. Dashed lines represent the 2-Ma contours of the age of the oceanic Nazca plate and dotted lines represent 50-km iso-surface contours of the subducting slab from the Nazca plate [*Hayes et al.*, 2012]. Triangles denote Holocene volcanic centers. Modified from Dalmayrac, [1978; and Carlotto et al., [2009].

3.2. Overall characteristics of large earthquakes along the Peruvian subduction zone

The historical earthquake catalogs for Peru date back to the 16th century, since the Spanish conquest, and they are based on reports, narrations and chronicles from civil and ecclesiastic authorities [*Silgado*, 1978]. The compilation of historical large earthquakes highlights a drastically different behavior of the earthquake cycle from

south to north [*Dorbath et al.*, 1990]. While in the southern and central Peru segments large earthquakes (M≥8) occurred with a recurrence interval of ~100 to 250 years, the northern segment shows a sparse and rare occurrence of lower to moderate (M≤~7.5) magnitude events [*Kelleher*, 1972; *Beck and Ruff*, 1989; *Dorbath et al.*, 1990; *Nishenko*, 1991; *Bilek*, 2010]. According to chronicles the largest events ever known in Peru occurred in 1746 in the central segment and in 1604, 1868 in the southern segment. These events generated devastating tsunamis, whose magnitude were used to infer moment magnitudes of 8.6, 8.7 and 8.8, respectively [*Dorbath et al.*, 1990]. For northern Peru, chronicles only report a moderate event that occurred in 1619 near Trujillo (estimated in 7.7Mw) and another moderate event occurred in 1912 near Piura though their attribution to interplate events remained uncertain [*Dorbath et al.*, 1990] (Figure 1.9).

Instrumental records of large subduction earthquakes in Peru started with the 1913 (7.8M) earthquake in the southern segment (~17ºS, near Nazca). This event was preceded by a foreshock of M~7.0 nine days before [*Abe and Noguchi*, 1983]. Three larger earthquakes within this segment occurred in 1942 (~8.0M) and 1996 (7.6Mw) near Nazca, and 2001 (8.4Mw) near Arequipa [*Swenson and Beck*, 1999; *Salichon et al.*, 2003; *Pritchard et al.*, 2007; *Chlieh et al.*, 2011], rupturing almost the entire segment except by a remaining length of 150–200 km of the southernmost rupture area of the 1868 (8.8 Mw) earthquake (Figure 1.9). In the central Peru segment a sequence of four large earthquakes occurred in 1940 (8.0Mw) near Huacho, 1966 (8.0Mw) Casma, 1974 (7.9Mw) Lima, and 2007 (8.0Mw) Pisco [*Beck and Ruff*, 1989; *Sladen et al.*, 2010], rupturing almost the entire central segment, although their magnitudes only represent a fraction of the seismic moment released by the 1746 ~8.6Mw) [*Beck and Nishenko*, 1990; *Chlieh et al.*, 2011]. In the northern Peru segment the records of large earthquakes only show moderate magnitude earthquakes, confirming the particular behavior seen during the historical period. These events occurred near Tumbes in 1953 (7.8Mw) and 1959 (7.5Mw), Piura 1960 (7.6Mw) and Chimbote 1996 (7.5Mw) [*Pelayo and Wiens*, 1990; *Ihmle et al.*, 1998; *Bourgeois et al.*, 1999]. The two latter, due to their slow rupture velocity, long source time duration and tsunamis significantly greater than expected, were categorized as tsunami-earthquake type events.

3.3. Further research of historical earthquakes in northern and central Peru

It appeared useful to further investigate the earthquake history of Peru, especially of its northern segment. I noticed that recent compilations of subduction thrust or tsunamigenic earthquakes [*Dorbath et al.*, 1990; *Bilek*, 2010] do not include the 1953 (7.8M) and 1959 (7.5M) events of northern Peru. However we notice that tsunami catalogs report local tsunamis for these events with runup > 1 m near Tumbes and southern Ecuador (Lat. 3°S - 4°S) [*NGDC http://www.ngdc.noaa.gov*, n.d.; *Soloviev and Go*, 1975; *Lockridge*, 1985; *Espinoza*, 1992]. Tsunami observation suggests that these events originated at the plate interface and that they must be included in future catalogs. Another particular case is the 1619 event (~7.5M, Lat. 8ºS), which was not associated with a tsunami in the historical catalogs [*Silgado*, 1978; *Dorbath et al.*, 1990], remaining its origin as a doubt. A recent paleotsunami study by [*Spiske et al.*, 2013], found evidence of tsunami deposits layers in the coast of Casma (Lat. 9°S) with an age of 370 ± 30 yrs, which seems to correlate with the 1619 earthquake, suggesting that this events can be classified as an interplate event.

Additional information of historical earthquakes for Peru comes from an exhaustive revision of the chronicles and reports of historical earthquakes done by Seiner, [2009, 2011]. We found that several historical events documented by Seiner, [2009, 2011] were not included in the widely used catalog of Silgado, [1978] on which most seismological studies rely. Two significant events are worth to be added to the history of subduction large earthquakes in Peru. The first occurred in northern Peru in 1759 causing destruction, five casualties and severe damages in the Trujillo region. The chronicles compare this event with that occurred in 1619. The second occurred in 1806 near Lima, causing destruction and disturbances in the sea in front of the Callao port where some vessels were pulled out from the sea, suggesting that a tsunami was associated to this event. For these 2 events there is no a magnitude assigned but based on the intensity and tsunami characteristics, a magnitude of the order of ~7.5Mw or even greater is plausible. Figure 1.9 shows an updated temporal and spatial distribution of large (M>7.5) historical and recent earthquakes since 1513 to date for the entire Peruvian subduction zone.

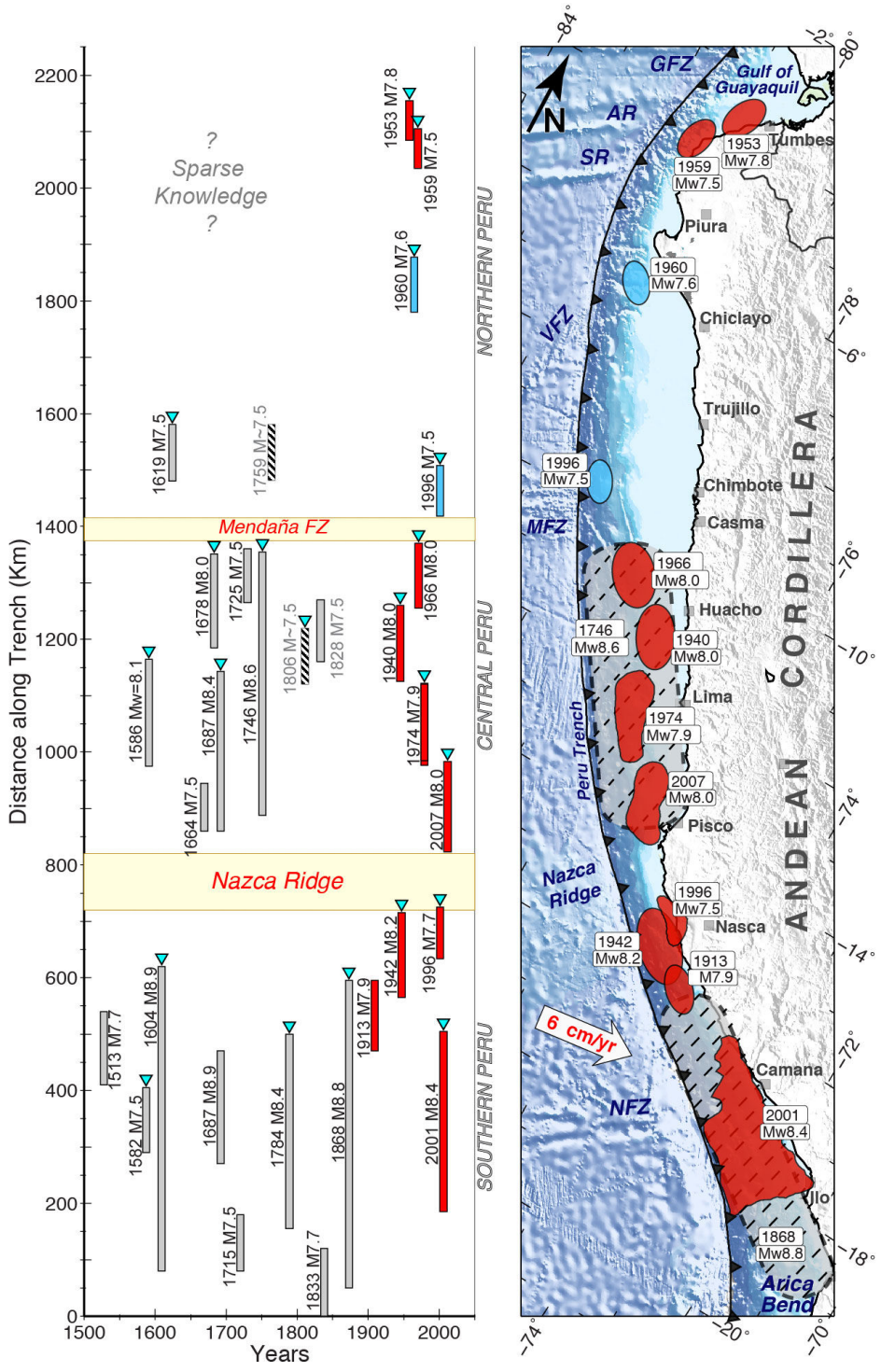

Figure 1.9: Updated compilation of large earthquakes occurred along the Peruvian subduction zone. Left: Rupture length as a function of time of large historical and instrumental earthquakes with M>7.5 occurred since the XV century. Right: Seismotectonic setting of the Peruvian subduction zone, showing the rupture area of large earthquakes occurred during the last century, blue polygons are events that were characterized as tsumami-earthquakes. Polygons in gray represent the approximate rupture area of the greatest 1868 (south) and 1746 (central) events. See text for more details.

The background seismicity (M<7) in the Peruvian subduction for the last 5 decades appears to be uniformly spatially distributed all along the margin (Figure 1.10) (ISC reprocessed catalog (http://www.isc.ac.uk/)). Figure 1.10B shows a comparison of the number of events every 0.2º of latitude and their seismic moment released for events of magnitude M≥4.5 since 1960 to 2012. We note, however, that the earthquakes occurred in the northern segment does not release significant stress as large earthquakes do. A cluster of seismicity is distinguished at the entrance of the Nazca Ridge. *Holtkamp et al.*, [2011] using a global earthquake catalog identified this and a series of swarms along the Nazca South America subduction, and suggested that the swarms are related to segments that undergo aseismic slip.

In general, this panorama shows that the northern Peru subduction segment remains as the sole portion of entire South American subduction where no large earthquake (M>8) occurred at least since the XVI century. Whether the convergence is being accommodated through aseismic processes, that is the plates are practically freely sliding one respect to each other, or whether the strain is accumulating over several centuries to produce a very large earthquake in the future is one of the questions that has remained unknown so far. In this manuscript I address this issue.

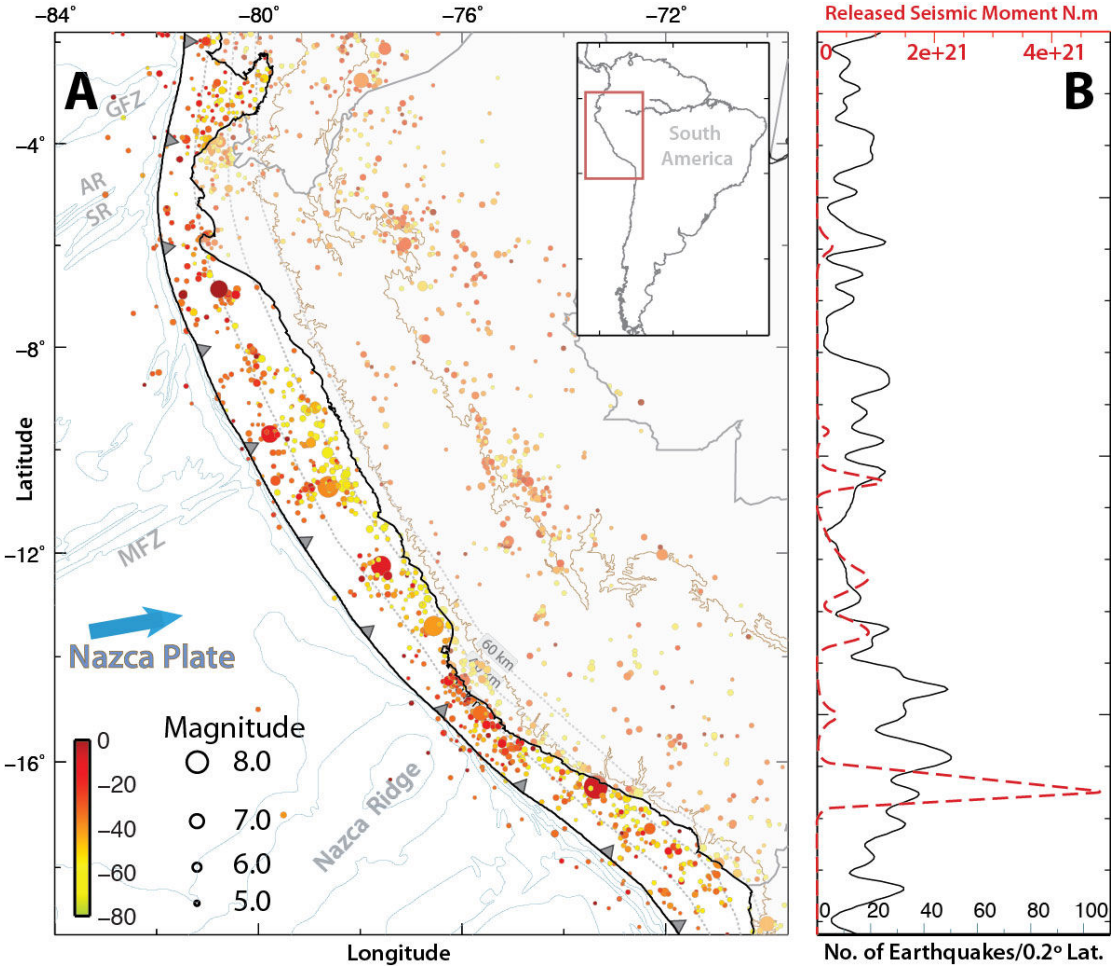

Figure 1.10: A: Spatial distribution of the shallow (<70 km) seismicity extracted from the ISC declustered catalog for the period 1960-2012. Sized circles show the events of magnitude M ≥ 4.5. B: Continuous line indicates the number of shallow earthquakes located in the seismogenic zone every 0.2º of latitude and red dashed line the seismic moment released by such events.

4. Previous studies using space geodesy (GPS) in the Peruvian Subduction

Spatial geodetic studies in the South American subduction zone have been carried out in almost the entire margin of the subduction zone including Colombia, northern Ecuador, central and southern Peru and Chile. These studies have evidenced for a generally high level of interseismic coupling. Moreover, these studies evidenced a long-term deformation of the continental lithosphere, which is accommodated by crustal deformation and mountain building via crustal shortening in the sub-Andean region [*Norabuena et al.*, 1998; *Bevis et al.*, 2001; *Kendrick et al.*, 2001; *Trenkamp et*

al., 2002; *Brooks et al.*, 2003; *Chlieh et al.*, 2004; *Ruegg et al.*, 2009; *Moreno et al.*, 2010; *Vigny et al.*, 2011; *Métois et al.*, 2013].

The first GPS measurements carried out in Peru, specifically in the central and southern regions, initiated in 1994 with the SNAPP project [*Norabuena et al.*, 1998]. In that study the authors showed the simultaneous contributions of locking at the plate interface and the remaining deformation on the overriding plate contributing to the Andean mountain building via crustal shortening. *Bevis et al.*, [1999] analyzed previous results and suggested a bias of 50% of the velocity field proposed by *Norabuena et al.*, [1998] due to an issue in the definition of the reference frame, that then impact the level of locking at the plate interface. In 2005 *Gagnon et al.*, [2005] published one of the first studies using sea bottom geodesy in a subduction zone, offshore central Peru. They combined sea bottom geodetic measurements with land based GPS along a profile and found that the shallow part of the plate interface is highly locked from 2 to a depth of 40 km, therefore suggesting that central Peru can host large earthquake and tsunami. More recently *Chlieh et al.*, [2011] compiled previous studies observations to model the interseismic coupling at the plate interface and compute the seismic source of recent large earthquakes in the central Andes subduction zone. They found that the plate interface is heterogeneously locked and that areas undergoing high interseismic coupling were loci of rupture areas of past large earthquakes. They hypothesized that if all the stress accumulated before the 1868 and 1746 events (M>8.6) had entirely been released with these events, the moment deficit accumulated since those great earthquakes is high enough to produce similar size events. They further show that the 7 M~8.0 events occurred in central (1940, 1966,1974, 2007) and south (1942, 1996, 2001) Peru only released a fraction of the slip deficit, still leaving the potential for earthquakes of large magnitude in these segments.

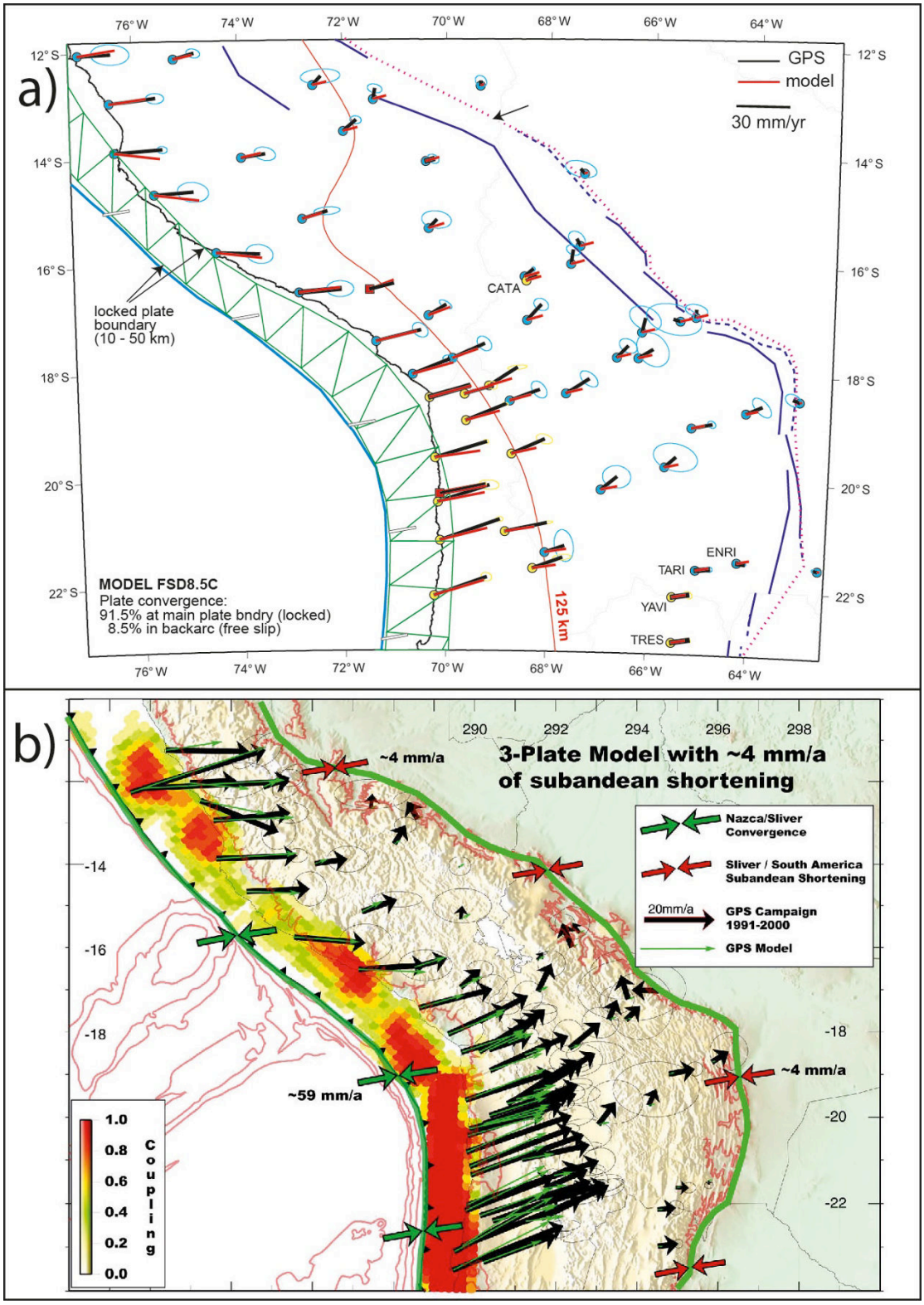

Figure 1.11: Interseismic GPS velocities and coupling models for the central Andes subduction zone. a) Velocities are compared with the prediction of simple uniform model produced by elastic loading of the upper plate in response to locking on the plate interface [*Bevis et al.*, 2001]. b) Distribution of interseismic coupling on the megathrust derived from the inversion of GPS velocities. The model shows that the pattern of interseismic coupling is heterogeneous. [*Chlieh et al.*, 2011].

Understanding the problem of partitioning in subduction zones has been evidenced to be fundamental. In subduction zones where the plate convergence is oblique, as it is the case in Central America, south of Chile or Sumatra, major strike-slip lateral faults in the back of the forearc are found parallel to the trench axis accommodating the lateral motion of large continental slivers [*Mccaffrey*, 1992; *Wang et al.*, 2007]. In the Central Andes the problem of partitioning has been adopted in terms of shortening in the Sub-Andean fold and thrust belt [*Norabuena et al.*, 1998; *Bevis et al.*, 2001; *Chlieh et al.*, 2011]. Other studies adopt this issue in terms of a sliver motion [*Métois et al.*, 2013]. Those approaches are usually adopted for subduction segments where a clear volcanic forearc and major faults systems accommodating are present.

The northern and central Peru subduction segment also shows oblique convergence, however, it is characterized by the absence of a volcanic forearc. Despite obliquity has been suspected to induce significant trench-parallel motion [*Dewey and Lamb*, 1992; *Veloza et al.*, 2011], the partitioning has not been well characterized nor demonstrated. In this manuscript I analyze this issue and evaluate how partitioning is accommodated in Peru.

5. Main questions addressed in this thesis

Mega-tsunamigenic earthquakes of the decade 2004-2014 have pointed out the importance of correctly assessing the seismic hazard in subduction zones and the need to improve our understanding on the processes that lead to the occurrence of giant earthquakes. Indeed, the mechanisms whereby stresses are being accumulated and released along the plate interface are not well understood. The ANR-ADN (Andes du Nord) project financed by the French government between 2008 and 2012 proposed an integrated approach involving geodesy, seismology, tectonics, marine geophysics and modeling in order to address these issues. My thesis was done in the frame of that project considering the Peruvian subduction segment.

So far, GPS studies have focused in southern and partially in central Peru. The northern Peru segment (from 9ºS to -3ºS) remained as the sole portion without being studied using this technique. No information about was available before this thesis for

this segment, from the north of Lima to the Gulf of Guayaquil. As a consequence, even first order information was not available to assess neither the level of deformation and stress accumulation nor the associated seismic risk at the beginning of this thesis.

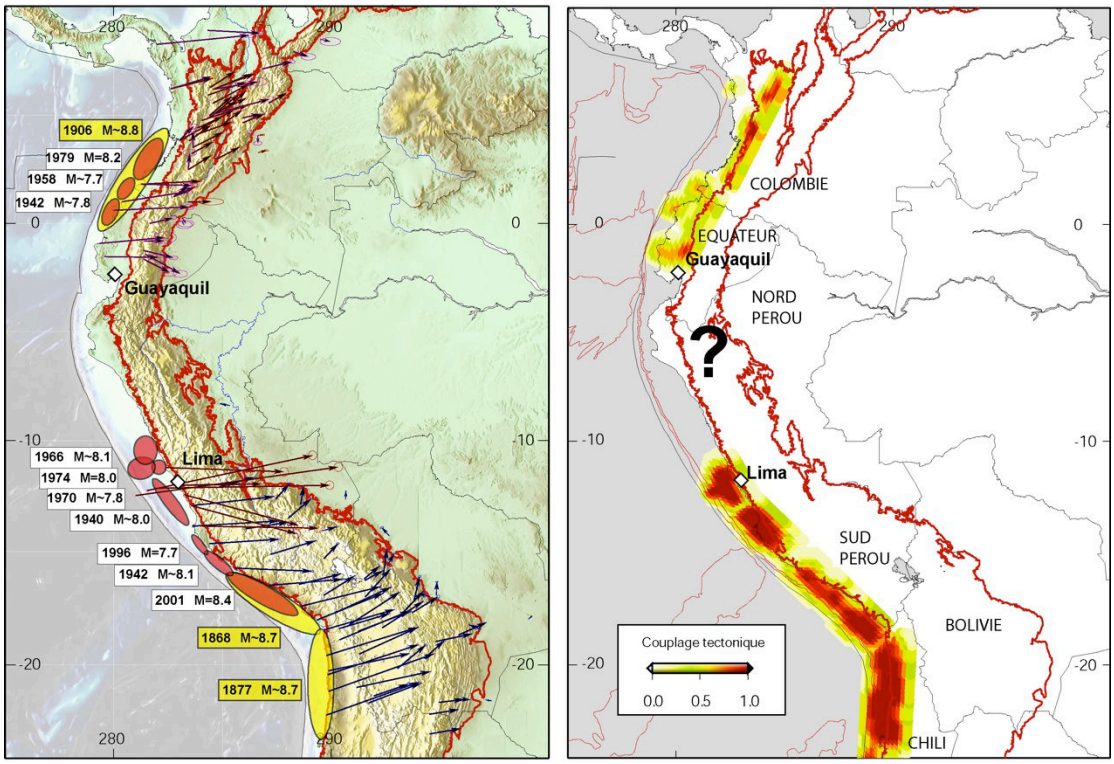

Figure 1.12: Left: Rupture area for known earthquakes with M>7.6 and GPS campaigns measurements since 1990 [*Norabuena et al.*, 1998; *Bevis et al.*, 2001; *Kendrick et al.*, 2001; *Trenkamp et al.*, 2002; *Chlieh et al.*, 2004]. Right: GPS derived model of mechanical coupling along the subduction interface. Highly coupled zones are shown in red. They show similar sizes to ruptures of past large earthquakes. At the beginning of this thesis, no information was currently available to constrain the level of stress accumulation along a ~1200 km long segment between Lima (Peru) and Guayaquil (Ecuador).

The fundamental questions addressed in this thesis are:

- How the convergence is being accommodated along the Peruvian subduction zone, especially in its northern segment?

- What portion of the GPS surface deformation field could be attributed to the permanent continental deformation and what portion to the mechanical coupling at the megathrust interface? Where are the principal seismic asperities?

- The atypical seismic silence of the northern Peru segment over the last 5 centuries is either an indicator that the stress is currently accumulating on the plate interface to produce large earthquakes in the future. Alternatively, this silence would reflect an interface where plates are sliding aseismically explaining the absence of large (M>8.0) earthquakes?

- Where are the weakly locked areas on the plate interface? Can we map those areas that arrest the rupture of large earthquakes (barriers)? Do these areas correlate with any geomorphological features?

- Tsunami-earthquake type events seem to be characteristic of the northern subduction segment. Is it possible to map those coupled areas that generate this kind of events?

- Could areas of low interseismic coupling host slow slip events? If yes, what role do they play in accommodating the convergence or triggering earthquakes?

- What are the physical parameters controlling the earthquake behavior and its drastic change from south to north of Peru?

- Could the results of this thesis provide a reliable model of the seismic and tsunami hazard?

In order to answer these questions, I analyze all the GPS data collected in the frame of the ADN project (a collaborative project involving Géoazur and the Institute of Geophysics of Peru among others, funded by the ANR-France and led by Jean-Mathieu Nocquet). Since 2008 up to 2013, I have been participating in each step of the project: the reconnaissance and installation in Spring 2008, the GPS campaigns in 2008, 2009, 2010, 2011, 2012, 2013, the maintenance and management of the data flow for continuous GPS, the processing and the modeling of GPS data of this project. In this thesis, I also did the effort of collecting all the GPS data available in Peru concretizing an extensive database at the scale of the country. I also benefited from the GPS data from the Instituto Geográfico Nacional (IGN) of Peru network, trough a convention with the Institut de Recherche pour le Développement (IRD). This study

also benefits from continuous support provided by the IRD to perform GPS measurements along three trench perpendicular profiles crossing the Andean cordillera from the coast to the sub-Andean region. Finally, this study also benefits from GPS data from LISN project [*Valladares and Chau*, 2012] of the Instituto Geofísico del Perú (IGP).

6. Outline of this thesis

This manuscript consists of 5 chapters including this introductory chapter.

Chapter 2 presents the large-scale results for continental deformation and interseismic interplate coupling from central Peru to southern Colombia. This study found that a large segment of the subduction in northern Peru and southern Ecuador is accommodating the convergence almost aseismically. We also discovered that the diverging motion of two continental slivers dominates the tectonic of the western margin of the north Andean subduction zone: the North Andean Sliver and the recently evidenced Inca Sliver. These results were published in the Nature Geosciences journal in March 2014 in *Nocquet et al.*, [2014].

Chapter 3 contains a more detailed study on the Inca Sliver kinematics and its impact on the pattern of interseismic coupling along the whole Peruvian subduction zone. Thanks to an augmented dataset including new GPS observations from collaborative networks and new campaign sites including 3 profiles crossing the Andean cordillera, we better constrain the boundary of the Inca sliver and its kinematics. We re-evaluate the level of interseismic coupling along the Peruvian subduction by taking this new Sliver as a reference. There, I provide possible scenarios for future large earthquakes. This chapter is expected to be submitted to the Journal of Geophysical Research.

Chapter 4 contains a detailed study of a sequence of seismicity synchronous to a slow slip event (SSE) that occurred in 2009 near Piura in northern Peru. This finding is one the first observed SSE in the South American subduction zone and one of the first that shows significant seismicity synchronous to the aseismic slip. I analyzed not only GPS data but also seismological data to depict the temporal evolution and relationships between seismic/aseismic slips, providing new insights about the

anatomy of the subduction interface in northern Peru. The results of this chapter are under final corrections for publication in peer-reviewed journal.

Finally, Chapter 5 includes a synthesis and conclusions of the main findings and a view of the anatomy of the Peruvian subduction zone. The conclusions and ideas for future work are also presented.

Chapter 2

Motion of continental slivers and creeping subduction in the northern Andes

In this chapter I present the first results of a large-scale GPS network installed in northern Andes from Lima (lat. 12.5ºS) to north Ecuador (lat. 2ºN), to study the continental deformation and interplate coupling in the northern Andes. Here, we put in evidence the existence of a tectonic sliver in Peru that together with the North Andean Sliver diverge in motion from the Gulf of Guayaquil moving southeastward and northeastward, respectively. We also found that a large portion of the subduction the subduction segment (~1000 km) from northern of Lima sot the Gulf of Guayaquil (lat. 9ºS to lat. -2ºS,) shows a weak interseismic coupling compared to the central Peru and central-north Ecuador segments where the coupling is high. The results of this study have been published in the journal Nature Geosciences and are presented here in the published version.

Motion of continental slivers and creeping subduction in the northern Andes

Nature Geosciences 7, 287–291 (2014) doi:10.1038/ngeo2099.

J-M. Nocquet, **J. C. Villegas-Lanza**, M. Chlieh, P. A. Mothes, F. Rolandone, P. Jarrin, D. Cisneros, A. Alvarado, L. Audin, F. Bondoux, X. Martin, Y. Font, M. Régnier, M. Vallée, T. Tran, C. Beauval, J. M. Maguiña, W. Martinez, H. Tavera & H. Yepes

nature geoscience

LETTERS

PUBLISHED ONLINE: 2 MARCH 2014 | DOI: 10.1038/NGEO2099

Motion of continental slivers and creeping subduction in the northern Andes

J-M. Nocquet[1]*, J. C. Villegas-Lanza[1,2], M. Chlieh[1,3], P. A. Mothes[4], F. Rolandone[5], P. Jarrin[4], D. Cisneros[6], A. Alvarado[4], L. Audin[7], F. Bondoux[8], X. Martin[1], Y. Font[1,4], M. Régnier[1], M. Vallée[1†], T. Tran[1], C. Beauval[7], J. M. Maguiña Mendoza[9], W. Martinez[10], H. Tavera[2] and H. Yepes[4,7]

Along the western margin of South America, plate convergence is accommodated by slip on the subduction interface and deformation of the overriding continent[1–6]. In Chile[1–4], Bolivia[6], Ecuador and Colombia[5,7], continental deformation occurs mostly through the motion of discrete domains, hundreds to thousands of kilometres in scale. These continental slivers are wedged between the Nazca and stable South American plates. Here we use geodetic data to identify another large continental sliver in Peru that is about 300–400 km wide and 1,500 km long, which we call the Inca Sliver. We show that movement of the slivers parallel to the subduction trench is controlled by the obliquity of plate convergence and is linked to prominent features of the Andes Mountains. For example, the Altiplano is located at the boundary of converging slivers at the concave bend of the central Andes, and the extending Gulf of Guayaquil is located at the boundary of diverging slivers at the convex bend of the northern Andes. Motion of a few large continental slivers therefore controls the present-day deformation of nearly the entire Andes mountain range. We also show that a 1,000-km-long section of the plate interface in northern Peru and southern Ecuador slips predominantly aseismically, a behaviour that contrasts with the highly seismic neighbouring segments. The primary characteristics of this low-coupled segment are shared by ~20% of the subduction zones in the eastern Pacific Rim.

Along the western margin of South America, rapid convergence (~60–70 mm yr^{-1}) of the oceanic Nazca Plate towards South America has produced three of the ten largest subduction earthquakes since 1900. Almost its entire length has been ruptured by $M > 8$ megathrust earthquakes since the 1500s (ref. 8). Contrasting with this observation, north of the 1746 $M_w \sim 8.6$ Lima earthquake[9] and south of the 1906 M_w 8.8 Ecuador–Colombia event[10], no $M > 8$ megathrust earthquake has occurred at least since the Spanish conquest of the Inca Empire in 1532 (Fig. 1a). The only noteworthy historical events occurred in 1619, when the city of Trujillo was destroyed, and in 1912 in the Piura area, but their attribution to subduction events remains uncertain[9]. Among the four events with magnitude larger than 7 recorded by seismometers in this region, the 1960 M_w 7.6 and 1996 M_w 7.5 earthquakes displayed abnormally long source duration, slow rupture velocity, enhanced long-period source spectrum and both induced relatively large tsunamis[11,12]. Both events have been categorized as tsunami earthquakes, rupturing the shallow, weaker material of the accretionary prism. In the absence of direct measurements, several behaviours are plausible to explain the observed seismic gap: a first endmember view is that the subduction interface is freely slipping, with no potential to generate great earthquakes. In contrast, a second possible model is that this interface is significantly locked and great earthquakes may have recurrence time greater than 500 yr. If the latter hypothesis is true, a total length of 1,200 km and a convergence rate of ~60 mm yr^{-1} would imply an overall seismic moment deficit equivalent to a $M_w > 9$ earthquake, if released in a single event. Of course, intermediate scenarios are also possible, but even a single 300-km-long segment being significantly coupled would still leave the potential for a $M_w > 8$ earthquake to occur in the future. Quantitatively assessing the seismic potential of this segment of the subduction is therefore essential not only for Peru and Ecuador but also for the whole circum-Pacific zone, because of the associated tsunami hazard. Besides the hazard associated with the subduction megathrust, significant crustal seismicity also takes place in the Andean domain. For instance, Ecuador has experienced at least 28 damaging crustal earthquakes since 1541 (ref. 13). Among them, the 1797 Riobamba event is one of the largest crustal earthquakes ever documented in the Andes with a magnitude recently estimated of between 7.5 and 7.9 (ref. 13).

Here, we use global positioning system (GPS) data to quantify the surface deformation in the northern Andes using a network of 100 sites, from Lima in central Peru (latitude 12° S) to Bogota in Colombia (Latitude 4.6° N; Fig. 1b). With respect to stable South America, the velocity field shows a diverging pattern, with velocities directed east to northeastwards in Ecuador and Colombia, and directed southeastwards in northern Peru. Superimposed on this general pattern, larger velocities whose magnitude decreases with increasing distance from the trench indicate areas of strong interseismic coupling in central Peru and northern Ecuador. A more detailed analysis reveals that the southern Ecuadorian Andes and northern Peru moves coherently 5–6 mm yr^{-1} southeastwards, with negligible internal deformation (Fig. 2a). In central Peru, south

[1]Geoazur, IRD, Université de Nice Sophia-Antipolis, Observatoire de la Côte d'Azur, CNRS, 250, Rue A. Einstein, 06560 Valbonne, France, [2]Instituto Geofísico del Perú, Calle Badajoz 169, Urbanización Mayorazgo IV Etapa, Ate, 15012 Lima, Perú, [3]IRD, Calle 17, San Isidro, 15036 Lima, Perú, [4]Instituto Geofísico, Escuela Politécnica Nacional, Ladrón de Guevara, 2759 Quito, Ecuador, [5]Institut des Sciences de la Terre de Paris, CNRS UMR 7193, Université Pierre et Marie Curie, 75005 Paris, France, [6]Instituto Geográfico Militar de Ecuador IGM-EC, Sector El Dorado, 2435 Quito, Ecuador, [7]ISTerre, IRD, CNRS, UJF, OSUG, 38041, Grenoble, France, [8]Laboratoire des Mécanismes et Transferts en Géologie, Université Paul Sabatier, IRD, CNRS, Observatoire Midi-Pyrénées , 31400 Toulouse, France, [9]Instituto Geográfico Nacional del Perú IGN, Av. Aramburú 1190 Surquillo, 15036 Lima, Perú, [10]Instituto Geográfico Agustín Codazzi de Colombia IGAC, Carrera 30 N48, Bogotá, Colombia. †Present address: Institut de Physique du globe de Paris, Sorbone Paris Cité, Université Paris Diderot, UMR 7154 CNRS, Paris, France. *e-mail: nocquet@geoazur.unice.fr

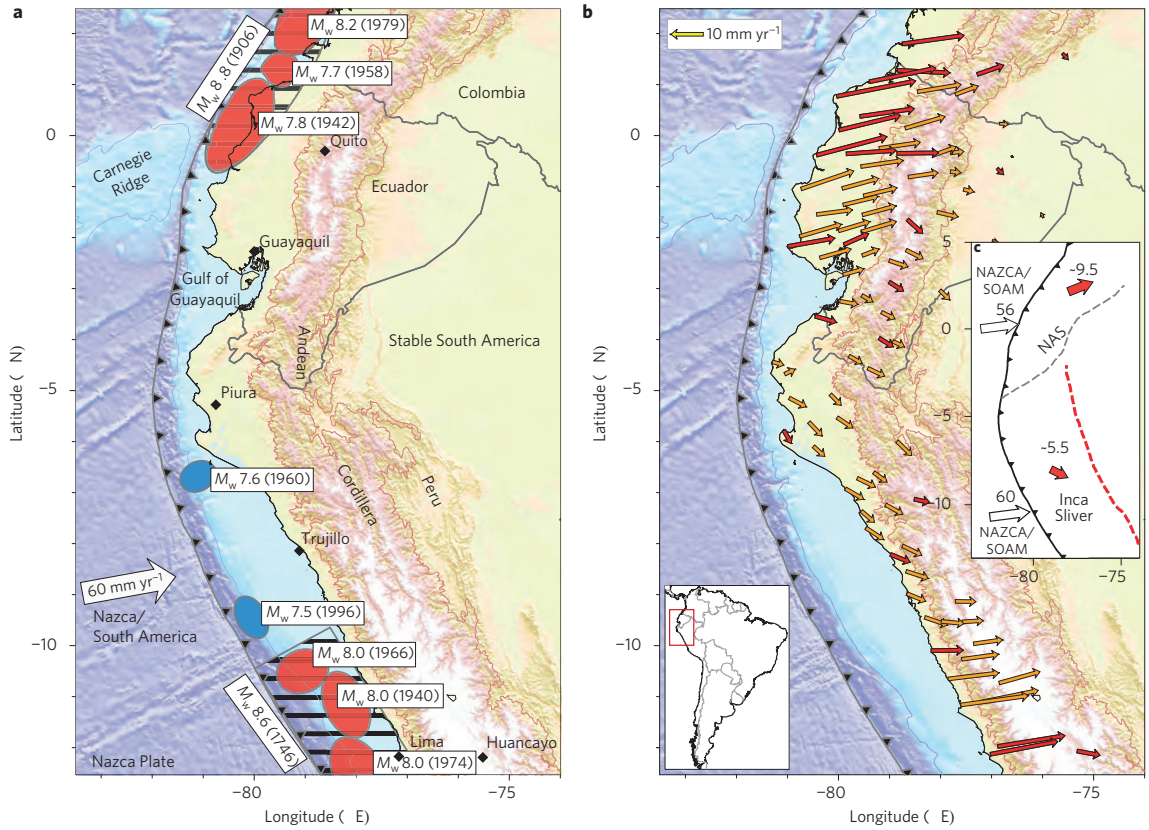

Figure 1 | Major subduction earthquake ruptures and GPS velocity field along the Ecuador/northern Peru margin. a, Rupture areas of major past earthquakes. Red ellipses indicate large earthquakes ($M_w \geq 7.7$) since 1900 (ref. 8). Hatched ellipses indicate the approximated rupture areas of great ($M_w \geq 8.5$) earthquakes[9,10]. Blue ellipses indicate tsunami earthquakes[8,11,12]. **b**, GPS velocity field with respect to stable South America. Red and orange arrows denote continuous and campaign sites, respectively. **c**, Kinematic sketch showing the motion of the NAS and Inca Sliver. SOAM, South America Plate. Numbers are velocities in mm yr^{-1}.

of latitude 9° S, the geodetic velocity field is dominated by the contribution of high interseismic coupling along the subduction interface, which masks the smaller signal of the sliver motion. Nonetheless, sites located far away from the trench and as far south as Ayacucho (74.2° W, 13.2° S) and Cuzco (72° W, 13.5° S) show <2 mm yr^{-1} residual velocities with respect to northern Peru, indicating that the sliver also encompasses these southern areas. Furthermore, subduction event slip vectors show a systematic anticlockwise rotation with respect to the Nazca/South America convergence all along the Peruvian subduction (Supplementary Fig. 1). Independently from the geodetic data, this further suggests that the trench-parallel motion of the sliver encompasses the whole Peruvian margin and extends as far south as the Bolivian Andes. As the possible limit of the sliver roughly matches the extent of the Inca Empire, we propose the name Inca Sliver for the continental domain wedged between the Nazca Plate and stable South America in Peru and southern Ecuador (Figs 1c and 2a).

North of the Gulf of Guayaquil, previous studies have identified a large sliver (North Andean Sliver, NAS) encompassing the Andes and its western margin from Ecuador to western Venezuela[5,7]. We find that a rigid block motion of 7.5–9.5 mm yr^{-1} towards the northeast explains the kinematics from central Ecuador to Colombia. Dense GPS measurements allow us to define the NAS eastern boundary in Ecuador. The limit includes the Gulf of Guayaquil, obliquely cuts the Andean Cordillera and then runs along the eastern front of the Eastern Cordillera (Figs 1c and 2b). The boundary outlined by GPS results correlates with previously described active faults[14], the location of major historical earthquakes[13] and the style of faulting of recent earthquakes (Fig. 2b). GPS velocities are also consistent with previously proposed Holocene slip rates[15,16] suggesting that the motion of the sliver is accommodated by a small number of major faults. Less information is available for past earthquakes and active faults that could be associated with the eastern boundary of the Inca Sliver. Nonetheless, ~20 shallow thrust and transpressive crustal earthquakes with magnitude between 5.5 and 7.0 have occurred along the proposed boundary since 1960[17,18]. Although internal deformation of both slivers probably exists at some level, the sliver boundaries delimit strips of localized deformation accommodating rapid (4– 10 mm yr^{-1}) motion and define areas of high seismic hazards.

Both slivers have a width of 300–400 km and a total length of >1,500 km. Their motions dominate the present-day kinematics for about half of the length of the Andean Cordillera, from south of the Caribbean Plate to the central Andes. The separation between the two slivers occurs across the Gulf of Guayaquil, located close to the apex of the convex bend of the South America subduction zone, where the sense of the convergence obliquity changes as a consequence of the change of orientation of the trench. The sense of the trench-parallel component of each sliver motion is consistent with the obliquity of the convergence, indicating active strain partitioning along this portion of the plate boundary. Kinematic triangles show ~6 mm yr^{-1} of left-lateral and ~4.5 mm yr^{-1} of right-lateral trench-parallel motion in Ecuador and

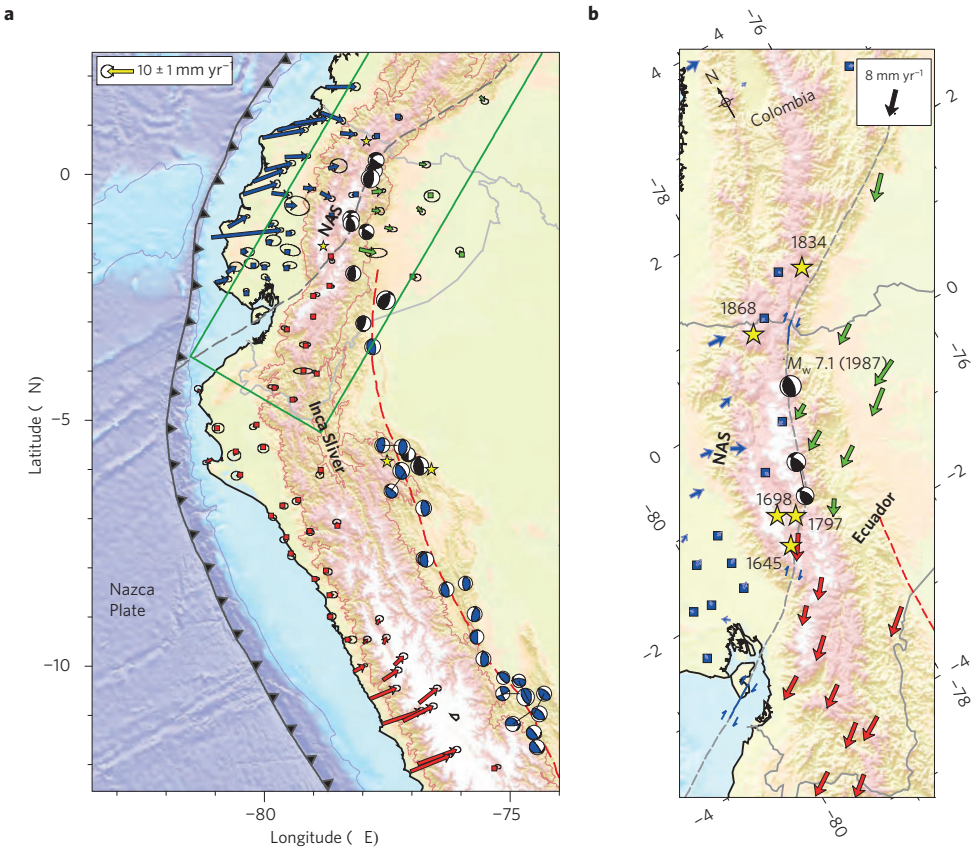

Figure 2 | North Andean Sliver and Inca Sliver boundaries. a, Blue and red arrows are velocities with respect to the North Andean Sliver (NAS) and the Inca Sliver, respectively. Green arrows are velocities in the sub-Andean domain with respect to stable South America. Error ellipses are 95% confidence level. Squares indicate GPS with <1 mm yr^{-1} velocities. Black focal mechanisms are from the Global CMT catalogue (http://www.globalcmt.org) and blue focal mechanisms from refs 17,18. The green rectangle indicates the area shown in **b**. **b**, Velocity field along the boundary of the NAS. All velocities are now with respect to the NAS. Yellow stars show the major historical earthquakes in Ecuador with their dates[13].

Peru, respectively, leading to a similar percentage of partitioning (~20–25%) for the two domains (Supplementary Fig. 2). Trench-normal motion also seems to be slightly partitioned and results in a thrusting component accommodated along the eastern front of the Andes and to a lesser extent in the sub-Andean domain.

Previous studies have identified sliver motion in the central and southern Andes, with pure arc-parallel motion for the Chiloé Forearc Sliver[1] in southern Chile and an additional trench-normal component for the Central Andes Sliver[3,4,6]. All proposed slivers in Chile show a northwards, left-lateral trench-parallel component of motion[1–4] consistent with the sense of the plate convergence obliquity. Our results therefore support a view of strain partitioning nearly throughout the entire Nazca/South America plate boundary zone, with a first-order organization controlled by the plate convergence obliquity. Sliver motion further provides an obvious link to prominent features of the Andes. The Altiplano in the central Andes is located at the boundary zone between the Central Andes Sliver in northern Chile and the Inca Sliver in Peru. Converging trench-parallel component of sliver motion in the concave bend of the Central Andes induces crustal thickening and growth of the Altiplano, whereas diverging sliver motion occurs in the convex bend of the northern Andes inducing crustal thinning and opening of the Gulf of Guayaquil. This observation departs from the classical view of the Andes evolution, usually seen as a two-dimensional process involving progressive thickening of the crust and widening of the mountain range. In contrast, our results indicate that trench-parallel transportation of the continental lithosphere driven by the convergence obliquity exerts a major control on the widescale deformation of the Andes, at least for their recent evolution.

Residual velocities with respect to the two slivers (Fig. 2a) reflect the interseismic elastic strain induced by coupling along the subduction interface. Our modelling results provide a simple view of the seismic cycles in Peru and Ecuador. High interseismic coupling in central Peru and in northern Ecuador correlates with rupture areas of the great 1746 (ref. 9) and 1906 (ref. 10) earthquakes. In these regions, elastic strain is released through great earthquakes, sometimes alternating with sequences of smaller (M_w 7.5–8.2) events[8–10]. Conversely, along a ~1,000-km-long segment from latitude 10° S to 3° S, all models show weak to negligible interplate coupling. This subduction segment must therefore accommodate the Nazca/South America convergence predominantly through aseismic creep along the interface, explaining the lack of great subduction earthquakes over the past five centuries[8,9]. As the coastline is located about 200 km away from the trench south of the Piura Peninsula (Fig. 1), GPS data are insensitive to coupling in the upper shallowest portion of the plate interface. As a consequence, GPS data do not exclude the possibility of significant coupling along a shallow (<15–20 km depth) 60-km-wide strip close to the trench (Fig. 3c). Historically, tsunami earthquakes[11,12] have occurred in this weakly coupled segment, possibly releasing stresses accumulated in the very shallow part of the plate interface. This model also possibly holds for central Ecuador, where denser measurements along a

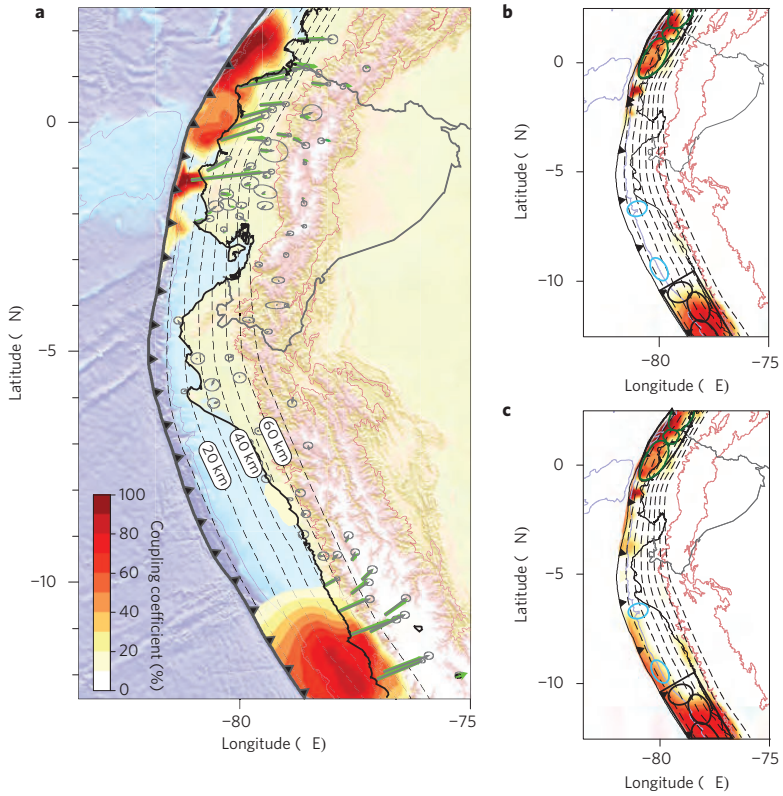

Figure 3 | Spatial distribution of interseismic coupling along the subduction plate interface. a, Model showing no interseismic coupling between 10° S and 3° S. Dashed lines are depth contours of the subduction interface every 10 km. Coupling level is indicated by the colour scale. Green arrows are the model predicted velocities. The misfit (wrms, weighted root mean square) to the observed velocities (grey arrows) for this model is 0.9 mm yr^{-1}. **b**, Model shown in **a**, together with the rupture areas of large and great earthquakes[8–10]. Blue ellipses indicate tsunami earthquakes. **c**, Same as **b** for an alternative model also permitted by GPS data showing interseismic coupling close to the trench. The misfit for this model is wrms = 1.0 mm yr^{-1}.

coastline located 50–80 km from the trench enable us to resolve local, intermediate to high interseismic coupling in the shallowest 20 km of the subduction interface.

The southern Ecuador–northern Peru subduction zone exhibits a fundamentally different mode of stress accumulation and release compared with its neighbouring segments. Previous geodetic studies in southern Peru and Chile have led to a view of highly coupled asperities of variable size, usually separated by narrower zones of low interseismic coupling[3,4,19]. Here, the area of predominantly creeping zone is a continuous ~1,000-km-long segment, representing 15–20% of the total length of the Nazca/South America subduction zone. Possible shallow (<20 km) interseismic coupling, very weak to zero coupling at the usual seismogenic depths (20–45 km), a lack of great earthquakes, the occurrence of moderate size tsunami earthquakes, and sliver motion are the primary characteristic of this subduction zone. How frequent such a category of subduction zone is globally still remains to be evaluated, but the Shumagin Islands[20] segment of the Alaska–Aleutian Arc, the Central America[21–23], Hikurangi[24], Java[25,26] and Ryukyu[27] subduction zones share most or all of the same characteristics. Along the eastern side of the Pacific Rim, of the ~13,000 km of subduction from Chile to the central Aleutians almost continuously studied by geodesy, the predominantly creeping segments in the Shumagin Islands (~450 km; ref. 20), Central America (~1,200 km; refs 21–23) and northern Peru/southern Ecuador (~1,000 km) represent as much as ~20% of the subduction length. Low-coupled subduction zone sections might therefore be a common feature. As elastic strain does not accumulate over a wide seismogenic zone, low-coupled subduction zones are unlikely to produce great M_W~9 earthquakes, for which rupture along the megathrust typically occurs from depths of 45 to 50 km up to the trench. Moderate to large tsunami earthquakes can occur in these zones, but they are unlikely to be sources of trans-Pacific tsunamis.

Methods

GPS. We derived a horizontal velocity field of 130 sites from GPS data, including 65 sites recorded in survey mode since 1994 for Ecuador and since 2008 for Peru and 35 continuous GPS sites in Peru, Ecuador and Colombia. The velocity field (Supplementary Table 1) is expressed with respect to a reference frame realized using 20 GPS sites sampling the stable South America Plate. All velocity uncertainties account for time-correlated noise (Supplementary Information).

Sliver kinematics and boundaries. We take advantage of segments with low interseismic coupling along the subduction interface to determine the kinematics of the slivers, idealized as non-deforming blocks. Twenty-eight GPS sites located in the southern Ecuadorian Andes and in northern Peru show a consistent southeastwards motion, which can be modelled by a single block, with negligible internal deformation (weightedrootmeansquare, wrms = 0.8 mm yr^{-1}, Euler pole at −63.8° E, 22.5° N, angular velocity: 0.092 ° Myr^{-1}, Fig. 2a and Supplementary Table 2). No east–west shortening is detected in the residual velocities that could indicate an unmodelled small signal induced by weak coupling along the subduction interface. In southern Ecuador, the easternmost GPS sites, located in the sub-Andean thrust-and-fold belt region, together with the thrust focal mechanisms indicating southwest–northeast-directed shortening, suggest a boundary for this sliver along the eastern front of the subandean domain in Ecuador (Fig. 2a). In Peru, owing to the difficulty of making measurements in the eastern Andes and Amazonia, our velocity field provides little constraintson the eastern boundary of the sliver. We therefore used the distribution of shallow crustal $M_w > 5.5$ earthquakes[17,18] to tentatively propose an eastern boundary for

the Inca Sliver in Peru (Fig. 2a). Inspection of slip vectors for subduction events show that, if compared with the Nazca/South America convergence direction, they are rotated ~5° clockwise in Ecuador, whereas they are rotated anticlockwise by the same amount in Peru (Supplementary Fig. 1). This observation provides an independent evidence of trench-parallel motion of the forearc with opposite sense in Ecuador and Peru and is consistent with an Inca Sliver extending until southernmost Peru. The NAS kinematics is determined using a subset of 14 sites located in the coastal plain of Ecuador north of the Gulf of Guayaquil, in the Andean Cordillera of central Ecuador and southern Colombia. The chosen subset of sites samples the NAS over a distance of >1,000 km with no detectable internal deformation (Supplementary Table 3, wrms = 0.8 mm yr^{-1}, Euler pole at −83.4° E, 15.2° N, angular velocity: 0.287 ° Myr^{-1}). A sharp velocity gradient of 7 mm yr^{-1} accommodated over a distance of ~50 km (Fig. 2b) allows us to define the eastern boundary of the NAS that matches the active faults system of Chingual–Cosanga–Pallatanga–Puná[14]. In northern Ecuador, sites located in the sub-Andean domain show a residual ~3 mm yr^{-1} motion with respect to stable South America (Fig. 1b).

Interseismic coupling modelling. We model the spatial distribution of interseismic coupling using the virtual back-slip approach in a semi-infinite homogeneous elastic half-space[28]. The input data set consists of the horizontal velocities corrected for the sliver motion previously determined. Sites located close to the NAS/Inca Sliver boundaries are probably impacted by the elastic effects of major crustal faults (Fig. 2b) and so were excluded from the inversion. The subduction interface is divided into 1,024 quasi-equilateral triangular subfaults with an average edge length of 30 km, following the Slab1.0 (ref. 29) geometry subduction interface, except in the Lima area, where short-scale variations have been simplified. We fixed the rake and the convergence velocity to be consistent with the Nazca Plate motion relative to the slivers. Our inversion scheme follows a linear Bayesian formulation[30], which enables us to explore the range of possible models, by varying an a priori model (from null to fully coupled plate interface), damping and smoothing parameters through a model covariance matrix (Supplementary Information and Supplementary Figs 3 and 4). All models show high coupling in central Peru ending at latitude 10°– 11° S, very low to null coupling between 10° S and 3° S, and shallow and laterally heterogeneous coupling north of 3° S. The main variation among models is the amount of coupling close to the trench between 7° S and 10° S where GPS sites are located more than 200 km away from the trench. Secondary differences are the size of highly coupled areas and in general the amount of coupling close to the trench. For the purpose of illustration in the main text, we used a L-curve (Supplementary Fig. 5) to choose the smoothest model that still correctly explains the GPS data (Fig. 3a,b). Furthermore, we show an alternative model with shallow interseismic coupling also permitted by the GPS data (Fig. 3c).

Received 16 October 2013; accepted 23 January 2014; published online 2 March 2014

References

1. Wang, K. *et al.* Crustal motion in the zone of the 1960 Chile earthquake: Detangling earthquake-cycle deformation and forearc-sliver translation. *Geochem. Geophys. Geosys.* **8,** Q10010 (2007).
2. Brooks, B. A. Crustal motion in the southern Andes (26°–36° S): Do the Andes behave like a microplate? *Geochem. Geophys. Geosys.* **4,** 1085 (2003).
3. Metois, M. *et al.* Revisiting the north Chile seismic gap segmentation using GPS-derived interseismic coupling. *Geophys. J. Int.* **194,** 1283–1294 (2013).
4. Chlieh, M. *et al.* Interseismic coupling and seismic potential along the central Andes subduction zone. *J. Geophys. Res.* **116,** 1–21 (2011).
5. White, S. M., Trenkamp, R. & Kellogg, J. N. Recent crustal deformation and the earthquake cycle along the Ecuador– Colombia subduction zone. *Earth Planet. Sci. Lett.* **216,** 231–242 (2003).
6. Brooks, B. A. *et al.* Orogenic-wedge deformation and potential for great earthquakes in the central Andean backarc. *Nature Geosci.* **4,** 380–383 (2011).
7. Pennington, W. Subduction of the Eastern Panama Basin and seismotectonics of northwestern South America. *J. Geophys. Res.* **86,** 10753–10770 (1981).
8. Bilek, S. L. Invited review paper: Seismicity along the South American subduction zone: Review of large earthquakes, tsunamis, and subduction zone complexity. *Tectonophysics* **495,** 2–14 (2010).
9. Dorbath, L., Cisternas, A. & Dorbath, C. Assessment of the size of large and great historical earthquakes in peru. *Bull. Seismol. Soc. Am.* **80,** 551–576 (1990).
10. Kanamori, H. & McNally, K. Variable rupture mode of the suduction zone along the Ecuador–Colombia coast. *Bull. Seismol. Soc.* **72,** 1241–1253 (1982).
11. Pelayo, A. & Wiens, D. The November 20, 1960 Peru tsunami earthquake: Source mechanism of a slow event. *Geophys. Res. Lett.* **17,** 661–664 (1990).
12. Ihmlé, P. & Gomez, J. The 1996 Peru tsunamigenic earthquake: Broadband source process. *Geophys. Res.* **25,** 2691–2694 (1998).
13. Beauval, C. *et al.* An earthquake catalog for seismic hazard assessment in Ecuador. *Bull. Seismol. Soc. Am.* **103,** 773–786 (2013).
14. Eguez, A. *et al. Database and Map of Quaternary Faults and Folds of the Ecuador and its Offshore Regions, International Lithosphere Program Task Group II-2, Major Active Faults of The World, Denver, US Department of the Interior* 1–71 (US Geol. Surv., 2003).
15. Dumont, J. F., Santana, E. & Vilema, W. Morphologic evidence of active motion of the Zambapala Fault, Gulf of Guayaquil (Ecuador). *Geomorphology* **65,** 223–239 (2005).
16. Ego, F., Sébrier, M., Lavenu, A., Yepes, H. & Egues, A. Quaternary state of stress in the northern Andes and the restraining bend model for the Ecuadorian Andes. *Tectonophysics* **259,** 101–116 (1996).
17. Suárez, G., Molnar, P. & Burchfiel, B. Fault plane solutions, depth of faulting, and active tectonics of the Andes of Peru, Ecuador, and southern Colombia. *J. Geophys. Res.* **88,** 10403–10428 (1983).
18. Devlin, S., Isacks, B. L., Pritchard, M. E., Barnhart, W. D. & Lohman, R. B. Depths and focal mechanisms of crustal earthquakes in the central Andes determined from teleseismic waveform analysis and InSAR. *Tectonics* **31,** TC2002 (2012).
19. Métois, M., Socquet, A. & Vigny, C. Interseismic coupling, segmentation and mechanical behavior of the central Chile subduction zone. *J. Geophys. Res.* **117,** B03406 (2012).
20. Fournier, T. J. & Freymueller, J. T. Transition from locked to creeping subduction in the Shumagin region, Alaska. *Geophys. Res. Lett.* **34,** L06303 (2007).
21. Franco, A. *et al.* Fault kinematics in northern Central America and coupling along the subduction interface of the Cocos Plate, from GPS data in Chiapas (Mexico), Guatemala and El Salvador. *Geophys. J. Int.* **189,** 1223–1236 (2012).
22. Correa-Mora, F. *et al.* GPS-derived coupling estimates for the Central America subduction zone and volcanic arc faults: El Salvador, Honduras and Nicaragua. *Geophys. J. Int.* **179,** 1279–1291 (2009).
23. LaFemina, P. *et al.* Fore-arc motion and Cocos Ridge collision in Central America. *Geochem. Geophys. Geosys.* **10,** Q05S14 (2009).
24. Wallace, L. M., Beavan, J., McCaffrey, R. & Darby, D. Subduction zone coupling and tectonic block rotations in the North Island, New Zealand. *J. Geophys. Res.* **109,** B12406 (2004).
25. Simons, W. J. F. *et al.* A decade of GPS in Southeast Asia: Resolving Sundaland motion and boundaries. *J. Geophys. Res.* **112,** B06420 (2007).
26. Ammon, C. J., Kanamori, H., Lay, T. & Velasco, A. A. The 17 July 2006 Java tsunami earthquake. *Geophys. Res. Lett.* **33,** L24308 (2006).
27. Nishimura, S., Hashimoto, M. & Ando, M. A rigid block rotation model for the GPS derived velocity field along the Ryukyu arc. *Phys. Earth Planet. Int.* **142,** 185–203 (2004).
28. Savage, J. A dislocation model of strain accumulation and release at a subduction zone. *J. Geophys. Res.* **88,** 4984–4996 (1983).
29. Hayes, G. P., Wald, D. J. & Johnson, R. L. Slab1.0: A three-dimensional model of global subduction zone geometries. *J. Geophys. Res.* **117,** B01302 (2012).
30. Tarantola, A. *Inverse Problem Theory and Methods for Model Parameter Estimation* (SIAM, 2005).

Acknowledgements

This work has been financially supported by the Agence Nationale de la Recherche (ANR; contract number ANR-07-BLAN-0143-01) and has continuously been supported by the Institut de Recherche pour le Développement (IRD). We acknowledge additional support from the Secretaría Nacional de Educación Superior, Ciencia, Tecnología e Innovación (SENESCYT, Ecuador), the European Commission (DIPECHO project) and the CNRS-INSU. This work has been carried out in the frame of the Joint International Laboratory 'Seismes & Volcans dans les Andes du Nord'.

Author contributions

J.M.N. designed the study and did field work, GPS processing, modelling and wrote the paper. J.C.V.L. did field work, GPS processing, modelling and edited the paper. M.C. did modelling and edited the paper. P.A.M. did field work, GPS processing and edited the paper. F.R. did field work and edited the paper. P.J. and D.C. did field work and GPS processing. M.C., P.A.M., F.R., P.J. and D.C. equally contributed to the work. A.A. edited the paper. L.M., Y.F., M.R., M.V. and C.B. did field work and edited the paper. T.T. did GPS analysis. J.M.M.M. and W.M. managed the GPS data for Peru and Colombia. F.B. and X.M. did field work. H.T. helped with logistics. H.Y. helped with logistics and edited the paper.

Additional information

Supplementary information is available in the online version of the paper. Reprints and permissions information is available online at www.nature.com/reprints. Correspondence and requests for materials should be addressed to J-M.N.

Competing financial interests

The authors declare no competing financial interests.

Supplementary information

DOI: 10.1038/NGEO2099

Motion of continental slivers and creeping subduction in the northern Andes

J.-M. Nocquet[1], J. C. Villegas-Lanza[1,2], M. Chlieh[1,†], P. A. Mothes[3], F. Rolandone[4], P. Jarrin[3], D. Cisneros[5], A. Alvarado[3], L. Audin[6], F. Bondoux[7], X. Martin[1], Y. Font[1,3], M. Régnier[1], M. Vallée[1,††], T. Tran[1], C. Beauval[6], J. M. Maguiña Mendoza[8], W. Martinez[9], H. Tavera[2] and H. Yepes[3,6].

[1]Geoazur, IRD, Université de Nice Sophia-Antipolis, Observatoire de la Côte d'Azur, CNRS, 250, rue A. Einstein, Valbonne, France.

[2]Instituto Geofísico del Perú, Calle Badajoz 169, Urbanización Mayorazgo IV Etapa, Ate, Lima, Perú.

[3]Instituto Geofísico, Escuela Politécnica Nacional, Ladrón de Guevara, Quito, Ecuador.

[4]Institut des Sciences de la Terre de Paris, CNRS UMR 7193, Université Pierre et Marie Curie, Paris, France.

[5]Instituto Geográfico Militar de Ecuador IGM-EC, Sector El Dorado, Quito, Ecuador.

[6]ISTerre, IRD, CNRS, UJF, BP53, Grenoble, France.

[7]Laboratoire des Mécanismes et Transferts en Géologie, Université Paul Sabatier, IRD, CNRS, Observatoire Midi-Pyrénées, Toulouse, France.

[8]Instituto Geográfico Nacional del Perú IGN, Av. Aramburú 1190 Surquillo, Lima, Perú.

[9]Instituto Geográfico Agustín Codazzi de Colombia IGAC, Carrera 30 N48, Bogotá, Colombia.

† Also at IRD, Calle 17, San Isidro, Lima, Perú.

††Now at Institut de Physique du globe de Paris, Sorbone Paris Cité, Université Paris Diderot, UMR 7154 CNRS, Paris, France.

GPS Data Set

The data set includes 100 GPS sites in the northern Andes from Peru to Colombia analysed together with 30 additional sites in the surrounding regions from the global network of the International GNSS Service for Geodynamics (http://igscb.jpl.nasa.gov). It includes 13 continuous GPS (CGPS) stations in Ecuador and 3 in Peru installed in the framework of the ADN project as collaboration between Geoazur (CNRS-IRD-OCA-University of Nice, France), the Institute of Geophysics, National Polytechnic School (IG-EPN) in Quito, Ecuador[31], and the Institute of Geophysics, Lima, Peru. It also includes 5 CGPS stations from the National Geographical Institute of Peru (IGN), 3 CGPS sites from the Low Latitude Ionospheric Sensor Network (LISN) of IGP (http://lisn.igp.gob.pe/), and 3 CGPS sites from the Military Geographical Institute of Ecuador (IGM), and 8 CGPS sites from the Instituto Geográfico Agustin Codazzi (Colombia). Aside from the CGPS data, the velocity field in Peru is derived from 3 campaigns in 2008, 2010 and 2012, except for site CUYC observed each year since 2009 (30 sites). Campaigns in Peru were carried out at the same dates (July) to mitigate the possible effect of seasonal signals on the velocity estimates. The campaign data in Ecuador are 35 sites from the IGM, observed since 1994 and re-measured progressively between 2009 and 2011. In Ecuador, our velocity field includes most of the sites published in [32], but our new estimate now includes at least an additional measurement in 2009-2011. Each site selected in the present study benefits from at least 3 campaigns spanning at least 4 years. All CGPS shown here have a minimum of 2.5 years of measurements to mitigate the impact of seasonal variations on the velocity estimates.

GPS Data Analysis

Campaign and continuous data have been analyzed simultaneously for the 1994.0-2012.5 period, with the GAMIT/GLOBK software[33], using a standard strategy for Geodynamics. All velocity uncertainties account for time-correlated noise in the GPS time series. More specifically, noise parameters (level of white noise, fractional integer noise index and level of fractional integer noise) were first estimated from the time series for continuous sites, using the Maximum Likelihood Estimator

implemented in the CATS software[34]. Then, the noise values are converted to "equivalent" Markov noise values so that the Kalman filter implemented in GLOBK provides the same uncertainty as the CATS results, following the relation provided in [35]. The mean equivalent Markov noise derived from CGPS time series is also applied to campaign data. This strategy offers the advantage of keeping the strength of a cumulated solution (compared to velocities simply estimated from the time series) and of providing realistic uncertainties for both continuous and survey GPS sites. We used the cumulative up-to-date solution of the IGS as our reference to express our velocity field with respect to the ITRF2008[36], using a 14-parameters transformation. The use of the IGS solution rather than the original ITRF2008 solution is justified by the 2010 Maule earthquake, which largely impacted many reference sites in South America. We then estimated a rigid rotation rate vector for the South America plate using a subset of 20 sites that behaves rigidly together. The velocities are provided as Supplementary Table T2.1.

#site	long.	lat.	Ve	Vn	SVe	SVn	corr_en	obs_span	#obs	wrms_E	wrms_N
AHUA	-77.55	-1.06	3.16	-0.75	0.69	0.37	-0.01	16.4	6	5.8	4.0
AMAL	-79.42	-4.58	5.18	-2.43	0.52	0.34	0.00	15.2	5	3.5	5.2
ARCA	-70.75	7.08	0.62	-0.30	0.54	0.54	0.00	2.8	783	1.7	1.7
AUCA	-76.88	-0.64	1.90	-1.92	0.45	0.46	-0.00	2.9	947	1.5	1.9
AY01	-74.22	-13.15	4.20	-1.16	0.67	0.43	-0.01	2.7	737	1.1	1.8
AYAN	-80.75	-1.98	12.94	3.76	1.02	0.75	-0.04	14.7	6	1.6	1.9
AYRA	-77.71	-9.14	6.33	-0.09	0.62	0.49	-0.03	4.0	7	1.7	0.8
BALZ	-79.90	-1.36	10.89	2.64	1.20	0.86	-0.03	3.9	7	3.1	1.7
BAYO	-81.06	-5.79	2.30	-4.03	0.41	0.33	0.00	2.9	1009	1.1	1.4
BOGT	-74.08	4.64	5.13	5.11	0.29	0.27	-0.01	6.5	1910	2.5	2.0
BUEN	-77.01	3.88	10.79	3.80	0.37	0.34	0.00	3.8	1274	1.9	1.9
CABP	-80.42	-0.38	21.66	5.74	0.48	0.62	-0.00	2.7	682	1.5	1.4
CALI	-76.53	3.37	8.04	3.99	0.36	0.32	0.00	3.7	810	1.6	1.8
CASM	-78.30	-9.45	7.13	-2.40	0.75	0.57	-0.04	4.0	8	2.1	0.8
CBLA	-79.30	-6.62	4.11	-3.05	0.64	0.51	-0.02	4.0	9	2.2	0.7
CCHO	-80.96	-5.16	5.18	-2.73	0.94	0.77	0.00	4.0	9	0.6	0.9
CHAC	-78.67	-8.55	6.88	-2.21	0.62	0.49	-0.01	4.0	8	0.9	1.0
CHIS	-80.72	-1.05	16.24	5.56	0.40	0.26	0.00	5.4	1849	1.3	2.6
CHRI	-76.85	-10.72	12.59	3.52	0.61	0.48	-0.11	4.0	8	0.8	0.7
CHSQ	-77.57	-10.26	11.26	1.55	0.59	0.46	-0.08	4.0	7	0.8	2.2
CHUL	-80.15	-5.09	3.40	-3.47	0.56	0.46	-0.01	4.0	7	1.1	1.0
CJ01	-78.50	-7.14	4.74	-1.02	0.65	0.45	-0.00	2.6	589	1.5	1.9
CNJO	-76.84	0.23	2.69	-0.23	0.63	0.51	0.03	7.0	8	1.6	5.3
CUEC	-79.00	-2.88	4.37	-2.75	0.36	0.32	0.00	3.5	1117	1.2	1.5
CUER	-79.53	-2.35	5.17	1.99	0.78	0.46	-0.04	8.8	5	2.1	4.2
CULA	-78.69	0.14	12.28	3.62	1.34	1.09	-0.02	9.2	5	1.3	3.6
CUYC	-78.85	-6.01	4.55	-4.41	0.63	0.52	-0.02	2.9	12	2.1	1.6
CUZC	-71.95	-13.52	4.69	0.14	0.37	0.30	-0.00	4.6	713	2.5	4.2
DAUL	-79.99	-1.87	9.66	2.89	0.73	0.38	-0.03	5.9	3	1.4	1.6
DESV	-79.92	-1.04	11.33	3.13	0.64	0.47	-0.03	6.8	4	2.8	3.4
ELCH	-77.80	-0.33	4.24	0.47	0.39	0.30	0.03	15.8	4	2.0	0.7
ESMR	-79.72	0.93	21.68	5.35	0.33	0.27	0.00	5.2	1814	1.4	1.5
ETEN	-79.85	-6.94	5.67	-3.27	0.55	0.44	-0.03	4.0	9	1.6	0.8
FLFR	-79.84	-0.35	15.30	1.05	0.43	0.53	0.00	3.2	1113	1.9	1.7
FLOR	-75.60	1.62	1.71	-1.91	0.57	0.43	0.00	2.7	726	1.7	1.9
GPH1	-79.91	-2.73	6.45	1.81	0.91	0.75	-0.05	3.6	19	4.5	2.3
GYEC	-79.89	-2.14	7.59	3.38	0.53	0.44	-0.00	3.9	1037	1.6	1.8
GYVT	-78.74	-8.05	5.97	-2.93	0.68	0.53	-0.02	4.0	8	0.9	1.7
HONA	-79.15	-3.47	4.21	-2.11	0.87	0.43	0.01	17.0	9	4.6	1.7
HSPR	-78.85	-0.35	12.78	0.16	0.53	0.43	-0.00	3.7	1173	1.8	2.3
HUAC	-77.80	-0.70	3.23	-0.34	0.58	0.59	-0.16	15.7	9	4.5	3.6
HUAL	-77.57	-9.54	6.51	0.42	0.59	0.47	-0.01	4.0	9	1.2	1.6
HUAN	-75.32	-12.04	7.02	-1.30	0.52	0.35	-0.00	4.8	626	2.0	3.7
HUAP	-77.60	-11.15	20.86	2.84	0.60	0.47	-0.03	4.0	8	1.0	2.4

HUAR	-78.18	-10.10	9.93	0.14	0.35	0.25	-0.00	4.0	1255	1.1	1.6
IQTS	-73.27	-3.76	0.10	0.19	0.40	0.28	-0.00	4.7	748	2.2	2.8
ISPT	-81.07	-1.26	35.82	4.08	0.43	0.34	0.00	3.6	1196	1.4	1.7
JICA	-76.87	-11.95	20.71	3.35	0.62	0.50	-0.01	3.2	358	1.4	2.2
JUJA	-79.55	-1.89	10.82	3.21	1.08	0.56	-0.04	13.1	3	1.9	0.6
LATA	-78.62	-0.81	9.27	1.37	0.24	0.20	-0.00	17.1	43	2.7	4.5
LCOL	-79.20	-0.24	12.64	1.85	0.28	0.23	-0.01	15.7	13	3.0	4.5
LGCB	-79.57	0.38	16.78	2.39	0.49	0.34	0.00	3.3	912	1.8	1.7
LI01	-77.01	-12.10	20.83	3.94	0.35	0.29	-0.00	3.9	1043	1.3	1.5
LIMO	-76.62	-0.40	0.59	-0.26	1.24	0.93	0.00	9.4	4	2.1	2.9
LITS	-78.44	0.87	13.51	2.25	0.31	0.26	-0.01	15.7	10	2.4	3.1
LJEC	-79.19	-3.98	4.33	-2.67	1.50	0.47	0.00	3.5	1150	1.8	3.1
LORO	-75.98	-1.61	-0.76	1.47	0.62	0.54	0.01	6.3	7	2.7	3.1
MACH	-79.96	-3.25	5.58	-1.02	0.69	0.37	-0.00	15.2	6	2.6	2.0
MOCA	-79.50	-1.18	10.33	2.49	0.51	0.39	0.00	15.8	9	2.9	4.5
MONT	-76.98	-2.06	1.63	-0.35	0.62	0.54	0.01	6.3	11	2.2	2.4
MORA	-80.02	-5.54	4.85	-3.23	0.88	0.70	0.00	4.0	9	1.0	0.7
NARI	-79.53	-3.14	3.42	-2.08	0.50	0.34	-0.02	15.2	4	3.9	0.6
NEVA	-75.29	2.93	7.97	3.92	0.67	0.81	0.00	2.5	728	1.7	1.9
PAJA	-80.42	-1.55	11.06	1.44	0.98	0.68	-0.03	7.0	10	4.5	5.0
PAPA	-78.14	-0.38	7.05	2.55	0.46	0.39	0.00	6.7	8	0.8	0.8
PAST	-77.35	-9.97	8.91	1.25	0.67	0.52	-0.04	4.0	7	0.5	1.2
PCMY	-79.55	-7.38	4.09	-3.50	0.61	0.49	-0.04	4.0	8	2.3	1.6
PDNS	-79.99	0.11	18.87	4.54	0.55	0.44	0.00	2.7	958	1.3	1.8
PLOB	-81.28	-4.45	3.55	-1.02	0.59	0.49	-0.01	4.0	6	1.1	2.3
PPRT	-80.21	-0.12	20.03	6.14	0.53	0.51	-0.01	3.0	962	1.7	1.6
PRMG	-77.85	-10.65	15.76	1.88	0.61	0.48	-0.02	4.0	8	1.3	1.9
PROG	-80.36	-2.41	9.69	2.73	0.45	0.33	-0.01	15.8	6	3.7	5.3
PSNT	-78.65	-8.99	5.71	-2.35	0.70	0.55	0.02	4.0	8	0.6	1.0
PSTO	-77.27	1.21	8.13	2.82	0.50	0.42	0.00	3.5	1002	1.7	1.9
PTGL	-80.03	0.78	24.33	4.73	0.47	0.39	0.00	3.1	1073	1.4	1.5
PTPO	-79.62	-6.74	5.54	-2.68	0.62	0.49	-0.02	4.0	7	1.2	1.1
PUEB	-79.53	-1.55	10.34	2.79	1.57	0.91	-0.33	7.0	7	4.5	2.1
PUMA	-79.46	-7.71	5.47	-3.57	0.64	0.52	-0.01	4.0	7	3.7	5.3
PUYX	-78.06	-1.50	6.41	-1.43	1.71	0.73	0.01	8.6	6	1.9	1.9
RIOP	-78.65	-1.65	4.75	-4.28	0.39	0.35	0.00	3.1	1085	1.6	1.6
RVRD	-79.38	1.06	20.43	4.20	0.43	0.41	-0.00	3.2	1037	1.9	2.0
SABA	-80.22	-1.84	8.72	2.46	1.16	0.79	-0.09	8.8	3	1.0	1.1
SALN	-80.99	-2.18	14.45	2.56	0.59	0.43	0.00	2.9	1028	1.5	1.9
SALY	-78.97	-8.22	6.00	-2.44	0.43	0.22	0.00	3.6	915	1.1	2.1
SAYA	-77.17	-11.08	17.13	3.50	0.62	0.48	-0.05	4.0	10	1.2	1.3
SCH1	-80.49	-6.11	3.43	-3.09	0.82	0.68	-0.01	4.0	12	1.3	2.4
SCH2	-80.57	-5.63	4.07	-4.29	1.04	0.84	-0.01	4.0	12	6.0	3.0
SNLR	-78.84	1.29	16.20	-0.79	0.42	0.54	0.00	2.7	903	1.8	1.8
SNTI	-78.01	-3.04	3.04	-2.97	1.15	1.26	0.00	16.5	4	3.0	13.4
SOZO	-79.79	-4.33	4.10	-2.35	0.84	0.36	-0.16	15.4	5	0.5	2.7
SRAM	-79.56	-0.60	13.00	1.92	1.96	1.51	-0.11	3.5	4	1.2	2.0
STCL	-79.07	-7.25	5.28	-2.95	0.60	0.50	-0.04	4.0	11	1.9	1.1
STIS	-77.98	-9.53	6.97	-0.66	0.59	0.46	-0.03	4.0	8	1.3	0.9
SUNW	-81.05	-4.69	3.23	1.51	0.88	0.72	0.00	4.0	7	0.6	0.8
TOTO	-78.67	-2.25	5.33	-2.67	0.29	0.23	0.00	15.2	9	4.6	7.3
TU01	-80.45	-3.55	6.46	-1.85	0.60	0.73	-0.01	2.6	612	1.6	1.8
TUCO	-78.74	1.81	19.08	2.64	0.66	0.62	-0.00	2.5	646	1.6	1.8
TULC	-77.70	0.81	7.02	2.64	0.38	0.33	0.01	10.7	12	0.9	1.8
ZAMO	-78.93	-4.05	3.61	-1.68	0.31	0.26	0.00	10.8	14	1.5	2.4
ZHUD	-79.00	-2.46	5.78	-1.93	0.45	0.30	-0.10	15.3	6	2.2	7.3

Supplementary Table T2.1: GPS velocities with respect to Stable South America and related information. Longitude, latitude in decimal degrees. Ve, Vn: east & north components of velocity in mm/yr; SVe, SVn: formal error (1-sigma confidence level) of Ve, Vn. Corr_en: correlation coefficient between Ve & Vn; Obs_span: observation period in decimal year. #obs: number of observation used in velocity estimation; wrms_E, wrms_N: long-term repeatability for the east & north components in mm.

Euler Pole Estimation for the Inca Sliver

```
ROTATION RATE VECTOR (geocentric cartesian coordinates)
Wx (rad/yr):  6.5387E-10 +- 4.3423E-11
Wy (rad/yr): -1.3264E-09 +- 2.0855E-10
Wz (rad/yr):  6.1159E-10 +- 2.5619E-11

EULER POLE
longitude (dec. degree)    : -63.76
latitude  (dec. degree)    :  22.47
angular velocity (deg/Myr ):  0.092

ASSOCIATED ERROR ELLIPSE (all values in decimal degrees)
```

```
semi major axis            :  4.02
semi minor axis            :  0.44
azimuth of semi major axis : -116.4

angular velocity error     : 0.010 degree per Myr

STATISTICS
----------
Number of sites       =         28
Chi**2                =      198.9
Deg. of. freedom      =         53
Reduced chi-square    =        1.9

RESIDUALS
----------
```

site	R_ve	R_vn	S_ve	S_vn	RN_ve	RN_vn
AMAL	0.57	0.12	0.52	0.34	1.10	0.34
AY01	-1.70	0.55	0.67	0.43	-2.54	1.28
CBLA	-0.81	-0.52	0.64	0.51	-1.27	-1.02
CCHO	0.49	0.06	0.94	0.77	0.52	0.08
CHUL	-1.29	-0.81	0.56	0.46	-2.30	-1.76
CJ01	-0.26	1.38	0.65	0.45	-0.40	3.07
CUEC	0.02	-0.27	0.36	0.32	0.05	-0.84
CUYC	-0.28	-1.95	0.63	0.52	-0.44	-3.75
CUZC	-1.27	1.48	0.37	0.30	-3.44	4.94
ETEN	0.71	-0.66	0.55	0.44	1.29	-1.49
GYVT	0.84	-0.49	0.68	0.53	1.23	-0.93
HONA	-0.24	0.40	0.87	0.43	-0.27	0.93
LJEC	-0.18	-0.16	1.50	0.47	-0.12	-0.34
MORA	0.09	-0.59	0.88	0.70	0.11	-0.84
NARI	-0.97	0.49	0.50	0.34	-1.94	1.44
PCMY	-0.93	-0.94	0.61	0.49	-1.53	-1.91
PSNT	0.44	0.07	0.70	0.55	0.63	0.13
PTPO	0.61	-0.10	0.62	0.49	0.99	-0.21
PUMA	0.39	-1.01	0.64	0.52	0.61	-1.95
RIOP	0.59	-1.86	0.39	0.35	1.50	-5.31
SALY	0.84	0.04	0.43	0.22	1.96	0.16
SCH1	-1.41	-0.37	0.82	0.68	-1.72	-0.54
SCH2	-0.69	-1.56	1.04	0.84	-0.66	-1.85
SOZO	-0.47	0.25	0.84	0.36	-0.56	0.70
STCL	0.27	-0.45	0.60	0.50	0.45	-0.91
TOTO	1.07	-0.24	0.29	0.23	3.69	-1.06
ZAMO	-0.92	0.79	0.31	0.26	-2.97	3.05
ZHUD	1.49	0.55	0.45	0.30	3.31	1.85

```
rms =       0.84 mm/yr    wrms =       0.83 mm/yr
```

Supplementary Table T2.2: R_ve, R_vn, S_ve, S_vn, in the table are residuals velocities and formal errors for the east and west component, in mm/yr. RN_ve, RN_vn are normalized residuals for the east & north components.

Euler Pole Estimation for the North Andean Sliver

```
ROTATION RATE VECTOR (geocentric cartesian coordinates)
Wx (rad/yr):  5.5585E-10 +- 6.7414E-11
Wy (rad/yr):  -4.801E-09 +- 3.1882E-10
Wz (rad/yr):  1.3141E-09 +- 1.9304E-11
ASSOCIATED VARIANCE-COVARIANCE MATRIX (rad/yr)**2
        Wx          Wy            Wz
-----------------------------------
Wx |4.5446E-21 -2.0897E-20 1.0665E-22
Wy |           1.0165E-19 -5.0274E-22
Wz |                       3.7264E-22
-----------------------------------

EULER POLE
longitude (dec. degree)    : -83.40
latitude  (dec. degree)    :  15.21
angular velocity (deg/Myr ):  0.287
ASSOCIATED ERROR ELLIPSE
```

```
semi major axis            :  1.03
semi minor axis            :  0.18
azimuth of semi major axis :  74.4

angular velocity error     : 0.018 degree per Myr

STATISTICS
----------
Number of sites       =         14
Chi**2                =      124.0
Deg. of. Freedom      =         27
Reduced Chi-square    =        2.1

RESIDUALS
----------
```

site	R_ve	R_vn	S_ve	S_vn	RN_ve	RN_vn
BALZ	1.78	0.77	1.20	0.86	1.48	0.89
BOGT	-0.78	0.12	0.29	0.27	-2.69	0.44
DAUL	0.28	1.06	0.73	0.38	0.38	2.78
JUJA	1.43	1.14	1.08	0.56	1.32	2.04
LATA	0.45	-1.19	0.24	0.20	1.89	-5.95
MOCA	1.32	0.40	0.51	0.39	2.59	1.03
NEVA	1.15	-0.42	0.67	0.81	1.72	-0.52
PAJA	1.85	-0.16	0.98	0.68	1.89	-0.24
PAPA	-1.53	-0.27	0.46	0.39	-3.33	-0.70
PROG	0.03	1.10	0.45	0.33	0.07	3.32
PSTO	0.39	-0.47	0.50	0.42	0.78	-1.11
PUEB	1.13	0.72	1.57	0.91	0.72	0.79
SABA	-0.64	0.75	1.16	0.79	-0.55	0.95
TULC	-0.93	-0.41	0.38	0.33	-2.45	-1.26

```
rms =       0.95 mm/yr    wrms =       0.85 mm/yr
```

Supplementary Table T2.3: R_ve, R_vn, S_ve, S_vn, in the table are residuals velocities and formal errors for the east and west component, in mm/yr. RN_ve, RN_vn are normalized residuals for the east & north components.

Subduction Earthquake Slip Vectors and Partitioning of oblique Nazca/South America Convergence

Figure S2.1 demonstrates that, on average, subduction earthquake slip vector in Colombia-Ecuador are rotated clockwise of ~5° compared to the direction of the Nazca/South America convergence[37], while they are rotated counter-clockwise by the same amount in Peru. A rotation of ~10° of the slip vector direction clearly occurs across the Gulf of Guayaquil, while the average strike of the trench and the plate convergence direction are constant. This result provides an independent evidence for the Gulf of Guayaquil being the boundary between the Inca and the North Andean slivers. The existence of systematic rotation with respect to the Nazca/South America convergence requires a component of trench parallel motion of the sliver, with a right-lateral strike-slip component for Peru and left-lateral strike-slip component for Ecuador-Colombia. The histograms of slip vector direction for Central Peru and Southern Peru show the same amount of divergence with respect to the Nazca/South

America convergence direction, with perhaps an increasing rotation in southern Peru. We therefore conclude that the study of subduction events slip vector supports the hypothesis of an Inca sliver extending in southern Peru as far south as to the Arica bend.

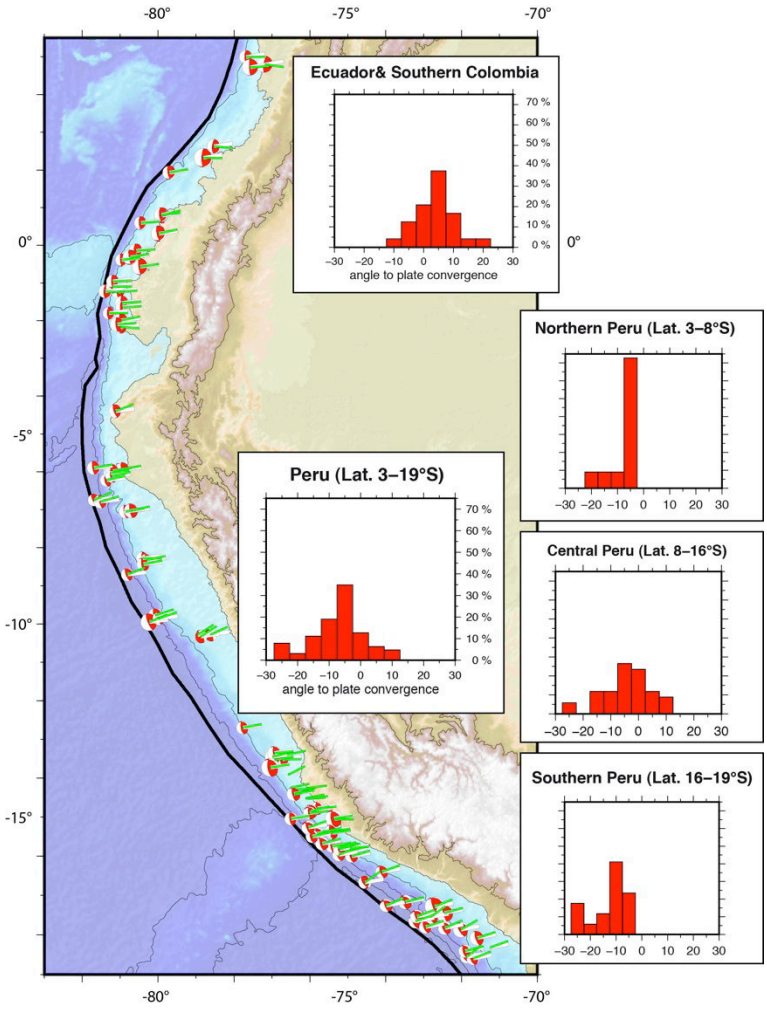

Supplementary Information Figure S2.1: Focal mechanisms for subduction interface events from the CMT catalog (http://www.globalcmt.org) for the 1976-2012 period. Their associated slip vector is shown by the green line, together with the direction of the Nazca/South America convergence direction37 (white line). Histograms show the angle between Nazca/South America convergence direction and subduction events slip vectors, expressed as percentages over the total number of earthquakes of a given segment, by bins of 5 degrees. Aftershocks following the Pisco 2007 (M_w7.9) and the Arequipa 2001 (M_w8.4) earthquakes have been removed to avoid bias of the statistics.

The level of partitioning is similar between the two domains (Fig. S2.2): the motion of the Inca sliver accommodates about ¼ of the along-trench component of the Nazca/South America convergence. In Ecuador-southern Colombia, the Euler pole for the NAS predicts a larger trench along-strike component away from the trench, so

the amount of partitioning slightly depends on the location where it is calculated, but it is around 20±3%. Normal trench convergence is also partitioned with ~ 6% of the convergence being transferred to the motion of the Inca sliver, and 12-17% for the North Andean Sliver in Ecuador, decreasing to almost 0% in Colombia.

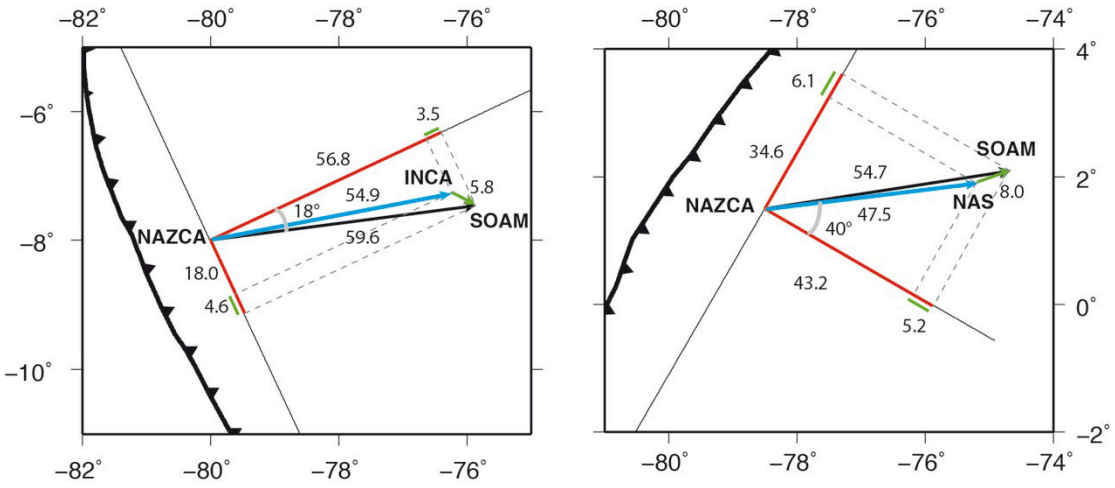

Supplementary Information Figure S2.2: Sketch of kinematics triangles and obliquity partitioning in Peru (left) and in Ecuador-Colombia (right). Red lines indicate along & normal trench components of Nazca/South America (SOAM) convergence vector shown by the black arrow. Green arrow is the sliver convergence vector with respect to SOAM. Along & normal trench components are also shown in green. Inca/SOAM & NAS/SOAM convergence vectors are shown in blue. All numbers are in mm/yr. Calculation is performed at (long. -80°E, lat. 8°S) for Peru and at (long. -78.5°E, lat. 1.5°N) for Ecuador-Colombia.

Inversion of Interseismic Coupling

The input data set for the inversion of interseismic coupling along the subduction interface consists of the residual velocity field with respect to the sliver they belong to. Sites located close to the North Andean Sliver / Inca Sliver boundary, are most probably also impacted by elastic effect of major crustal faults, as can be seen in Fig. 2B of the main text. Thus the sites TU01, MACH, GPH1, CUER have been removed from the inversion, and 60 GPS sites were used in the inversion. We use the virtual back-slip approach[28] to model the inter-seismic coupling. The rake and the convergence velocity have been fixed to be consistent with the Nazca plate/Inca Sliver motion south of lat. 3.5°S and with the Nazca/North Andean Sliver north of 3.5°S. The subduction interface has been divided into 1024 quasi-equilateral triangular subfaults with an average edge length of 30 km. Our triangular mesh

follows the Slab1.0 geometry[29] for the South America subduction interface, except in the Lima area, where short scale variations have been simplified. Our inversion strategy follows the linear Bayesian approach proposed by [30,37], which minimizes a cost function:

$$S(m) = \frac{1}{2}\left[(Gm-d)^t C_d^{-1}(Gm-d) + (m-m_0)^t C_m^{-1}(m-m_0)\right] \quad (1)$$

where m is the vector of back-slip amount in each subfault, m_0 is an a priori model for coupling distribution, d is the vector of observations including the GPS velocity components. G is the model matrix including each individual subfault back-slip contribution to d. C_d and C_m are the variance-covariance matrices associated with the data and the model respectively. C_d is taken as a diagonal matrix including the standard deviation derived from the geodetic analysis. C_m is an exponential matrix of the form:

$$C_m(i,j) = \sigma_m^2 \exp\left(-\frac{d(i,j)}{L}\right) \quad (2)$$

where $d(i,j)$ is the distance between two subfaults i and j, L is the critical distance for correlation for slip. The cost function is minimized using a sequential least-squares approach, using the constraints that values of m are searched in the interval $[0; \nu_{plate}]$, where ν_{plate} is the Nazca plate /Inca Sliver convergence rate (resp. Nazca plate / North Andean Sliver) velocity for subfaults located south (resp. north) of lat. 3°S.

Rather than providing just our "best" model, the chosen inversion formalism offers the advantage to explore a range of possible models by varying 3 parameters only: m_0, σ_m and L (Fig. S2.3). L controls the smoothness of the solution, σ_m the weight given to smoothing and damping with respect to the *a priori* model m_0. Within this approach, the slip on subfaults that are not resolved by the data tends to follow the a priori model m_0. Thus, possible models with maximum (resp. minimum) coupling will be obtained for an a priori model taken as a fully coupled (resp. fully uncoupled) subduction ($m_0 = \nu_{plate}$, resp. $m_0 = 0$) and a relatively small damping factor σ_m (σ_m <10mm/yr). The range of acceptable models is fixed to a conventional value of chi-square=1050, corresponding to 2.5 times the minimum chi-square (Fig. S2.3),

equivalent to a wrms=1.1 mm/yr. Fig. S2.4 shows a selection of 9 models illustrating the effects of different values for m_0, σ_m and L.

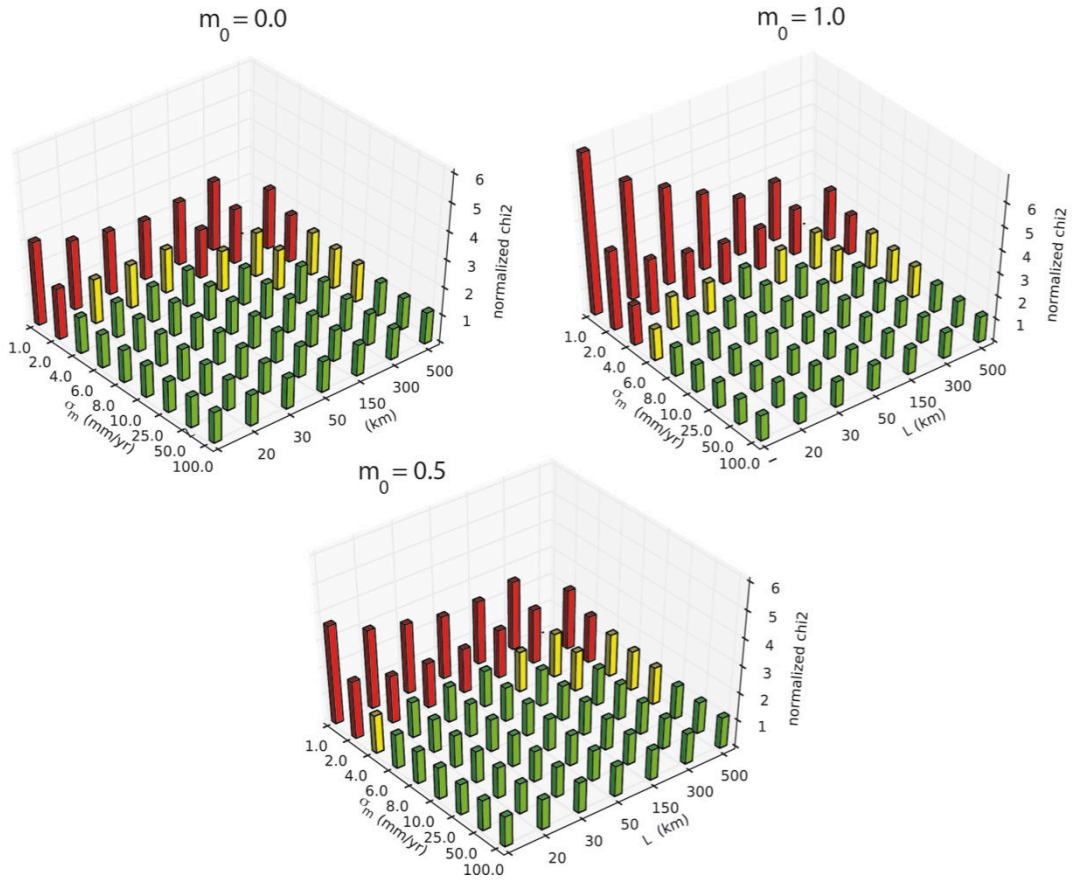

Supplementary Information Figure S2.3: Model misfits obtained as a function of a priori constraint σ_m and smoothing distance L for null, intermediate and a priori coupling (m0=0.0, 0.5 and 1.0 x convergence rate). Normalized chi-square (chi2) are chi-square divided by the chi-square providing the lowest misfit. The range of acceptable models is shown in green (2 times the minimum chi-square) and yellow (2.5 times the minimum chi-square).

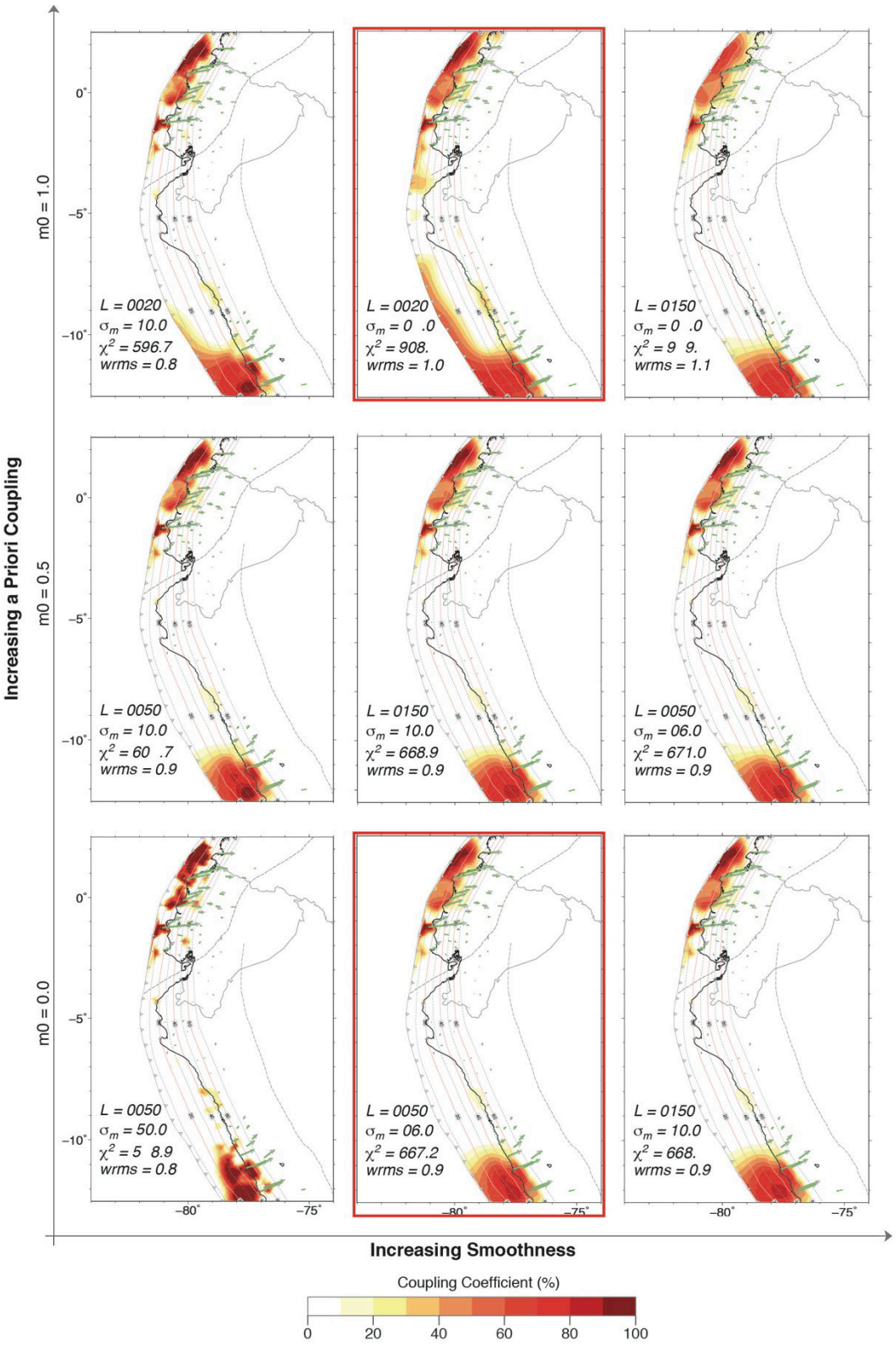

Supplementary Information Figure S2.4: Selection of 9 possible models for the spatial distribution of interseismic coupling. Models are vertically ordered by increasing values of *a priori* model from null to full coupling and horizontally ordered by increasing smoothness. Coupling coefficient is indicated by the color scale. Parameters values from equation (2) in the Supplementary Methods (L in km, σm in mm/yr) are indicated, together with the obtained chi-square and wrms (mm/yr). The red frames indicate the models selected for Fig. 3 of the main text.

All models show (1) high coupling in central Peru ending at latitude 10-11°S (2) low to null coupling between 10°S and 3°S (3) shallow and laterally heterogeneous coupling north of latitude 3°S. The major variation among models is the amount of coupling close to the trench between latitude 7°S and 10°S. Because the coastline in Peru is about 200 km away from the trench south of latitude 7°S, GPS data has little sensitivity to coupling close to the trench. Inverted coupling therefore tends to follow the a priori model. Secondary differences are the size of high coupling areas and in general the amount of coupling close to the trench.

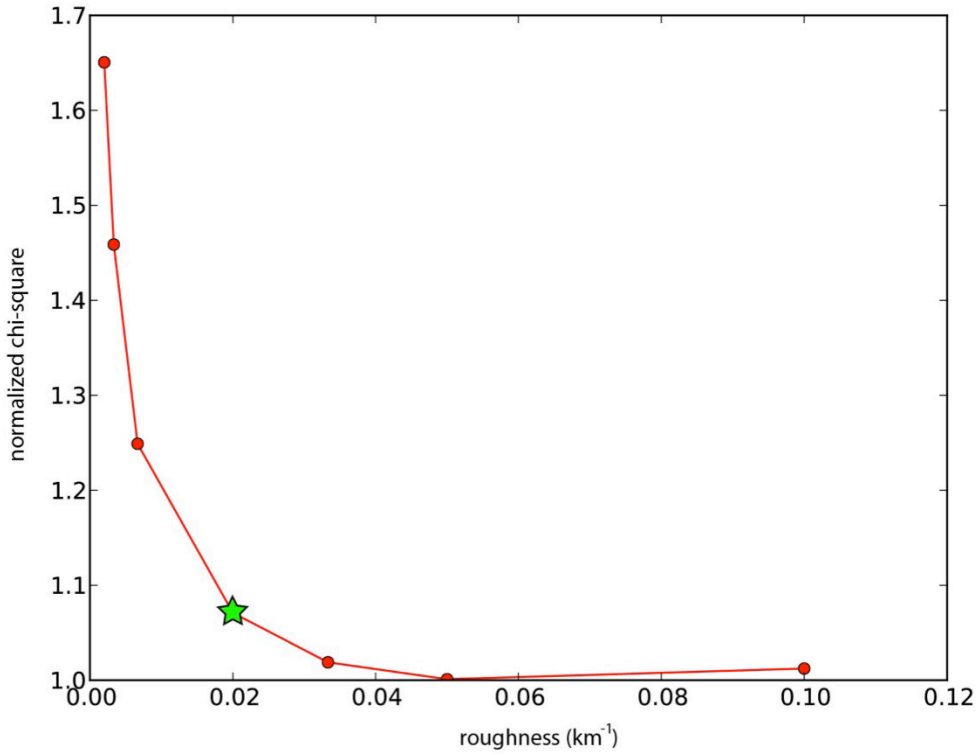

Supplementary Information Figure S2.5: Normalized chi-square as a function of the roughness ($1/L$) for σ_m=6mm/yr and m_0=0.0. The green star indicates the chosen value (L=50km) for the model shown in Fig. 3A of the main text.

For the purpose of illustration in the main text, we used a L-curve[38] to choose the smoother model correctly explaining the GPS data for σ_m=6mm/yr and m_0=0.0. The obtained value in L=50 km (Fig. S2.5).

Supplementary References

31. P. A. Mothes, J.-M. Nocquet and P. Jarrín, Continuous GPS Network Operating Throughout Ecuador, Eos Trans. AGU, 94(26), 229 (2013).

32. R. Trenkamp, J. N. Kellogg, J. T. Freymueller, H. P. Mora, Wide plate margin deformation, southern Central America and northwestern South America, CASA GPS observations. *Journal of South American Earth Sciences*, *15*(2), 157–171 (2002).

33. Herring, T. A., King, R. W. & Mcclusky, S. C. Introduction to GAMIT/GLOBK,Release 10.5, MIT, (2013).

34. S. P. Williams, CATS: GPS coordinate time series analysis software. *GPS Solutions*, *12*(2), 147–153. doi:10.1007/s10291-007-0086-4. (2008)

35. M. A. Floyd , et al. (2010), A new velocity field for Greece: Implications for the kinematics and dynamics of the Aegean, J. Geophys. Res., 115, B104036.

36. Z. Altamimi, X. Collilieux, L. Métivier, ITRF2008: an improved solution of the international terrestrial reference frame. *Journal of Geodesy, 85*(8), 457–473 (2011).

37. E. Kendrick, M. Bevis, R. Smalley Jr., B. Brooks, R. B. Vargas, et al., The Nazca–South America Euler vector and its rate of change. *Journal of South American Earth Sciences*, *16*(2), 125–131 (2003).

38. M. Radiguet, F. Cotton, M. Vergnolle, M. Campillo, A. Walpersdorf, N. Cotte, & V. Kostoglodov *(*2012*),* Slow slip events and strain accumulation in the Guerrero gap, Mexico, J. Geophys. Res., 117, *B04305, doi:*10.1029/2011JB008801.

39. P. C. Hansen, D. P. O'Leary, The use of the L-curve in the regularization of discrete ill-posed problems. *SIAM Journal on Scientific Computing*, *14*(6), 1487-1503 (1993).

Chapter 3

Present-day deformation of the Peruvian margin from 2008-2013 GPS measurements: The Inca Sliver kinematics and interseismic coupling along the megathrust

J. C. Villegas-Lanza[1, 2]*, M. Chlieh[1], J.-M. Nocquet[1], H. Tavera[2], J. Maguiña[3], D. Cisneros[4], F. Bondoux[5], P. Baby[5], X. Martin[1], F. Rolandone[6] and O. Cavalié[1]

[1]Geoazur, Université Nice Sophia Antipolis, IRD, CNRS, OCA, Nice, France.

[2]Instituto Geofísico del Perú, Lima, Peru.

[3]Instituto Geográfico Nacional, Lima, Peru.

[4]Instituto Geográfico Militar, Quito, Ecuador.

[5] Observatoire Midi-Pyrénées, Univ. Paul Sabatier, IRD, CNRS, 31400 Toulouse, France.

[6]Université Pierre et Marie Curie, Paris, France.

Corresponding authors: JC. Villegas-Lanza, M. Chlieh

E-mail address: juancarlos.villegas@igp.gob.pe

Abstract

Over 100 GPS measurements acquired in Peru and southern Ecuador between 2008 and 2013 provide new insight into the present-day deformation of the Peruvian margin. The Inca sliver is defined as the continental domain wedged between the subduction trench axis and the inter-cordillera fault systems that delimit the discontinuous boundary between the Occidental and the Oriental cordillera. This boundary is well localized along the Marañon fault in north of Peru and becomes diffuse in central and south Peru. We confirm that the Inca sliver has a southeastward motion at a rate of about 4-5 mm/yr, suggesting that its eastern boundary has a transpressional mechanism. In the oriental cordillera, the tectonic is dominated by 2-4 $mm.yr^{-1}$ of crustal shortening along the sub-andean fold and thrust belts. Along the coastal areas, the variable interseismic GPS gradients indicate a highly heterogeneous pattern of interplate coupling along the Peruvian megathrust interface. Interseismic models indicate weak and shallow coupling in northern Peru consistent with past moderate tsunami-earthquakes. In central and southern Peru, we found that highly coupled patches correlate well with the rupture areas of large megathrust earthquakes supporting that seismic asperities might be persistent features of the megathrust. The interseismic coupling drops abruptly where oceanic fracture zones and ridges enter in subduction, suggesting that these geomorphologic structures play a major role in the seismic segmentation of the Peruvian megathrust. In Central of Peru, where the great 1746 Mw~9.0 Lima-Callao occurred, the current interseismic moment deficit would suggest a recurrence time of at least 266-347 yrs to reproduce a similar event.

1. Introduction

Two simultaneous processes take place along ocean-continent subduction zones that control the occurrence of large earthquakes. First, mechanical coupling along the megathrust interface at shallow depth (<50-60km) results in elastic stress accumulation during the interseismic period. The level of interseismic coupling and its spatial distribution control the elastic energy available for future mega-earthquakes. Second, long-term motion within the overriding continent results in permanent deformation of the continental lithosphere accommodated by active faulting in the brittle crust. Although crustal earthquakes usually have lower magnitude than the large subduction events, their proximity to populated areas and infrastructures makes them potentially highly hazardous. Spatial geodetic measurements and more specifically the Global Positioning System (GPS) by quantifying the surface deformation at the millimeter per year accuracy over distances of thousands of kilometers, provides a direct observation of both the motion of the overriding continent and the interseismic deformation induced by stress accumulation along the plate interface, thus enabling us to assess the seismic potential posed by the subduction megathrusts and crustal faults inland.

The Andean margin where the oceanic Nazca plate converges rapidly (~60-70 mm/yr, [*Kendrick et al.*, 2003]) toward the South American continent is among the subduction zones where both high mechanical coupling at the megathrust and permanent continental deformation have been evidenced. Previous GPS studies carried out in Chile, Argentina, Bolivia, southern Peru and Ecuador-Colombia [*Norabuena et al.*, 1998; *Bevis et al.*, 2001; *Trenkamp et al.*, 2002; *Chlieh et al.*, 2004; *Ruegg et al.*, 2009; *Moreno et al.*, 2010; *Métois et al.*, 2012] have demonstrated a usually high level of mechanical coupling along the subduction interface, which correlates with areas where repeated large megathrust earthquakes (Mw~7.5 to 9.5, Figure 1) have occurred during the last centuries [*Kelleher*, 1972; *Dorbath et al.*, 1990]. Inland, the deformation of the continental overriding plate occurs predominantly through the translation of large continental domains referred as slivers, wedged between the subduction trench and the stable part of the South American continent [*Bevis et al.*, 2001; *Trenkamp et al.*, 2002; *Brooks et al.*, 2003; *Chlieh et al.*,

2007, 2011; *Wang et al.*, 2007; *Nocquet et al.*, 2014]. In contrast to previous geodetic results in South America, *Nocquet et al.*, [2014] show that a ~1000km long segment in the north of the Andes shows very weak interseismic coupling, indicating that the plate convergence is predominantly accommodated by aseismic creep along the megathrust. Furthermore, *Nocquet et al.*, [2014] identified a large continental sliver (called the Inca sliver) encompassing southern Ecuador and northern Peru, moving southeastward at ~5 mm/yr with respect to Stable America.

Here, we focus on the 2200km long of the Peruvian subduction zone located between the two bends of the western South America subduction, namely the Gulf of Guayaquil at latitude ~3°S and the Arica bend at latitude ~19°S. We derive a new velocity field including 102 GPS sites covering the whole Peruvian Andean margin. We use the horizontal velocities to quantify both the elastic interseismic coupling along the megathrust and the continental deformation. Our geodetic solution allows us to refine the eastern boundary and the kinematics of the Inca sliver as well as the interseismic coupling along the Peruvian subduction zone.

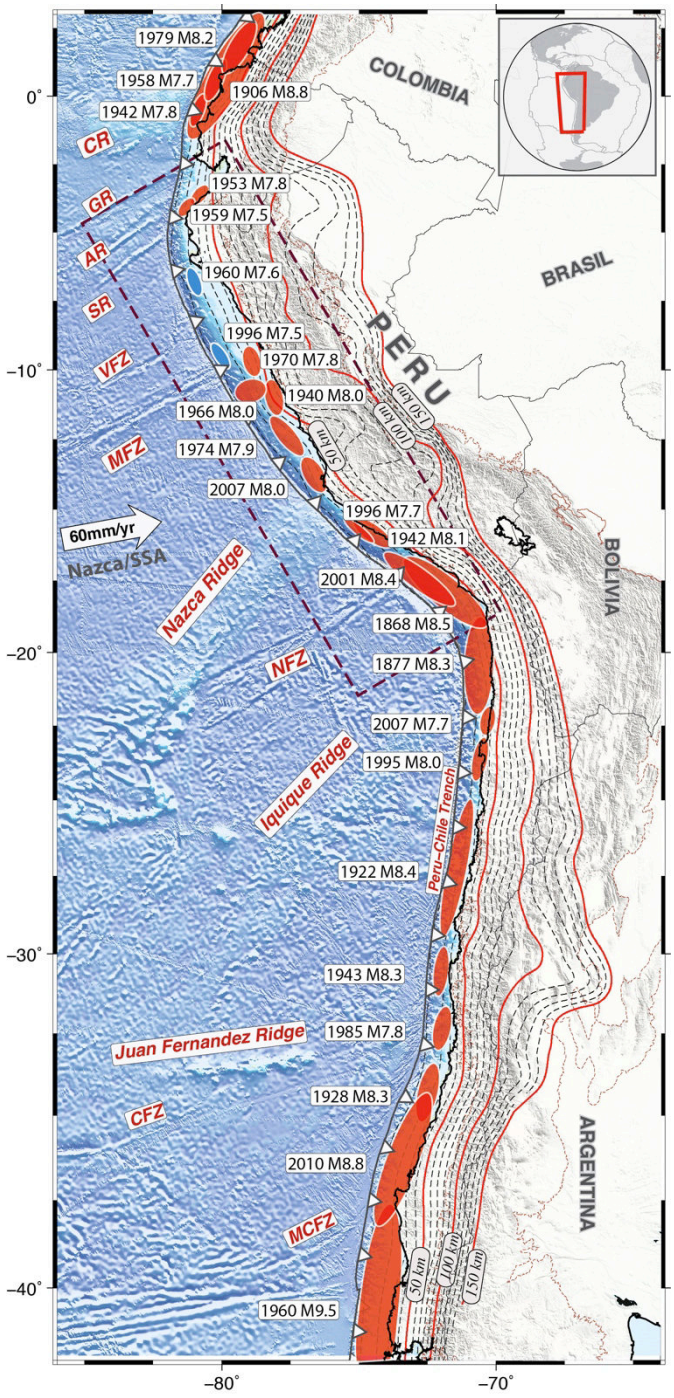

Figure 3.1: Seismotectonic setting of the South-American subduction zone. Red ellipses indicate the approximate rupture areas of large subduction earthquakes (M>7.5) between 1868 and 2013 *[Silgado, 1978; Beck and Ruff, 1989; Dorbath et al., 1990; Beck et al., 1998]*. Blue ellipses indicate location of moderate tsunami-earthquake *[Pelayo and Wiens, 1990; Ihmle et al., 1998]*. The bathymetry from GEBCO30s highlights the main tectonic structures of the subducting Nazca plate which are from north to south: the Carnegie (CR), the Grijalva (GR), the Alvarado (AR) and the Sarmiento (SR) ridges, the Virú fracture zone (VFZ), the Mendaña fracture zone (MFZ), the Nazca ridge, the Nazca fracture zone (NFZ), the Iquique and Juan Fernandez ridges and the Challenger (CFZ) and Mocha fracture zones (MCFZ). White arrow indicates the convergence of the Nazca plate relative to the Stable South American *[Kendrick et al., 2003]*. Slab geometry iso-depth contours are reported every 50 km (red lines) and 10 km (dashed lines) respectively, from the Slab1.0 model *[Hayes et al., 2012]*. Dashed rectangle is the area shown in Figure 3.2.

2. Historical seismicity and Seismotectonic setting

2.1 Updated historical large megathrust earthquakes in Peru

The history of seismicity, together with morphological features of the subducting Nazca plate have led previous authors to differentiate three segments along the Peruvian subduction zone [*Silgado*, 1978; *Dorbath et al.*, 1990; *Nishenko*, 1991; *Tavera and Buforn*, 1998; *Bilek*, 2010]: 1) a northern segment from the Gulf of Guayaquil at latitude 3°S to latitude 10ºS, 2) a central segment limited by the intersections with the trench of the Mendaña fracture zone at ~10°S and the Nazca ridge at ~15ºS, and 3) a southern Peru segment that extends south to the Arica bend at 19ºS (Figure 3.2). The southern and central Peru segments are characterized by recurrent great (M>8.5) and large megathrust earthquakes with characteristic recurrence times of ~100 to ~300 yr [*Kelleher*, 1972; *Dorbath et al.*, 1990]. By contrast, the northern Peru segment is characterized by a lack of great earthquakes and the sparse occurrence of moderate magnitude (Mw<8.0) earthquakes that trigger local tsunamis. The largest subduction earthquakes reported so far for northern Peru are the 1619 (Mw=7.7), 1953 (Mw=7.8), 1959 (Mw=7.5), 1960 (Mw=7.6) and 1996 (Mw=7.5) events (Figure 3.2). The two latter events showed slow rupture velocity, long source time duration and local tsunamis significantly greater than expected for their initial Ms value, sharing all characteristics of tsunami earthquakes [*Pelayo and Wiens*, 1990; *Ihmle et al.*, 1998; *Bourgeois et al.*, 1999]. However, we notice that for the 1953 and 1959 events, the tsunami catalogs [*NGDC http://www.ngdc.noaa.gov*, n.d.; *Soloviev and Go*, 1975; *Lockridge*, 1985; *Espinoza*, 1992] report local tsunamis with runup heights > 1m near Tumbes and surrounding areas including southern Ecuador (lat. 3°S to 4°S), indicating that they most probably also were interface events. The latter observations/events were not considered in recent compilations of large earthquakes (i.e. [*Dorbath et al.*, 1990; *Bilek*, 2010]).

Little information about more ancient events is available. The 1619 event that damaged the city of Trujillo [*Silgado*, 1978; *Seiner Lizárraga*, 2009] was not associated with a tsunami in historical catalogs. However, further south, *Spiske et al.*, [2013] recently found tsunami deposits layers in Casma (lat. 9°S) with an estimated age of 370 ± 30 yr, therefore possibly induced by the 1619 earthquake. *Seiner Lizárraga*, [2011] performed an exhaustive revision of the historical chronicles and

reports of earthquakes in Peru for the last five centuries. He found two significant events missing in catalogs of historical earthquakes of the Peruvian subduction zone. The first one occurred in 1759 near Trujillo. It produced severe damages in the infrastructures and caused 5 casualties in Trujillo. The historical chronicles of the epoch compare this event to that of 1619 in terms of the destruction of the city. The second event occurred in 1806 in central Peru near Lima causing severe damages in this city and presumably a tsunami in Callao (Lima port) where an anchor and some vessels were pulled inland within the two hours following the earthquake. For these two latter events, there is no magnitude assigned. However based on their intensity and tsunami characteristics, a range of magnitudes of 7.0-7.5 or greater is plausible.

Figure 3.2 shows an updated temporal distribution of historical and recent subduction earthquakes (M>7.5), together with their presumed rupture areas along the whole Peruvian subduction zone. Although the 1970 Mw=7.8 Ancash earthquake is by far the most catastrophic event in Peru so far, this event is not accounted in our compilation of subduction thrust events since it was a normal fault type event that occurred within the downgoing Nazca plate [*Abe*, 1972]. Although the northern segment exhibits a fundamentally different behavior from the central and southern segment, the existence of moderate earthquakes indicates that some stress is accumulating along the subduction interface. *Nocquet et al.*, [2014] did not find any significant strain in northern Peru. Their modeling indicates that either no coupling occurs at the megathrust in northern Peru or that if it exists, it is restricted to the shallowest part of the megathrust. We further investigate this aspect using our new dataset.

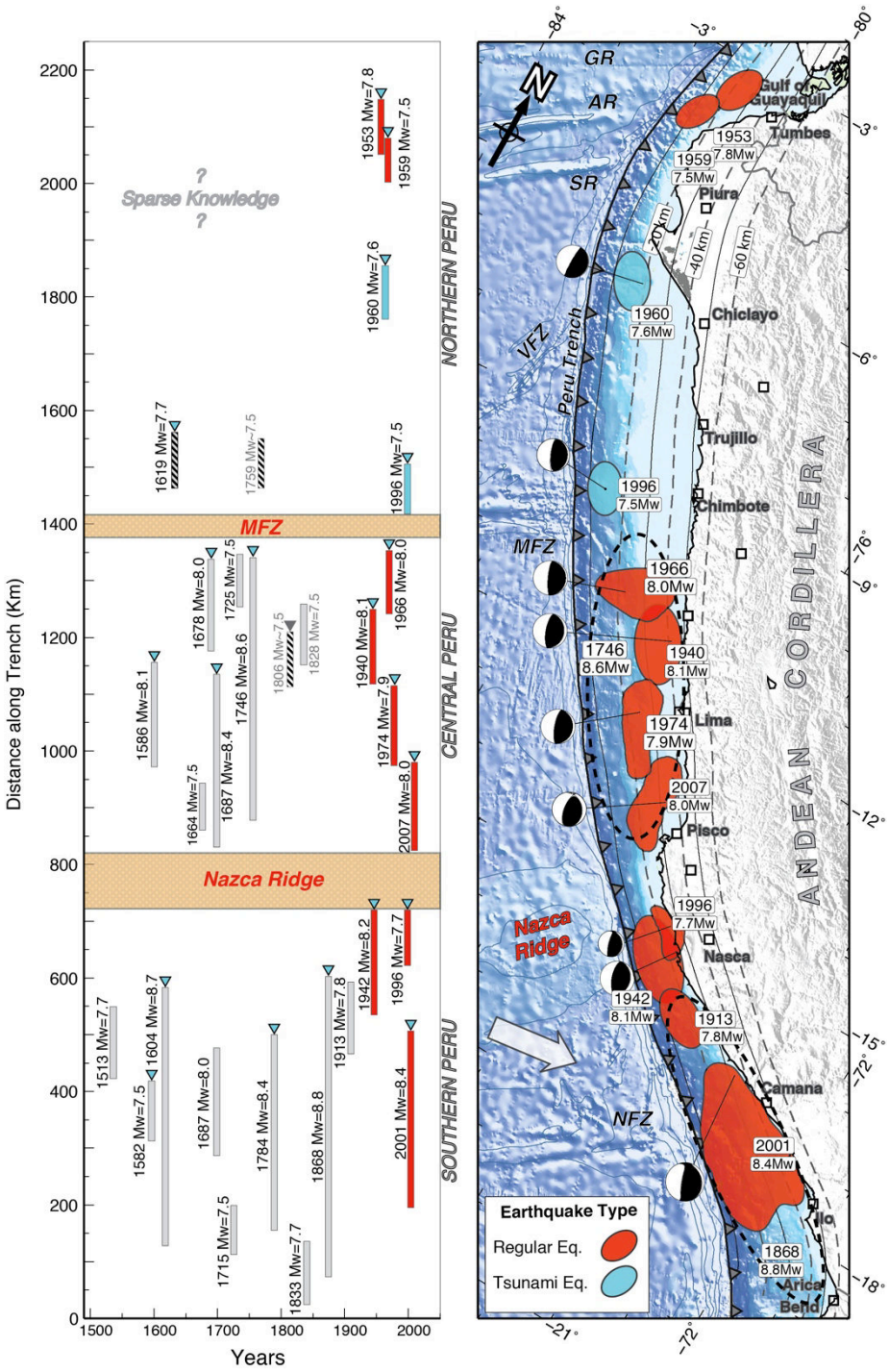

Figure 3.2: Temporal and spatial distribution of large subduction earthquakes with Mw>7.5 since the 16th century occurred in Peru. Left: Approximate rupture extent (in km) of historical (gray) and recent (red) megathrust earthquakes along the Peruvian margin as function of time (yrs) *[Dorbath et al., 1990; Swenson and Beck, 1999; Seiner Lizárraga, 2009, 2011]*. Triangle indicates if a tsunami was associated to the event. The orange bands delimit the north, central and south Peru subduction segments. Right: Map view of approximate rupture areas of the large subduction earthquakes that occurred in the 20th century *[Silgado, 1978; Beck and Ruff, 1989; Dorbath et al., 1990; Ihmle et al., 1998; Giovanni et al., 2002; Sladen et al., 2010]* with their associated gCMT focal mechanisms. In the northern of Peru, the earthquakes of Piura 1960 (Mw=7.6) and of Chimbote 1996 (Mw=7.5) (cyan colored polygons) were identified as tsunami-earthquake events *[Pelayo and Wiens, 1990; Ihmle et al., 1998; Bilek, 2010]*.

2.2 Geological structures on the Nazca plate

The most prominent subducting geomorphological structures well identified on Peruvian segment of the oceanic Nazca plate from south to north are: the Nazca fracture zone (NFZ), the Nazca ridge (NR), the Mendaña fracture zone (MFZ), the Virú fracture zone (VFZ), the Sarmiento (SR), Alvarado (AR) and Grijalva (GR) ridges (Figures 3.1 and 3.2). These structures are suspected to play a major role in the subduction earthquake segmentation [*Sparkes et al.*, 2010; *Wang and Bilek*, 2014]. The Mendaña fracture zone and Nazca ridge that delimit the central Peru segment appear to be strong and persistent barriers to the seismic rupture propagation [*Perfettini et al.*, 2010; *Chlieh et al.*, 2011]. Some of these features such as the NFZ can stall the rupture propagation as it occurred during the 2001 Arequipa earthquake [*Robinson et al.*, 2006] but could also fail like during the great 1604 and 1868 earthquakes. In the section 7.3 we discuss the correlation of our interseismic coupling models and the presence of these structures.

2.3 Active faults inland Peru

Three compilations of active faults have been proposed for Peru during the last years [*Macharé et al.*, 2003; *Veloza et al.*, 2011, and http://neotec-opendata.com]. Active reverse faulting is found all along the sub-andean domain, through thrust and fold belts. The shortening axis varies from E in northernmost Peru to NNE in southern Peru. Geological and paleomagnetic reconstructions [*Baby et al.*, 1997; *Oncken et al.*, 2006; *Arriagada et al.*, 2008] suggest that since the mid-Neogene, the sub-andean domain is the most deforming part of the Andes. In the central Andes, quaternary shortening rates higher than 10 mm/yr are estimated contrasting with geodetic rates of 4-10 mm/yr [*Norabuena et al.*, 1998; *Bevis et al.*, 2001; *Hindle et al.*, 2002; *Khazaradze and Klotz*, 2003; *Brooks et al.*, 2011; *Chlieh et al.*, 2011]. The seismicity distribution shows that most significant crustal earthquakes have occurred in this area, but at the junction between the eastern Andean cordillera and the sub-andean domain, which was proposed to be the main eastern boundary of the Inca sliver. Within the Andes, a complex pattern of deformation is observed, with a combination of reverse, normal and strike-slip faults. We note that a segmented active fault zone exists along the boundary between the Occidental and the Oriental cordilleras (Figure 3.3),

running from northern to southern Peru. This inter-cordillera fault systems is composed by the Marañon Fault System (MFS) in the north Peru proposed to be a reverse fault, the Chonta Fault System that is the continuation of the MFS in central Peru and is proposed to be a thrust fault [*Rodriguez Mejia*, 2008; *Pfiffner and Gonzalez*, 2013; *Scherrenberg et al.*, 2014], and the Urcos-Ayaviri-Copacabana-Coniri Fault System (UACCSF) near Cuzco in South Peru described as a left-lateral strike-slip fault [*Sempere et al.*, 2004]. No slip rate is available on these faults that would contribute to some internal deformation of the Inca sliver. Preliminary values of slip rates on those faults will be proposed according to the GPS results.

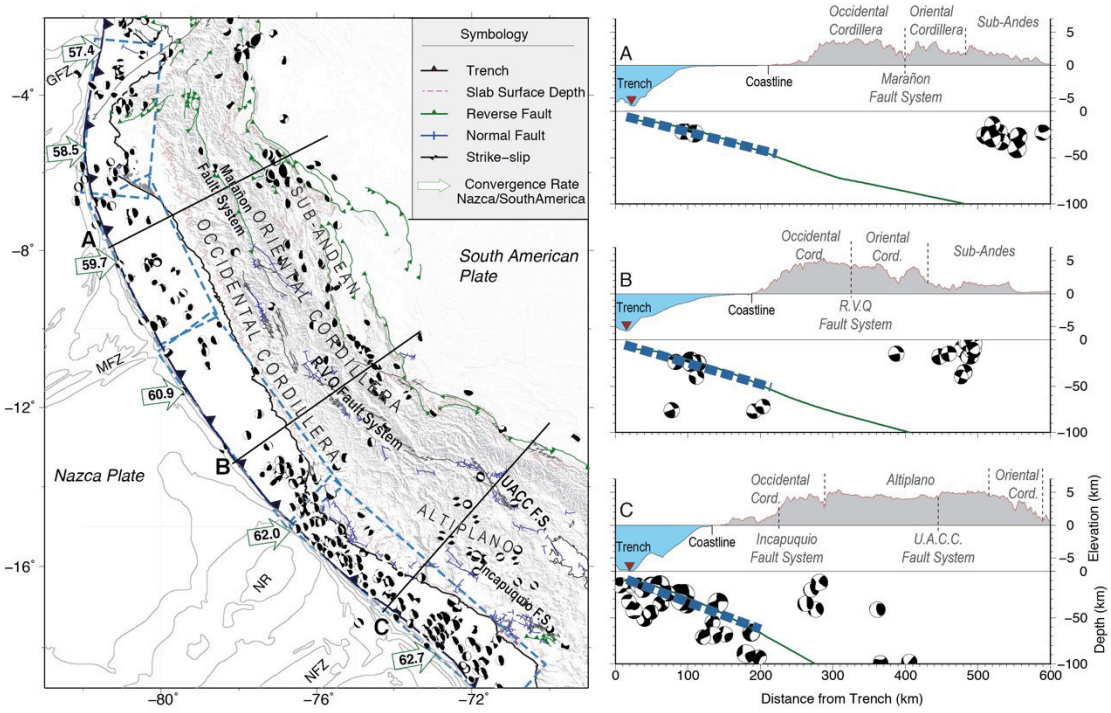

Figure 3.3: Left: Neotectonic setting of the Peruvian margin. Arrows indicate the convergence of the Nazca Plate relative to the Stable South America as predicted by the Euler pole of *Kendrick et al., [2003]*. Main quaternary faults are reported from the compilation of *Macharé et al., [2003] and Veloza et al., [2011]*. Note the location of the inter-cordillera fault zone that delimits the Occidental Cordillera from the Oriental Cordillera. Focal mechanism for M>5 earthquakes are from the gCMT catalog (black beach-balls) and from local seismological studies (red beach-balls, *[Suarez et al., 1983; Devlin et al., 2012]*. The rectangles (blue dashed lines) follow the slab geometry used in the modeling (Table 3.1) Right: Normal-Trench sections in Chiclayo, north Peru (A), in Lima, central Peru (B) and in Arequipa, south Peru (C) of the bathymetry, topography and the slab geometry (green lines).

3. GPS Datasets and processing

3.1 Datasets and Analysis strategy

In addition to the data already included in the study of *Nocquet et al.*, [2014], we add here 52 new GPS measurements (Table T3.1, Figure S3.1). The GPS data are composed by 48 continuous GPS (CGPS) and 54 survey GPS (SGPS) sites located from southern Ecuador (Lat. 2.8ºS) to southern Peru (Lat. 18ºS). The new data set includes three trench-perpendicular profiles of 12 SGPS sites that cross the Andean Cordillera and the sub-andean regions in northern Peru (latitude 6°S) and central Peru (latitude 10°S and 12°S, Figure S3.1 of the supplements). The velocity of campaign sites is derived from at least 3 surveys that were performed every two years since 2008. Our final geodetic solution further includes 32 continuous GPS sites from the Instituto Geográfico Nacional del Perú (IGN) and 8 CGPS sites from the Low Latitude Ionospheric Sensor Network project (LISN - IGP) distributed in central and northern Peru and installed progressively since 2007 [*Valladares and Chau*, 2012]. All CGPS velocities benefit from at least 2.5 years of measurements, a minimum period required to avoid bias coming from seasonal contributions to the velocity estimates [*Blewitt and Lavalle*, 2002]. Details about the data acquisition are provided in the Supplementary Information.

Both campaign and continuous GPS data have been analyzed simultaneously for the period 2007.60–2013.75. The analysis was carried out using the GAMIT/GLOBK software 10.50 [*Herring et al.*, 2010] in three steps. In the first step, we produce daily loosely constrained solutions, meaning that relative station coordinates are well determined, but in an undefined reference frame. In the second step, we express the daily solutions in the ITRF2008 reference frame [*Altamimi et al.*, 2012] using a seven-parameters Helmert transformation. Position outliers and offsets due to antenna changes in the continuous stations are automatically identified and removed. Then each time series is visually inspected to remove remaining outliers using the matlab toolbox Tsview [*Herring and Mcclusky*, 2009]. We exclude data between 2009.1 and 2009.7 near the Bayovar Peninsula in northern Peru because of a transient signal [*Villegas-Lanza et al.*, 2012] that is described in a separate paper (Villegas-Lanza et al., submitted). The average repeatability of the daily station coordinates for the East, North and vertical components are 1.5, 1.5 and 5.0 mm, respectively. The obtained

time series are then fitted by a weighted linear regression to a model consisting of a linear trend, seasonal variations (for continuous sites), and offsets. Finally, in the third step, when all outliers and offsets have properly been identified, daily solutions are passed to the Kalman filter implemented in GLOBK in order to estimate a consistent set of coordinates and velocities with respect to the ITRF2008 together with their associated variance-covariance matrix. All velocity uncertainties account for time-correlated noise in the GPS time series. More specifically, noise parameters (white noise, fractional integer noise index and level of fractional integer noise) are first estimated from the cleaned time series for continuous sites, using the CATS software [*Williams*, 2008]. As for most studies on time series [*Mao et al.*, 1999; *Williams et al.*, 2004], a combination of white and flicker noise (spectral index of -1, or close when estimated) best explains the noise characteristics. Then, the flicker noise values were converted to Markov noise equivalent values, so that the Kalman filter implemented in GLOBK provides the same velocity uncertainty as CATS results [*Floyd et al.*, 2010; *Nocquet*, 2012]. The mean equivalent Markov noise derived from CGPS time series in Peru was also applied to campaign data. To express the velocity field, we use the cumulated up-to-date solution of the IGS with respect to the ITRF2008 [*Rebischung et al.*, 2011; *Altamimi et al.*, 2012] using a 14-parameter transformation, which minimizes the departure of the positions and velocities at the 45 sites from the International GNSS Service for [*Dow et al.*, 2009, http://www.igs.org).

3.2 Definition of the Stable South America reference frame

In order to analyze the crustal deformation, the GPS velocities are expressed with respect to a Stable South American (SSA) reference frame. We estimate a rigid rotation vector for the South American plate using a subset of 20 sites that behave rigidly following the criterions of [*Nocquet et al.*, 2001]. We find that a subset of 12 sites located on the South American craton defines the optimal stable reference frame with a wrms = 0.40 mm/yr. The motion of the South America plate relative to the ITRF2008 is defined by an Euler pole located at 18.66ºS, 132.72ºW with an angular velocity of 0.118º/Myr (Table S2 and Figure S3.2). These values are very similar with the solutions from *Altamimi et al.*, [2012] and *Nocquet et al.*, [2014]. Table S1 shows the GPS Velocities with their associated formal errors with respect to the Stable South

American reference frame. We analyze and use this velocity field to constraint the boundaries of the Inca sliver and to define the interseismic coupling along the Peruvian megathrust.

4. Main patterns of the GPS velocity field

Our GPS velocity field samples the entire Peruvian and southern Ecuador Andean margin. The density of sites is ~70km along the coast from latitude 14°S to latitude 3°S. Owing to access difficulties, it includes sparser measurements within the high Andes and the sub-andean domain, and in southern Peru. Figure 3.4 shows the GPS velocity field relative to the Stable South America reference frame. Four main trends can be observed:

(1) In northwestern Peru (north of latitude 9.5ºS) and in southern Ecuador, the velocity field shows a fairly constant southeastward motion at ~5-6 mm/yr with respect to Stable South America, as previously found by *Nocquet et al.*, [2014]. In particular, no clear shortening in the plate convergence direction is observed, testifying a very small contribution from the interseismic elastic strain rate induced by locking along the megathrust (Figure 3.5A).

(2) In northeastern Peru, GPS sites located in the Oriental cordillera at the latitude of Yurimaguas (Figure 3.4) show an east to northeast direction of motion at velocities 3-4 mm/yr. This direction agrees with the sense of shortening accommodated across northwest-southeast reverse trending faults in the sub-andean domain [*Macharé et al.*, 2003; *Veloza et al.*, 2011] and direction of shortening indicated by the reverse focal mechanisms [*Suarez et al.*, 1983] (Figure 3.3). The transition between the ~5 mm/yr southeastward motion seen in the Piura peninsula and this domain occurs between the Marañon valley which separates the western and eastern Andean Cordilleras. A similar direction of motion, perpendicular to the strike of the Andean cordillera is also found throughout the sub-andean domain near Pucallpa and Puerto Maldonado (Figure 3.4), but with lower velocities (1-3 mm/yr).

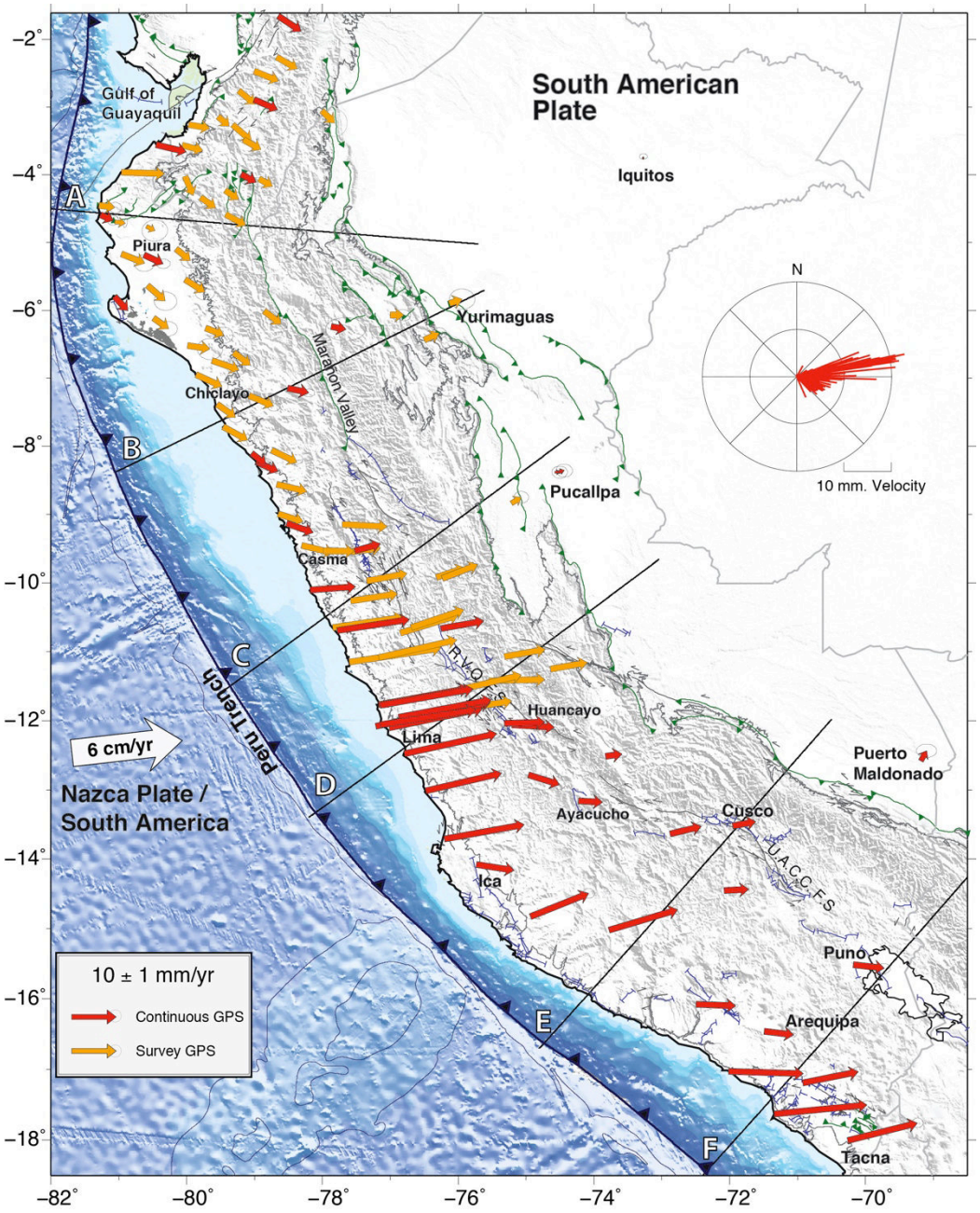

Figure 3.4: GPS velocity field expressed with respect to the Stable South America reference frame. Red and orange arrows correspond respectively to continuous (CGPS) and survey (SGPS) velocities. The GPS velocity field shows a complex pattern of deformation that considerably varies from north to south of Peru (see text for a description). Our velocity field is less dense in the coast of southern than in central and north Peru. The rose diagram is dominated by eastward direction of the GPS vector, being consistent with the plate convergence direction. The southeastward motion of sites in northern Peru shows an azimuth of 100°-135°.

(3) In central Peru, high velocities in the direction of the plate convergence are observed, systematically decreasing inland with increasing distance from the trench. Maximum rates of up to 22 mm/yr are found in the area of Lima. There are also

significant lateral variations of velocities along the coast, with lower velocity magnitude north and south of Lima, reflecting lateral variations of the strength of the interseismic coupling.

(4) In southern costal Peru, high (14-20mm/yr) velocities are also observed, decreasing inland, indicating significant coupling. Lateral variation are also seen, with smaller velocities in front of the Nazca ridge (8.5 mm/yr), about half of the velocities of neighboring GPS sites, suggesting lower mechanical coupling at the megathrust there. The obtained velocity field significantly differs from previous studies in the same area [*Norabuena et al.*, 1998; *Kendrick et al.*, 2001; *Chlieh et al.*, 2011]. Reasons for this discrepancy are discussed in section 6.3.3.

The velocity field therefore reflects the superimposed effects of both contribution coming from spatially heterogeneous coupling along the subduction interface and the long-term deformation of the overriding continent. In order to discuss and separate the two effects, we perform a careful step-by-step analysis. First, we show that the effect of elastic strain induced by locking along the megathrust is unable to explain the velocity field. Second, we discuss the continental deformation and more precisely propose a new eastern boundary for the Inca sliver. Third, we present a joint modeling for the interseismic spatial coupling along the subduction interface and motion for the Inca sliver kinematics. Finally, we discuss the implications of our results in terms of seismic hazards and the factors controlling the large variations of interseismic along the Peru subduction zone.

5. Interseismic models

We first perform a series of tests in order to verify whether the velocity field can be modeled by the single effect of interseismic locking along the subduction interface, that is a 2-plates model. Clearly, as stated in [*Nocquet et al.*, 2014], the low-to-null strain rate in northern Peru together with the nearly constant ~5mm/yr southeastward motion requires some translational motion. However, in central Peru and southern Peru, the larger interseismic contribution from locking along the subduction interface hides the small signal of sliver motion and more generally

continental deformation. In these tests, we use the residuals as a guide to define the Inca sliver boundaries.

5.1 Finite fault approach

The response of a slip at a finite-fault observed at a GPS station can be approached by summing the contributions of a regular grid of subfaults (i.e., [*Hartzell and Heaton*, 1983; *Hartzell et al.*, 1996] as:

$$u = \sum \sum d_{ij} [G^{s}_{ij} \cos (\lambda_{ij}) + (G^{d}_{ij} \sin (\lambda_{ij})] \quad (1)$$

where u is the displacement at an arbitrary station, i is the i^{th} subfault along strike, and j is the j^{th} subfault along dip. The terms G^{s}_{ij} and G^{d}_{ij} are the subfault Green's functions for a unit slip in the strike direction and down-dip direction, respectively. Each function is obtained by summing the responses of point sources uniformly distributed over it. d_{ij} and λ_{ij} are the average dislocation amplitude or slip and the rake angle, respectively.

We adopt the above finite-fault description to define four rectangular dislocations that follow the subduction interface geometry based on the Slab1.0 model [*Hayes et al.*, 2012] and modified by *Nocquet et al.*, [2014]. The major difference is in the Lima area where the Slab1.0 model predicts short wavelengths undulations that are not evidenced from local seismicity catalogue and add unnecessary complexities to the model. The sub-faults parameters are listed in Table 3.1. The Green's functions for each sub-faults are embedded in layered elastic half-space following the Crust2.0 model [*Bassin et al.*, 2000] (Table T3.4 in Supplements).

5.2 Forward uniformly locked fault zone models

Using a back-slip approach [*Savage*, 1983], we first produce forward interseismic models considering a fully locked fault zone that extends from the trench to successively 10, 20, 30, 40, 50 and 60km depths. We fix the back-slip dislocation amplitude to equate the plate convergence rate and constraint the rake to the average rake proposed by the local focal mechanisms of the gCMT catalogue

(http://www.globalcmt.org/CMTsearch.html) for each segment. Figure 3.5 reports the predicted horizontal interseismic displacements together with the observed along profiles GPS velocities across 6 trench-normal profiles. The location of the profiles is shown in Figure 3.4. As a preliminary test, profiles are useful to evaluate the first order of coupling and assess the need to invoke additional sliver motion to explain the data.

In the two northernmost profiles (5A, Piura and 5B, Chiclayo), no overall shortening is detected and it is impossible to explain simultaneously velocities in the far field (>350km from the trench) and velocities along the coast. This result demonstrates the need to account for some motion of a sliver and provides an upper bound of 20km for an average locking depth in that area. A general pattern of velocity decrease with increasing distance from the trench is evidenced from profiles 5C to 5F, south of latitude ~10°S, testifying of significant coupling along central and southern Peru. Nonetheless, simple 2-plates models again fail to explain simultaneously velocities in the far field and along the coast. For profile 5D, the gradient observed between the oriental Cordillera and the sub-andean domain, if induced by the locking would predict too high velocities along the coast by at least 5mm/yr, therefore demonstrating the need for a contribution in addition to the effect of locking along the subduction megathrust. Figure 3.5E and 3.5F further support this conclusion although with sparser data. We therefore conclude from this simple test that continental motion significantly contributes to the observed velocity field all along the Peruvian margin, and need to be accounted for any further modeling of the interseismic coupling along the megathrust.

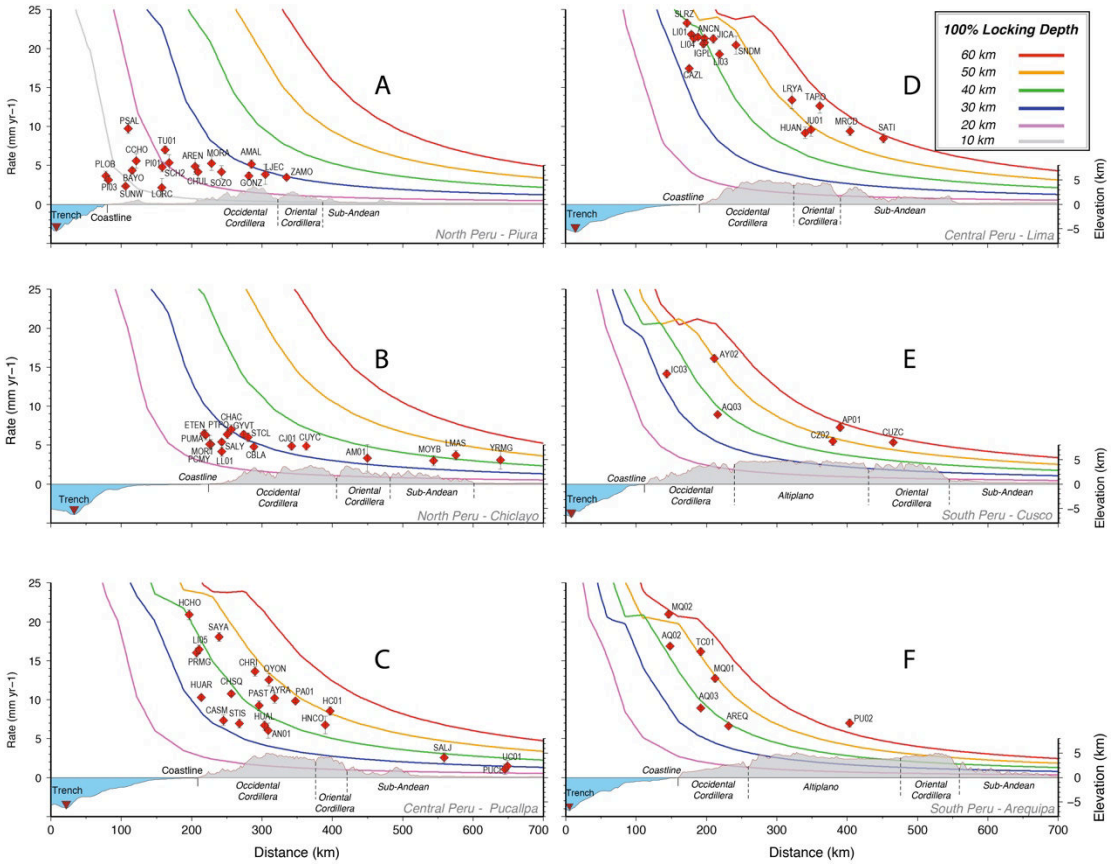

Figure 3.5: Normal trench sections of the horizontal GPS velocities with respect to the Stable South America reference frame. Color lines represent predicted horizontal gradient of forward back-slip models considering a fully locked fault zone extending from the trench up to 10, 20, 30, 40, 50 and 60 km-depth. In northern Peru A) Piura and B) Chiclayo, the low GPS gradients indicate a weak and shallow (< 30 km depth) interseismic coupling. In central Peru C) Pucallpa and D) Lima, where the highest GPS velocities are measured, we find that models with a locked fault zone extending up to 40-60 km depth bound the gradients. In southern of Peru E) Cusco and F) Arequipa models with LFZ between 40 and 50-km depth explain the GPS gradients. These profiles indicate that there is a significant lateral variation of the interseismic coupling along the Peruvian margin.

5.3 Inversion procedure for spatially variable interseismic coupling

Using the finite-fault approach described above, a full representation of the fault response relies on two parameters: dislocation amplitudes and rake angles. We can invert these parameters by matching the static displacements to the observations. The general forward problem is written as:

$$\mathbf{d} = \mathbf{G}(\mathbf{m}) \qquad (2)$$

where: **G** represents the Green functions linking the observables to the model**, d** is the data vector (here, east and north components of the GPS velocities), **m** the model

vector (here, slip amplitude and rake direction). The inversion is performed using a simulated annealing algorithm called the heat-bath algorithm [*Rothman*, 1986]. Compared to other simulated annealing algorithms, it offers two advantages. First, it speeds up the calculation of the cost function by a factor of 100 or more because when the parameters of one subfault are perturbed, the response of the rest of the fault can be saved. Second, it is a recommended computational method to solve problems with a large number of free parameters [*Sen and Stoffa*, 1991; *Tarantola*, 2005]. Two types of regularization constraints can be chosen: one that minimizes the difference between the slip on adjacent subfaults and a second that minimizes the total moment (or moment deficit rate in the case of back-slip) of the model [*Hartzell et al.*, 1996]. The corresponding cost function is:

$$\text{Cost} = \text{wrms}^2 + \lambda 1\ \text{Dc}^2 + \lambda 2\ (\text{Mo} - \text{M}_d)^2 \qquad (3)$$

Where Dc represents the differences in back-slip rate between adjacent cells and Mo is an a priori moment deficit rate, and M_d the final moment deficit rate for each source point. $\lambda 1$ controls the smoothing coefficient through a L1+L2 norm [*Sen and Stoffa*, 1991] and $\lambda 2$ modulates the weight assigned to minimize the final moment deficit rate [*Ji et al.*, 2002]. Finally, we impose the backslip rate (V_{back}) to not overshoot the relative plate convergence rate (V_{pl}). The interseismic coupling (ISC) is defined as $0 \leq V_{back}/V_{pl} \leq 1$, resulting in pure creeping when ISC=0 and full locking when ISC=1.

5.4 Evidence for internal deformation within the Inca sliver

In the previous simple forward model, we saw larger scatter of velocity along the coast. The scatter probably reflects along strike variations of interseismic coupling that was not accounted for in the uniformly locked subduction segments forward models. As an additional test, we perform an inversion of spatially variable interseismic coupling using the approach described in the previous paragraph, but we impose the rake to not vary more than +/- 10° of the average gCMT rake (See Figure S3.4 in the Supplements). We fixed $\lambda 1=1$ for this test (3. S6). Clearly, this approach is not correct, but this test will provide a first order correction of the interseismic strain. The misfit to data can then be used to enlighten how the continental deformation takes place. Figure 3.6 shows the residuals velocity field. It shows a general pattern of

southeastward motion at 4-5mm/yr from southern Ecuador to southern Peru. This approach shows that the scatter of velocity sites along the coast noticed in the forward uniformly locked segments models can be explained by local variations of interseismic coupling at the megathrust. When corrected from this effect, the velocity field shows a more uniform southeastward motion at the scale of Peru and southern Ecuador. At a first order, it confirms the proposition of *Nocquet et al.*, [2014] that the Inca sliver encompasses the whole margin from south of the Gulf of Guayaquil to the Arica bend and the Bolivian Altiplano.

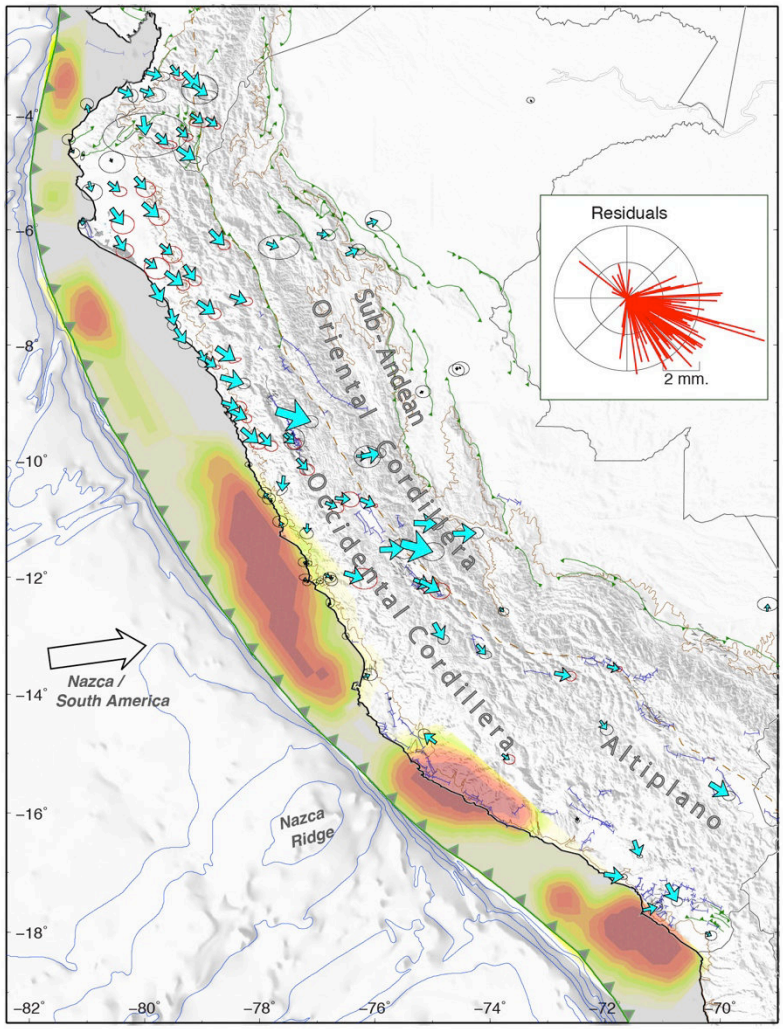

Figure 3.6: Residuals GPS velocities resulting from the inversion of the GPS velocity field with respect to the SSA frame. Southeastward motion along the Occidental cordillera reflects the motion of the Inca sliver from the Gulf of Guayaquil to the Arica bend. The inset wind-rose diagram is another representation of the residuals (inset) and shows a preferential southeast direction. Table 3.2 contains the best Euler pole for the Inca Sliver/SSA motion obtained from a subset of 34 GPS residuals (red ellipses).

The GPS velocity field reveals another feature. While the sites located in the western Cordillera and west of it show a coherent pattern of constant southeastward motion, a systematic counter-clockwise rotation is observed for sites located in the eastern cordillera and the sub-andean domain. This rotation is clearly seen along the northern profile and occurs across the Marañon fault system. It also can be seen for the sites HNCO/HC01 (76.3°W, 9.9°S), along the Lima profile between sites TAPO and MRCD (near 75.4°W, 11.2°S) and to a lesser extend at sites AP01 and CUZC (near 72.4°W, 13.6°S). We note that this change in direction occurs across or in the vicinity previously proposed active faults systems: the Rio Marañon fault in the north, the Chonta fault system in central Peru (Figure 3.3). In southern Peru, our velocity field provides little constraints because of its sparse coverage. Focal mechanisms are predominantly extensional and are widespread distributed in the Andean cordillera, perhaps reflecting a more diffuse deformation mode.

We conclude from this test that the Inca sliver geometry proposed by *Nocquet et al.*, [2014] needs to be refined and split into two subdomains: (1) a western sliver encompassing the western Cordillera and its western margin and (2) an eastern sliver encompassing the eastern Cordillera possibly encompassing partly the sub-andean domain, as evidenced from GPS data along the northern profile. On the contrary, in central Peru, sites located east of the eastern Cordillera in the sub-andean domain are negligible with respect to SSA, indicating that the major boundary rather runs along the eastern slope of the eastern Cordillera, a hypothesis also supported by the distribution of seismicity and the focal mechanisms (Figure 3.3). Finally, splitting the Inca sliver also provides an explanation of a major kinematics discrepancy. *Nocquet et al.*, [2014] Euler pole for the Inca sliver predicts a significant left-lateral strike-slip component of motion along the eastern Andes. However, Figure 3.3 shows that focal mechanisms are in average with a strike parallel to the Andes with a shortening direction in average perpendicular to the Andes, that is NE-SW. This direction is also in agreement with the shortening axis of the major sub-andean faults, therefore providing an additional evidence for the new sliver definition proposed here. A comparison of the Euler poles for the Inca sliver computed either directly from the data or from misfit residuals and that from *Nocquet et al.*, [2014] is provided in the Supplements (Table T3.3, T3.4, Figure S3.3).

6. Inversion of the interseismic coupling

Our previous analysis showed that long-term deformation within the overriding plate affects significantly the observed velocity field and needs to be accounted for in detailed modeling of the effect of mechanical coupling at the megathrust. In order to mitigate this effect, we chose the following strategy: Because a model of motion is uncertain for the eastern Inca sliver, we remove the sites located in the eastern Inca sliver or close to its boundary to invert the interseismic coupling. Second, we determine the best Euler pole for the western Inca sliver by choosing only sites showing no internal deformation (Table 3.2). Finally, in order to account for possible trade-off between the motion of the western Inca sliver and the interseismic coupling along the subduction interface, we vary the angular velocities of the western Inca/SSA Euler pole by steps of 0.02°/Myr, equivalent to 0.1 mm/yr over the studied area. For each model, we adjust adequately the backslip rate (V_{back}) of the Nazca/western Inca Sliver relative convergence rate.

6.1 Inversion Results

Assuming that a wrms threshold of 2 mm/yr or lower satisfies the GPS measurements, we find that the best models work for an Inca Sliver Euler pole having an angular velocity of 0.104 ± 0.02°/Myr (Table 3.3). All the models in that range can be taken as models acceptable given the data uncertainties. Figure 3.7A shows our preferred interseismic coupling model (model 3-Plate-C in Table 3.3) that best fits the GPS data (See also inset in Figure 3.7A) and Figure 3.7B presents the predicted rigid motion of the western Inca sliver for an Euler pole with an angular velocity of 0.104°/Myr.

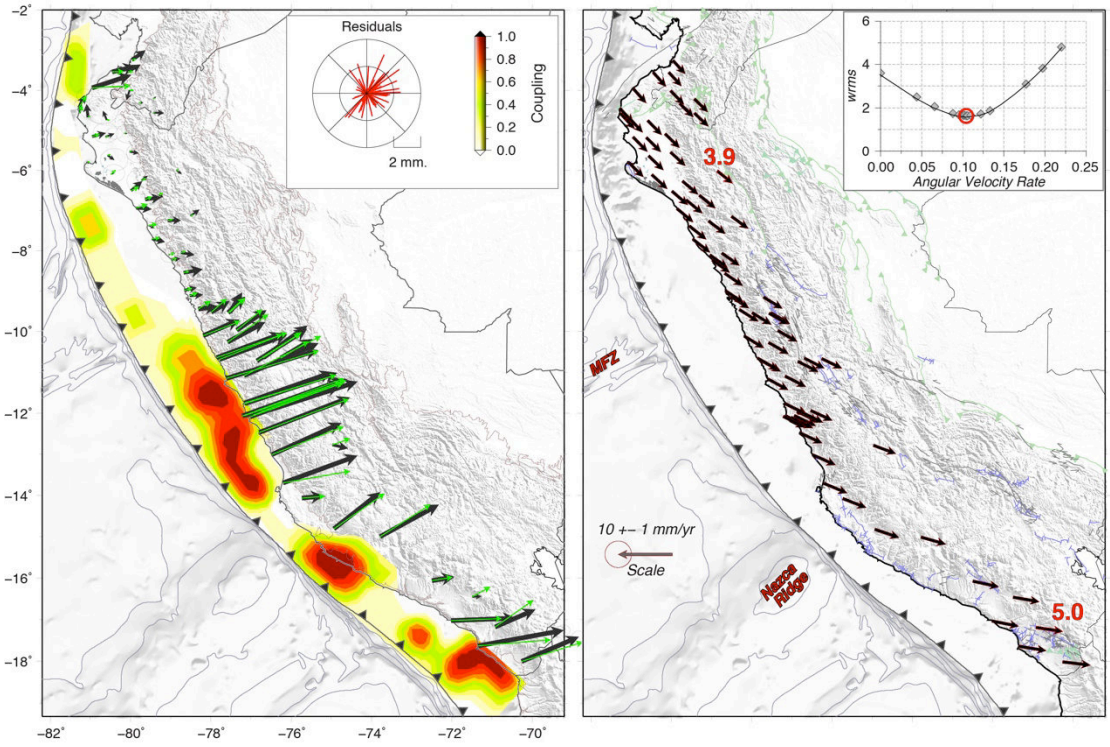

Figure 3.7: Best GPS-fitting 3-plate model composed by the rigid motion of the Inca sliver (right) and an interseismic coupling model that results from the inversion of the GPS data in the Inca sliver reference frame (left). Left - Best interseismic coupling (ISC) model for Peru. Observed and predicted interseismic GPS displacements are shown as black and green vectors respectively. The wind-rose diagram of the GPS residuals (inset) shows azimuthally random distribution of residues lower than 2mm/yr. Right - Rigid motion predicted from the Inca Sliver/SSA Euler pole location found from the analysis of the 2-plate model GPS residuals (Table 3.2) and an angular velocity of 0.104°/Myr.

To fully account for the model uncertainties due to the limited spatial resolution of our geodetic data, we further run a final series of model where we force the final rate of moment deficit to vary from Md=1.0E10^{20} Nm/yr (Mw~7.3) to 7.0E10^{20} Nm/yr (Mw~7.9) (Table 3.4). We found that ISC models with a rate of moment deficit ranging from 2.4E10^{20} Nm/yr (Mw~7.6) to 4.0E10^{20} Nm/yr (Mw~7.7) fit relatively well the GPS data within their uncertainties (Figure S3.7 in Supplements). Figure 3.8 shows the family of acceptable interseismic coupling distribution if we consider a *wrms* lower than 2mm/yr. When the moment deficit rate is increased, the asperities widen and the coupling increases significantly near the trench where GPS data provide no constraints. Spatial resolution checkerboard tests indicate that the along-strike spatial resolution is relatively high everywhere along the Peruvian margin. The along-dip resolution is also high in the Piura Peninsula but lowers significantly south of it, especially near the trench axis. Interpretation of shallow

locking should be done with more caution there (See Figure S3.5 and details in Supplements).

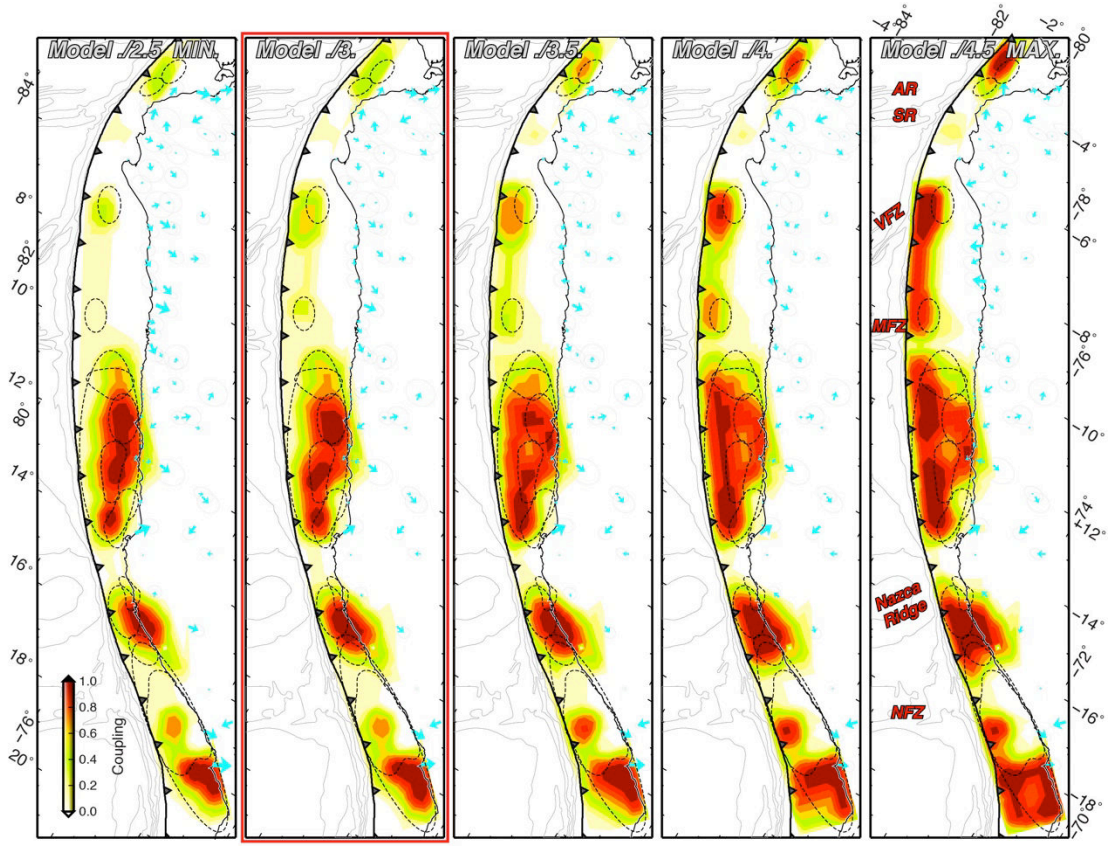

Figure 3.8: Best GPS-fitting interseismic models with rate of moment deficit ranging from 2.4E1020 Nm/yr (Mw~7.6) to 4.0E1020 Nm/yr (Mw~7.7). Blue arrows show the GPS residuals. Increasing the rate of moment deficit extends the updip limit of the coupling near the trench where the slip resolution is low and where uncertainties are the highest. Note that where the Nazca ridge and fractures zones subduct, the ISC remains very low.

As a whole, the ISC appears heterogeneous at the scale of Peru, with weak coupling found along the northern segment from latitude 10°S to the Gulf of Guayaquil, a large area of high coupling, 550km long in the central segment and two ~100-200km long highly coupled asperities in the south. South of 10°S, areas of high coupling are separated by ~100-200km long corridors of weak coupling.

6.2. Along-strike variations of the rate of moment deficit

To quantify the along strike variation of the interseismic coupling, we define the rate of moment deficit *dMo(t)/dt* as :

$$\frac{dMo(t)}{dt} = \mu S \frac{d(vo - v)(t)}{dt} \qquad (4)$$

where, *d(vo-v)(t)/dt* is the mean convergence rate (or back-slip offset) across a surface *S* embedded in a medium with an average rigidity μ. Using this definition, we compute the along-strike variations of the rate of moment deficit for previously discussed inversion models. The moment deficit is computed at each node taking into account its local back-slip rate and rigidity. Then, we sum up the moment deficit of all the nodes within 20 km strip normal to the trench. Figure 3.9 shows the variation of the rate of moment deficit along the 2200-km long Peruvian subduction zone.

Although the final coupling models indicate differences, we can notice that the global rate of moment deficit remains in a limited range of Md=2.4-4.0E10^{20} Nm/yr corresponding to energy accumulation equivalent to a Mw~7.6-7.7 yearly earthquake (Figure 3.9, Table 3.4) at the scale of the whole Peruvian subduction zone. The uncertainties vary along strike and mainly reflect the distance of the GPS sites from the trench.

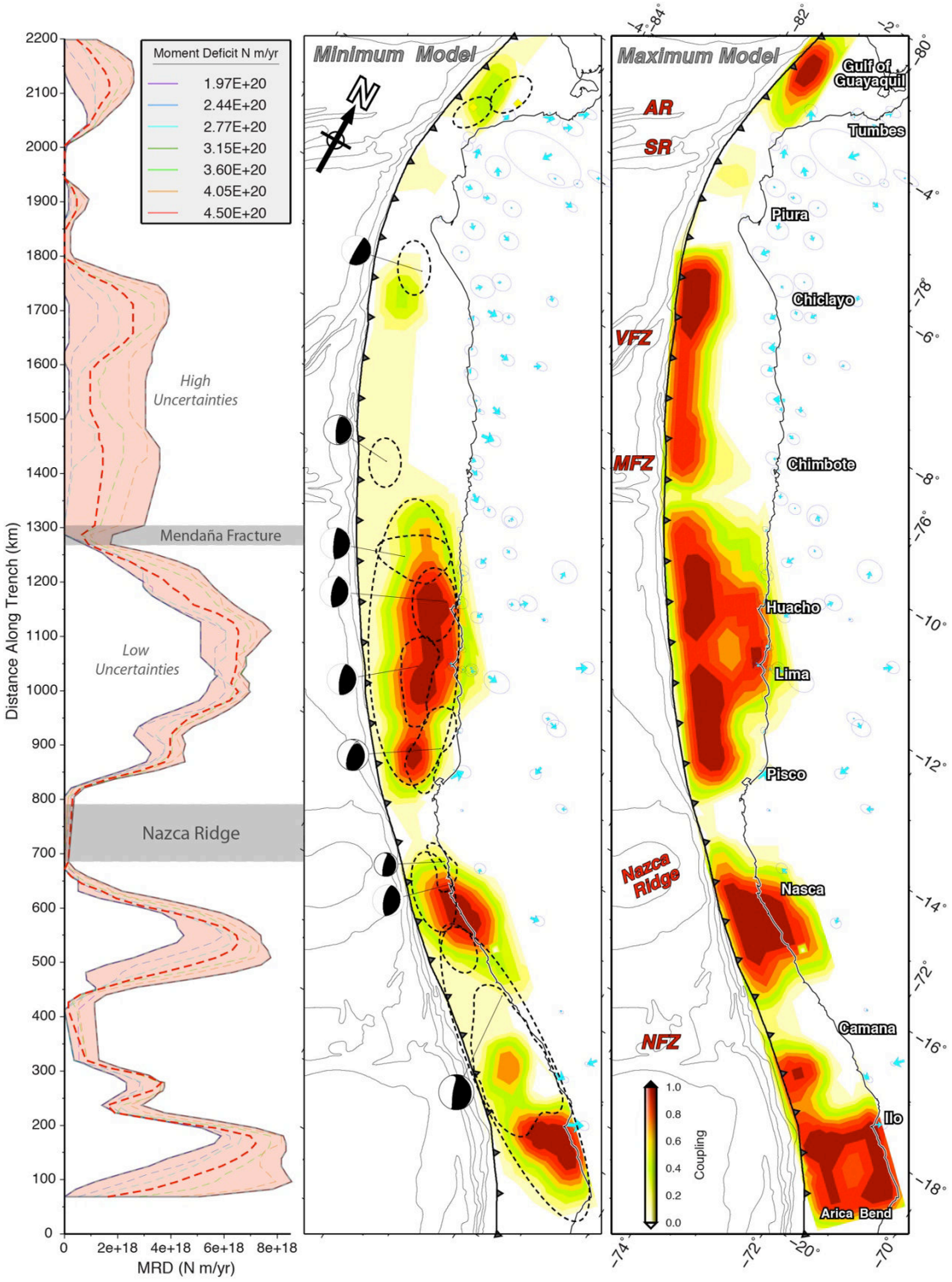

Figure 3.9: Along-trench variations of the rate of moment deficit (left) for the minimum (center) and maximum (right) interseismic models. Even though, the interseismic pattern might vary significantly between models, note that the location of the peaks and valleys in the rate of moment deficit are quite persistent characteristics that highlight the locations of principal asperities (peaks) and creeping barriers (valleys). Dashed contours of center map show the approximate rupture area of large earthquakes as described in Fig. 2.

7. Discussion

7.1. Continental deformation: motion and deformation of the Inca sliver

As for most subduction zones accommodating oblique convergence, partitioning of the convergence takes place in the Peruvian margin through the motion of the Inca sliver at 4-5 mm/yr (Figure 3.7) [*Nocquet et al.*, 2014] and sub-andean domains accommodating the crustal shortening at about 2-3 mm.yr. The velocity agreement for sites located in southern Peru (Puno (71.2ºW, 15.5ºS), Cuzco (71.9ºW, 13.5ºS) and Ayacucho (74.2ºW, 13.2ºS)) with our proposed Inca sliver Euler pole supports that the Inca Sliver encompasses most of the 2200km of the Peruvian margin from south of the Gulf of Guayaquil to the Arica bend and the Bolivian Altiplano. Thus, together with the already identified North Andean Sliver encompassing western Venezuela, Colombia and Ecuador [*Pennington*, 1981; *Trenkamp et al.*, 2002; *White et al.*, 2003], the central Andes Sliver [*Brooks et al.*, 2003; *Métois et al.*, 2013] and the Chiloe sliver [*Wang et al.*, 2007] in central-southern Chile, it confirms that the motion of continental slivers control the present-day kinematics of the Andes Cordillera all along the Nazca / South America plate boundary. Because the sense of trench parallel motion of the slivers documented agrees with the along trench component of the Nazca/South America convergence vector, it suggests that the oblique convergence and stress along the subduction interface controls the motion of the slivers.

For the Inca sliver, our Euler pole predicts southeastward motion at ~4 mm/yr in northern Peru, slowly rotating counterclockwise with decreasing latitudes, so that the velocity becomes eastward directed in southern Peru and with slightly larger magnitude (~5 mm/yr). This Euler pole indicates that both trench-parallel and trench-normal partitioning coexist. The Inca sliver motion trench-parallel component remains fairly constant all along Peru (~4 mm/yr, Figure 3.10) indicating a level of partitioning decreasing southward from 35% in northern Peru to 16% in southern Peru near the Arica bend. Trench-normal component partitioning is small of the order of 5% all along Peru.

While the motion of the Inca sliver dominates the velocity field, we now find that a single block does not correctly explain the GPS data in the eastern Andes, suggesting that the Inca sliver accommodates a significant internal deformation. According to the GPS data a counterclockwise rotation of the velocity field occurs in the eastern Andes. As a consequence of the rotation, the relative motion between the eastern Andes and the Stable South America is not a left-lateral dominant strike-slip system as would predict the Inca sliver/South America pole, but an almost pure reverse shortening boundary, with a shortening direction usually perpendicular to the main strike of the Andes. This direction agrees with the reverse focal mechanisms (Fig. 3) and the shortening direction indicated by the active folds and faults in the sub-andean domain.

We find that the onset of this counterclockwise rotation usually occurs between the western and eastern Cordillera. In northern Peru, we find that main velocity direction change occurs across the Marañon fault. Although the Marañon fault has been proposed to be a reverse fault [*Megard*, 1984; *Carlotto et al.*, 2009], a direct measurement of relative motion for GPS sites located either side of the fault (CUYC/AM02) indicate a predominant left-lateral motion at 1.2-2.5 mm/yr. No clear fault-perpendicular motion can be reliably determined from our GPS data, but it is certainly smaller than 1mm/yr. The GPS sites located east of the Marañon fault show little internal deformation and move coherently at 2-3 mm/yr eastwards, indicating active shortening at these rates between the sub-andean domain and the stable South America craton.

In central Peru, a short-scale gradient is seen in the velocity field between the western and eastern Cordillera crossing the Chonta Fault System. However, the estimates of the relative motion to be accommodated there are dependent on the models of the interseismic coupling along the subduction. For instance, the velocities between sites LRYA and TAPO located on each side of the RVQ fault system show 1.2±1.5 mm/yr of right-lateral motion and 2.6±1.3 mm/yr of relative shortening. When corrected for the interseismic contribution of the subduction, using our best model, we find now that 2.5±1.7 mm/yr of right-lateral motion and 1.0 ±1.3 mm/yr of shortening. Furthermore, if we use the sites in Huancayo (HUAN and JU01), we even find extensional strain regime at 1-2 mm/yr. Therefore, the GPS network is not dense

enough to provide reliable constraints on the eastern Inca sliver boundary in south central Peru.

In general, the direction of shortening (NE-SW) in the sub-andean domain requires either counter-clockwise rotation of small blocks in the eastern Andes with respect to the Inca sliver or some extensional strain rate on the NE-SW direction. Extension is further evidenced in southern Peru by the widespread distribution of normal faulting earthquakes within the Altiplano. Along the eastern Andes, our Euler pole for the Inca sliver would predict 4.5 mm/yr of motion in a 95°N direction with respect to stable South America. Extensional strain therefore should contribute to a change of counterclockwise ~30° of the velocity field in order to be compatible with the sense of shortening in the sub-andean domain. This requires ~4 mm/yr of extension to be accommodated within the Altiplano. Alternatively, a left-lateral constant shear rate of 15 nstrain/yr, accommodated over 150km across the eastern Cordillera and sub-andean domain would also explain the rotation of the velocity field. Therefore, a combination of NE-SW extension and left-lateral faulting is expected in the Cordillera. In the sub-andean zones, reverse faulting is evidenced by thrust focal mechanisms that limit the easternmost flank of the Oriental cordillera and accommodate crustal shortening.

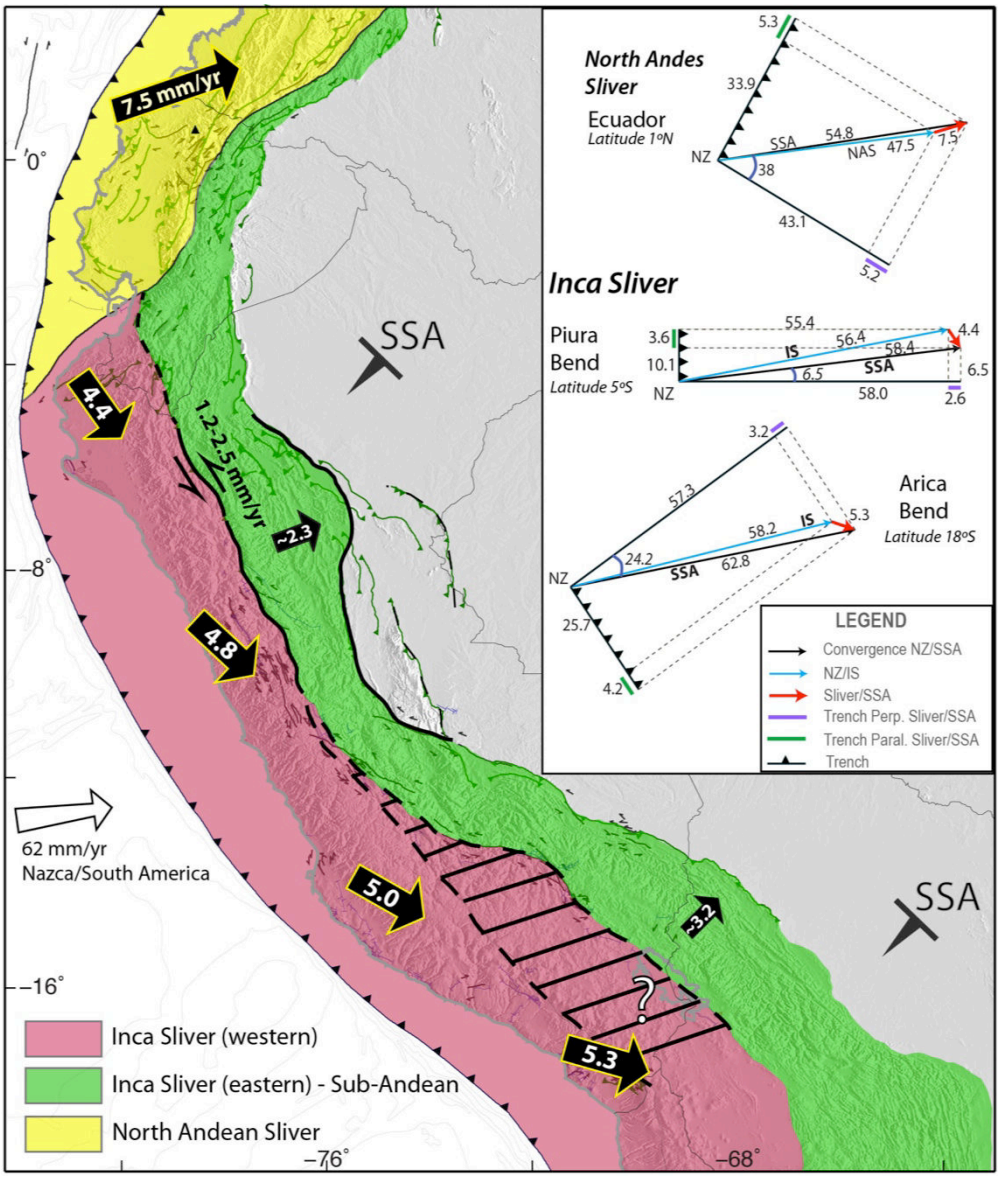

Figure 3.10: Schematic description of the principal continental slivers that contribute to the deformation partitioning of the Peruvian margin: the North Andean Sliver (NAS; yellow) the western Inca Sliver (in red) and eastern Inca Sliver (in green), the later are separated by the limit between the occidental and oriental cordillera, respectively. All the motions are referred to a Stable South America (SSA) reference frame and are expressed in mm/yr. The inset shows kinematics triangles and obliquity partitioning vectors for Ecuador (Latitude 1°N), the Guayaquil bend (Latitude 5°S) and Arica Bend (Latitude 18°S). The lines with triangle symbols indicate the local trench axis. Green and purple lines are respectively the along and normal trench components of Nazca/SSA convergence vector. The blue arrows indicate the Nazca/NAS and Nazca/IS convergence vectors and the red arrows are the NAS/SSA and IS/SSA convergence vectors.

7.2 Interseismic Coupling along the Peruvian subduction zone

In the following paragraphs, we describe the main pattern of the interseismic coupling along the three segments of the Peruvian subduction zone and discuss the implication for their seismic behavior.

7.2.1 Weak coupling in northern Peru

In northern Peru, the interseismic coupling appears to be confined within the shallowest 30km and is found to be weak (<40%). High locking confined close to the trench is not excluded by the data south of the Piura peninsula and possibly in the Gulf of Guayaquil. However, a very weak coupling is found along the Piura peninsula where the coastline located at about ~100km from the trench enables a better resolution. Our models further suggest that interseismic coupling consists of local asperities with typical sizes less than 100km long along strike and 70km along dip. In overall, we find that the rate of moment deficit could vary from Md=0.1E10^{20} Nm/yr (Mw~6.8) to Md=0.8E10^{20} Nm/yr (Table 3.4, Figure S3.8). This range of values is equivalent to M_0=4E10^{21}-3.2E10^{22} Nm over 400 yrs. According to our updated catalogue for historical earthquakes (see section 2.1), the total moment released through the earthquakes has been M_0=2E10^{21} Nm, that is 50% of the geodetic lower bound value. Furthermore, it is likely that the earthquake catalogue is not complete for the XVI and XVIIth centuries. Over last two centuries, the geodetic moment rate deficit would agree with 20% with the moment released through earthquakes. We further note that the location of highly coupled patches correlates within their uncertainties with proposed rupture areas for the XXth century earthquakes in this area. The 1960 and 1996 events share all the characteristics of tsunami earthquakes. Our model results, with locking patches located close to the trench is agreement with the view that these earthquakes ruptured the shallowest, less rigid part of the megathrust. This mode of stress release would therefore be the dominant seismic behavior for the northern Peru segment.

7.2.2 High coupling in the central Peru segment

In contrast with northern Peru, the central Peru segment indicates a high and homogeneous level of coupling along a 550km long segment. Although the level of

coupling close to the trench is not well constrained by the GPS data, all our models indicate that high coupling is required at depths between 20 and 50 km. These numbers are similar or even larger than the locked zones documented in the Tohoku [*Loveless and Meade*, 2010] and Maule [*Vigny et al.*, 2011] areas before the occurrence of these two earthquakes and the area certainly has the potential for generating Mw 9+ earthquakes.

Our models indicate that the moment rate deficit for this segment is Md=1.1E10^{20}-1.5E10^{20} Nm/yr, equivalent to a Mw~7.3-7.4 every year. If we consider that the 1746 earthquake ruptured the whole central Peru segment and released all previously accumulated stress, the actual rate of moment deficit would then lead to an estimate of M_0=2.7E10^{22}-4.0E10^{22} Nm accumulated since 1746. The XXth century sequence with 4 Mw~8 released only M_0~5E10^{21} Nm, that is between 10 to 20% of the accumulated stress, leaving the space for a Mw 8.8 to 9.0 earthquake to occur presently (Figure S3.10).

Of course, these simple calculations cannot be used as a direct guide for a future great earthquake. They however show that Lima and its region have the highest hazard in Peru and possibly along the Nazca/South America subduction zone, with a potential for a great earthquake to happen in the next years or decades.

7.2.3 Highly heterogeneous coupling and evidence for ongoing post-seismic deformation along the southern Peru segment

In southern of Peru, interseismic coupling appears to be localized within two 100-150km large asperities at latitude 16°S and 18°S spatially correlating with the presumed rupture areas of the 1913 and 1868 earthquakes, respectively. While the existence of the two asperities were also found in previous modeling of the area [*Chlieh et al.*, 2011], they are found to be of smaller size in our modeling. In order to understand the differences, we first compare our velocity field with the one derived from the SNAPP project in the 1990's and used by *Norabuena et al.*, [1998], *Kendrick et al.*, [2001] and finally *Chlieh et al.*, [2011] to derive interseismic models for this segment. We find that there are many differences in sites located near Lima

city (*e.g. sali* = 27.6 mm/yr at N89.7ºE and *HCHO* = 20.9 mm/yr at N81.4ºE; also for the sites *quil* = 25.9 mm/yr at N83.8ºE and *CAZL* = 17.5 mm/yr at N76.9ºE) reaching 8.5 mm/yr and systematic differences in orientation further inland (Figure S3.9). The SNAPP velocity field has been derived from only two campaigns spanning 1994 – 1996, a period that is now known to be too short to derive reliable velocity estimates even for continuous GPS stations [*Blewitt and Lavalle*, 2002]. Further problems as lower orbit quality and the sparse network of reference stations around South America at that time might also have degraded their results.

However, the large difference noticed at the IGS station AREQ between previous and our solution still remains intriguing. This area has been affected by the 2001 Mw=8.4 Arequipa earthquake, which has been shown to have a large postseismic displacement in the years following the earthquake [*Perfettini and Avouac*, 2004]. In order to evaluate the potential impact of post-seismic processes to our velocity field, we determine the full time series for this site since 1998, using our own solution from the second reprocessing campaign of the IGS (http://acc.igs.org/reprocess2.html). Figure 3.11 shows the resulting time series. It clearly shows that the post-seismic phase has not ended yet. The velocity with respect to the stable south America is of 6.6mm/yr estimated for the 2007-2013 period in our solution is about half the interseismic velocity before the earthquake (13.6 mm/yr) in magnitude and is rotated clockwise by 30°. This results indicates that the southern segment of the subduction zone in Peru is still experiencing significant post-seismic deformation. The low coupling found in the rupture area of the 2001 Mw 8.4 earthquake might be explained by this on-going deformation.

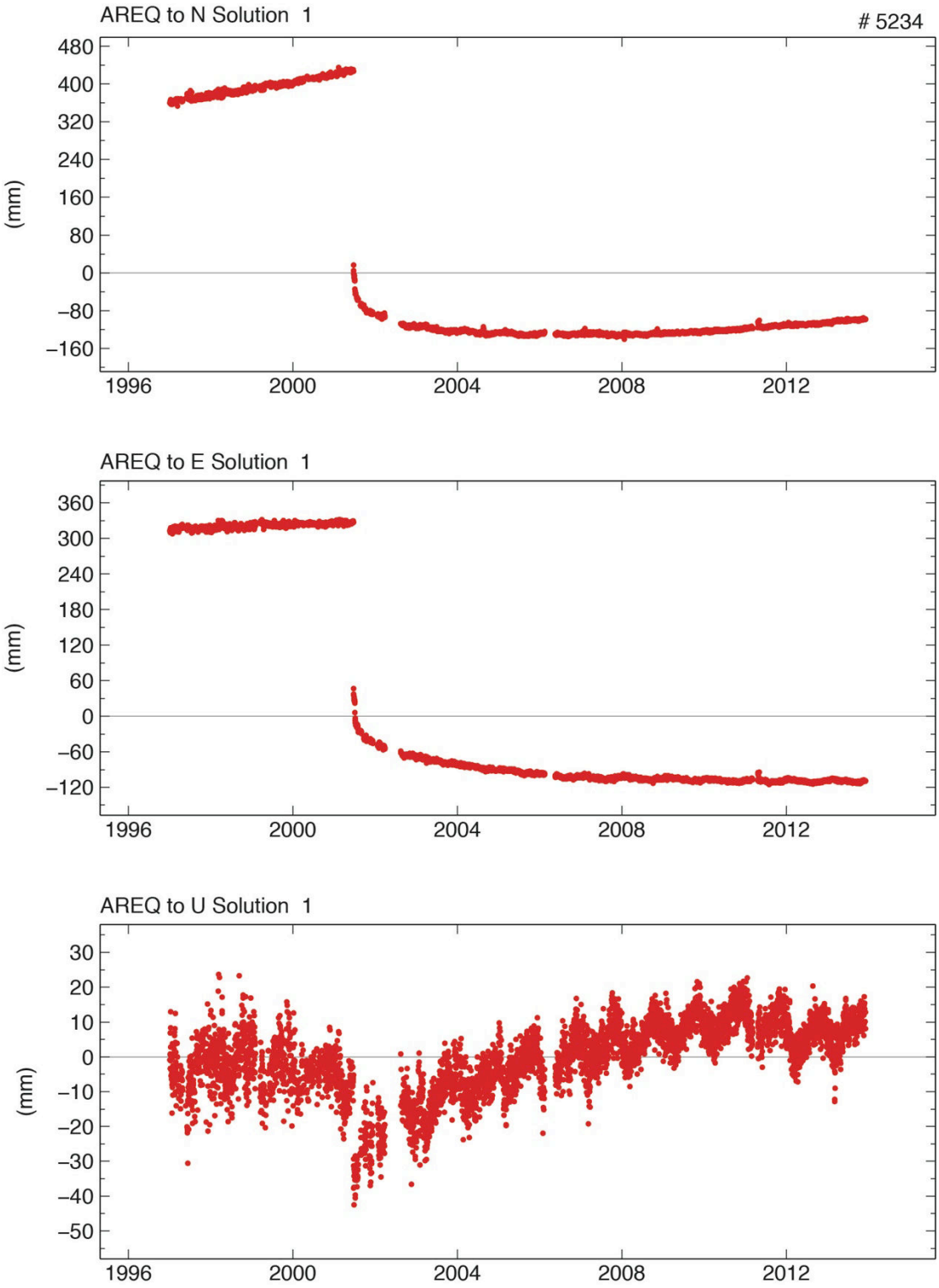

Figure 3.11: Full time series for the east, north and vertical components of the AREQ GPS station since 1998. We use our own solution from the second reprocessing campaign of the IGS (http://acc.igs.org/reprocess2.html). Green line indicates the date of occurrence of the Mw=8.4 Arequipa 2001 earthquake, whose epicenter is about 230km from the station.

7.3 Factors controlling the interseismic coupling

The existence of a segment of 1000 km long predominantly creeping raises the questions about the factors controlling the interseismic coupling variations along the subduction interface. Our new observation offers an opportunity to test previously empirical or physical laws proposed to control seismic coupling along subduction zones.

7.3.1. Thermal Modeling

A first category of models relates the coupling to the thermal state of the subduction interface, which mainly depends on the age of the subducting plate, the convergence rate, the interface dip profile and the sediment thickness at the trench [*Oleskevich et al.*, 1999]. Convergence rate and interface dip profile (at shallow <60km depth) remains fairly constant along Ecuador and Peru and more generally along the Nazca/South America subduction zone. A recent compilation of sediment thickness at the trench [*Heuret et al.*, 2012] shows low values (≤0.5km) from Ecuador to southern Peru, with higher thickness (1.0-1.5km) between latitude 5.5°S and 9°S. Variation of trench sediment thickness therefore does not correlate with change in coupling. Here we explore the link between temperature and interseismic coupling through modeling the steady-state thermal structure of the Peruvian megathrust interface from analytical expressions describing the dissipative heating in the lithosphere [*Royden*, 1993]. We adopt the approach developed by *Royden*, [1993], in which the heat transfer equation is solved in 2D:

$$\frac{\partial h}{\partial t} = \kappa \nabla^2 T + v \frac{\nabla T}{\partial z} + SH + R \qquad (5)$$

where, $\kappa \nabla^2 T$ describe the term of conduction, $v \frac{\nabla T}{\partial z}$ is the advection, SH the shear heating and R the crustal radiogenic production. We assume the case where the radiogenic production is small, about 1.3 μ W/m^3. The shear heating (fixed to 45mW/m^2) is calculated for a uniform shear stress of 40MPa and a friction coefficient of 0.1 in highly locked zones. In weakly coupled zones (like found in north of Peru), the shear heating might be lower due to a lower coupling coefficient or shear stress.

We fixed the temperature at the base of the oceanic lithosphere at 1250°C. For an instantaneous heating or cooling of a semi-infinite half-space, the thickness H of the subducting plate is proportional to the thermal diffusion distance (κ *A)$^{0.5}$:

$$H=2.32 * (\kappa *A)^{0.5} \qquad (6)$$

where κ is the thermal diffusivity (fixed to 1mm^2/s), A is the age of the subducting plate [*Turcotte and Schubert*, 2002]. Following this relation the thickness of the megathrust increases from about 70km in the north of Peru where the age of subducting oceanic plate is about 30Ma old, to 80km in central Peru and 85-90km in southern Peru where is the oceanic seafloor age reach about 45Ma old (see Table T3.6 in Supplements). As a consequence of the change in the strike of the trench axis, the normal convergence rate decreases southward from about 58mm/yr at the latitude of Chiclayo to 55mm/yr at the latitude of Lima and 46mm/yr at the latitude of Arequipa.

In map view, Figure 3.12 shows that the isotherms 100°C-300°C bracket relatively well the location of highly locked fault patches especially in central and southern Peru. In north of Peru (profile A), if we use the same coefficient of friction than used for the profiles in central and south Peru (B, C, D), we found that the isotherm 300°C crosses the slab at about 20 km deeper than the downdip limit of the locked fault zone found between latitudes 7°S and 8°S. The low coupling found in north Peru may suggests that the friction coefficient might be much lower than in central and southern Peru. If we test that hypothesis, we found that for a shear heating of 20mW/m2 or lower, the distances between the isotherms 100°C and 300°C is squeezed and more consistent with the lower width of the locked fault patches found there (Profile A). Overall, these thermal models indicate that the updip and downdip limits of the locked areas could be controlled by the thermal structure of the slab interface. However these models fail to explain the along-strike segmentation observed in the interseismic coupling models suggesting that other parameters may be involved in the control of the seismogenesis at subduction zones.

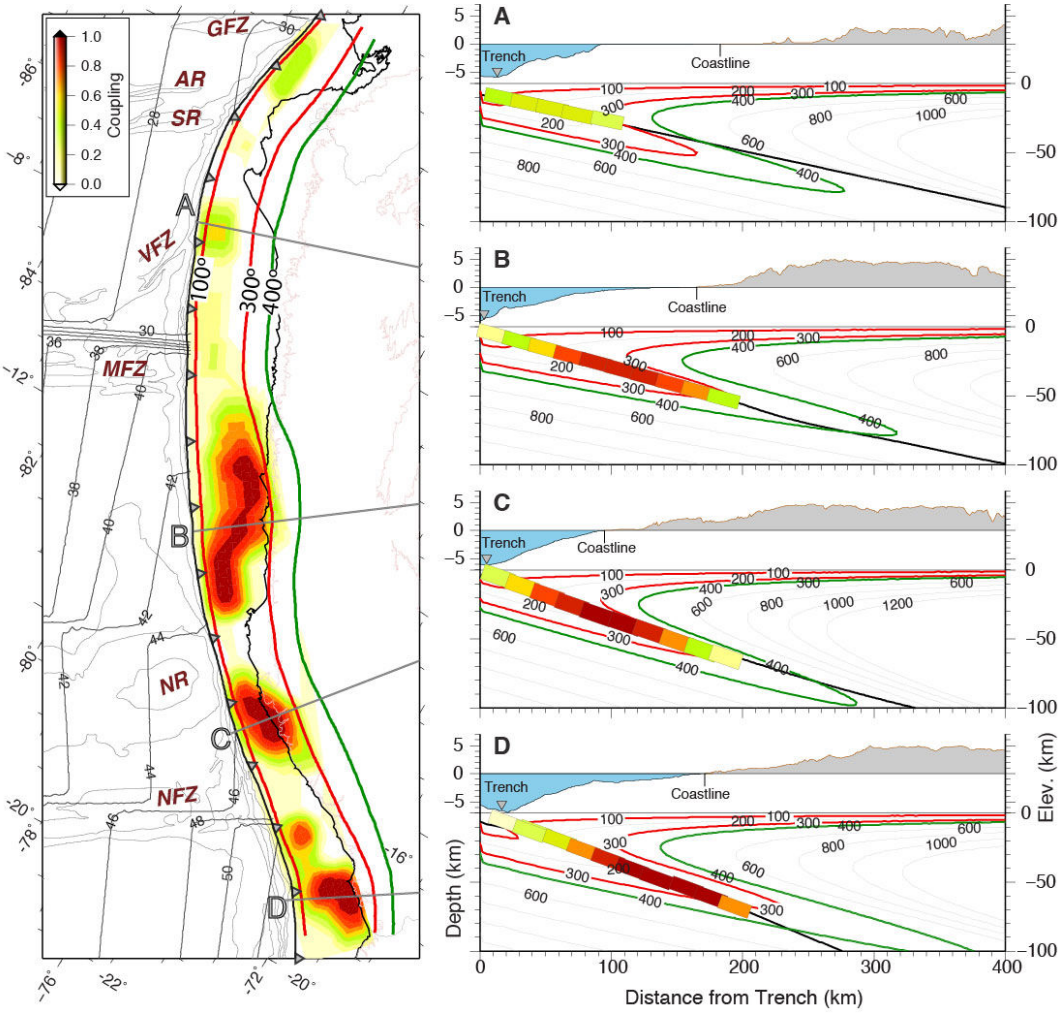

Figure 3.12: Steady-state thermal structure of the Peruvian megathrust Left: Age of the oceanic floor [Müller et al., 2008], which increases southward. It is about 20 Myr north of the Gulf of Guayaquil and reaches 55 Myr in southern Peru. Three major discontinuities appear in the ages of the oceanic seafloor at the Grijalva Fracture Zone (GFZ) where the ages are shifted from 20 Myr to 30 Myr, at the Mendaña Fracture Zone (MFZ) with a jump from 29 Myr to 40 Myr, and at the Nazca Fracture Zone (NFZ) with a jump from 46 Myr to 51 Myr. Solid lines A, B, C and D, indicate the location of the three sections showed on the right. Right: Normal-trench Sections for A (Chiclayo), B (Lima), C (Nazca) and D (Moquegua) showing the bathymetry and topography from GEBCO30s model. For each section, the steady-state thermal model is computed using the Hayes slab geometry, the local normal convergence rate and age of the subducting Nazca Plate.

7.3.2. Forearc structure

A second category of empirical laws relates the forearc structure [*Wells et al.*, 2003] and negative free-air gravity anomalies along the trench to the distribution of highly coupled segments [*Song and Simons*, 2003]. Positive free-air anomalies were used to predict low elastic stress accumulation from latitudes 1°N to 3°S, increasing from 4°S to 8°S [*Song and Simons*, 2003]. Both predictions are in contradiction with

recent results, which show significantly high coupling between 1°N and 1°S [*Nocquet et al.*, 2014], and low coupling between 4°S and 8°S.

7.3.3 Seismic segmentation controlled by oceanic structures

Another key parameter suspected to control the lateral variation of the coupling is the subduction of topographic high or fracture zones that reduce locally the interplate coupling and play the role of mechanical barriers. In the regions where major geomorphologic features as fracture zones and ridges intersecting the trench axis, we notice that the interseismic coupling is always low, even in maximum coupling models (Figures 3.9, 3.11). These low-coupled regions correlate relatively well with the rupture extremities of large megathrust earthquakes suggesting that the subduction of prominent geomorphologic structures play a key role in the segmentation and control of large subduction ruptures. In central Peru the subducting seafloor is smooth and the Nazca ridge and Mendaña FZ bounding this segment can be interpreted as strong barriers since no historical large earthquakes ruptured through them. In south of Peru, the Nazca fracture zone appears to act as a weak barrier that can sometimes slow down or stop large rupture like in 2001 [*Robinson et al.*, 2006] and sometimes fail with the neighboring asperities like during the 1868 Mw=8.8 event. In northern Peru the subduction zone is more segmented than the central and south segments, due to the entrance of five structures (the Mendaña FZ, the Virú FZ, the Sarmiento and Alvarado ridges, and the Grijalva FZ) separated by 100-250 km over a distance of 900km along trench. The lateral persistence of these structures may inhibit stress accumulation at the plate interface.

8. Conclusions

This study presents a detailed description of both the deformation partitioning and the pattern of interseismic coupling along the Peruvian subduction margin. Our results allow us to conclude that:

(1) The GPS velocity field expressed with respect to the stable South America shows distinct patterns of deformation along strike. In central and southern Peru we observe high velocities in the direction of the convergence (from 8 to 23 mm/yr) decreasing as

going inland, suggesting significant interseismic coupling on the plate interface. Contrasting with these observations, in northwestern Peru we observe a consistent southeastward motion of 5-6 mm/yr, without a clear gradient of deformation that would suggest significant coupling on the plate interface, thus confirming the hypothesis of a sliver motion stated by *Nocquet et al.*, [2014]. New GPS velocities in northeastern Peru rotate differently in an east–northeast direction, this new data allow to constraint the kinematic and boundary of the Inca sliver.

(2) We found evidence that allow us to discriminate that the former Inca sliver proposed by *Nocquet et al.*, [2014] can be split into sub-domains: a western sliver encompassing the oceanic wedge and the occidental cordillera and sub-andean domains including the oriental cordillera. This evidence comes from the differences in the pattern of deformation between the sites located on each side of both cordilleras. The boundary between the Inca sliver and sub-andean domains would be limited by fault systems aligned along the boundary between the cordilleras; these are: the Marañon in the north, the Chonta in central, and the Urcos-Ayaviri-Coniri Fault Systems in the south of Peru. The newly defined Inca sliver is in southeastward translation at a rate of 4-5 mm/yr, and is wedged by the subduction trench and the inter-cordillera fault systems encompassing all the 2200 km of the Peruvian subduction margin from south of the Gulf of Guayaquil to the Arica bend. Sub-andean domains show an east to northeast direction of motion consistent at a rate of 2-4 mm/yr with shortening along the northwest-southeast reverse trending faults in the sub-andean domain and thrust focal mechanism [*Suarez et al.*, 1983; *Devlin et al.*, 2012].

(3) The oblique convergence appears as the principal driving mechanism for the motion of the Inca sliver. At the scale of the entire Nazca/South American subduction zone, various slivers have been reported there where the convergence is oblique [*Trenkamp et al.*, 2002; *Brooks et al.*, 2003; *Métois et al.*, 2013; *Nocquet et al.*, 2014]. In northern Andes the divergent motion of the North Andean sliver towards the northeast and of the Inca sliver towards the southeast explains the opening of the Gulf of Guayaquil. In central Andes at the Arica bend the convergent motion of the Inca sliver and a northward moving sliver in northern Chile [*Métois et al.*, 2013] play a role in the development of the Altiplano plateau holding it laterally.

(4) The interseismic coupling determined in this study appears highly heterogeneous at the scale of the Peruvian subduction margin. The northern segment extending from the Gulf of Guayaquil to the Mendaña Fracture Zone is characterized by weak to moderate coupling confined to the first 20-30km depths. Three localized patches of ~100km long correlate with the rupture area of moderate megathrust earthquake and tsunami-earthquakes (~7.5) occurred in 1953, 1960 and 1996. The central Peru segment bounded by the Mendaña Fracture Zone and the Nazca ridge is characterized by a high interseismic coupling that vary laterally along 550 km long and also in depth up to 50 km. The coupling in this segment correlates with the rupture area of the great 1746 (~M9.0) earthquake that encompasses the cumulative rupture extents of large earthquakes M~8.0 occurred in 1940, 1966, 1974 and 2007. In the southern Peru segment, besides the scarce density of coastal GPS sites, our model shows two ~100-150km long highly coupled asperities in front of Nazca (16ºS) and Tacna (18ºS) that correlate with the location of the 1913 (M~8.2) and the remaining rupture segment of the 1868 (M8.8) earthquake, respectively. Moreover, we found evidence for ongoing postseismic deformation taking place in the rupture area of the M8.4 2001 Arequipa earthquake; future studies in this region must take into account and correct this effect. We cannot discard high ISC in the shallow portion of the seismogenic zone; our maximum coupling models allow more coupling in the updip seismogenic zone there where the trench-coast distance is more than ~150 km. Our model also shows that the areas of high coupling are usually separated by ~100 km long corridors of weak coupling that coincide with geomorphic structures entering to the trench. We find evidence of low to weak coupling where the crest of the Nazca ridge intersect the trench from 14.5ºS to 15.5ºS, similarly at the entrance of the Mendaña fracture zone the coupling descend drastically. Further north the ISC in general is low and the presence of ridges (SR, AR) and fracture zones (GRFZ, VFZ) may correlate with the aseismic behavior acting as permanent barriers that impede the stress accumulation and arrest the propagation of the seismic rupture.

(5) While the factors controlling the along strike variation of interseismic coupling still remain to be understood, the southern Ecuador and northern Peru subduction zone highlight a fundamentally different mode of stress accumulation and release compared to its neighboring segments. Our results differ from most studied subduction zones, where geodetic measurements of interseismic strain have led to the

view of coupled asperities of variable size usually separated by narrower zones of low interseismic coupling. Although a few subduction segments had proven to accumulate very low stress [*Fournier and Freymueller*, 2007; *Correa-Mora et al.*, 2009], the length of low interseismic coupling segments was not exceeding ~500km, a small percentage of the total length of the subduction. Here, the area predominantly creeping is a continuous segment representing ~20% of the total length of NSASZ. Shallow (<20-30km) interseismic coupling, very weak to null coupling at usual seismogenic depths (20-45km), lack of great (Mw>8) earthquakes, and occurrence of tsunamigenic earthquakes are the primary characteristic of this subduction zone segment.

Finally, we present novel results that show high variability in the pattern of interseismic coupling along the 2200 km of the Peruvian subduction zone and continental deformation at the scale of the Peruvian Andes. Our results have great implications both from the point of view of the seismic hazard and in the impact on the active tectonics and long-term deformation of the Andes. In the near future it will be important and necessary to densify with new GPS measurements the coastal areas in order to map with better detail the distribution of the interseisimc coupling on the plate interface. Continuous GPS and seismological monitoring with near-real time processing in the areas that undergo high interseismic coupling, such as central (Lima) and southern Peru, would be of benefit for tsunami and earthquake early warning. Pre-seismic signals as the recently observed in Iquique - Chile (2014) and Arequipa (2001) seem to be characteristic feature of this subduction zone. Similarly, more measurements in the frontiers of the Inca sliver, both between the cordilleras (occidental and oriental) and in the sub-Andean region will help to refine precisely the boundaries and to better assess the seismic hazard inland.

Acknowledgements

This work has been financially supported by the Agence Nationale de la Recherche (ANR; contract number ANR-07-BLAN-0143-01) and has continuously been supported by the Institut de Recherche pour le Développement (IRD). This work has been possible through support provided by the IRD-DSF. We acknowledge additional support from the CNRS-INSU and RESIF-CORE for the use of the GPS-national pool. This work has been carried out in the frame of the Joint International Laboratory 'Seismes et Volcans dans les Andes du Nord'. JCVL acknowledges support provided by the IRD-DSF for his PhD grant. We used the GMT software [*Wessel and Smith*, 1998] to prepare most of the figures.

Table 3.1: Fault geometry of the rectangular dislocations used in this study to describe the megathrust interface.

Segment	Geographical Location	Southwestern corner Long., Lat.	Length (km)	Strike (º)	Dip (º)
1	Southern Peru	71.2ºW 19.6ºS	780	312	20
2	Central Peru	76.7ºW 14.9ºS	620	324	15
3	North Peru	80.0ºW 10.4ºS	460	334	12
4	Piura Peninsula	81.9ºW 6.5ºS	460	5	12

Table 3.2: Characteristics of the poles of rotation for the Inca Sliver and the Amazonas micro-block relatively to Stable South America (SSA). Column 2 and 3 indicates the method and number of GPS sites used to define the pole. Columns 4, 5, 6 are the pole location and angular velocity.

Pole Name	Method	# GPS sites	Long. (º)	Lat. (º)	Ang. Vel. (º/Myr)	wrms	Reference
Inca/SSA	GPS data	28	63.76ºW	22.47ºN	0.092	0.83	Nocquet etal14
Inca/SSA	GPS data	35	73.66ºW	4.26ºN	0.215	0.66	This Study
Inca/SSA	Residuals	34	67.23ºW	8.36ºN	0.095	0.55	This Study
Amazonas/SSA	GPS data	6	72.79ºW	17.21ºS	0.122	0.72	This Study

Table 3.3: Characteristics of the 2-plate and 3-plate models. Column 2 shows the angular velocity of the Inca sliver in °/Myrs. Column 3 the misfit of the GPS data. Columns 4 shows how vary the moment deficit rate Md of the model in 1020 N.m/yr. In bold are the best-family models.

Model Name	Inca Sliver Ang. Velocity (°/Myrs)	wrms (mm.yr)	Md Total 10^{20} N.m/yr
2-plate	0	3.79	3.82
3-plate-A	0.044	2.50	3.42
3-plate-B	**0.084**	**1.77**	**3.00**
3-plate-C	**0.104**	**1.63**	**2.74**
3-plate-D	**0.124**	**1.75**	**2.51**
3-plate-E	0.177	3.08	1.91
3-plate-F	0.199	3.92	1.65

Table 3.4: Variation of the final moment deficit rate (Md). Units of the moment Md in 1020 N.m/yr (Here in the WRMS column I have this values because I divided the chi2 resulting from the inversion by the number of subfaults). In bold are the best GPS-fitting familly of acceptable models.

Model Name	**A priori**		**wrms**	**South**		**Central**		**North-Chiclayo**		**North-Piura**	
	Md	**Mw**		Md	**Mw**	Md	**Mw**	Md	**Mw**	Md	**Mw**
Mo1.0	9.88	7.3	3.99	0.2	6.8	0.78	7.2	0	-	0	5.3
Mo1.5	1.48	7.4	2.85	0.55	7.1	0.91	7.3	0	-	0.02	6.2
Mo2.0	1.97	7.5	2.12	0.89	7.2	1.03	7.3	0.02	6.1	0.04	6.4
Mo2.5	**2.44**	**7.6**	**1.85**	**1.12**	**7.3**	**1.15**	**7.3**	**0.1**	**6.6**	**0.08**	**6.6**
Mo3.0	**2.80**	**7.6**	**1.74**	**1.23**	**7.4**	**1.2**	**7.4**	**0.23**	**6.9**	**0.11**	**6.7**
Mo3.5	**3.15**	**7.6**	**1.70**	**1.36**	**7.4**	**1.32**	**7.4**	**0.34**	**7**	**0.13**	**6.7**
Mo4.0	**3.60**	**7.7**	**1.71**	**1.56**	**7.4**	**1.43**	**7.4**	**0.45**	**7.1**	**0.16**	**6.8**
Mo4.5	**4.05**	**7.7**	**1.80**	**1.75**	**7.5**	**1.5**	**7.4**	**0.61**	**7.2**	**0.19**	**6.8**

Mo5.0	4.95	7.8	2.01	2.19	7.5	1.69	7.5	0.81	7.2	0.26	6.9
Mo6.0	6.30	7.8	2.94	2.81	7.6	2.09	7.5	1.03	7.3	0.38	7.0
Mo7.0	7.19	7.9	4.57	3.24	7.6	2.42	7.6	1.09	7.3	0.45	7.1

References

Abe, K. (1972), Mechanisms and tectonic implications of the 1966 and 1970 Peru earthquakes, *Phys. Earth Planet. Inter.*, *5*, 367–379.

Altamimi, Z., L. Métivier, and X. Collilieux (2012), ITRF2008 plate motion model, *J. Geophys. Res.*, *117*(B07402), 1–14, doi:10.1029/2011JB008930.

Arriagada, C., P. Roperch, C. Mpodozis, and P. R. Cobbold (2008), Paleogene building of the Bolivian Orocline: Tectonic restoration of the central Andes in 2-D map view, *Tectonics*, *27*(TC6014), 1–14, doi:10.1029/2008TC002269.

Baby, P., P. Rochat, G. H. Mascle, and G. Herail (1997), Neogene shorthening contribution to crustal thickening in the back arc of the Central Andes, *Geology*, *25*(10), 883–886.

Bassin, C., G. Laske, and G. Masters (2000), The current limits of resolu- tion for surface wave tomography in North America, *Eos Trans. AGU*, *S12A-03*.

Beck, S., S. Barrientos, E. Kausel, and M. Reyes (1998), Source characteristics of historic earthquakes along the central Chile subduction zone, *J. South Am. Earth Sci.*, *11*(2), 115–1129, doi:10.1016/S0895-9811(98)00005-4.

Beck, S. L., and L. J. Ruff (1989), Great earthquakes and subduction along the Peru trench, *Phys. Earth Planet. Inter.*, *57*(3-4), 199–224, doi:10.1016/0031-9201(89)90112-X.

Bevis, M., E. Kendrick, B. Brooks, R. Allmendinger, B. Isacks, and R. Smalley Jr. (2001), On the strength of interplate coupling and the rate of back arc convergence in the central Andes: An analysis of the interseismic velocity field, *Geochemistry Geophys. Geosystems*, *2*(11), doi:10.1029/2001GC000198.

Bilek, S. L. (2010), Invited review paper: Seismicity along the South American subduction zone: Review of large earthquakes, tsunamis, and subduction zone complexity, *Tectonophysics*, *495*(2), 2–14, doi:10.1016/j.tecto.2009.02.037.

Blewitt, G., and D. Lavalle (2002), Effect of annual signals on geodetic velocity, *J. Geophys. Res.*, *107*(B7), 1–11.

Bourgeois, J., C. Petroff, H. Yeh, V. Titov, C. E. Synolakis, B. Benson, J. Kuroiwa, J. Lander, and E. O. Norabuena (1999), Geologic Setting, Field Survey and Modeling of the Chimbote, Northern Peru, Tsunami of 21 February 1996, *Pure Appl. Geophys.*, *154*(February 1996), 513–540.

Brooks, B. A., M. Bevis, E. Kendrick, R. Maturana, and M. Araujo (2003), Crustal motion in the Southern Andes (26°–36°S): Do the Andes behave like a microplate?, *October*, *4*(10), 1–14, doi:10.1029/2003GC000505.

Brooks, B. A. et al. (2011), Orogenic-wedge deformation and potential for great earthquakes in the central Andean backarc, *Nat. Geosci.*, *4*(5), 1–4, doi:10.1038/ngeo1143.

Carlotto, V., J. Quispe, H. Acosta, R. Rodriguez, D. Romero, and Et.al (2009), Dominios geotectónicos y metalogénesis del Perú, *Bol. la Soc. Geolofgica del Peru*, *103*, 1–89.

Chlieh, M., J. B. De Chabalier, J. C. Ruegg, R. Armijo, R. Dmowska, J. Campos, and K. L. Feigl (2004), Crustal deformation and fault slip during the seismic cycle in the North Chile subduction zone , from GPS and InSAR observations, *Geophys. J. Int.*, *158*, 695–711, doi:10.1111/j.1365-246X.2004.02326.x.

Chlieh, M. et al. (2007), Coseismic Slip and Afterslip of the Great M w 9 . 15 Sumatra – Andaman Earthquake of 2004, *Bull. Seismol. Soc. Am.*, *97*(1), 152–173, doi:10.1785/0120050631.

Chlieh, M., H. Perfettini, H. Tavera, J.-P. Avouac, D. Remy, J.-M. Nocquet, F. Rolandone, F. Bondoux, G. Gabalda, and S. Bonvalot (2011), Interseismic coupling and seismic potential along the Central Andes subduction zone, *J. Geophys. Res.*, *116*(B12405), 1–21, doi:10.1029/2010JB008166.

Correa-Mora, F., C. DeMets, D. Alvarado, H. L. Turner, G. Mattioli, D. Hernandez, C. Pullinger, M. Rodriguez, and C. Tenorio (2009), GPS-derived coupling estimates for the Central America subduction zone and volcanic arc faults: El Salvador, Honduras and Nicaragua, *Geophys. J. Int.*, *179*(3), 1279–1291, doi:10.1111/j.1365-246X.2009.04371.x.

Devlin, S., B. L. Isacks, M. E. Pritchard, W. D. Barnhart, and R. B. Lohman (2012), Depths and focal mechanisms of crustal earthquakes in the central Andes determined from teleseismic waveform analysis and InSAR, *Tectonics*, *31*(TC2002), 1–33, doi:10.1029/2011TC002914.

Dorbath, L., A. Cisternas, and C. Dorbath (1990), Assessment of the size of large and great historical earthquakes in Peru, *Bull. Seismol. Soc. Am.*, *80*(3), 551–576.

Dow, J. M., R. E. Neilan, and C. Rizos (2009), The International GNSS Service in a changing landscape of Global Navigation Satellite Systems, *J. Geod.*, *83*(3-4), 191–198, doi:10.1007/s00190-008-0300-3.

Espinoza, J. (1992), Terremotos tsunamigenicos en el Ecuador, *Acta Ocean. del Pacifico.*, *7*(1), 1–8.

Floyd, M. a. et al. (2010), A new velocity field for Greece: Implications for the kinematics and dynamics of the Aegean, *J. Geophys. Res.*, *115*(B10403), 1–15, doi:10.1029/2009JB007040.

Fournier, T. J., and J. T. Freymueller (2007), Transition from locked to creeping subduction in the Shumagin region , Alaska, *Transition*, *34*(1), 1–5, doi:10.1029/2006GL029073.

Giovanni, M. K., S. L. Beck, and L. Wagner (2002), The June 23 , 2001 Peru earthquake and the southern Peru subduction zone, *Geophys. Res. Lett.*, *29*(21), 1–4, doi:10.1029/2002GL015774.

Hartzell, B. Y. S. H., and T. H. Heaton (1983), Inversion of strong motion and teleseismic waveform data for the fault rupture history of the 1979 Imperial Valley, California, Earthquake, *Bull. Seismol. Soc. Am.*, *73*(6), 1553–1583.

Hartzell, S., A. Leeds, A. D. Frankel, and Michael J (1996), Site response for urban Los Angeles using aftershocks of the Northridge earthquake, *Bull. Seismol. Soc. Am.*, *86*(1B), S168–S192.

Hayes, G. P., D. J. Wald, and R. L. Johnson (2012), Slab1.0: A three-dimensional model of global subduction zone geometries, *J. Geophys. Res.*, *117*(B01302), 1–15, doi:10.1029/2011JB008524.

Herring, T., and S. Mcclusky (2009), GAMIT/GLOBK MATLAB TOOLS,

Herring, T. A., R. W. King, and S. C. Mcclusky (2010), *Documentation for the GAMIT software analysis, release 10.40*, Cambridge.

Heuret, A., C. P. Conrad, F. Funiciello, S. Lallemand, and L. Sandri (2012), Relation between subduction megathrust earthquakes, trench sediment thickness and upper plate strain, *Geophys. Res. Lett.*, *39*(L05304), 1–6, doi:10.1029/2011GL050712.

Hindle, D., J. Kley, E. Klosko, S. Stein, T. Dixon, and E. O. Norabuena (2002), Consistency of geologic and geodetic displacements during Andean orogenesis, *Geophys. Res. Lett.*, *29*(0), 1–4, doi:10.1029/2001GL013757.

Ihmle, P. F., J.-M. Gomez, P. Heinrich, and S. Guibourg (1998), The 1996 Peru tsunamigenic earthquake : Broadband source process, *Geophys. Res. Lett.*, *25*(14), 2691–2694, doi:10.1029/98GL01987.

Ji, C., D. J. Wald, and D. V Helmberger (2002), Source Description of the 1999 Hector Mine , California , Earthquake , Part I : Wavelet Domain Inversion Theory and Resolution Analysis, *Bull. Seismol. Soc. Am.*, *92*(4), 1192–1207.

Kelleher, J. A. (1972), Rupture Zones of Large South American Earthquakes and Some Predictions, *J. Geophys. Res.*, *77*(11), 2087–2103.

Kendrick, E., M. Bevis, R. Smalley Jr., and B. Brooks (2001), An integrated crustal velocity field for the central Andes, *Geochemistry Geophys. Geosystems*, *2*, 11, doi:10.1029/2001GC000191.

Kendrick, E., M. Bevis, R. Smalley, B. Brooks, R. Barriga, E. Lauria, and L. P. S. Fortes (2003), The Nazca–South America Euler vector and its rate of change, *J. South Am. Earth Sci.*, *16*(2), 125–131, doi:10.1016/S0895-9811(03)00028-2.

Khazaradze, G., and J. Klotz (2003), Short- and long-term effects of GPS measured crustal deformation rates along the south central Andes, *J. Geophys. Res.*, *108*(1), 1–15, doi:10.1029/2002JB001879.

Lockridge, P. A. (1985), *Tsunamis in Peru-Chile, Report SE-39,*, Boulder, WDC-A for Solid Earth Geophysics, 97p.

Macharé, B. J., C. H. Fenton, M. N. Machette, C. Costa, and R. L. Dart (2003), *Database and Map of Quaternary Faults and Folds in Perú and its Offshore Region FOLDS IN PERÚ AND ITS OFFSHORE REGION*.

Mao, A., G. A. Harrison, and T. H. Dixon (1999), Noise in GPS coordinate time series, *J. Geophys. Res.*, *104*(B2), 2797–2816.

Megard, F. (1984), The Andean orogenic period and its major structures in central and northern Peru, *J. Geol. Soc. London.*, *141*, 893–900, doi:10.1144/gsjgs.141.5.0893.

Métois, M., A. Socquet, and C. Vigny (2012), Interseismic coupling, segmentation and mechanical behavior of the central Chile subduction zone, *J. Geophys. Res.*, *117*(B3), 1–16, doi:10.1029/2011JB008736.

Métois, M., A. Socquet, C. Vigny, D. Carrizo, S. Peyrat, A. Delorme, E. Maureira, M.-C. Valderas-Bermejo, and I. Ortega (2013), Revisiting the North Chile seismic gap segmentation using GPS-derived interseismic coupling, *Geophys. J. Int.*, *194*(3), 1283–1294, doi:10.1093/gji/ggt183.

Moreno, M., M. Rosenau, and O. Oncken (2010), 2010 Maule earthquake slip correlates with pre-seismic locking of Andean subduction zone, *Nature*, *467*(7312), 198–202, doi:10.1038/nature09349.

Müller, R. D., M. Sdrolias, C. Gaina, and W. R. Roest (2008), Age, spreading rates, and spreading asymmetry of the world's ocean crust, *Geochemistry, Geophys. Geosystems*, *9*(4), 1–19, doi:10.1029/2007GC001743.

NGDC http://www.ngdc.noaa.gov (n.d.), NGDC-NOAA, *Natl. Geophys. Data Cent. NGDC*.

Nishenko, S. P. (1991), *Circum-Pacific Seismic Potential*, U.S. Geological Survey, National Earthquake Information Center.

Nocquet, J.-M. (2012), Present-day kinematics of the Mediterranean: A comprehensive overview of GPS results, *Tectonophysics*, *579*(0), 220–242, doi:10.1016/j.tecto.2012.03.037.

Nocquet, J.-M. et al. (2014), Motion of continental slivers and creeping subduction in the northern Andes, *Nat. Geosci.*, *7*(March), 287–291, doi:10.1038/NGEO2099.

Norabuena, E. O., L. Leffler-griffin, A. Mao, T. Dixon, S. Stein, I. S. Sacks, L. Ocola, and M. Ellis (1998), Space Geodetic Observations of Nazca-South America Convergence Across the Central Andes, *Science (80-.).*, *279*(5349), 358–362, doi:10.1126/science.279.5349.358.

Oleskevich, D. A., R. D. Hyndman, and K. Wang (1999), The updip and downdip limits to great subduction earthquakes: Thermal and structural models of Cascadia, south Alaska, SW Japan, and Chile, *J. Geophys. Res.*, *104*(B7), 14,965–14,991.

Oncken, O., D. Hindle, J. Kley, K. Elger, P. Victor, and K. Schemmann (2006), Deformation of the Central Andean Upper Plate System – Facts, Fiction, and Constraints for Plateau Models, in *The Andes*, edited by Springer Berlin Heidelberg, pp. 3–27.

Pelayo, A. M., and D. A. Wiens (1990), The November 20, 1960 Peru Tsunami Earthquake: Souce Mechanism of a Slow Event, *Geophys. Res. Lett.*, *17*(6), 661–664, doi:10.1029/GL017i006p00661.

Pennington, W. D. (1981), Subduction of the Eastern Panama Basin and seismotectonics of northwestern South America, *J. Geophys. Res.*, *86*(B11), 10753–10770, doi:10.1029/JB086iB11p10753.

Perfettini, H., and J. Avouac (2004), Postseismic relaxation driven by brittle creep: A possible mechanism to reconcile geodetic measurements and the decay rate of aftershocks, application to the Chi-Chi earthquake,Taiwan, *J. Geophys. Res.*, *109*(B02304), 1–15, doi:10.1029/2003JB002488.

Perfettini, H. et al. (2010), Seismic and aseismic slip on the Central Peru megathrust, *Nature*, *465*(7294), 78–81, doi:10.1038/nature09062.

Pfiffner, O., and L. Gonzalez (2013), Mesozoic–Cenozoic Evolution of the Western Margin of South America: Case Study of the Peruvian Andes, *Geosciences*, *3*(2), 262–310, doi:10.3390/geosciences3020262.

Rebischung, P., J. Griffiths, J. Ray, R. Schmid, X. Collilieux, and B. Garayt (2011), IGS08: the IGS realization of ITRF2008, *GPS Solut.*, *16*(4), 483–494, doi:10.1007/s10291-011-0248-2.

Robinson, D. P., S. Das, and A. B. Watts (2006), Earthquake rupture stalled by a subducting fracture zone, *Science (80-.).*, *312*(5777), 1203–5, doi:10.1126/science.1125771.

Rodriguez Mejia, R. (2008), El sistema de fallas Chonta y sus implicancias Metalogenéticas entre 12°15'S y 13°30'S (Huancavelica - Perú), 116 pp., Universidad Politecnica de Madrid.

Rothman, D. (1986), Automatic estimation of large residual statics corrections, *Geophysics*, *51*(2), 332–346.

Royden, L. H. (1993), The steady state thermal structure of eroding orogenic belts and accretionary prisms, *J. Geophys. Res.*, *98*(B3), 4487–4507.

Ruegg, J. C., A. Rudloff, C. Vigny, R. Madariaga, J. B. de Chabalier, J. Campos, E. Kausel, S. Barrientos, and D. Dimitrov (2009), Interseismic strain accumulation measured by GPS in the seismic gap between Constitución and Concepción in Chile, *Phys. Earth Planet. Inter.*, *175*(1-2), 78–85, doi:10.1016/j.pepi.2008.02.015.

Savage, J. C. (1983), A dislocation model of strain accumulation and release at a subduction zone, *J. Geophys. Res.*, *88*(B6), 4984–4996, doi:10.1029/JB088iB06p04984.

Scherrenberg, A. F., R. J. Holcombe, and G. Rosenbaum (2014), The persistence and role of basin structures on the 3D architecture of the Marañon Fold-Thrust Belt, Peru, *J. South Am. Earth Sci.*, *51*, 45–58.

Seiner Lizárraga, L. (2009), *Historia de los sismos en el Perú. Catálogo: Siglos XV-XVII*, edited by F. Editorial, Universidad de Lima, Lima.

Seiner Lizárraga, L. (2011), *Historia de los Sismos en el Perú Catálogo: Siglos XVIII-XIX*, edited by Universidad de Lima, Universidad de Lima (Fondo Editorial).

Sempere, T. et al. (2004), Sistemas transcurrentes de escala litosférica en el sur del perû, *Publicación Espec. Bol. la Soc. Geológica del Perú*, *5*, 105–110.

Sen, M., and P. Stoffa (1991), Nonlinear one-dimensional seismic waveform inversion using simulated annealing, *Geophysics*, *56*(10), 1624–1638.

Silgado, E. (1978), *Historia de los sismos más notables ocurridos en el Perú (1513-1974)*, Lima.

Sladen, A., H. Tavera, M. Simons, J. P. Avouac, A. O. Konca, H. Perfettini, L. Audin, E. J. Fielding, F. Ortega, and R. Cavagnoud (2010), Source model of the 2007 Mw 8.0 Pisco, Peru earthquake: Implications for seismogenic behavior of subduction megathrusts, *J. Geophys. Res.*, *115*(B22405), 1–27, doi:10.1029/2009JB006429.

Soloviev, S. L., and C. N. Go (1975), *A catalogue of tsunamis on the eastern shore of the Pacific Ocean, Moscow, "Nauka" Publishing House, 202p. English translation: Soloviev S.L., Go Ch.N. (1984). A catalogue of tsunamis on the eastern shore of the Pacific ocean, Translation by Canada Instit*, Ottawa, Canada KIA OS2.

Song, T.-R. A., and M. Simons (2003), Large Trench-Parallel Gravity Variations Predict Seismogenic Behavior in Subduction Zones, *Science (80-.).*, *301*(August), 630–633, doi:10.1126/science.1085557.

Sparkes, R., F. Tilmann, N. Hovius, and J. Hillier (2010), Subducted seafloor relief stops rupture in South American great earthquakes: Implications for rupture behaviour in the 2010 Maule, Chile earthquake, *Earth Planet. Sci. Lett.*, *298*, 89–94, doi:10.1016/j.epsl.2010.07.029.

Spiske, M., J. Piepenbreier, C. Benavente, A. Kunz, H. Bahlburg, and J. Steffahn (2013), Historical tsunami deposits in Peru: Sedimentology, inverse modeling and optically stimulated luminescence dating, *Quat. Int.*, *305*, 31–44, doi:10.1016/j.quaint.2013.02.010.

Suarez, G., P. Molnar, B. C. Burchfiel, and G. Suárez (1983), Seismicity, fault plane solutions, depth of faulting, and active tectonics of the Andes of Peru, Ecuador, and southern Colombia, *J. Geophys. Res.*, *88*(B12), 10403–10428, doi:10.1029/JB088iB12p10403.

Swenson, J. L., and S. L. Beck (1999), Source Characteristics of the 12 November 1996 M w 7.7 Peru Subduction Zone Earthquake, *Pure Appl. Geophys.*, *154*(3-4), 731–751, doi:10.1007/s000240050250.

Tarantola, A. (2005), *Inverse Problem Theory*, SIAM, Paris, France.

Tavera, H., and E. Buforn (1998), Sismicidad y sismotectónica del Perú, *Fis. la Tierra*, *10*, 187–219.

Trenkamp, R., J. N. Kellogg, J. T. Freymueller, and H. P. Mora (2002), Wide plate margin deformation, southern Central America and northwestern South America, CASA GPS observations, *J. South Am. Earth Sci.*, *15*(2), 157–171, doi:10.1016/S0895-9811(02)00018-4.

Turcotte, D. L., and G. Schubert (2002), *Geodynamics*, 2nd Editio., Cambridge University Press.

Valladares, C. E., and J. L. Chau (2012), The Low-Latitude Ionosphere Sensor Network (LISN): Initial Results, *Radio Sci.*, *47*(RS0L17), doi:doi:10.1029/2011RS004978.

Veloza, G., R. Styron, M. Taylor, and A. Mora (2011), Open-source archive of active faults for northwest South America, *Gsa Today*, *22*(10), 4–10, doi:10.1130/GSAT-G156A.1.

Villegas-Lanza, J.-C., J. Nocquet, M. Chlieh, M. Valle, H. Tavera, and F. Rolandone (2012), *A Slow Slip Event and synchronous seismicity in the northern Peru subduction zone, AGU Fall Meeting 2012*, American Geophysical Union, San Francisco.

Wang, K., and S. L. Bilek (2014), Invited review paper: Fault creep caused by subduction of rough seafloor relief, *Tectonophysics*, *610*, 1–24, doi:10.1016/j.tecto.2013.11.024.

Wang, K., Y. Hu, M. Bevis, E. Kendrick, R. Smalley, R. Barrriga, and E. Lauria (2007), Crustal motion in the zone of the 1960 Chile earthquake: Detangling earthquake-cycle deformation and forearc - sliver translation, *Geochemistry, Geophys. Geosystems*, *8*(10), 1–14, doi:10.1029/2007GC001721.

Wells, R. E., R. J. Blakely, Y. Sugiyama, D. W. Scholl, and P. A. Dinterman (2003), Basin-centered asperities in great subduction zone earthquakes: A link between slip, subsidence, and subduction erosion?, *J. Geophys. Res.*, *108*(B10), 2507, doi:10.1029/2002JB002072.

Wessel, P., and W. H. F. Smith (1998), New, improved version of generic mapping tools released, *Eos, Trans. Am. Geophys. Union*, *79*(47), 579–579, doi:10.1029/98EO00426.

White, S. M., R. Trenkamp, and J. N. Kellogg (2003), Recent crustal deformation and the earthquake cycle along the Ecuador–Colombia subduction zone, *Earth Planet. Sci. Lett.*, *216*(3), 231–242, doi:10.1016/S0012-821X(03)00535-1.

Williams, S. D. P., Y. Bock, P. Fang, P. Jamason, R. M. Nikolaidis, L. Prawirodirdjo, M. Miller, and D. J. Johnson (2004), Error analysis of continuous GPS position time series, *J. Geophys. Res.*, *109*(B03412), B03412, doi:10.1029/2003JB002741.

Williams, S. P. D. P. (2008), CATS: GPS coordinate time series analysis software, *GPS Solut.*, *12*(2), 147–153, doi:10.1007/s10291-007-0086-4.

Supplemental material:

Active Tectonics of the Peruvian margin from 2008-2013 GPS measurements: The Inca Sliver kinematics and interseismic coupling along the megathrust

J. C. Villegas-Lanza[1, 2]*, M. Chlieh[1], J.-M. Nocquet[1], H. Tavera[2], J. Maguiña[3], D. Cisneros[4], F. Bondoux[5], P. Baby[5], X. Martin[1], F. Rolandone[6] and O. Cavalié[1]

[1]Geoazur, Université Nice Sophia Antipolis, IRD, CNRS, OCA, Nice, France.

[2]Instituto Geofísico del Perú, Lima, Peru.

[3]Instituto Geográfico Nacional, Lima, Peru.

[4]Instituto Geográfico Militar, Quito, Ecuador.

[5] Observatoire Midi-Pyrénées, Univ. Paul Sabatier, IRD, CNRS, 31400 Toulouse, France.

[6]Université Pierre et Marie Curie, Paris, France.

Introduction

The material provided in this supplement contains descriptions, tables and figures that support and help to illustrate this study. We also present here the tables containing the GPS velocity field and the poles used to constraint the stable reference frame and the definition of the Inca Sliver kinematics.

1. GPS Dataset

We use data from 102 continuous and survey GPS sites located in Peru and southern Ecuador, covering the coastal rages and crossing the Andean cordillera up to the Sub-Andean region. GPS data was acquired since 2008 in the frame of the ADN project, a collaborative research initiative between research institutes from France (Geoazur, IRD, IsTerre), Peru (Instituto Geofísico del Perú, IGP) and Ecuador (Instituto Geofisico –EPN-Quito) (Figure S3.1). In this study we extend and densify

the dataset used in *Nocquet et al.*, [2014] with 52 new GPS velocities. New measurements from continuous and campaign GPS sites collected in the frame of the ADN project are here included. This study is also benefited with a set of continuous GPS data of more than three years of time span provided by local Peruvian networks. With these new data we not only extend our study area further south covering the whole Peruvian territory, but we extend our measurements up to eastern side of the Andes through 3 trench-perpendicular profiles crossing the Andean cordillera up to the sub-andean region. All the sites are showed in Figure S3.1.

The ADN network is composed by 6 continuous (CGPS) and 42 campaign (SGPS) GPS sites progressively installed since mid-2008. CGPS sites are equipped with Trimble NetRS GPS receivers recording at intervals rates of 30s (and 0.2s) and Trimble Zephyr Geodetic antennas that are anchored in bedrock according international monumentation standards for geodetic studies (http://facility.unavco.org). Data is stored on site without being transmitted, so we collected the data on a yearly basis. The SGPS-ADN network was installed and measured in July 2008 with a set of 31 sites, distributed from Lima (Lat -13ºS) to Tumbes (Lat -3ºS), covering approximately the first ~150 km between the coastline and the occidental cordillera of the Andes. Markers were generally fixed in bedrock. In 2010 and 2012 we re-measured the ensemble of sites, always during the month of July thus mitigating possible effects of seasonal signals in the time series and in the velocity estimation. Campaign measurements were performed in general using Trimble NetRS, NetR9 and occasionally TopCon TPS GB-1000 receivers recording at interval rates of 30 seconds during least 2 complete UTC daily sessions of 24 h, using in most of the cases Trimble Zephyr Geodetic antennas and eventually Topcon TPSPG_A1 antennas. Additional measurements for some campaign sites (SCH1, SCH2 and PSAL) were performed in February 2009 and September 2011 in northwestern Peru right after a sequence of seismicity near the Bayovar Peninsula. It is worth to mention for the future that there are a couple of sites (CHAC and PJNA) near the city of Cajamarca that were not re-measured after its first measurement in 2008, so they need to be reoccupied in a next campaign.

Additionally, 3 trench perpendicular GPS profiles were installed and measured since 2009, as part of the ADN project, consisting of 11 sites crossing the Andean

Cordillera from the coast to the sub-andean region near the cities of Yurimaguas (CUYC, LMAS, MOYB, YRMG), Pucallpa (HNCO, SALJ, PUCP) and Satipo (SNDM, LRYA, MRCD, TAPO, SATI) in the sub-Andean ranges. We reoccupied these profiles in mid-2011 and 2013. The campaign GPS site CUYC constitutes the common measured site between campaigns of the coastal and profile sites, since it was measured on a yearly basis since 2009. With all these new sites our ADN network sum a total of 43 SGPS and 6 CGPS covering a time span from 3.4 to 5.2 years.

In addition to our network we benefit from a dataset consisting in 32 CGPS sites from the Instituto Geográfico Nacional del Perú (IGN) distributed along the Peruvian territory and spanning a time period of minimum 3 years of data since 2009. We also include 8 CGPS sites from the Low Latitude Ionospheric Sensor Network (LISN - IGP) [*Valladares and Chau*, 2012] distributed in Peru and covering a time span of 2.6 to 6.6 years since 2007. It is worth to mention that despite the LISN network was not intended to study crustal deformation but ionospheric studies its utility for tectonic deformation studies was examined in *Villegas-Lanza*, [2009]. We also include to our dataset 14 GPS (two are continuous) located in southern Ecuador that belong to the Instituto Geográfico Militar de Ecuador (IGM) that were already used in *Nocquet et al.*, [2014]. In order to provide more constraints and calibrate our regional observations we use 30 sites from the global IGS network (International GNSS Service, http://igscb.jpl.nasa.gov) located on the Nazca and South American plates, from which 2 (CALL and AREQ) are located in our study area, thus we use them in our analysis (Table T3.1).

The global dataset used in this study comprises a total of 102 geodetic sites that include 48 permanent stations and 54 campaign sites distributed from southern Peru (Lat. 18ºS) to northern Peru (Lat 3ºS) and extending from the coast up to the sub-Andean ranges (Figure S3.1). The continuous observations have a time span ranging between 3.0 to 6.6 years of daily measurements, and the campaign sites with at least three measurements every two years a time span superior to ~3.5 years. This dataset covers for the first time an extraordinary spatial and temporal extent that allow us to study not only the crustal deformation associated to the subduction process and estimate the interseismic plate coupling along the interface, but also with much more

data further inland provide more constraints on the kinematics of the Inca sliver and estimate rates of crustal shortening in the sub-Andean region.

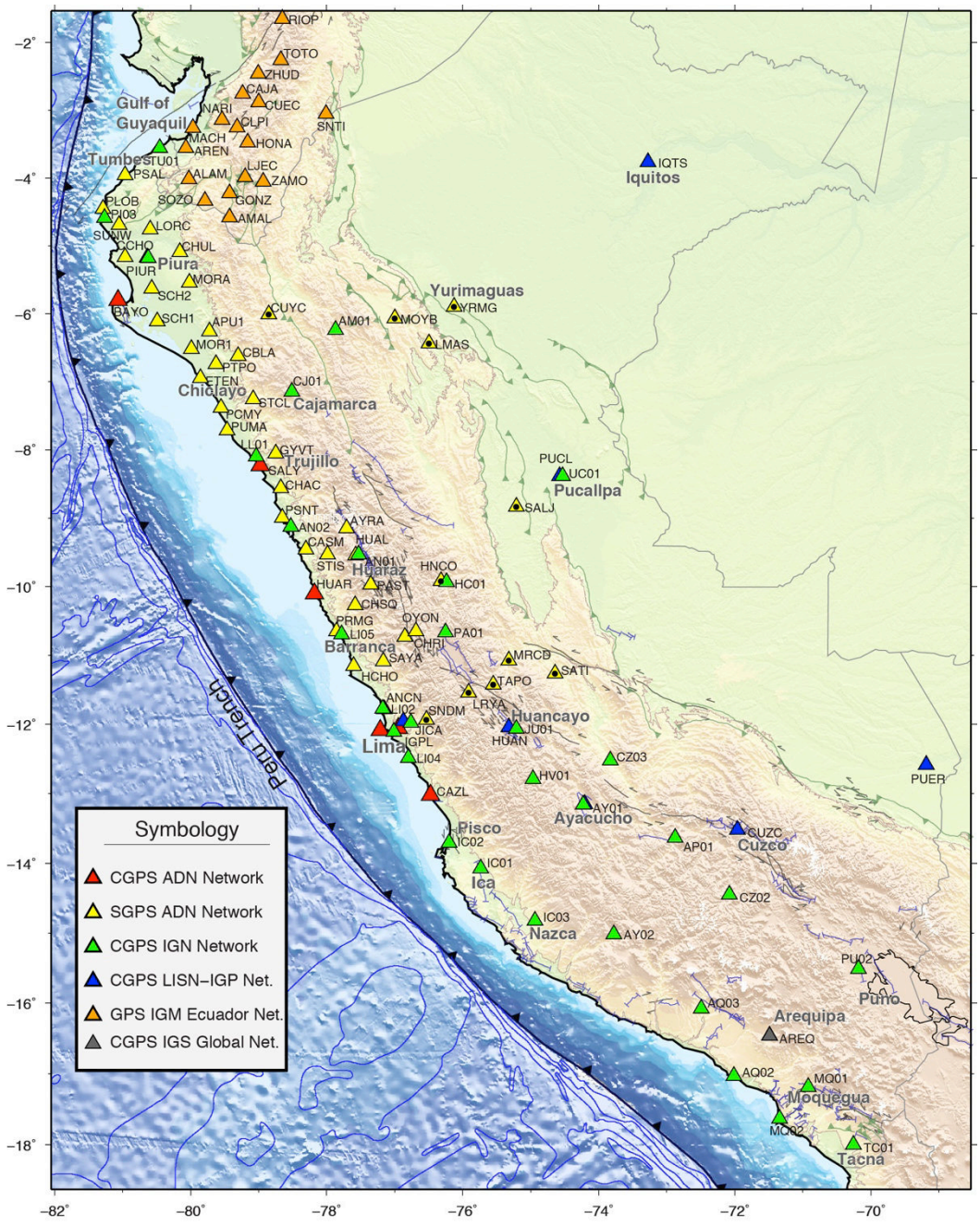

Figure S3.1: Location of the GPS stations used in this study. Colored triangles indicate that the stations correspond to a specific network. Red triangles are continuous GPS stations (CGPS) and yellow are survey SGPS stations both from the ADN ("Andes du Nord") project. Our survey sites include three profiles perpendicular to the trench (triangles with dot inside) crossing the Andean cordillera from the coast up to the sub-andean region. The first profile is extending from Lima to Satipo, the second from Barranca to Pucallpa and the third one from Chiclayo to Yurimaguas. Networks corresponding data is indicated by the colored triangles in the legend.

Table T3.1: GPS interseismic velocities expressed with respect to the stable South American reference frame and related information are enlisted. From left to right: site name, longitude, latitude in decimal degrees, Ve east and Vn north components of velocity in mm/yr, SVe and SVn are the formal error (1-sigma confidence level) of Ve, Vn, Corr_en is the correlation coefficient between Ve and Vn, #days is the number of observation days used in the velocity estimation, and the last column indicates the span of the observation period in decimal years.

site	longitude	latitude	Ve	Vn	Sve	Svn	corr	#days	span
						ADN CGPS			
BAYO	-81.0659	-5.7989	2.98	-3.17	0.36	0.28	-0.00	1649	5.2
CAZL	-76.4734	-13.0201	16.99	3.96	0.32	0.30	-0.00	1137	3.3
HUAR	-78.1808	-10.1027	10.28	0.76	0.32	0.23	-0.00	1541	4.6
IGPL	-76.9442	-12.0551	20.36	4.17	0.31	0.27	-0.00	872	5.2
SALY	-78.9782	-8.2274	4.92	-2.17	0.37	0.19	0.00	1376	4.8
SLRZ	-77.2114	-12.0814	22.77	4.74	0.57	0.31	0.00	1184	3.3
						ADN SGPS			
APU1	-79.7244	-6.2634	4.06	-1.57	0.90	0.75	-0.01	7	2.0
AYRA	-77.7103	-9.1464	10.18	-0.51	0.69	0.54	-0.02	8	4.0
CASM	-78.3068	-9.4540	7.15	-1.69	0.73	0.57	-0.02	9	4.0
CBLA	-79.3050	-6.6246	3.84	-2.87	0.59	0.48	-0.02	10	4.0
CCHO	-80.9618	-5.1665	5.19	-2.08	0.94	0.77	0.00	9	4.0
CHAC	-78.6778	-8.5568	6.82	-1.62	0.61	0.48	-0.01	9	4.0
CHRI	-76.8535	-10.7278	13.02	4.02	0.61	0.48	-0.11	10	4.0
CHSQ	-77.5797	-10.2654	10.65	1.67	0.49	0.39	0.63	9	4.0
CHUL	-80.1583	-5.0919	3.26	-2.62	0.87	0.70	-0.01	7	4.0
ETEN	-79.8583	-6.9474	5.88	-2.69	0.54	0.44	-0.03	13	4.0
GYVT	-78.7489	-8.0551	5.75	-2.74	0.54	0.23	0.58	9	4.0
HCHO	-77.6026	-11.1520	20.67	3.14	0.68	0.52	-0.04	9	4.0
HUAL	-77.5741	-9.5454	6.64	0.89	0.62	0.49	-0.01	9	4.0
LORC	-80.5940	-4.7612	1.90	-0.96	1.18	0.98	0.03	4	4.0
MOR1	-79.9876	-6.5223	5.04	-0.75	1.16	0.97	-0.03	6	2.0
MORA	-80.0220	-5.5444	4.45	-2.82	0.93	0.75	-0.00	9	4.0
OYON	-76.6881	-10.6471	11.89	4.03	0.85	0.68	-0.05	7	2.0
PAST	-77.3503	-9.9715	9.09	1.69	0.67	0.52	-0.04	7	4.0
PCMY	-79.5524	-7.3826	4.17	-2.96	0.60	0.49	-0.04	9	4.0
PLOB	-81.2888	-4.4527	3.62	-0.49	0.59	0.48	-0.01	7	4.0
PRMG	-77.8519	-10.6512	15.86	2.36	0.61	0.49	-0.02	8	4.0
PSAL	-80.9623	-3.9577	9.72	-0.33	0.60	0.50	-0.01	9	3.4
PSNT	-78.6537	-8.9904	5.65	-1.77	0.72	0.56	0.02	9	4.0
PTPO	-79.6281	-6.7402	6.03	-2.08	0.59	0.48	-0.01	8	4.0
PUMA	-79.4644	-7.7125	5.53	-3.01	0.64	0.52	-0.01	8	4.0
SAYA	-77.1710	-11.0891	17.59	4.01	0.61	0.48	-0.05	11	4.0
SCH1	-80.4911	-6.1119	3.44	-2.45	0.81	0.66	-0.01	12	4.0
SCH2	-80.5746	-5.6346	4.02	-3.52	1.04	0.85	-0.01	13	4.0
STCL	-79.0793	-7.2547	5.54	-2.34	0.59	0.49	-0.04	12	4.0
STIS	-77.9886	-9.5323	6.96	-0.06	0.59	0.47	-0.03	9	4.0
SUNW	-81.0554	-4.6934	2.33	-0.33	0.19	0.40	0.44	7	4.0
						ADN SGPS Tras-Andean Profile			
CUYC	-78.8550	-6.0122	3.88	-2.96	0.55	0.45	-0.04	18	4.1
HNCO	-76.3225	-9.9188	6.38	2.20	1.19	0.99	-0.00	15	3.6
LMAS	-76.4986	-6.4379	3.35	1.58	0.65	0.49	-0.02	10	4.1
LRYA	-75.9156	-11.5355	13.01	3.09	1.15	0.90	-0.04	12	3.8
MOYB	-77.0020	-6.0683	3.01	-0.01	0.66	0.51	-0.10	12	4.1
MRCD	-75.3216	-11.0749	9.25	1.65	0.63	0.53	0.02	16	3.8
SALJ	-75.2132	-8.8346	2.17	1.35	0.68	0.54	-0.01	13	3.6
SATI	-74.6422	-11.2583	8.33	1.50	0.63	0.51	-0.02	16	3.8
SNDM	-76.5303	-11.9283	20.15	3.35	1.24	0.93	-0.07	12	3.8
TAPO	-75.5488	-11.4216	12.63	0.25	1.04	0.81	0.04	14	3.8
YRMG	-76.1302	-5.8966	2.91	0.97	1.17	0.92	-0.03	8	4.1
						LISN CGPS			
ANCN	-77.1500	-11.7766	20.95	3.68	0.30	0.23	-0.00	1441	5.2
CUZC	-71.9593	-13.5204	5.26	1.00	0.27	0.23	-0.00	935	5.8
HUAN	-75.3214	-12.0424	9.17	0.26	0.81	0.54	-0.01	1894	6.2
IQTS	-73.2747	-3.7673	0.04	0.58	0.35	0.26	-0.00	1014	6.6
JICA	-76.8757	-11.9524	20.86	3.95	0.58	0.47	-0.02	886	3.7
PUCL	-74.5738	-8.3839	1.06	0.08	0.71	0.56	-0.01	675	2.6
PUER	-69.1870	-12.5860	1.32	2.30	0.93	0.62	-0.00	1081	5.6
						IGN CGPS			

AM01	-77.8728	-6.2351	3.28	-0.65	1.85	1.08	-0.00	946	3.2
AN01	-77.5271	-9.5312	5.81	1.62	0.95	0.97	-0.00	1161	3.4
AN02	-78.5298	-9.1284	5.93	-2.07	0.46	0.39	-0.00	632	3.7
AP01	-72.8782	-13.6384	7.05	1.71	0.51	0.43	-0.01	755	3.1
AQ02	-72.0157	-17.0296	16.85	-0.51	0.33	0.26	-0.00	860	3.8
AQ03	-72.4922	-16.0762	8.92	-0.35	0.19	0.14	-0.01	439	2.5
AY01	-74.2266	-13.1593	5.45	-0.31	0.56	0.36	-0.01	1156	3.8
AY02	-73.7813	-15.0171	15.43	4.60	0.51	0.43	-0.01	250	3.1
CJ01	-78.5094	-7.1469	4.75	-1.04	0.54	0.37	-0.00	1018	3.7
CZ02	-72.0811	-14.4495	5.48	0.28	0.58	0.49	-0.00	530	2.5
CZ03	-73.8294	-12.5197	3.66	0.51	0.49	0.35	-0.01	789	3.2
HC01	-76.2352	-9.9323	7.96	3.13	0.53	0.44	-0.05	781	3.3
HV01	-74.9677	-12.7865	7.04	-2.20	0.52	0.44	-0.01	505	3.0
IC01	-75.7349	-14.0753	8.44	-1.31	0.14	0.10	0.18	1006	3.8
IC02	-76.2004	-13.7086	18.05	3.24	0.66	0.55	-0.01	573	3.6
IC03	-74.9374	-14.8266	13.13	5.24	0.54	0.45	-0.01	745	3.2
JU01	-75.2113	-12.0618	9.57	-0.60	0.92	0.72	-0.02	492	1.6
LI01	-77.0169	-12.1030	21.05	4.31	0.31	0.25	-0.00	1534	5.0
LI02	-77.1724	-11.7700	20.25	3.71	0.48	0.41	-0.00	578	3.4
LI03	-76.7625	-11.9736	18.93	3.65	0.56	0.47	-0.01	654	2.7
LI04	-76.7974	-12.4818	20.80	4.55	0.39	0.41	-0.00	1032	3.6
LI05	-77.7804	-10.6963	16.27	2.51	0.59	0.50	-0.00	720	2.3
LL01	-79.0394	-8.0983	3.25	-2.58	0.62	0.52	0.01	979	3.1
MQ01	-70.9223	-17.1906	12.46	2.51	0.50	0.42	-0.00	719	3.7
MQ02	-71.3421	-17.6345	20.86	2.04	0.49	0.41	-0.00	923	3.3
PA01	-76.2521	-10.6655	9.67	1.72	0.21	0.15	-0.04	745	3.1
PI01	-80.6278	-5.1799	4.35	-2.02	0.64	0.43	-0.00	991	3.6
PI03	-81.2692	-4.5871	2.85	-1.28	0.53	0.45	-0.00	534	3.0
PU02	-70.1794	-15.5144	6.95	-0.80	0.57	0.44	-0.01	967	3.3
TC01	-70.2568	-18.0045	15.68	3.93	0.52	0.44	-0.00	925	2.9
TU01	-80.4524	-3.5572	6.79	-1.63	0.46	0.58	-0.00	1131	3.9
UC01	-74.5312	-8.3839	1.43	0.44	0.76	0.60	-0.03	444	3.0
					IGS Global Network				
AREQ	-71.4928	-16.4655	6.59	-0.80	0.26	0.16	-0.00	6387	19.8
CALL	-77.1493	-12.0629	21.55	3.41	0.37	0.26	-0.03	1410	5.8
					ECUADOR-IGM CGPS				
CUEC	-79.0025	-2.8833	5.29	-2.29	0.31	0.27	0.00	1429	4.4
LJEC	-79.1985	-3.9883	3.40	-1.81	1.29	0.40	-0.00	1477	4.5
					ECUADOR-IGM SGPS				
ALAM	-80.0252	-4.0198	1.87	-4.37	3.84	1.99	0.07	2	4.0
AMAL	-79.4266	-4.5812	4.54	-2.50	0.52	0.34	0.00	8	16.0
AREN	-80.0685	-3.5591	4.73	-1.23	1.03	0.65	0.03	5	13.7
CAJA	-79.2370	-2.7531	3.72	-3.05	4.47	2.29	-0.34	7	15.3
CLPI	-79.3200	-3.2549	4.22	-3.69	1.65	1.32	-0.01	2	4.2
GONZ	-79.4307	-4.2264	3.03	-2.08	0.46	0.33	0.03	7	15.3
HONA	-79.1599	-3.4766	3.91	-2.21	0.87	0.43	0.01	10	17.0
MACH	-79.9685	-3.2565	4.80	-0.81	0.75	0.41	-0.05	7	15.2
NARI	-79.5365	-3.1414	2.55	-2.20	0.51	0.34	-0.02	8	15.2
SNTI	-78.0102	-3.0495	2.92	-2.80	1.15	1.26	0.00	5	16.5
SOZO	-79.7924	-4.3338	3.40	-2.40	0.84	0.37	-0.16	7	15.4
ZAMO	-78.9320	-4.0548	3.03	-1.73	0.31	0.26	0.00	56	17.1

2. Definition of the Stable South America reference frame

To express our GPS velocity field we establish a local/regional reference frame. For that we estimate a rigid rotation vector for the South American (SOAM) plate using a subset of 20 sites that behave rigidly together following the strategy described in *Nocquet et al.*, [2001]. 12 sites located on the South American craton defines the best stable reference frame showing a wrms = 0.40 mm/yr with the best fitting angular velocity (Euler pole) for the motion of the SOAM plate relative to the

ITRF2008 located at 18.66ºS, 132.72ºW with an angular velocity of 0.118º Myr-1 (Figure S3.2, Table T3.2). These values are very similar with the solutions from *Altamimi et al.*, [2012] and *Nocquet et al.*, [2014].

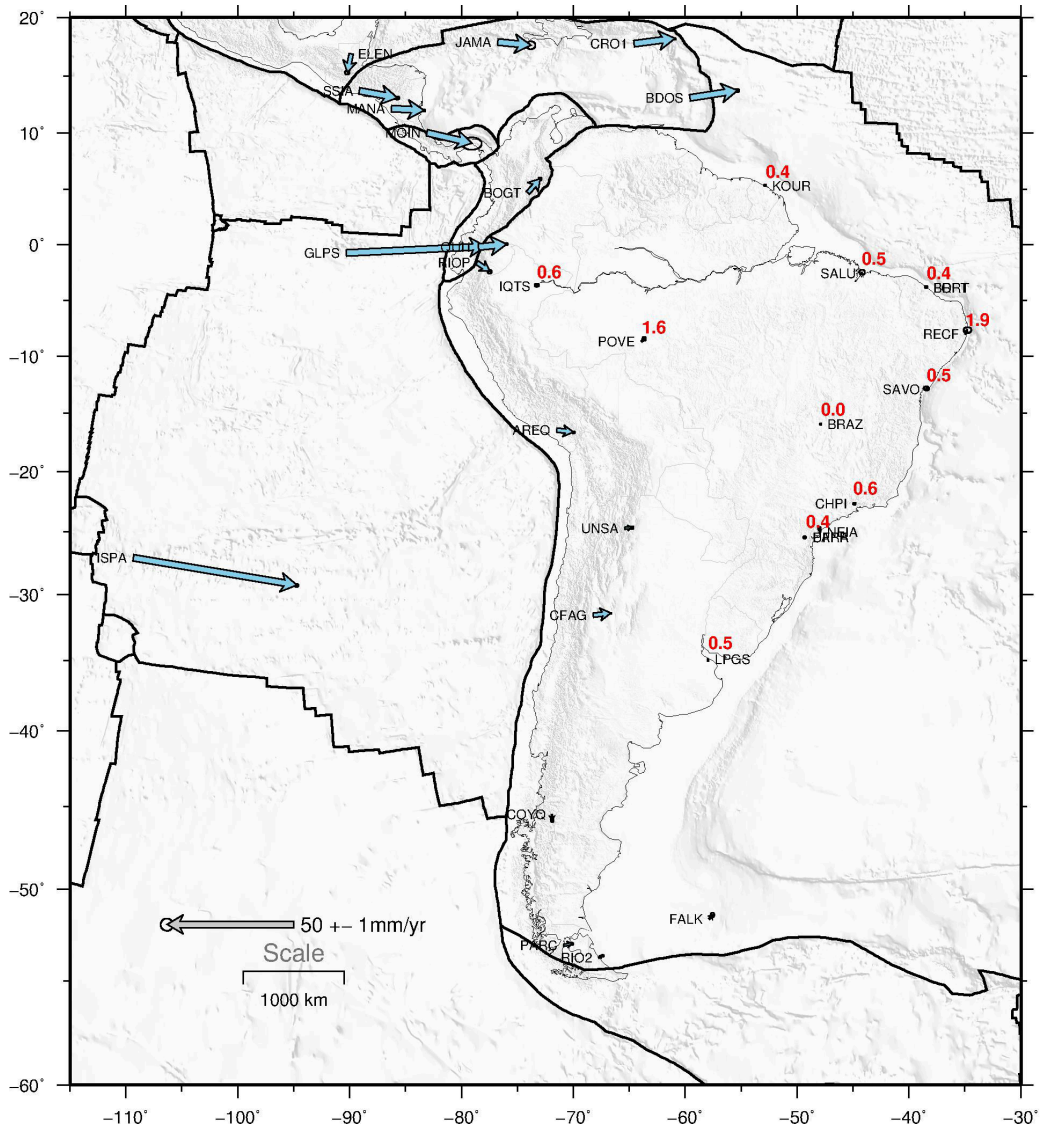

Figure S3.2: Large scale GPS network showing the 12 sites (labeled with its corresponding horizontal velocities) used to establish our stable South American reference frame.

Table T3.2: Euler Pole and residual velocities that define the stable South America reference frame (See Figure S3.2).

```
ROTATION RATE VECTOR
Wx (rad/yr): -1.3217E-09 +- 1.9155E-11
Wy (rad/yr): -1.4311E-09 +- 2.2832E-11
Wz (rad/yr): -6.5783E-10 +- 1.3291E-11
ASSOCIATED VARIANCE-COVARIANCE MATRIX (rad/yr)**2
        Wx           Wy            Wz
-------------------------------------
Wx |3.6691E-22 -3.7239E-22 -1.6099E-22
```

```
Wy |           5.2131E-22 1.9921E-22
Wz |                       1.7665E-22
-------------------------------------

EULER POLE
longitude (dec. degree)    : -132.72
latitude  (dec. degree)    : -18.66
angular velocity (deg/Myr ):  0.118
ASSOCIATED ERROR ELLIPSE
semi major axis            :  0.82
semi minor axis            :  0.26
azimuth of semi major axis : -63.6
std(angular velocity)      : 0.001

STATISTICS
----------
Number of sites     =         12
Chi**2              =      113.7
Deg. of. freedom    =         21
A post. var. factor =        2.3

RESIDUALS
----------
site                       R_ve       R_vn       S_ve       S_vn      RN_ve      RN_vn
-------------------------------------------------------------------------------------
ASC1                      -0.12      -1.11       0.40       0.34      -0.31      -3.26
BRAZ                      -0.04       0.03       0.14       0.12      -0.28       0.24
CHPI                       0.59       0.01       0.20       0.18       2.93       0.06
FORT                      -0.12       0.35       0.21       0.18      -0.58       1.95
IQTS                       0.03       0.58       0.35       0.26       0.10       2.23
KOUR                      -0.23       0.37       0.16       0.13      -1.46       2.83
LPGS                      -0.10      -0.48       0.10       0.09      -1.00      -5.30
PARA                      -0.38       0.00       0.23       0.18      -1.65       0.02
POVE                       1.01       1.19       0.28       0.34       3.62       3.51
RECF                       0.84       1.69       0.62       0.48       1.35       3.52
SALU                       0.13       0.51       0.43       0.42       0.30       1.21
SAVO                       0.01       0.48       0.40       0.34       0.02       1.42
-------------------------------------------------------------------------------------
rms =       0.62 mm/yr    wrms =       0.40 mm/yr
```

3. Inca Sliver pole determination directly from GPS observations

We determined the sliver motion of the Inca Sliver following the same approach as in *Nocquet et al.*, [2014]. Our GPs velocity field with respect to the stable south American shows that sites located in northwestern Peru and southern Ecuador do not show a gradient of deformation, contrarily they show a constant southeastward pattern of deformation. We selected a subset of 35 GPS sites showing a persistent average magnitude and a consistent southeastward direction and invert them to evaluate if an Euler rotation pole explain this pattern. We found that an Euler pole located at long. -73.66ºW, latitude 4.26ºN with an angular velocity of 0.215 deg/Myr fit with a wrms = 0.66 the trend motion of the 35 sites (Table T3.3). Compared to the solution of *Nocquet et al.*, [2014] (63.76ºW/22.47ºE/0.092 deg/Myr), we found that our Euler pole change of location moving southwestward and increasing its rate more than twice the previous angular velocity. This change is probably due to the fact that here we use more sites to constraint the Inca sliver pole.

Table T3.3: Euler Pole and residual velocities that define the Inca Sliver derived directly from GPS observations.

```
ROTATION RATE VECTOR
Wx (rad/yr):  1.0536E-09 +- 4.8244E-11
Wy (rad/yr): -3.5948E-09 +- 2.4076E-10
Wz (rad/yr):  2.7897E-10 +- 3.3585E-11
ASSOCIATED VARIANCE-COVARIANCE MATRIX (rad/yr)**2
        Wx          Wy            Wz
-----------------------------------
Wx |2.3275E-21 -1.1329E-20 -1.4134E-21
Wy |           5.7967E-20 7.1857E-21
Wz |                       1.1279E-21
-----------------------------------

EULER POLE
longitude (dec. degree)    : -73.66
latitude  (dec. degree)    :   4.26
angular velocity (deg/Myr ):  0.215
ASSOCIATED ERROR ELLIPSE
semi major axis            :  0.84
semi minor axis            :  0.18
azimuth of semi major axis : -96.3
std(angular velocity)      : 0.014

STATISTICS
----------
Number of sites     =         35
Chi**2              =      151.0
Deg. of freedom     =         67
A post. var. factor =        1.5

RESIDUALS
----------
```

site	R_ve	R_vn	S_ve	S_vn	RN_ve	RN_vn
AMAL	0.88	-0.10	0.52	0.34	1.70	-0.30
AN02	0.42	-0.04	0.46	0.39	0.91	-0.10
AP01	-0.28	1.38	0.51	0.43	-0.55	3.21
APU1	-0.28	0.95	0.90	0.75	-0.32	1.27
AY01	-1.69	-0.08	0.56	0.36	-3.02	-0.22
BAYO	-1.17	-0.09	0.36	0.28	-3.24	-0.31
CASM	1.51	0.24	0.73	0.57	2.07	0.42
CBLA	-0.65	-0.52	0.59	0.48	-1.11	-1.08
CCHO	1.30	0.96	0.94	0.77	1.38	1.24
CHAC	1.54	0.47	0.61	0.48	2.53	0.98
CHUL	-0.60	0.09	0.87	0.70	-0.69	0.12
CJ01	0.05	0.98	0.54	0.37	0.09	2.65
CLPI	1.10	-1.34	1.65	1.32	0.67	-1.02
CUYC	-0.36	-0.80	0.55	0.45	-0.66	-1.79
ETEN	1.26	-0.12	0.54	0.44	2.34	-0.27
GONZ	-0.48	0.32	0.46	0.33	-1.05	0.97
GYVT	0.67	-0.62	0.54	0.23	1.25	-2.73
HONA	0.71	0.08	0.87	0.43	0.81	0.19
HV01	0.06	-1.65	0.52	0.44	0.11	-3.76
LJEC	-0.01	0.49	1.29	0.40	-0.01	1.23
LL01	-1.84	-0.34	0.62	0.52	-2.96	-0.66
MOR1	0.59	1.88	1.16	0.97	0.51	1.94
MORA	0.40	-0.18	0.93	0.75	0.43	-0.24
NARI	-0.52	0.25	0.51	0.34	-1.01	0.73
PCMY	-0.63	-0.51	0.60	0.49	-1.05	-1.05
PI01	0.45	0.87	0.64	0.43	0.71	2.03
PSNT	0.20	0.31	0.72	0.56	0.28	0.55
PTPO	1.49	0.40	0.59	0.48	2.52	0.83
PUMA	0.59	-0.59	0.64	0.52	0.93	-1.14
SALY	-0.23	0.04	0.37	0.19	-0.61	0.23
SCH1	-0.84	0.39	0.81	0.66	-1.04	0.59
SCH2	-0.06	-0.65	1.04	0.85	-0.06	-0.76
SOZO	-0.16	0.15	0.84	0.37	-0.19	0.40
STCL	0.79	-0.08	0.59	0.49	1.34	-0.17
ZAMO	-0.42	0.47	0.31	0.26	-1.34	1.80

```
rms =       0.78 mm/yr    wrms =       0.66 mm/yr
```

4. Inca Sliver pole determined from the misfits between the data and modeled displacements (former 2-plates inversion)

Following the same approach we invert the residual velocities derived from the former inversion. We made a selection 34 of sites that show a similar pattern of velocity and direction to search for an Euler pole. The location of this pole (Table T3.4) is relatively close to the location of the Euler pole found indirectly from the residuals suggesting that the two approaches provide quite consistent results in the spatial location of the pole. However, we can notice that the angular velocity this Euler pole is about 50% slower than the Euler pole found directly form the data (see Table 3.2 of the main text). Both Euler poles have a consistent spatial location but with quite different angular velocities. To discriminate the trade-off between the sliver motion and inteseismic coupling, we propose now to modulate the angular velocity of both Euler poles found from direct and indirect approaches.

Table T3.4: Euler Pole and residual velocities that define the Inca Sliver derived from residuals of the former inversion.

```
ROTATION RATE VECTOR
Wx (rad/yr):  6.3402E-10 +- 3.8335E-11
Wy (rad/yr): -1.5104E-09 +- 1.6919E-10
Wz (rad/yr):  2.4061E-10 +- 3.0395E-11
ASSOCIATED VARIANCE-COVARIANCE MATRIX (rad/yr)**2
        Wx           Wy            Wz
-----------------------------------
Wx |1.4696E-21 -6.2594E-21 -1.0016E-21
Wy |           2.8625E-20 4.5494E-21
Wz |                       9.2384E-22
-----------------------------------

EULER POLE
longitude (dec. degree)    : -67.23
latitude  (dec. degree)    :   8.36
angular velocity (deg/Myr ):  0.095
ASSOCIATED ERROR ELLIPSE
semi major axis            :  2.13
semi minor axis            :  0.39
azimuth of semi major axis : -122.2
std(angular velocity)      : 0.009

STATISTICS
----------
Number of sites     =         34
Chi**2              =      127.5
Deg. of. freedom    =         65
A post. var. factor =        1.4

RESIDUALS
----------
site                       R_ve       R_vn       S_ve       S_vn      RN_ve      RN_vn
-------------------------------------------------------------------------------------
AN02                       0.70       0.34       0.46       0.39       1.52       0.86
AP01                       0.08       0.74       0.51       0.43       0.16       1.72
APU1                      -0.04       0.15       0.90       0.75      -0.05       0.20
AY02                       0.14       0.07       0.51       0.43       0.27       0.17
CASM                       0.55      -0.73       0.73       0.57       0.76      -1.29
CBLA                      -0.33      -1.07       0.59       0.48      -0.55      -2.24
CHRI                      -1.20       0.68       0.61       0.48      -1.97       1.41
```

CHUL	-0.12	-0.27	0.87	0.70	-0.13	-0.39
CJ01	0.86	0.80	0.54	0.37	1.59	2.17
CUYC	0.49	-1.06	0.55	0.45	0.89	-2.37
CUZC	-1.05	0.32	0.27	0.23	-3.89	1.40
GONZ	0.08	0.12	0.46	0.33	0.18	0.36
GYVT	1.17	-0.64	0.54	0.23	2.16	-2.80
HUAL	-0.97	-0.16	0.62	0.49	-1.56	-0.33
HUAN	0.17	0.26	0.81	0.54	0.22	0.48
JU01	0.95	-0.54	0.92	0.72	1.03	-0.75
LJEC	0.58	0.32	1.29	0.40	0.45	0.79
MOR1	-0.20	0.51	1.16	0.97	-0.18	0.52
MORA	1.00	-0.67	0.93	0.75	1.08	-0.89
NARI	-0.17	-0.08	0.51	0.34	-0.33	-0.24
OYON	-0.36	1.43	0.85	0.68	-0.42	2.10
PA01	-0.23	0.31	0.21	0.15	-1.07	2.06
PAST	-1.11	-0.53	0.67	0.52	-1.66	-1.03
PI01	0.10	0.44	0.64	0.43	0.16	1.03
PSNT	0.46	0.94	0.72	0.56	0.64	1.68
PTPO	1.15	-0.50	0.59	0.48	1.94	-1.03
SALY	-0.18	0.09	0.37	0.19	-0.49	0.46
SCH1	-0.95	-1.02	0.81	0.66	-1.17	-1.55
SCH2	0.02	-1.07	1.04	0.85	0.02	-1.26
SNDM	0.73	0.94	1.24	0.93	0.59	1.01
SOZO	0.25	-0.07	0.84	0.37	0.30	-0.18
STCL	1.01	-0.45	0.59	0.49	1.72	-0.93
STIS	-0.75	-0.74	0.59	0.47	-1.27	-1.57
ZAMO	0.27	0.33	0.31	0.26	0.87	1.27

rms = 0.66 mm/yr wrms = 0.55 mm/yr

5. Earth Structure Model

We use a layered elastic half-space model, the Crust2.0 model [*Bassin et al.*, 2000] (Table T3.5), in which we establish the Green's functions of each elementary sub-fault. The characteristics of this layered elastic half-space are reported in Table T3.4. The distribution of this model predicts an average rigidity of ~39Gpa.

Table T3.5: Earth Structure Model from the Crust2.0 Model for the first Km of the lithosphere. Vp and Vs are the corresponding velocity of the P and S seismic waves in this layered model.

Thickness (km)	Vp (km/s)	Vs (km/s)	Density (kg/m^3)	Rigidity (GPa)
0.5	2.5	1.2	2.1	3.02
0.5	4.0	2.1	2.4	10.58
21	6.0	3.5	2.7	33.07
24	6.4	3.7	2.85	39.01
64	7.1	3.9	3.1	47.15

6. Determination of the best Euler pole for the eastern Inca sliver

In subduction zones the wavelength of the interseismic deformation can be of many hundred of kilometers and recover the sliver motion, which result on trade-off

between the rigid sliver motion and the interseismic deformation. Many approaches have been proposed to quantify from the GPS measurements the portion of the convergence that is taken up by the sliver motion and the portion that is accommodated by interplate locking. One method consists of selecting a sub-set of GPS data not affected by the interseismic coupling and search for an Euler pole able to fit these observations. Another method consists to analyze the GPS residuals resulting from an interseismic model and search an Euler pole explaining these residuals. Both methods have limitations. In the first one, a fraction of the real interseismic coupling could be interpreted as rigid motion, resulting in an over-estimated sliver motion. In the second method, we may under-estimate the sliver motion. In both cases, a modulation of the angular velocity of the Euler pole is necessary to find the best GPS-fitting partitioning model. In *Nocquet et al.*, [2014] and in the previous section, the first approach has been applied. To confirm the Euler pole characteristics that we use in this study (Pole obtained from the GPS residuals from a former inversion, see Section 6 of the main text), we propose to follow the second approach. So, we modulate the angular velocity of the western Inca/SSA Euler pole (Table 3.2 of the main text) by steps of 0.02°/Myr, equivalent to 0.1 mm/yr over the studied area. For each model, we adjust adequately the backslip rate (V_{back}) of the Nazca/western Inca Sliver relative convergence rate. We found that the best partitioning models work for a Inca Sliver Euler pole having an angular velocity of 0.104 ± 0.02°/Myr (Table T3.5).

Table T3.6: Characteristics of the modulation of the angular velocity of the Inca sliver Euler pole. Column 2 shows the angular velocity of the Inca sliver in °/106y. Column 3 and 4 the wrms and chi2 indicates the misfit of the GPS data. Columns 4, 5, 6, 7, 8, show how vary the moment deficit of the whole Peruvian margin (4), for the southern segment (5), central segment (6), northern segments (7, 8).

Model Name	Inca Sliver Ang. Vel. (°/Myrs)	wrms	Md Total 10e20 N.m	Md (south) Areq	Md (central) Lima	Md (north) Chiclayo	Md (north) Piura
2-plates	0	3.60	3.82	1.71	1.52	0.390	0.208
3-plates-B	0.044	2.51	3.42	1.56	1.39	0.299	0.169
3-plates-C	0.066	2.05	3.20	1.44	1.32	0.289	0.153
3-plates-F	**0.084**	**1.77**	**3.00**	**1.33**	**1.27**	**0.272**	**0.132**
3-plates-G	**0.104**	**1.63**	**2.74**	**1.23**	**1.19**	**0.217**	**0.106**
3-plates-H	**0.124**	**1.75**	**2.51**	**1.14**	**1.13**	**0.178**	**0.059**
3-plates-J	0.133	1.86	2.41	1.09	1.10	0.162	0.055
3-plates-L	0.177	3.08	1.91	0.85	0.96	0.074	0.021
3-plates-M	0.199	3.92	1.65	0.68	0.89	0.051	0.020
3-plates-N	0.221	4.85	1.43	0.58	0.83	0.023	0.010

7. Comparison of the location and prediction of the Euler Poles

A comparison of the location and prediction of the Euler Poles obtained in this study and in Nocquet et al., [2014] is shown in Figure S3.3. In northern Peru we observe a quite similar prediction of the poles both in magnitude and direction. In south Peru the pole computed by Nocquet et al., [2014] (blue arrows) and the obtained from the residuals (red arrows) show a consistent direction, but the first predicts a velocity that doubles its magnitude in the southernmost sites. In contrast the pole obtained directly from the observations (green arrows) predicts not only velocities that are greater than the two previous but an anticlockwise rotation of 6-10 degrees for the sites in southern Peru.

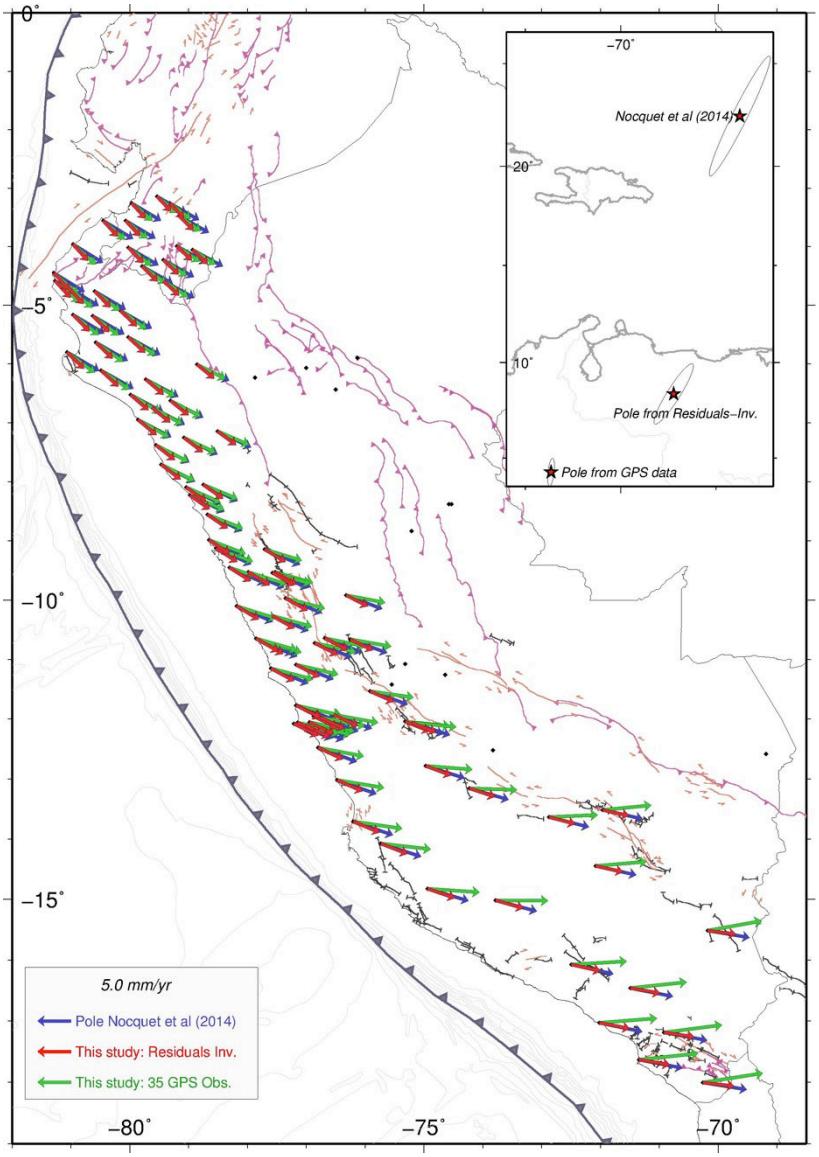

Figure S3.3: Predicted motions at each GPS site of our network from the Euler poles proposed in our studies. Blue predictions are based on the pole determined by Nocquet et al., [2014]. Green predictions (G) on the pole derived from GPS observations and red (R) on the pole computed from the residual of the former inversion. The Euler poles proposed in this study predict consistent directions with the proposed in Nocquet et al., [2014] but with velocities for (R) slower by about 4 mm/yr and for (R) by about 2mm/yr in central-south Peru at Lat. ~15ºS. The inset maps shows the geographical location of the poles.

8. Subduction earthquake Slip vectors and partitioning of the Nazca - South America convergence

The Peruvian segment of the Nazca/South America subduction zone is characterized by the oblique convergence of the Nazca plate towards South America. While the convergence direction of the Nazca plate toward South America remains constant within a few degrees at (~80°E) all along the Peruvian margin, there is a

large change of strike of the trench from 0°N in front of the Piura peninsula to 50°W in southernmost Peru. As a result, obliquity increases from -10° in the northern Piura peninsula to 40° immediately north of the Arica bend. Analysis of the slip vectors of crustal subduction earthquakes shows a systematic clockwise rotation of the slip vector angle from north to south (Figure S3.4). The existence of this systematic rotation responds to a component of trench parallel motion, which is induced by the partitioning of the convergence. Inland, the slip vectors are consistent with the northwest-southeast strike of active thrust faults in the sub-andean region.

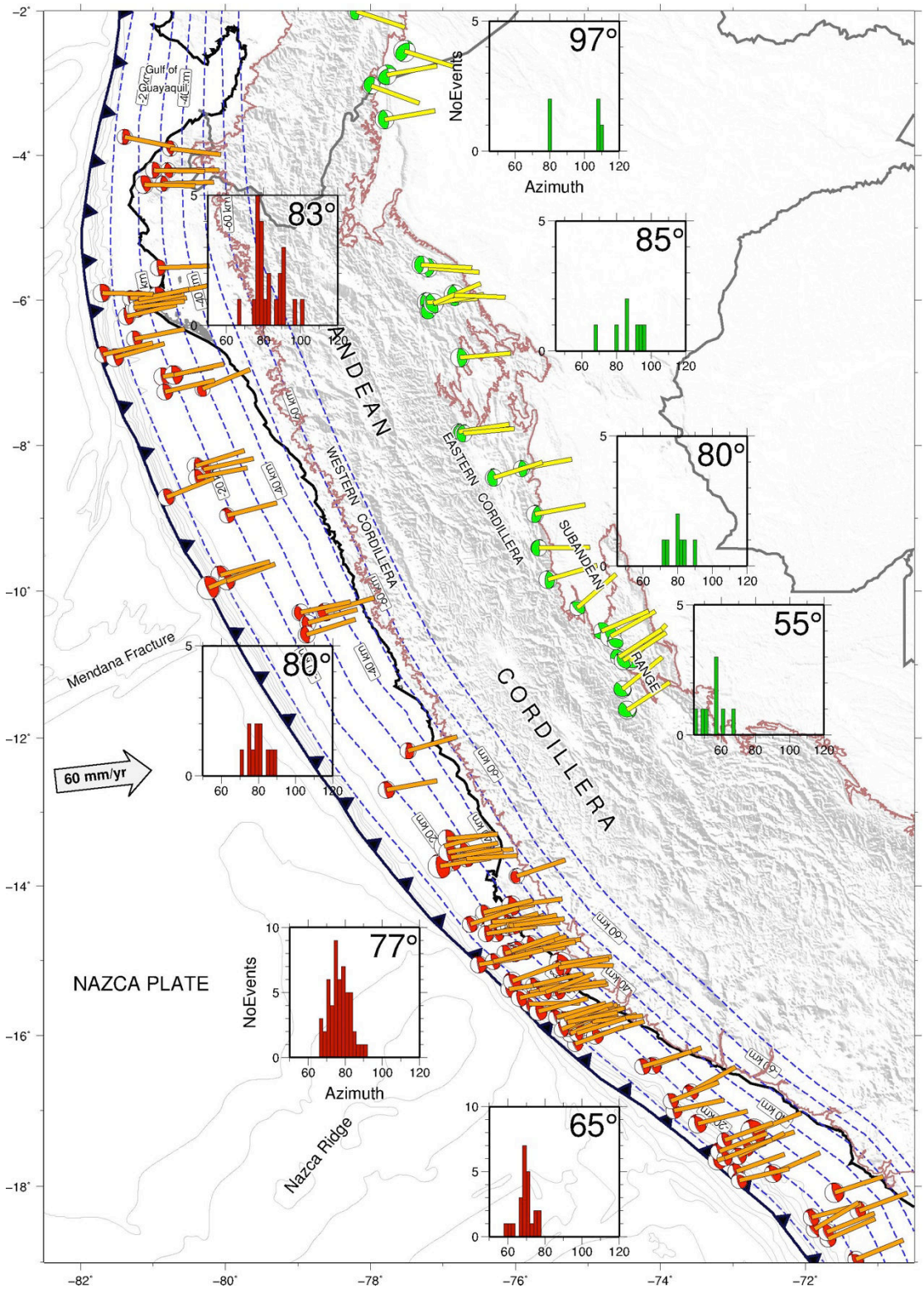

Figure S3.4: Shallow depth (<60km) focal mechanism for subduction (red) and sub-andean (green) thrust events with their associated slip vector denoted by the bars (data from gCMT and Devlin et al., [2012]). Histograms show the average of the slip vector angle for given subsets of events along-strike. We use these values as constraints in our modeling.

9. Spatial resolution of the formal inversion

To test the spatial resolution of our GPS network, we define a checkerboard with alternating fully locked and purely creeping patches of 120 km x 60 km. The predicted displacements of this checkerboard are computed at each GPS sites of the network. A formal inversion of the predicted displacements is performed to see what are the patches that spatially are well resolved by our dataset. In this inversion, we impose the final moment deficit rate to be the same as the initial checkerboard model (conservation of moment). We found that the spatial resolution is higher along-strike than along-dip (Figure S3.5). Indeed, the along-strike pattern of coupling of the initial checkerboard is relatively well preserved. All the patches near the subduction trench axis are not resolved, except near the Piura and the Paracas Peninsulas where the distance trench-coast is the shortest (~80km) where the resolution is better. Indeed, the trench-coast distance varies significantly along the Peruvian margin from about 100km in southern Peru to 175km in Lima and nearly 200km near Trujillo imposing a natural limitation of the spatial resolution of the shallowest patches of the subduction megathrust interface. The spatial resolution is improved for intermediate depth (20-40 km) patches and deep (40-60 km) patches.

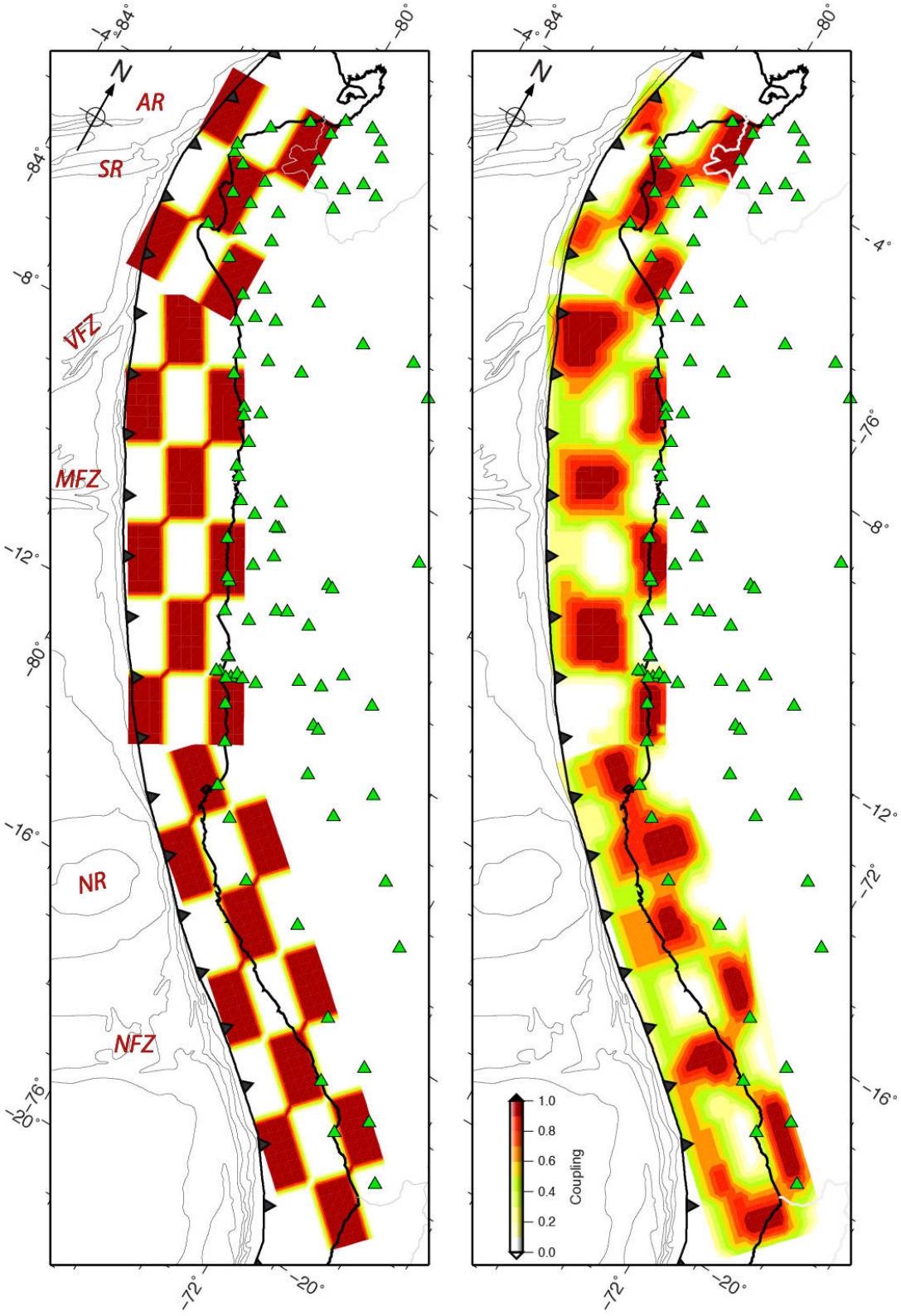

Figure S3.5: Checkerboard resolution tests for the GPS dataset used in this study. Theoretical displacements using 120 km x 60 km patches fully locked and fully creeping (black and white checkerboard) are computed at each point of the GPS network (triangles). Inter-site distance of our network is of the order of ~80km. Left: we leave the seismic moment to be free. Right: we impose the seismic moment to be the same as the forward model.

10. Misfit of the GPS data as function of the smoothing factor used in our inversion

We performed several inversions of spatially variable interseismic coupling using the approach described in the main text (section 5.3). For that we impose the rake to not vary more than +/- 10° of the average gCMT rake (Fig. S3) and leave the smoothing factor to vary from 0.01 to 10. We found that model with for λ=1 or closely lower explain relatively well the data (Figure S3.5). We fix this value for all of our inversions.

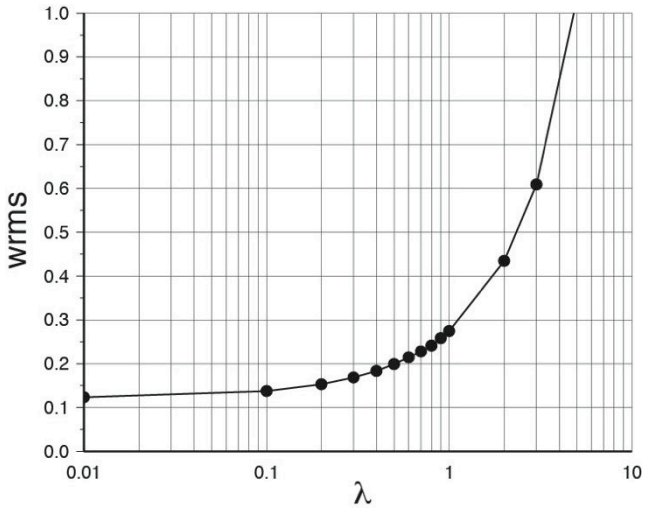

Figure S3.6: Misfit (wrms) of the GPS data as function of the smoothing factor. We found that a smoothing factor of 1 or lower explain relatively well the GPS data.

11. Trade-off between the Inca Sliver kinematic and the interseismic coupling

Figure S3.7 shows how vary the rate of moment deficit rate along the 2200-km long Peruvian subduction zone together with our best 3-plate model for all the models of Table T3.4. The highest curve corresponds to the 2-plate model and is reduced by about 35-40% than our preferred 3-plate model (red-dashed curve). This indicates the importance of well taking into account the sliver motion to not bias our estimation of the rate of moment deficit. In all models, we observe minimums of moment deficit rate where oceanic geomorphic structures (as fractures zones and ridges) enter in subduction. The maximums indicate the location of seismic asperities.

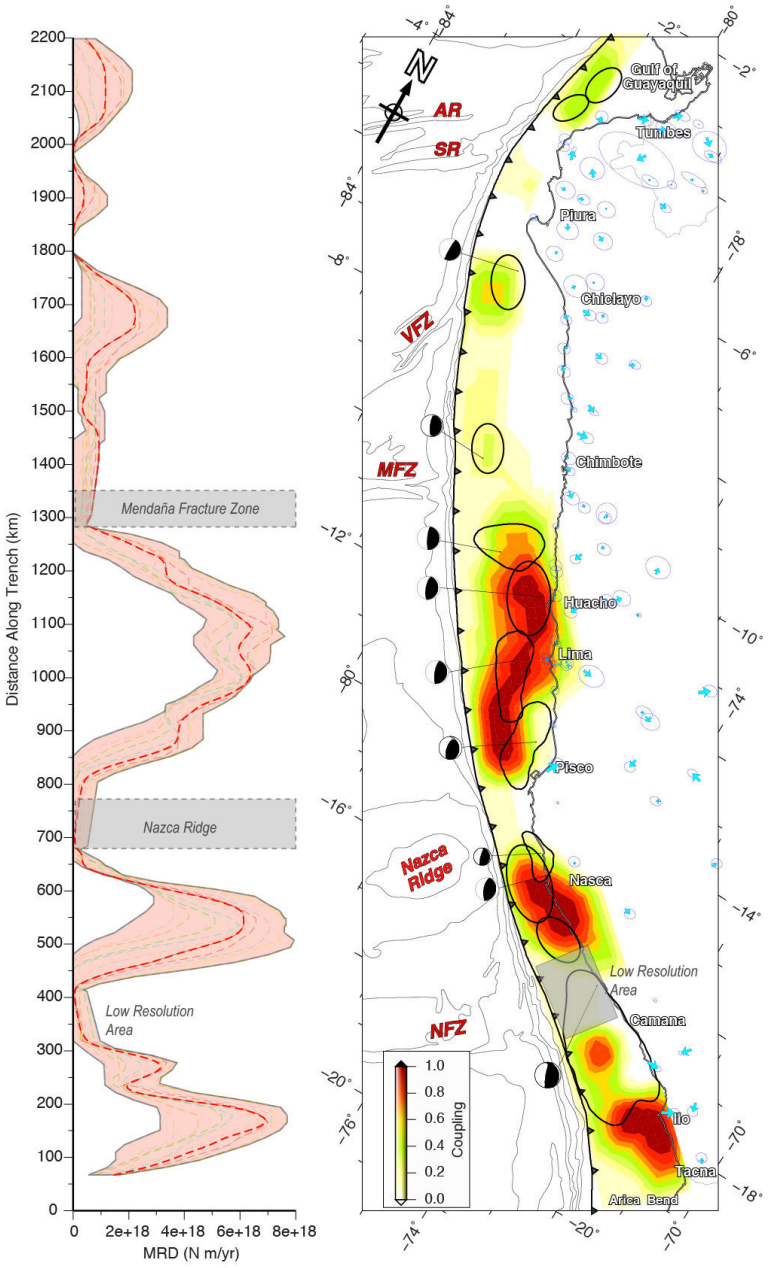

Figure S3.7: Left: Along-trench variations of the rate of moment deficit for all models listed in Table 3. These curves are constructed from the summation in the downdip direction of the rate of moment deficit computed at each node and integrated along strip band of 20km side. The dashed-red line corresponds to the model on the right. Right: Best interseismic coupling (ISC) model for Peru of Figure 3.7 compared with rupture areas of large subduction earthquakes of Figure 3.2. Blue arrows show the GPS residuals of that model. Dashed polygons represent the rupture areas of large earthquakes.

12. Misfit of data as a function of the final moment deficit rate

To fully account for the model uncertainties due to the limited spatial resolution of our geodetic data, we decide to run a final series of models where we force the

final rate of moment deficit to vary from Md=1.0×10^{20} Nm/yr (Mw~7.3) to 7.0×10^{20} Nm/yr (Mw~7.9). From this test we found that best fit of the data is for a series of models with a moment deficit ranging between 2.44E27 N m/yr and 4.05E27 N m/yr (Figure S3.8). The ISC contribution of these models is shown in Figure 3.9 of main text

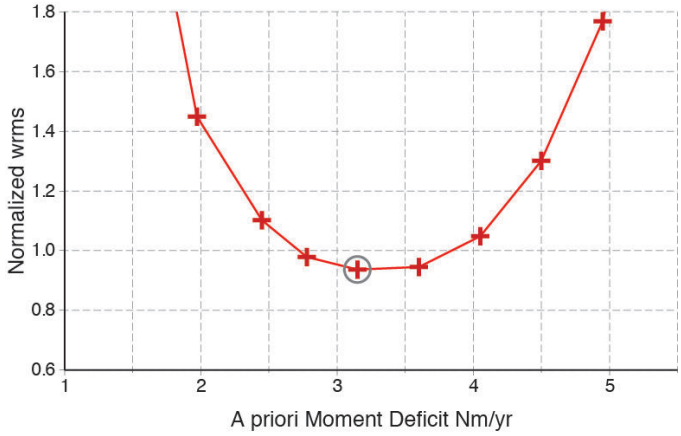

Figure S3.8: GPS misfit (normalized wrms) as a function of the final moment deficit rate of the model. We choose the model marked by circle.

13. Large differences with previous geodetic solutions in central Andes

We compared our velocity field with the published by the SNAPP project for central and southern Peru [*Norabuena et al.*, 1998; *Kendrick et al.*, 2001]. Figure S3.9 shows the differences of both solutions either in the rate as in the direction. Velocities differ for common located sites, for example the *CUZC =5.4* and *cuso = 9.4 mm/yr* with an offset of *30º* in azimuth, the same for *HCHO= 21.0* and *sali = 27.6* and 8º in azimuth. We discuss these differences in the main text.

Indeed, we found evidence of ongoing postseismic deformation in the region of the Mw=8.4 Arequipa 2001 earthquake. Current interseismic velocity for the AREQ site is 6.6 mm/yr. The velocity for this site from the SNAPP dataset is 13.6 mm/yr. For this particular site postseismic deformation would explain such differences. Difference for the other sites are discussed in section 6.3.3 of the main text.

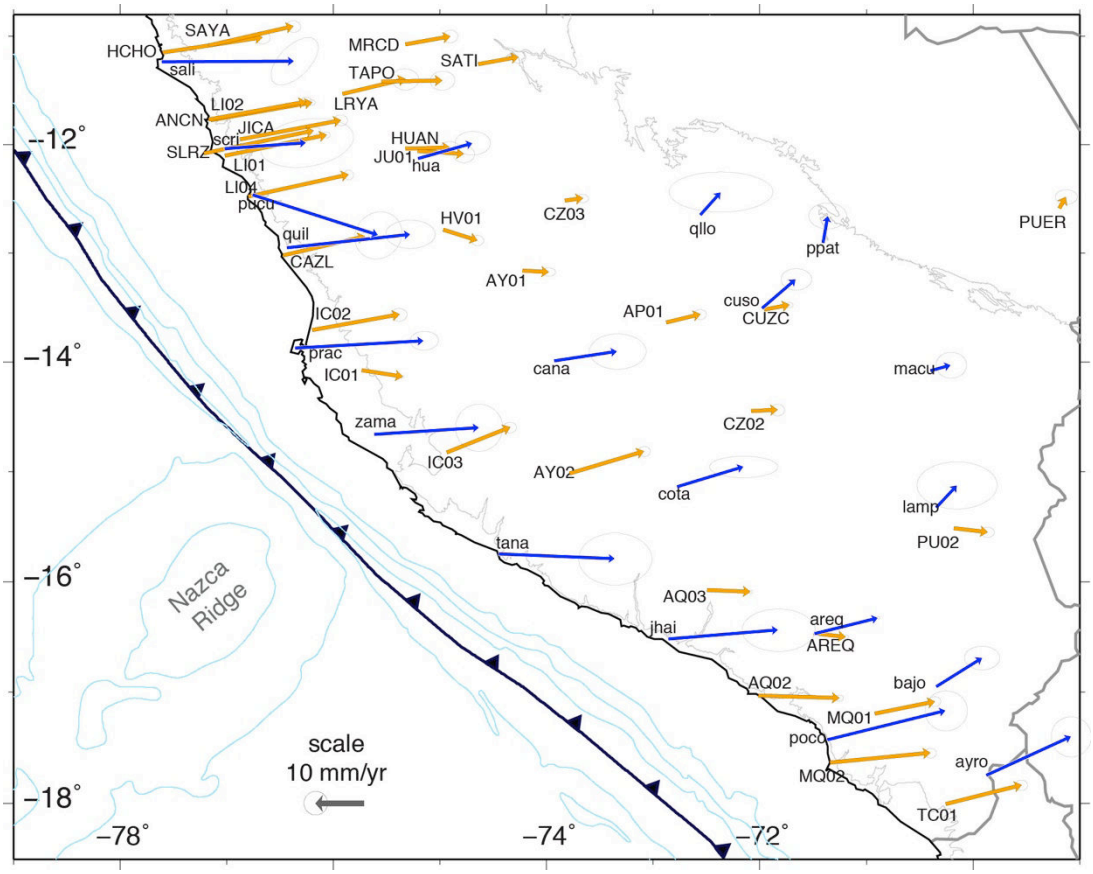

Figure S3.9: Comparison of our 2008-2013 GPS velocity field with previously published velocity fields acquired in southern Peru between 1994-1996 during the SNAPP project.

14. Thermal model parameters

We model the steady-state thermal structure of the Peruvian megathrust interface following the approach developed by *Royden*, [1993] (see section 7.2.1 of the main text). For that we establish various trench-perpendicular sections in which we compute the thermal structure. The parameters used for this purpose are presented in Table T3.6. The thermal model is shown in Figure 3.13 of the main text.

Table T3.7: Parameters used to compute the thermal structure along the Peruvian subduction zone. The coordinates are the origin of the sections where normal and parallel trench velocities, ocean floor age and slab thickness are estimated.

E Origin	N Origin	Trench Normal Velocity	Trench Parallel Velocity	Ocean Floor Age (Ma)	Slab Thickness (Km)
-81.51	-2.06	53.5	19.4	18.0	55.3
-81.49	-3.73	54.8	19.8	30.0	71.4
-81.99	-5.05	57.9	6.6	29.2	70.4
-81.53	-7.79	58.3	11.7	28.5	69.6

-80.79	-9.50	56.1	21.6	28.7	69.8
-80.37	-10.22	55.6	23.5	29.0	70.2
-79.53	-11.74	54.9	26.3	36.8	79.1
-78.42	-13.34	53.7	29.8	37.2	79.5
-77.72	-14.30	49.4	36.9	37.7	80.0
-76.80	-15.28	49.9	36.7	38.5	80.9
-75.43	-16.58	45.7	42.3	42.5	85.0
-74.22	-17.45	46.3	42.0	43.3	85.8
-73.06	-18.35	57.0	26.2	43.5	86.0
-72.00	-19.41	57.3	25.8	47.5	89.8

15. Simple forward models

The observed GPS velocity field results from the contribution of several processes that are: (1) the elastic strain induced by coupling along the subduction interface, (2) motion of the Inca Sliver and its potential internal deformation, and (3) the motion and internal deformation of the sub-andean domain (see section 4 with the description of the GPS velocity field in the main text). In order to evaluate the pattern associated with each process and guide us for further detailed modeling, we perform several simple forward models at the scale of the whole Peruvian subduction zone. The Peruvian segment of the Nazca/South America subduction zone is characterized by the oblique convergence of the Nazca plate towards South America. While the convergence direction of the Nazca plate toward South America remains constant within a few degrees at (~80°E) all along the Peruvian margin, there is a large change of strike of the trench from 0°N in front of the Piura peninsula to 50°W in southernmost Peru. As a result, obliquity increases from -10° in the northern Piura peninsula to 40° immediately north of the Arica bend. In the case of oblique subduction, two end-members kinematics models are possible [*Mccaffrey*, 2002]. A first model in that all the plate relative motion is taken up along the subduction interface, that is that there is no partitioning. Figure S3.10.A shows the surface velocity field predicted for this model in the case of a subduction interface idealized as a single dislocation extending from the surface to a depth of 50km and a dip of 15°. The calculation uses the backslip approach [*Savage*, 1983] with a slip of 60mm/yr and a rake of -117°, consistent with a 80°E convergence direction. As described in *Bevis et al.*, [2001], the velocity field predicted by the oblique convergence shows (1) a

pattern rotation (counter-clockwise in the case of Peru), being largely oblique close to the trench and almost trench-normal in the far field, (2) decreasing magnitude of velocities with increasing distances from the trench. This pattern is not observed in the velocity field (Figure 3.4). On the contrary, the velocity field usually shows a clockwise rotation with increasing distance from the trench. Furthermore, the null partitioning scenario would involve that the interface earthquakes slip vectors be directed 80°E, while they are rotated 5° counter-clockwise from this direction (See Figure S3.3 or Supplement material in *Nocquet et al.,* [2014]).

Figure S3.10.B shows the opposite end-member alternative model where all the trench-parallel component of the relative Nazca/South America motion is accommodated by a pure trench parallel motion of a sliver wedged between the trench and the stable South America. This model corresponds to 100% partitioning, a setting similar to Sumatra [*Sieh and Natawidjaja*, 2000] or Costa Rica [*Feng et al.*, 2012]. In this case, the slip at the interface is now 55mm/yr, normal to the trench. Full partitioning would involve ~27mm/yr of right-lateral trench-parallel motion to be accommodated. Such a model now predicts a clockwise rotation of the velocity field with increasing distances from the trench. However, velocities in the far field are larger by an order of magnitude to the observed velocities. These two simple models clearly show that slip partitioning in the Peru subduction zone is between these two models. Figure S3.10.C-D shows that 25% of partitioning provides the best qualitative agreement with the observed velocity field, providing a first order estimate of the slip partitioning.

Models shown in S10.A-D all implicitly assume that the motion of the sliver is accommodated by left-lateral strike-slip faulting. However, there are neither clear evidence of predominant strike-slip earthquakes nor large strike-slip faults like in Sumatra. The largest earthquakes occurred east of the eastern Cordillera are predominantly thrust events, some of them also having a usually small strike-slip component (Figure 3.2 and S3.4). In general, they show slip vectors roughly perpendicular to the strike of the Andean Cordillera. Furthermore, the sites located in the Piura peninsula also show a trench perpendicular component of the order of 3.5mm/yr.

Figure S3.10.E is the same as figure S3.10.D but adding 5% of trench-normal partitioning corresponding to ~3mm/yr trench normal motion. The new velocity field qualitatively fits the main pattern in the Piura peninsula. It further predicts a transpressive regime east of the Andean Cordillera. Nonetheless, it still fails to correctly predict the east-northeastward motion found in the eastern Cordillera. While the existence of additional microblocks could be invoked, we perform a simple test of adding a constant left-lateral shear rate parallel to the trench. This attempt is further supported by the recent map of active faults (*Veloza et al.*, [2011] and references therein) showing that large trench parallel left lateral strike-slip faults are found in the Andean Cordillera from latitudes 9°S to 14°S. Figure S3.10.F now shows the additional constant strain rate equivalent to 20 nstrain/yr (2 mm/yr over 100km) of dextral shear over the entire continental Peru. Adding this parameter now enables to reproduce the east-to-northeastward directed velocity in the eastern Cordillera.

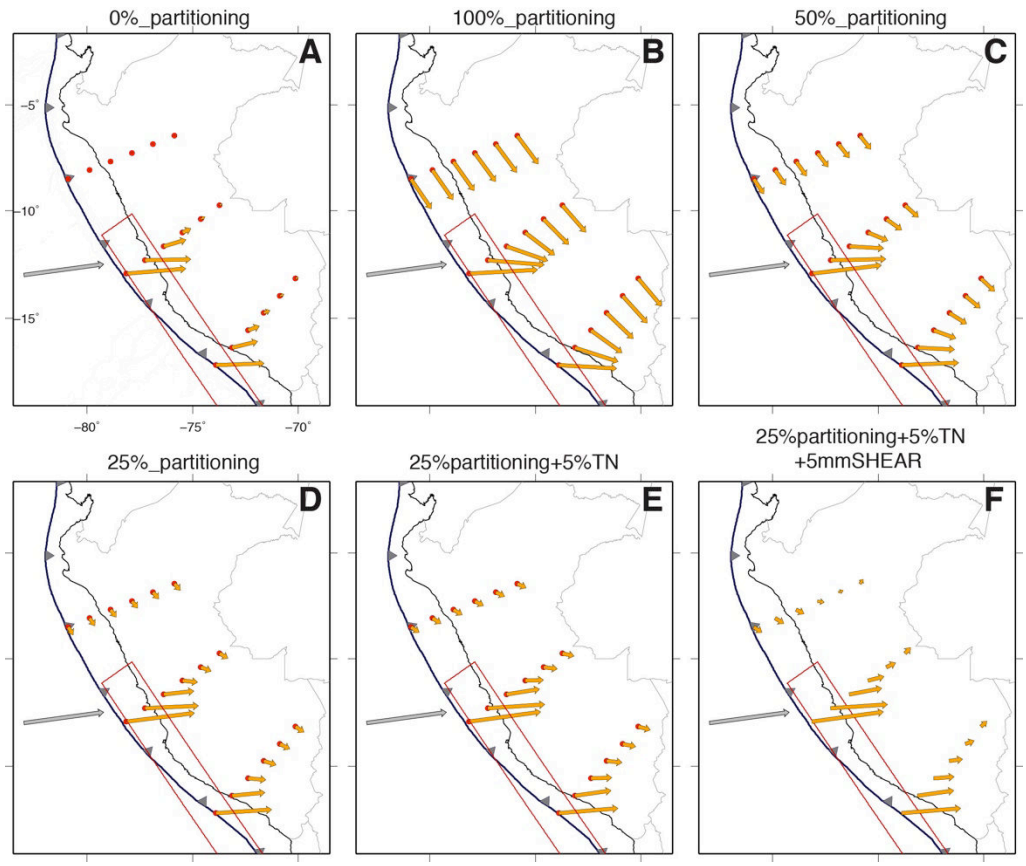

Figure S3.10: Simple forward models exemplifying at the first order the main patterns of the observed GPS velocity field. Different approaches, from model considering 0% of partitioning to partial partitioning plus a component of shear stress are considered (see text for a description).

16. Cumulative deficit of moment and seismic moment released due to major subduction earthquakes

In figure S3.11 we plot Cumulative deficit of moment and seismic moment released due to major subduction earthquakes since the 1746 earthquake in central Peru subduction segment. For that we assume that all the deficit of slip capable of being stored at the plate interface was released by the 1746 event. The cumulative deficit of moment is predicted from the rates for the maximum, mean and minimum models presented in Table 3.4 and Figure 3.8.

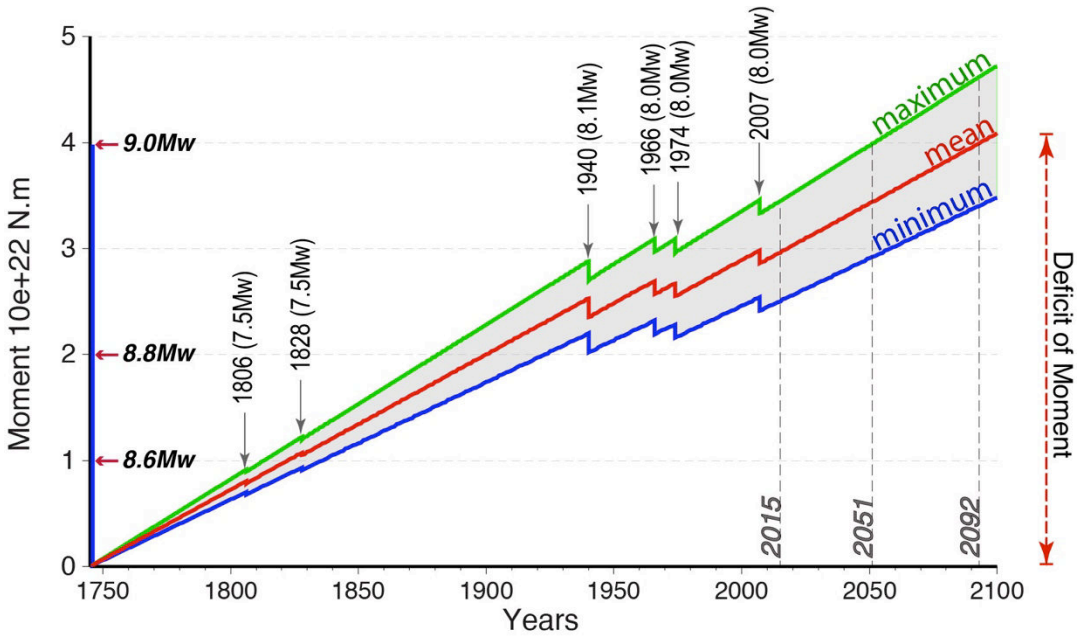

Figure S3.11: The cumulative deficit of moment is predicted from the rates for the maximum, mean and minimum models presented in the main text (Table 3.4 and Figure 3.8). Although this models could be simplistic it reflects at the first order the elastic strain available to drive future earthquakes in the central Peru segment.

17. Correlation of the age of the Nazca oceanic lithosphere and the ISC in Peru

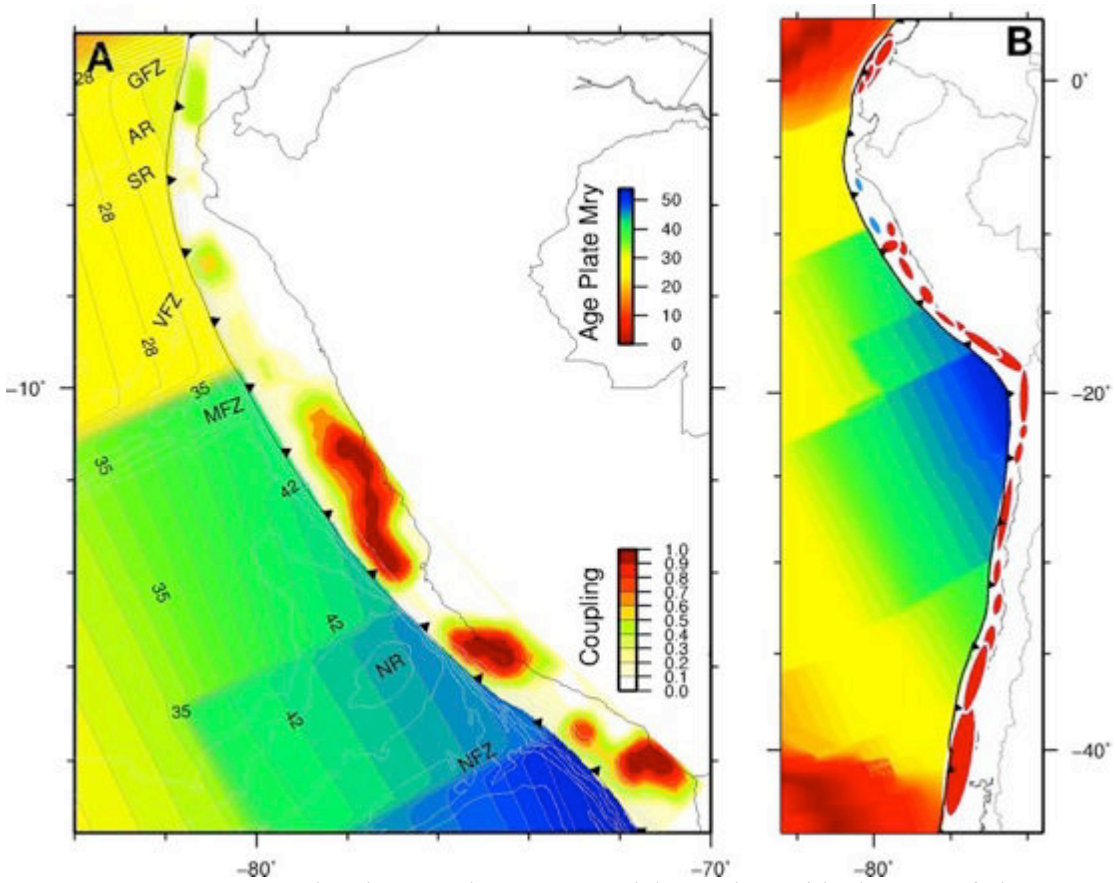

Figure S3.12: A. Map showing our best ISC model together with the age of the Nazca oceanic lithosphere. The age and level of coupling are indicated by the their respective color scales. E. Age of the Nazca lithosphere along the Nazca/South America subduction zone [Müller et al., 2008]. The ellipses indicate the rupture area of large subduction earthquakes (M>7.5) since 1850 as showed in Figs. 1 and 2.

References

Altamimi, Z., L. Métivier, and X. Collilieux (2012), ITRF2008 plate motion model, *J. Geophys. Res.*, *117*(B07402), 1–14, doi:10.1029/2011JB008930.

Bassin, C., G. Laske, and G. Masters (2000), The current limits of resolu- tion for surface wave tomography in North America, *Eos Trans. AGU*, *S12A-03*.

Bevis, M., E. Kendrick, B. Brooks, R. Allmendinger, B. Isacks, and R. Smalley Jr. (2001), On the strength of interplate coupling and the rate of back arc convergence in the central Andes: An analysis of the interseismic velocity field, *Geochemistry Geophys. Geosystems*, *2*(11), doi:10.1029/2001GC000198.

Devlin, S., B. L. Isacks, M. E. Pritchard, W. D. Barnhart, and R. B. Lohman (2012), Depths and focal mechanisms of crustal earthquakes in the central Andes determined from teleseismic waveform analysis and InSAR, *Tectonics*, *31*(TC2002), 1–33, doi:10.1029/2011TC002914.

Feng, L., A. V. Newman, M. Protti, V. González, Y. Jiang, and T. H. Dixon (2012), Active deformation near the Nicoya Peninsula, northwestern Costa Rica, between 1996 and 2010: Interseismic megathrust coupling, *J. Geophys. Res.*, *117*(B6), B06407, doi:10.1029/2012JB009230.

Kendrick, E., M. Bevis, R. Smalley Jr., and B. Brooks (2001), An integrated crustal velocity field for the central Andes, *Geochemistry Geophys. Geosystems*, *2*, 11, doi:10.1029/2001GC000191.

Mccaffrey, R. (2002), Crustal Block Rotations and Plate Coupling, in *Plate boundary zones*, edited by S. Stein and J. Freymueller, pp. 101–122, American Geophysical Union, Washington, D. C.

Nocquet, J.-M., E. Calais, Z. Altamimi, P. Sillard, and C. Boucher (2001), Intraplate deformation in western Europe deduced from an analysis of the International Terrestrial Reference Frame 1997 (ITRF97) velocity field, *J. Geophys. Res. Solid Earth*, *106*(B6), 11239–11257, doi:10.1029/2000JB900410.

Nocquet, J.-M. et al. (2014), Motion of continental slivers and creeping subduction in the northern Andes, *Nat. Geosci.*, *7*(March), 287–291, doi:10.1038/NGEO2099.

Norabuena, E., L. Leffler-griffin, A. Mao, T. Dixon, S. Stein, I. S. Sacks, L. Ocola, and M. Ellis (1998), Space Geodetic Observations of Nazca-South America Convergence Across the Central Andes, *Science (80-.).*, *279*(5349), 358–362, doi:10.1126/science.279.5349.358.

Royden, L. H. (1993), The steady state thermal structure of eroding orogenic belts and accretionary prisms, *J. Geophys. Res.*, *98*(B3), 4487–4507.

Savage, J. C. (1983), A dislocation model of strain accumulation and release at a subduction zone, *J. Geophys. Res. Solid Earth*, *88*(B6), 4984–4996, doi:10.1029/JB088iB06p04984.

Sieh, K., and D. Natawidjaja (2000), Neotectonics of the Sumatran fault, Indonesia, *J. Geophys. Res.*, *105*(B12), 28295, doi:10.1029/2000JB900120.

Valladares, C. E., and J. L. Chau (2012), The Low-Latitude Ionosphere Sensor Network (LISN): Initial Results, *Radio Sci.*, *47*(RS0L17), doi:doi:10.1029/2011RS004978.

Veloza, G., R. Styron, M. Taylor, and A. Mora (2011), Open-source archive of active faults for northwest South America, *Gsa Today*, *22*(10), 4–10, doi:10.1130/GSAT-G156A.1.

Villegas-Lanza, J.-C. (2009), *Proceesing and Analysis of the LISN permanent GPS network: Preliminary Tectonic Results*, Nice-France.

Chapter 4

Anatomy of a seismic swarm synchronous to slow aseismic slip: the northern Peru 2009 sequence

In the two previous chapters we put in evidence that the plate interface in the northern Peru subduction segment shows a weak to low interseismic coupling, suggesting that convergence is mostly accommodated aseismically. This subduction segments is characterized by the occurrence of low to moderate magnitude seismicity (M<6.5) and unusual ~M7.5 tsunami-earthquake events. No information about aseismic processes either swarms or slow slip events were documented before for this region. In this chapter, I present novel observations of a slow slip event associated with synchronous seismicity swarms that took place in 2009 near the Bayovar Peninsula in northern Peru. We perform a detailed analysis of the spatial and temporal evolution of the seismicity swarms and its relationship with the aseismic slip process. We then provide inferences about the anatomy of the plate interface in terms of the frictional properties of the subduction plate interface. The observations that we present here depart from usually observed SSE in other subduction zones. The results obtained in this study are under final edition to be submitted to the journal Nature Geosciences.

Anatomy of a seismic swarm synchronous to slow aseismic slip: the northern Peru 2009 sequence

To be submitted to Nature Geosciences

Juan Carlos Villegas-Lanza[1, 2], Jean-Mathieu Nocquet[2], Frédérique Rolandone[3], Martin Vallée[4], Hernando Tavera[1], Mohamed Chlieh[2]

[1]Instituto Geofísico del Perú, Calle Badajoz 169, Urbanización Mayorazgo IV Etapa, Ate, Lima, Perú.

[2]Geoazur, IRD, Université de Nice Sophia-Antipolis, Observatoire de la Côte d'Azur, CNRS, 250, rue A. Einstein, Valbonne, France.

[3]Institut des Sciences de la Terre de Paris, CNRS UMR 7193, Université Pierre et Marie Curie, Paris, France.

[4]Institut de Physique du globe de Paris, Sorbone Paris Cité, Université Paris Diderot, UMR 7154 CNRS, Paris, France.

Slow Slip Events (SSE) geodetically documented along subduction megathrusts worldwide fall into two categories. Deep (30-50km) events, located at the downdip limit of highly coupled segments tend to show duration of weeks to months and are often accompanied by tremors. Shallow (<25km) events on the contrary last days to weeks and are synchronous to intense micro-seismicity, accounting for less than a few percent of the total moment release. Here, we document a sequence mixing seismic and transient aseismic processes that departs from these two categories. The SSE occurred at shallow (<25km) depth of the northern Peru subduction zone, lasted ~7 months and its equivalent moment release was Mw 6.7. Significant seismicity occurred during that period, accounting for ~30% of the total moment, with 3 plate interface events of Mw 5.8-6.0. The sequence initiated with a foreshocks-mainshock-aftershocks sequence occurring at ~12km depth. It was followed 6 days later by a similar but deeper (~25km) sequence that triggered slow aseismic slip. The rate of aseismic slip eventually suddenly accelerated 39 days later, after a shallow (depth ~8km) Mw 5.8 earthquake, which shows an abnormally long source time function, and no aftershocks. We interpret the entire sequence as stress interactions between isolated velocity-weakening and conditionally stable patches in an overall velocity-strengthening plate interface. In particular, we show that the transient slip can be modeled as the response of a velocity-strengthening interface to small stress changes during the sequence. In overall, the sequence reveals the spatially variable frictional

properties of a weakly coupled plate interface and how area with different friction laws interact in time and space to release stress.

During the past decade, episodic slow slip events (SSE) detected by continuously recording GPS networks in various subduction zones led us to a refined view of the frictional anatomy of the subduction interface and a change of our conceptual model of the earthquake cycle. Modeling of the first SSE [*Dragert et al.*, 2001; *Ozawa et al.*, 2001] revealed that slip events lasting from weeks to months occur at depth of ~40 km, down-dip of the area of high locking, assumed to correspond to the rupture area of large megathrust earthquakes. Although little regular seismicity usually occurred during this type of SSE, non-volcanic tremors were often found during them [*Rogers and Dragert*, 2003]. More recently, SSE detected in shallowly (<20km) coupled subduction zones show duration of days to weeks [*Ozawa et al.*, 2003; *Douglas et al.*, 2005; *Wallace and Beavan*, 2010]. Shallow SSE are usually associated with intense microseismicity burst taking place inside or close to the slip area [*Ozawa et al.*, 2007; *Delahaye et al.*, 2009; *Wallace et al.*, 2012; *Vallée et al.*, 2013], although non-volcanic tremors may also coexist [*Walter et al.*, 2011]. In all cases documented so far, seismicity associated with shallow SSE accounts for at most 1-3% of the total moment released.

Here, we use geodetic and seismological observations (Fig. 4.1 and 4.2) to document a sequence where aseismic and seismic slips interact through time and space and contribute to the final slip at a similar level. The sequence took place offshore the Bayovar peninsula in northern Peru where the oceanic Nazca plate subducts beneath the Inca continental sliver at 59 mm/yr [*Nocquet et al.*, 2014]. GPS interseismic velocities reveal that the northern Peru subduction zone is a weakly coupled subduction segment [*Nocquet et al.*, 2014], explaining the lack of great subduction earthquakes for the last five centuries in that area. Nonetheless, among the few significant earthquakes recorded, the 1960 Mw 7.6 earthquake shares all the characteristics of tsunami earthquakes with abnormally long source duration, enhanced long-period source spectrum and it induced a relatively large tsunami, with run-up exceeding 9m [*Pelayo and Wiens*, 1990].

The 2009 sequence developed north of the assumed rupture of the 1960 tsunami earthquake, possibly overlapping with it. A transient trenchward displacement is seen

at the continuous GPS site BAYO, lasting 7 months from February to September 2009 with a cumulative displacement of 14 mm (Fig. 4.1). Inversion of the slip distribution from 9 geodetic displacements indicates that the main area of slip took place at shallow depth (<25 km), involving a patch of 100 km of diameter (Fig. 4.2f). The maximum slip reached 45-50 mm and the slip distribution is equivalent to a moment release of Mw 6.7. Between February and September 2009, the seismicity recorded by both the National Seismic Network of Peru and a temporary broad band seismometers network showed a sharp increase with 118 events of local magnitude ranging from 2.7 to 6.0, all located inside or close to the slip area. The moment released through earthquakes was equivalent to Mw 6.3, indicating that the process was ~70% aseismic.

The time series at BAYO (Fig. 4.1) further shows that the slip evolved through time with phases of acceleration, which correlate with the occurrence of the major earthquakes, before a final phase of deceleration that lasted five months (Fig. 4.1). The recorded seismicity also shows a spatial and temporal organization related to the occurrence of the major events, followed by a five months period of relative quiescence (Fig. 4.2). In the following, we describe the different phases of the sequence and discuss their implications on the frictional anatomy of the plate interface.

Prior to the sequence, interseismic GPS velocities indicate that the plate interface is predominantly creeping [*Nocquet et al.*, 2014], therefore implying a dominant velocity-strengthening friction regime. The Bayovar area shows regular moderate seismicity, with ~20 interface events in the magnitude range of Mw 5.1-6.0 recorded since 1976 [*Ekström et al.*, 2012]. The occurrence of moderate interface earthquakes indicates the existence of patches of velocity-weakening with typical size of 0.1 to 10 km, but still too small to induce significant strain rate detectable by GPS during the interseismic period.

The sequence studied here started at a depth of ~12 km, ~30 km from the trench. On February 8 2009, a series of five foreshocks (Mw 3.2 to 5.0) preceded 20 hours to 30 min, a Mw 5.9 thrust interface event that occurred on February 9. 14 aftershocks (Mw 3.5 to 4.2), clustered within 15km of the epicenter, were detected in the four days following the mainshock (Fig. 4.2a). Because the seismic sub-sequence took

place about ~100km from the Peruvian coast, we could not observe whether it was associated with a slow aseismic slip or not.

The seismic and possible aseismic slip seem to have increased the stress ~100km northeast to promote the second seismic sub-sequence at the deeper (~20-25km depth) part of the subduction interface. The main thrust event Mw 6.0 occurred on February 15. It was preceded by 8 foreshocks (Mw 3.2 to 4.7) within 30 hours to 10 min before the mainshock. 48 aftershocks with Mw 3.0-4.3 occurred during the following five weeks (Fig. 4.2b). Both the February 9 and 15 events showed aftershocks location within a ~15 km radius around the epicenter and in agreement with the rupture size for Mw~5.9-6.0 earthquakes. For both sequences, no clear aseismic slip is seen in the GPS time series prior to the mainshock, indicating that if it existed, it was small. By contrast, the GPS time series at BAYO shows a sudden velocity increase following a 2mm coseismic displacement with a trenchward motion of ~4 mm during the next 39 days (Fig. 4.1).

The next event (March 26, Mw 5.8) occurred at shallow (~8 km) depth, close to the trench. Its characteristics depart from the two previous events, with neither foreshocks nor clear sequence of spatially and timely clustered aftershocks. The seismicity in the next 5 months occurred over a wide area, at a rate not significantly different from the background seismicity prior to the sequence (Fig. 4.2c, d). Furthermore, the March 26 event significantly accelerated the rate of aseismic slip as seen in the BAYO GPS time series (Fig. 4.1). The transient displacement following the March 26 earthquake represents about 70% of the cumulated displacement observed at site BAYO, despite a magnitude about twice smaller than the February 15 event and it remote location. We further find that the March 26 earthquake had a duration of 11-12s for a moment magnitude of Mw 5.8, to be compared with the 10s duration for the Mw 6.0 February 15 event (Fig. 4.3). Fig. 4.3 shows that several abnormally long source duration earthquakes have occurred in northern Peru during the last two decades. Among them, the 2002 event exactly occurred in the area of the 2009 sequence and the 1996 event that occurred further source generated a tsunami with run-ups ranging from 1 to 5 m [*Ihmlé et al.*, 1998, *Bourgois et al.*, 1997]. If scaled by its magnitude, the March 26 event is similar to abnormal long source duration earthquakes previously highlighted in northern Peru from a larger seismicity catalogue analysis [*Bilek and Lay*, 2002].

We interpret the differences between this earthquake and the two February events by the spatially variable frictional properties of the plate interface. Both February events broke small velocity-weakening patches and share scaling laws of regular earthquakes for rupture duration, aftershocks decay and rupture area. The March 26 event occurred in the weak, low rigidity material within the accretionary prism, which promotes slow rupture and long duration of the source. This event occurred within the conditionally stable zone where slip is generally stable, but can be abrupt if it experiences significant rapid loading [*Bilek and Lay*, 2002].

The logarithmic-like displacement observed in the GPS time series after the February 15 and March 26 earthquakes is similar to the post-seismic deformation observed after many earthquakes (e.g., *Perfettini et al.*, [2010]). Within the rate-and-state friction law framework [*Dieterich*, 1979], a sudden stress increment associated with a co-seismic slip leads to an instantaneous increase of the sliding velocity in the nearby velocity-strengthening areas, then decreasing through time at a logarithmic decay. In Fig. 4.1, we show that the transient displacement observed at BAYO time series can be fitted by the prediction of a simple spring-slider model with a velocity-strengthening law. Because the stress increment induced by the co-seismic slip scales with the logarithm of the velocity increment, we find that the March 26 earthquake should have generated a Coulomb stress increment at least 5 times larger than that of the February 15 earthquake, despite a 2 times smaller moment. This further suggests that the March 26 earthquake had an abnormal large slip given its magnitude estimated from the seismic waves, as proposed by tsunami earthquakes.

Finally, a crustal Mw 5.3 event on August 27 marks the end of the sequence (Fig. 4.1 and 4.2e). Its normal focal mechanism indicates that the stress previously released was large enough to reach an extensional regime in the upper plate and to reactivate a normal fault.

In overall, the 2009 northern Peru sequence shows how the frictional properties control the response of the subduction interface to stress changes. The plate interface in northern Peru can be seen as a predominantly velocity-strengthening medium, comprising small localized patches of velocity weakening and conditionally stable local patches in the shallowest part of the interface close to the trench (Fig. 4.4). Small pulses of aseismic slips can lead to the destabilization of ~10km large velocity

weakening patches leading them to seismic ruptures. Although small, the stress increment is large enough to destabilize areas as remote as ~100km, the typical distance observed here between the three sub-sequences. In turn, the co-seismic stress increment trigger pulses of aseismic slip, similar to the afterslip following large earthquakes. Finally, the aseismic slip was strong and rapid enough to lead to the rupture of a small patch in the shallow conditionally stable zone. This latter earthquake shares most characteristics of tsunami earthquakes with a long rupture duration, large slip given its magnitude and a lack of aftershocks. As previously suggested, transients may serve as a mechanism of stress communication between distant seismicity clusters in shallow subduction zones [*Liu and Rice*, 2007], and therefore might be precursory signal to forthcoming seismic ruptures. The conditions in terms of size, amount of slip and possibly slip velocity of aseismic slip required to destabilize large patches of velocity-weakening have yet to be determined.

Figures

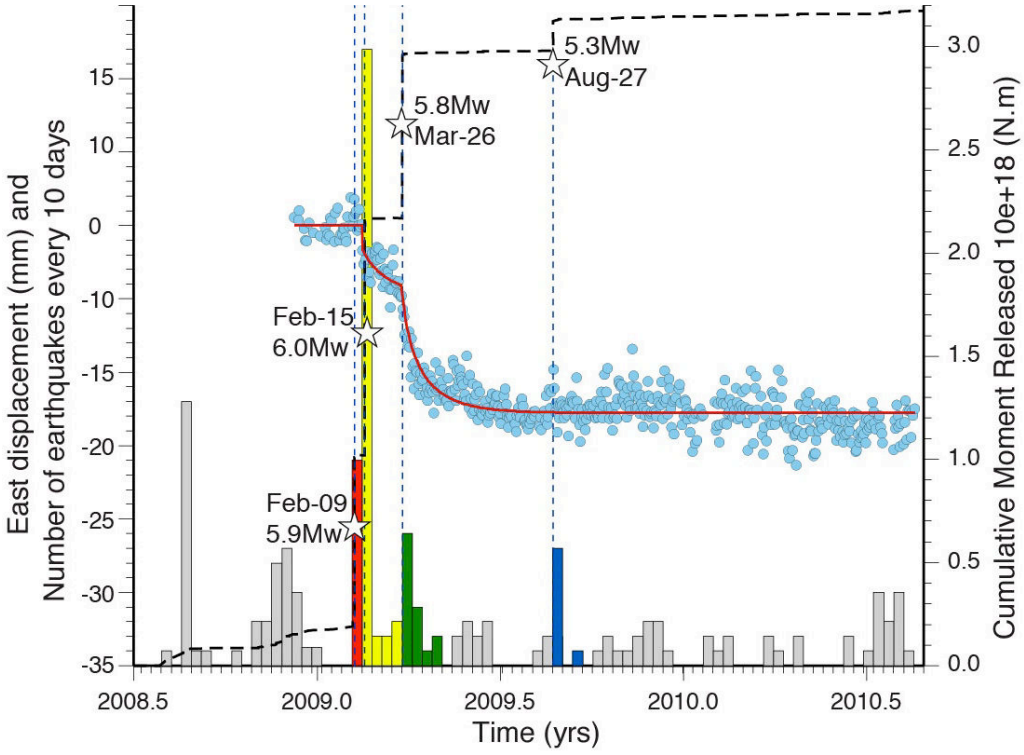

Figure 4.1. Geodetic time series and seismicity rate from 2008.5 to 2010.65. Blue dots indicate the east displacement recorded by the CGPS BAYO expressed with respect to the overriding plate. Histogram bars show the number of seismic events in 10 days intervals and the colors correspond to the time periods of the seismic sub-sequences shown in Figure 4.2.

The white stars show the date of the four main earthquakes. The cumulated seismic moment released is shown in black dashed line. The red curve overprinting the GPS time series is the prediction from a simple spring-slider model with a velocity-strengthening friction law.

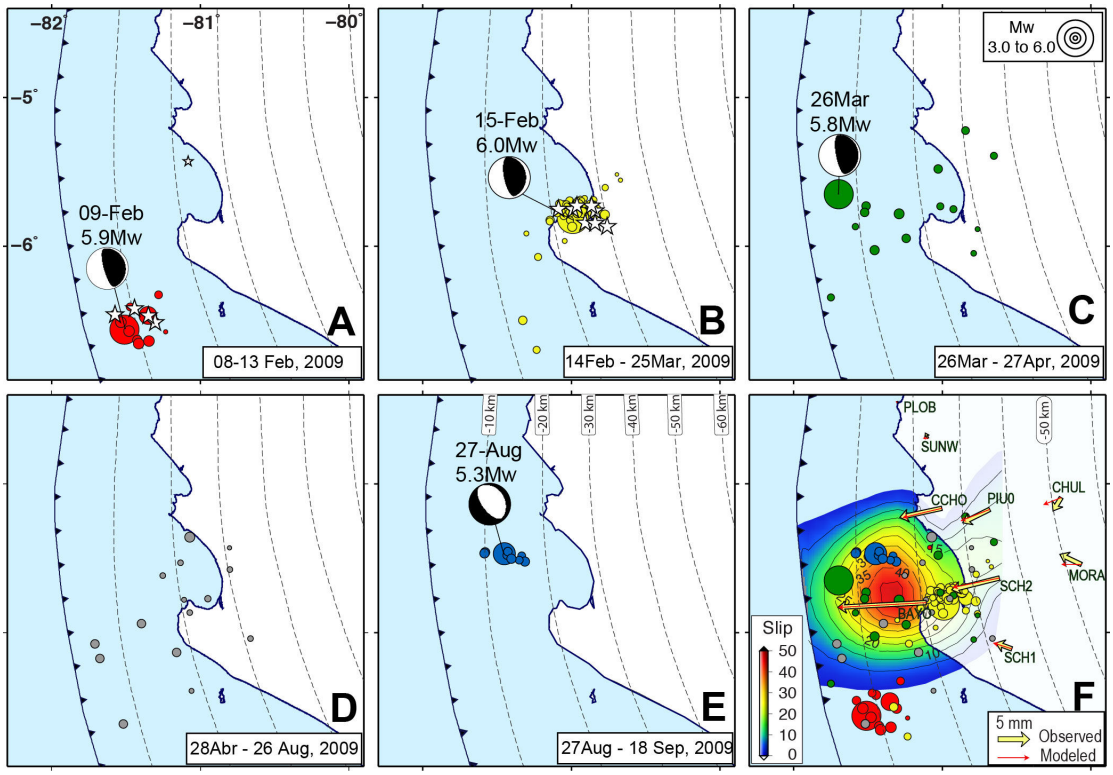

Figure 4.2. Seismicity maps and cumulated slip during the sequence. **2a-2e**: Snapshots of the spatio-temporal distribution of the seismicity. Circles scaled to magnitude show the location of the earthquakes. Focal mechanism and magnitude for the four largest events are displayed. White stars represent foreshocks. Colors of the seismicity are the same as in Fig. 1. Light gray dash lines are iso-depths of the subduction interface. **2f:** Slip distribution of the total cumulative displacement. Colors represent the slip amplitude with numbers along the concentric lines indicating isovalues of slip in mm. Yellow and red arrows are observed and modeled GPS displacements respectively.

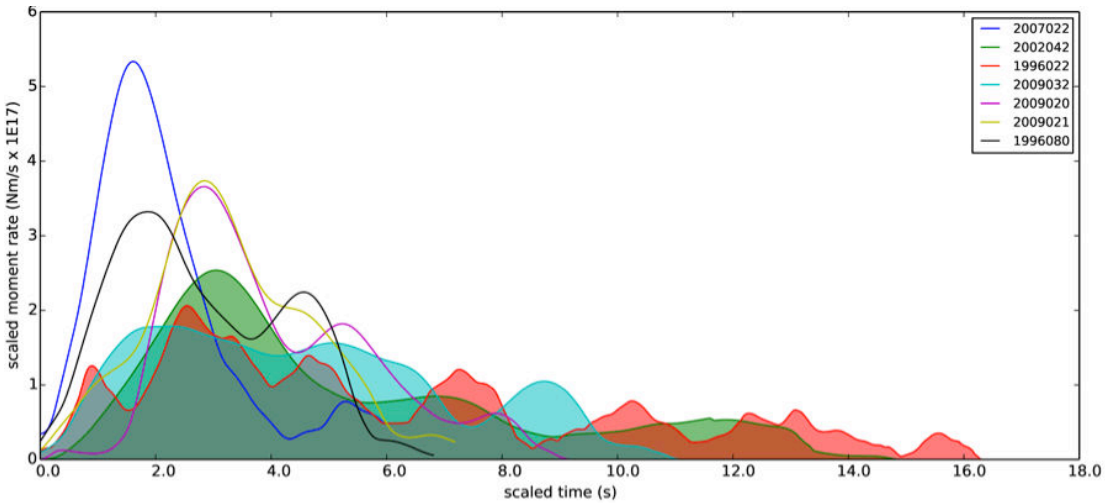

Figure 4.3. Source Time Function (STF) comparison for shallow interface earthquakes in northern Peru. Abnormally long STF are shown filled colors between the curve and the x-axis. The 2002 abnormally long earthquake occurred in the same area as the 2009 sequence.

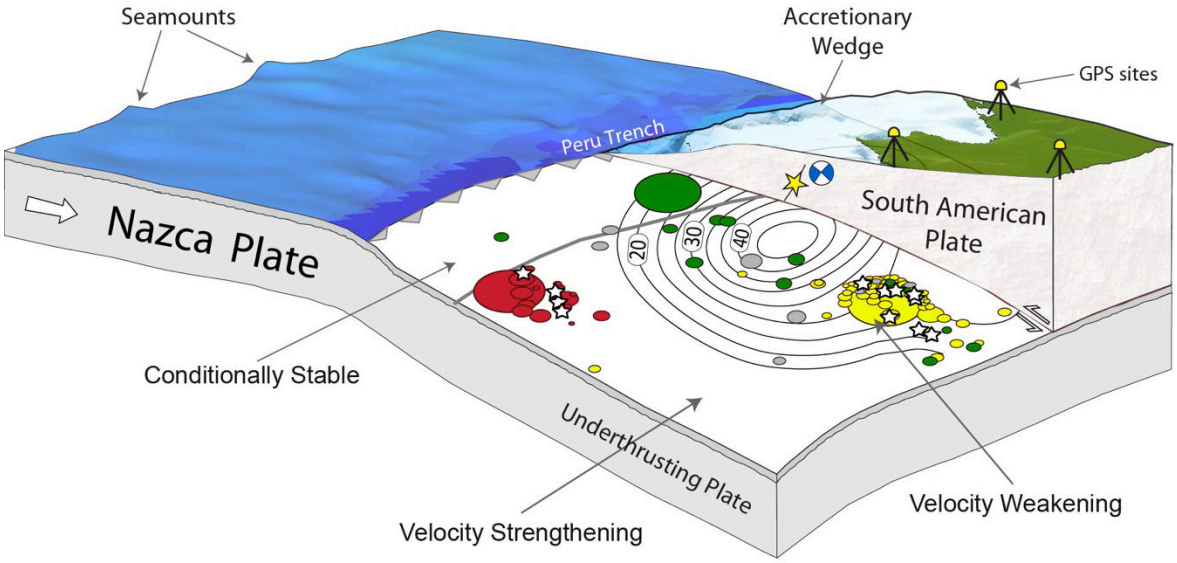

Figure 4.4. Cartoon illustrating the spatially variable frictional properties of the subduction interface in the Bayovar area. The plate interface is predominantly velocity-strengthening with small localized patches of velocity weakening and a conditionally stable friction region in the shallowest part of the interface close to the trench.

References

Bilek, S. L., and T. Lay (2002), Tsunami earthquakes possibly widespread manifestations of frictional conditional stability, *Geophys. Res. Lett.*, *29*(14), 1–4, doi:10.1029/2002GL015215.

Delahaye, E. J., J. Townend, M. E. Reyners, and G. Rogers (2009), Microseismicity but no tremor accompanying slow slip in the Hikurangi subduction zone , New Zealand, *Earth Planet. Sci. Lett.*, *277*, 21–28, doi:10.1016/j.epsl.2008.09.038.

Dieterich, J. H. (1979), Modeling of Rock Friction Experimental Results and Constitutive Equations, *J. Geophys. Res.*, *84*(B5), 2161–2168.

Douglas, A., J. Beavan, L. Wallace, and J. Townend (2005), Slow slip on the northern Hikurangi subduction interface, New Zealand, *Geophys. Res. Lett.*, *32*(L16305), 1–4, doi:10.1029/2005GL023607.

Dragert, H., K. Wang, and T. S. James (2001), A Silent Slip Event on the deeper Cascadia subduction interface, *Science (80-.).*, *292*(5521), 1525–8, doi:10.1126/science.1060152.

Ekström, G., M. Nettles, and A. M. Dziewonski (2012), The global CMT project 2004–2010: Centroid-moment tensors for 13,017 earthquakes, *Phys. Earth Planet. Inter.*, *201*, 1–9.

Liu, Y., and J. R. Rice (2007), Spontaneous and triggered aseismic deformation transients in a subduction fault model, *J. Geophys. Res.*, *112*(B9), 1–23, doi:10.1029/2007JB004930.

Nocquet, J.-M. et al. (2014), Motion of continental slivers and creeping subduction in the northern Andes, *Nat. Geosci.*, *7*(March), 287–291, doi:10.1038/NGEO2099.

Ozawa, S., M. Murakami, and T. Tada (2001), Time-dependent inversion study of the slow thrust event in the Nankai trough subduction zone, southwestern Japan, *J. Geophys. Res.*, *106*(B1), 787–802, doi:2000JB900317.

Ozawa, S., S. Miyazaki, Y. Hatanaka, T. Imakiire, M. Kaidzu, and M. Murakami (2003), Characteristic silent earthquakes in the eastern part of the Boso peninsula, Central Japan, *Geophys. Res. Lett.*, *30*(6), 16–19, doi:10.1029/2002GL016665.

Ozawa, S., H. Suito, and M. Tobita (2007), Occurrence of quasi-periodic slow-slip off the east coast of the Boso peninsula, Central Japan, *Earth Planets Sp.*, *59*, 1241-1245.

Pelayo, A. M., and D. A. Wiens (1990), The November 20, 1960 Peru Tsunami Earthquake: Souce Mechanism of a Slow Event, *Geophys. Res. Lett.*, *17*(6), 661–664, doi:10.1029/GL017i006p00661.

Perfettini, H. et al. (2010), Seismic and aseismic slip on the Central Peru megathrust, *Nature*, *465*(7294), 78–81, doi:10.1038/nature09062.

Rogers, G., and H. Dragert (2003), Episodic tremor and slip on the Cascadia subduction zone: the chatter of silent slip., *Science (80-.).*, *300*(5627), 1942–3, doi:10.1126/science.1084783.

Vallée, M. et al. (2013), Intense interface seismicity triggered by a shallow slow slip event in the Central Ecuador subduction zone, *J. Geophys. Res.*, *118*(6), 2965–2981, doi:10.1002/jgrb.50216.

Wallace, L. M., and J. Beavan (2010), Diverse slow slip behavior at the Hikurangi subduction margin , New Zealand, *J. Geophys. Res.*, *115*(B12402), doi:10.1029/2010JB007717.

Wallace, L. M., J. Beavan, S. Bannister, and C. Williams (2012), Simultaneous long-term and short-term slow slip events at the Hikurangi subduction margin, New Zealand: Implications for processes that control slow slip event occurrence, duration, and migration, *J. Geophys. Res.*, *117*(B11), B11402, doi:10.1029/2012JB009489.

Walter, J. I., S. Y. Schwartz, J. M. Protti, and V. Gonzalez (2011), Persistent tremor within the northern Costa Rica seismogenic zone, *Geophys. Res. Lett.*, *38*(1), 1–5, doi:10.1029/2010GL045586.

Acknowledgments:

This work has been financially supported by the Agence Nationale de la Recherche (ANR; contract number ANR-07-BLAN-0143-01) and has continuously been supported by the Institut de Recherche pour le Développement (IRD). JCVL acknowledges support provided by the IRD-DSF from France for his PhD grant.

Supplementary information

Anatomy of a seismic swarm synchronous to slow aseismic slip: the northern Peru 2009 sequence

Juan Carlos Villegas-Lanza[1, 2], Jean-Mathieu Nocquet[2], Frédérique Rolandone[3], Martin Vallée[4], Hernando Tavera[1], Mohamed Chlieh[2]

[1]Instituto Geofísico del Perú, Calle Badajoz 169, Urbanización Mayorazgo IV Etapa, Ate, Lima, Perú.

[2]Geoazur, IRD, Université de Nice Sophia-Antipolis, Observatoire de la Côte d'Azur, CNRS, 250, rue A. Einstein, Valbonne, France.

[3]Institut des Sciences de la Terre de Paris, CNRS UMR 7193, Université Pierre et Marie Curie, Paris, France.

[4]Institut de Physique du globe de Paris, Sorbone Paris Cité, Université Paris Diderot, UMR 7154 CNRS, Paris, France.

GPS analysis and aseismic slip inversion

The data set includes 1 continuous GPS (CGPS) station BAYO installed in July 2008 in the framework of the ADN project as collaboration between Geoazur (CNRS-IRD-OCA-University of Nice, France) and the Institute of Geophysics, Lima, Peru. It also includes 1 CGPS station PIUR from the Low Latitude Ionospheric Sensor Network (LISN). 7 campaign sites were measured in July 2008, 2010 and 2012 with some additional measurements in early 2009 and mid 2011 for PSAL, SCH1 and SCH2 sites. Data have been analyzed with the GAMIT/GLOBK software, using a standard strategy for Geodynamics as detailed in *Nocquet et al., [2014]*. No elastic effect of interplate coupling along the subduction interface is detected along the Bayovar Peninsula, however a sliver motion was highlighted *[Nocquet et al., 2014]*. Therefore the GPS velocities are expressed with respect to this Inca Sliver (Euler pole at long. -63.8°E, lat. 22.5°N, angular velocity: 0.092 deg/Myr) *[Nocquet et al., 2014]*, relevant to monitor the displacement induced by the SSE.

The input data set for the inversion includes transient trenchward displacements estimated at 7 SGPS between February and September 2009 together with the

cumulated displacement at CGPS sites BAYO and PIUR estimated from the time series for the same period. We invert the slip distribution therefore corresponding to the total displacement over the whole SSE. The modeled fault surface is discretized in 354 rectangular subfaults of 10x10 km, covering about 250 km along strike of the trench and ending at 60 km depth. We calculate the transfer function *G* relating the unit slip of each individual subfaults to the displacement components at each individual GPS site, using the dislocation formulation of *Okada [1992]* for an homogeneous semi-infinite elastic half-space, and using a rake fixed to 90°. Our inversion scheme follows the approach recently described *in Radiguet et al., [2011]*, following *Tarantola [2005]*, where we minimize the cost function S(m) defined as:

$$S(m) = \frac{1}{2}\left[(Gm - d)^t C_d^{-1} (Gm - d) + (m - m_0)^t C_m^{-1} (m - m_0)\right] \quad (1)$$

where m is the unknown parameter model including the slip for each subfault, m_0 is an a priori model for slip distribution taken here as 0, d is the vector of observation including the GPS velocity components, and C_d and C_m are the variance-covariance matrices associated with the data and the model respectively. C_d is taken as a diagonal matrix including the standard deviation derived from the geodetic analysis. C_m is an exponential matrix of the form:

$$Cm(i,j) = \left(\sigma_m \frac{\lambda}{\lambda_0}\right)^2 exp\left(-\frac{d(i,j)}{\lambda}\right) \quad (2)$$

where $d(i,j)$ is the distance between two subfaults i and j, l is the critical distance for correlation for slip, and l_0 a scaling factor fixed at 10 km. We show the results obtained for $l=50$ *km,* which is found to be a good trade-off value between the roughness of the model and the misfit to the observed GPS velocity.

The model finds that a single nearly circular patch with a diameter of 100 km, and a center located offshore 20 km northwest of BAYO explains the data with a

WRMS=0.5 mm. 45-50 mm of maximum slip is found. In order to assess the resolution of our inversion, we perform a simple test by modeling the slip distribution as a 2-D Gaussian function in the form

$$s(\lambda,\varphi) = e\ x\ p\ \left[-R_t^2\left(\frac{cos^2\varphi_0(\lambda-\lambda_0)^2}{D_\lambda^2}+\frac{(\varphi-\varphi_0)^2}{D_\varphi^2}\right)\right] \quad (3)$$

and search for the possible range of values of maximum slip S_{max}, location of the maximum slip (l, f). We find that the latitude and along-strike extension of the slip area is well defined (latitude 5.7°S and 45 < *Df* < 50 km). The along-strike extension of slip distribution is constrained by the southwards component of displacement observed for the sites north of Bayovar and northwards component at SCH1. On the contrary, there are some trade-offs between the longitude location of the maximum slip, the extent of slip in longitude (that is with depth) and to a less extent the maximum slip. Extreme range of possible values are (-81.7°E, 105 km, 46 mm) and (-81.3°E, 55 km, 44 mm). In other words, because GPS sites are located only east of the slip area, we only have good constraints on the downdip limit of the slip distribution and relatively poor constraints on the up-dip limit. Our inversion and the simple sensitivity test however demonstrate that the main area of slip occurred at shallow depth (<20 km) with no significant amount of slip deeper than 25 km. Whether some significant slip occurred at very shallow depth close to the trench cannot be constrained by the GPS data. The along strike distribution of the slip is well constrained with no significant slip occurring north of 4.6°S. The southern limit is found to be ~6.5°S, but again a southern extension of the slip close to the trench cannot be ruled out. The amount of maximum slip is well defined [45-50 mm] as well as the geodetic moment Mw=6.7.

Supplementary Table T4.1. SSE GPS displacements. Latitude and longitude in decimal degrees. Dn, De: north & east components of displacement in mm; s_n, s_e: formal error (1-sigma confidence level), Corr_ne: correlation coefficient between Dn & De.

GPS site	Lat	Long	Dn	De	σ_n	σ_e	Corr_ne
CCHO	-80.962	-5.166	-1.44	-6.68	0.81	1.00	-0.01

CHUL	-80.158	-5.092	-2.10	-1.28	0.79	1.01	-0.02
MORA	-80.022	-5.544	1.62	-3.42	0.88	1.19	-0.02
PIU0	-80.639	-5.171	-2.14	-4.32	0.60	0.79	-0.02
PLOB	-81.289	-4.453	0.18	0.12	0.74	0.91	-0.02
SCH1	-80.491	-6.112	0.94	-2.56	0.99	1.27	-0.03
SCH2	-80.575	-5.635	-1.88	-7.58	0.89	1.15	-0.03
SUNW	-81.055	-4.693	0.82	-0.42	0.85	1.08	-0.07
BAYO	-81.066	-5.799	-0.75	-14.02	0.39	0.50	-0.05

Relocation of the seismicity

We use the earthquake catalog from the Geophysical Institute of Peru (IGP) for the period 2008 to 2011. We analyze the seismogram records from five seismic stations of the National Seismic Network of IGP located at a distance ranging from 70 to 160 km from the Bayovar Peninsula. For the larger events, seismogram recorded at broadband seismic stations located at greater distances up to 500 km were also used. In order to better characterize the seismicity variations in the area of the SSE (Lat. -5.2 to 7.0, Long. -82.0 to 80.6) we manually re-measure the P and S-wave arrival times and the duration of the events. We use a modified version of the Hypoinverse algorithm *[Klein, 1978]* and a velocity model from *Tavera et al., [2006]*. We retain each event with a minimum of 4 P and S-wave arrival times. The average rms residual time in the inversion are ~0.5s, and formal errors of 5 and 8 km for the horizontal and depth, respectively. The magnitude for each event has been computed with the record duration of the earthquakes, using the relation proposed by *Ccallo et al., [2002]* that correlates the duration of the seismic signal records and the distance epicenter-station for all the short-period stations of the IGP seismic network. Then in a second step, we use the Velest algorithm *[Kisling, 1995]* to simultaneously derive an improved 1-D velocity model and obtain new hypocentral locations. The obtained new model introduces a new shallow layer and reduces slightly the velocity of the deeper layers, compared to the initial model. The new average rms is ~0.2s, and formal error locations are ~3km and ~5km, for the horizontal location and depth respectively. The relocated seismicity in the area of the SSE has magnitude ranging between 2.9 and 6.0Mw.

Supplementary Table T4.2. Relocated earthquake catalog of the seismicity swarms sequence. The events are illustrated in Figures 4.1, 4.2 and 4.4. The catalog parameters are date, time, longitude, latitude and depth with their corresponding errors and moment magnitude.

date	time	longitude	err_lo	latitude	err_la	depth	err_z	Mw
2009/02/08	18:23:57	-81.3174	±04	-6.5221	±03	19	±05	4.1
2009/02/08	21:23:06	-81.3623	±04	-6.4765	±03	11	±04	4.9
2009/02/09	07:30:35	-81.0941	±03	-5.4412	±01	23	±08	3.2
2009/02/09	13:39:37	-81.4558	±01	-6.4307	±01	15	±01	4.0
2009/02/09	13:46:05	-81.5874	±04	-6.4707	±04	12	±05	3.9
2009/02/09	14:08:57	-81.5208	±02	-6.5817	±02	12	±03	5.9
2009/02/09	14:47:54	-81.2905	±03	-6.3384	±02	26	±03	3.8
2009/02/09	15:34:40	-81.2428	±04	-6.5868	±04	8	±07	3.1
2009/02/09	17:04:08	-81.4895	±04	-6.5825	±03	8	±04	4.2
2009/02/09	19:57:02	-81.4827	±04	-6.4207	±03	13	±03	3.8
2009/02/10	06:48:21	-81.5445	±04	-6.5235	±04	14	±07	4.2
2009/02/11	01:38:04	-81.4337	±03	-6.6411	±03	15	±06	4.0
2009/02/11	03:15:41	-81.4258	±03	-6.6666	±02	12	±05	4.2
2009/02/11	03:25:20	-81.3568	±03	-6.6481	±02	7	±04	4.2
2009/02/14	05:24:56	-80.8415	±02	-5.7670	±02	26	±03	4.6
2009/02/14	05:30:48	-80.9097	±04	-5.8482	±04	30	±07	3.2
2009/02/14	06:37:50	-80.7623	±01	-5.8715	±03	28	±01	3.6
2009/02/15	04:41:57	-80.8662	±03	-5.7324	±02	22	±04	4.0
2009/02/15	06:09:09	-80.8426	±03	-5.8499	±03	23	±04	3.7
2009/02/15	09:13:50	-80.9905	±04	-5.7576	±02	20	±03	3.5
2009/02/15	09:18:03	-81.0893	±03	-5.7544	±02	21	±01	3.7
2009/02/15	10:03:04	-80.9649	±04	-5.7316	±03	25	±04	3.2
2009/02/15	10:04:47	-80.9890	±04	-5.8083	±02	24	±02	6.0
2009/02/15	10:09:53	-80.8510	±01	-5.6907	±01	9	±02	3.7
2009/02/15	10:11:23	-80.8673	±03	-5.7246	±03	15	±05	4.2
2009/02/15	10:16:31	-80.7753	±02	-5.7881	±01	23	±04	4.0
2009/02/15	10:19:24	-81.0060	±03	-5.7781	±02	21	±02	3.7
2009/02/15	10:26:55	-80.9891	±04	-5.7156	±04	21	±04	3.9
2009/02/15	10:36:05	-81.0160	±02	-5.7705	±01	23	±01	3.6
2009/02/15	10:37:53	-81.0126	±01	-5.6936	±00	23	±00	3.8
2009/02/15	10:48:19	-81.0096	±02	-5.8263	±02	22	±01	3.7
2009/02/15	11:07:21	-80.9777	±04	-5.7368	±04	23	±03	3.7
2009/02/15	11:27:25	-81.0951	±02	-5.7779	±03	21	±01	3.7
2009/02/15	11:36:40	-81.0531	±02	-5.7977	±03	23	±01	3.7
2009/02/15	12:06:38	-80.9400	±00	-5.6828	±00	22	±00	3.5
2009/02/15	12:37:54	-80.9429	±03	-5.7314	±02	26	±06	3.5
2009/02/15	13:02:45	-80.9593	±02	-5.6894	±02	24	±01	3.5
2009/02/15	13:47:53	-81.1435	±03	-5.8263	±02	21	±02	3.9
2009/02/15	15:51:32	-80.9952	±03	-5.7474	±02	23	±02	3.8
2009/02/15	16:45:20	-81.0441	±04	-5.7193	±02	21	±02	3.8
2009/02/15	16:48:18	-80.9671	±04	-5.7353	±02	27	±03	3.6
2009/02/15	18:09:39	-80.9710	±02	-5.7614	±01	20	±02	4.0
2009/02/15	19:07:52	-80.8460	±01	-5.7216	±01	9	±02	3.6
2009/02/15	20:09:32	-80.9165	±02	-5.7156	±01	24	±02	3.7
2009/02/15	22:11:52	-80.7718	±04	-5.6051	±04	15	±00	3.6
2009/02/15	23:44:54	-80.9104	±01	-5.6771	±01	27	±02	3.5
2009/02/16	00:41:14	-81.0778	±04	-5.7159	±02	22	±02	3.9
2009/02/16	01:04:38	-81.3029	±02	-5.9146	±01	18	±01	3.3
2009/02/16	05:15:12	-80.9958	±03	-5.8683	±01	24	±02	4.0
2009/02/16	10:06:17	-80.9252	±01	-5.7740	±01	24	±02	4.1
2009/02/17	16:45:50	-81.0340	±04	-5.7207	±04	23	±03	3.8
2009/02/18	06:05:19	-81.0447	±02	-5.9661	±03	16	±02	3.3
2009/02/18	06:43:26	-81.3282	±04	-6.4992	±04	9	±05	3.9
2009/02/19	09:27:26	-80.9312	±00	-5.6911	±00	26	±00	3.4
2009/02/19	12:36:43	-81.0296	±04	-5.7290	±02	24	±02	3.5
2009/02/22	01:01:25	-81.2243	±03	-6.0732	±02	21	±03	3.7
2009/02/24	11:57:54	-81.0633	±04	-5.7645	±03	23	±02	3.6
2009/03/02	08:33:29	-80.6946	±01	-5.5181	±01	24	±06	2.9
2009/03/09	19:18:19	-80.9577	±01	-5.7804	±01	25	±00	3.9
2009/03/15	03:41:07	-80.9474	±02	-5.7135	±02	22	±07	3.8
2009/03/22	22:09:17	-81.2332	±04	-6.6976	±04	15	±02	3.7
2009/03/23	13:38:36	-80.6692	±00	-5.5562	±00	30	±00	3.2
2009/03/24	06:02:31	-81.1444	±03	-5.8345	±03	15	±03	3.7
2009/03/26	17:35:09	-81.7065	±03	-5.6628	±03	8	±05	5.8
2009/03/26	18:50:18	-81.4651	±03	-6.0388	±03	6	±05	4.0

2009/03/26	21:12:14	-81.5957	±03	-5.8821	±03	9	±05	3.6
2009/03/27	21:34:57	-81.2518	±03	-5.9604	±03	17	±05	3.9
2009/03/28	06:21:24	-81.3009	±03	-5.7943	±03	16	±05	4.1
2009/03/28	14:40:01	-80.8543	±03	-5.2342	±03	19	±05	3.8
2009/03/30	06:30:28	-81.5231	±03	-5.7414	±03	10	±05	3.9
2009/03/31	09:11:56	-81.5321	±03	-5.7848	±03	11	±05	3.9
2009/04/05	09:56:53	-80.7978	±03	-6.0611	±03	28	±05	3.5
2009/04/05	10:30:43	-81.0223	±03	-5.7442	±03	16	±01	3.7
2009/04/07	07:21:40	-80.9345	±02	-5.7633	±02	29	±02	3.7
2009/04/07	19:14:43	-81.0368	±03	-5.4943	±01	22	±02	3.9
2009/04/16	03:06:06	-80.7713	±01	-5.8974	±02	26	±02	3.3
2009/04/25	06:40:51	-80.6614	±01	-5.4046	±01	32	±05	3.7
2009/04/27	02:58:17	-81.7602	±04	-6.3577	±04	8	±06	3.7
2009/05/19	18:42:53	-80.6635	±01	-6.0404	±02	34	±22	3.5
2009/05/22	11:59:24	-81.3968	±03	-5.9404	±04	17	±03	3.9
2009/05/30	10:00:07	-81.2537	±03	-5.6178	±02	21	±00	3.5
2009/05/31	00:58:51	-81.7093	±01	-6.0763	±04	9	±01	3.9
2009/06/02	05:26:12	-81.1102	±04	-5.7805	±03	24	±02	3.3
2009/06/04	07:37:14	-81.0713	±04	-5.8657	±03	21	±03	3.5
2009/06/12	23:05:27	-80.8014	±03	-5.5770	±03	32	±05	3.5
2009/06/15	00:13:48	-80.8046	±03	-5.4308	±03	28	±05	3.2
2009/06/15	10:18:07	-81.1337	±03	-5.5326	±03	26	±05	3.4
2009/06/15	10:30:08	-81.0723	±03	-5.3585	±03	23	±05	4.1
2009/08/06	20:09:19	-81.1599	±03	-6.1359	±03	17	±05	3.9
2009/08/15	02:05:50	-81.6753	±03	-6.1758	±03	16	±05	3.9
2009/08/21	19:26:47	-81.0597	±03	-6.3931	±03	23	±05	3.3
2009/08/24	06:41:40	-80.9495	±03	-5.7739	±01	18	±04	3.6
2009/08/24	08:53:28	-81.5189	±04	-6.6160	±03	14	±06	3.9
2009/08/27	14:56:36	-81.4504	±04	-5.4695	±02	11	±02	5.3
2009/08/27	15:31:38	-81.3338	±04	-5.4834	±01	12	±01	3.8
2009/08/27	15:33:58	-81.3136	±04	-5.5218	±01	19	±02	4.0
2009/08/27	15:52:18	-81.4317	±03	-5.4792	±01	13	±01	3.9
2009/08/28	01:43:06	-81.4285	±01	-5.4549	±00	11	±01	3.9
2009/08/30	08:01:04	-81.3511	±04	-5.5132	±02	26	±03	3.8
2009/08/30	11:29:37	-81.5802	±04	-5.4592	±03	11	±03	4.0
2009/08/30	16:24:42	-81.4029	±04	-5.5025	±02	18	±03	4.0
2009/09/18	06:56:56	-81.5845	±02	-5.4659	±01	13	±01	4.0

Source time function

We selected shallow thrust events (depth < 30km) in northern Peru and southern Ecuador. The source time functions were obtained using the methodology described in [*Vallée et al.*, 2011], which uses a deconvolution approach. Only events with a good signal-to-noise ratio were kept.

Rate and state model

We test the hypothesis that the time series of GPS site BAYO can be modeled using the rate-and-state formalism and a simplified model. For an area of velocity-strengthening submitted to a sudden stress increment induced by a co-seismic slip, the time evolution of slip *u(t)* for a spring-slider with velocity-strengthening law is given by *[Perfettini and Avouac, 2004]* :

$$u(t)=V_0 t_r \log[1+d(\exp(t/t_r)-1)] \quad (4)$$

where t is the time after the earthquake, V_0 is the sliding velocity prior to the earthquake, t_r is the relaxation time and d is the ratio of the velocity immediately after the earthquake. This equation shows that for $t>>t_r$, $u(t)$ returns to the pre-earthquake sliding velocity $V_0 t$. The transient slip is therefore:

$$u(t)=V_0 t_r \log[1+d(\exp(t/t_r)-1)]- V_0 t \quad (5)$$

For two earthquakes occurring at t_1 & t_2, equation (5) becomes:

$$u(t)= u_1\delta_{EQ1}+u_2\delta_{EQ2}+\delta_{EQ1}V_0 t_r \log[1+d_1(\exp((t-t_1)/t_r)-1)+ \delta_{EQ2}d_2(\exp((t-t_2)/t_r)-1)]- V_0 t \quad (6)$$

where δ_{EQi} is 0 when $t<t_i$ and 1 for $t>t_i$, u_1 and u_2 are the co-seismic displacements induced by the earthquakes, d_1 and d_2 are the velocity ratio increment after the first and second earthquakes. Because the second earthquake occurred about 80km from the BAYO CGPS station, the co-seismic displacement at BAYO is certainly below the precision of the GPS time series. Therefore u_2 was not estimated and set to 0.

Figure 4.1 shows the fit of equation (6) to the BAYO time series. We find a best fit for the following parameters:

d_1=1.92 ± 0.01

d_2=26.12 ± 0.12

t_r =0.09 ± 0.5 yr

u_1=-2.2 ± 0.1 mm

All errors are at the 1σ confidence level.

The parameter d is related to the Coulomb stress increment by

$$\log(d)= \mathrm{DCFF} / a\sigma \quad (7)$$

As a consequence, the ratio of the Coulomb stress increment between the two earthquakes is

$$DCFF_2 / DCFF_1 = \log(d_2) / \log(d_1) \quad (8)$$

which provides, using the estimated values for d_1 and d_2, $DCFF_2 / DCFF_1 \approx 5$, telling that the Coulomb stress increment for the March 26 earthquake was significantly larger than the Coulomb stress increment for the February 15 earthquake.

Assuming that $DCFF_1$ of the order 10^{-2} MPa in the slip area, we find using equation (4) that $a\sigma \approx 2\text{-}3.10^{-2}$ MPa for the two events. This result is an order of magnitude lower than values derived from laboratory experiments, but is similar to the value found by *Perfettini et al. [2010]* to explain the afterslip following the Mw 8.0 2007 Pisco earthquake in southern Peru. Such small values may explain the large slip triggered by moderate size earthquakes.

References

Ccallo, F., H. Tavera, and I. Valdivia (2002), Magnitud de Sismos locales y regionales ocurridos en Perú a partir de la onda Lg y la duración del registro, *Boletín la Soc. Geológica del Perú*, *94*, 61–69.

Kissling, E., U. Kradolfer, and H. Maufer (1995), *Velest user's guide*, Institute of Geophysics, ETH Zuerich.

Klein, F. (1978), *Hypocenter location program HYPOINVERSE*, U. S. Geol. Surv. Open-File Rept. 78-694, 102 pp.

Nocquet, J.-M. et al. (2014), Motion of continental slivers and creeping subduction in the northern Andes, *Nat. Geosci.*, *7*(March), 287–291, doi:10.1038/NGEO2099.

Okada, Y. (1992), Internal deformation due to shear and tensile faults in a half-space, *Bull. Seismol. Soc. Am.*, *82*(2), 1018–1040.

Perfettini, H., and J. Avouac (2004), Postseismic relaxation driven by brittle creep : A possible mechanism to reconcile geodetic measurements and the decay rate of aftershocks , application to the Chi-Chi earthquake , Taiwan, *J. Geophys. Res.*, *109*(B02304), 1–15, doi:10.1029/2003JB002488.

Perfettini, H. et al. (2010), Seismic and aseismic slip on the Central Peru megathrust, *Nature*, *465*(7294), 78–81, doi:10.1038/nature09062.

Radiguet, M., F. Cotton, M. Vergnolle, M. Campillo, B. Valette, V. Kostoglodov, and N. Cotte (2011), Spatial and temporal evolution of a long term slow slip event: the 2006 Guerrero Slow Slip Event, *Geophys. J. Int.*, *184*(2), 816–828, doi:10.1111/j.1365-246X.2010.04866.x.

Tarantola, A. (2005), *Inverse Problem Theory*, SIAM, Paris, France.

Tavera, H., R. Vilca, and G. Marin (2006), Inferences on the geometry of the Nazca plate in northwestern Peru based on data collected by a local seismograph network, *Earth Sci. Res. J.*, *10*(1), 15–24.

Chapter 5: Conclusions and Perspectives

Previous to this thesis, no GPS data was available along the subduction margin extending from the north of Lima to the Gulf of Guayaquil. The seismic behavior of that subduction segment is characterized by the occurrence of a regular M~5.0 – 6.0 background seismicity, moderate tsunami-earthquakes and the absence of large megathrust earthquake since at least the 16th century. Inland, active faults have been identified but neither slip rates had been proposed nor a relationship with a regional kinematics model. As a consequence, even first order questions about the earthquake cycle and continental deformation were poorly understood. The primary question was to know whether stress is currently accumulating at the plate interface with the potential of a future great megathrust great earthquake (M≥8.8, like in Sumatra 2004, Chile 2010 or Japan 2011) or whether creeping processes accommodates the plate convergence. The second question was to know whether significant long-term deformation of the overriding continent occurs in the Peruvian Andes and its margin. Finally, since episodic slow slip events have been documented in other subduction zones, we did not know whether they could also be found in Peru.

To address these questions, I benefit from new GPS data acquired in the frame of an international collaboration project (the ADN project funded by the ANR-France, P.I. Jean-Mathieu Nocquet). My contribution to the ADN project includes all the steps carried out for the Peruvian side of the project. Since 2008, I have participated in the reconnaissance and installation of both campaign and permanent GPS sites. I took part of the measurements campaign in 2008, 2009, 2010, 2011, 2012, and maintenance of the permanent GPS network. I have processed the GPS data and develop the modeling of both the pattern of interseismic coupling along the subduction interface and the continental deformation. I correlated the results with seismological information, and compiled information about large past historical earthquakes in Peru. Finally, I worked on the relocation of a seismicity sequence synchronous to a slow slip event that took place in the Piura Peninsula (north Peru, lat 5.5ºS) at the beginning of the project.

The results obtained in this thesis provide novel insights into the anatomy of the earthquake cycle and the continental deformation along the Peruvian margin. They successfully answered most of the initial questions stated in Chapter 1 and raise as much new questions for the future. Finally, they have implications on the geodynamics of the Andean orogeny and the assessment of earthquakes and tsunamis hazard, with consequences for the whole circumpacific coast. In the following, I summarize the main results obtained in the frame of this thesis, the limitations of some of our results and draw possible future research perspectives.

1. Continental deformation: The Inca Sliver and the oblique convergence partitioning

In subduction zones where the plate convergence is oblique the strain partitioning is taken-up by the lateral motion of a sliver on the overriding plate [*Jarrard*, 1986; *Mccaffrey*, 1992; *Chemenda et al.*, 2000; *Bevis and Martel*, 2001]. For example, in the Sumatra or Central America subduction zones the oblique convergence induces a slip partitioning accommodated by continental strike-slip faults parallel to the trench axis [*Mccaffrey et al.*, 2000; *DeMets*, 2001]. In Peru, the average strike of the trench is 330°E, with a Nazca/South America convergence direction of N78°E, leading to 18° obliquity of the convergence. While this obliquity had been suspected by *Dewey and Lamb*, [1992] or *Veloza et al.*, [2011] to induce significant trench-parallel motion in Peru, it had not been demonstrated.

In this thesis I provide evidence for a ~2200km long continental sliver in Peru, that was unknown previous to this study. The analysis of the GPS velocity field in northern Peru and southern Ecuador shows a rigid southeastward translation (with respect to stable South America) at a rate of 4-5 mm/yr. The area moving rigidly encompasses the whole Peruvian margin from south of the Gulf of Guayaquil to the Arica bend, including the western Andean Cordillera and the margin west of it. However, our analysis shows that Peru departs from the simple kinematics scheme of partitioning of oblique subduction where all the trench-parallel component of the obliquity is accommodated by a continental sliver. First, the motion of the Inca Sliver takes up only ~25% of the trench-parallel component. Second, this motion is not

accommodated by a single pure strike-slip fault system. Finally, there is a significant trench-perpendicular partitioning that also take place in the sub-Andean fold and thrusts belt in the form of crustal shortening. This pattern is clearly evidenced in northern Peru where the rio Marañon fault system (MFS) marks the transition between two rigid behaviors and the eastern boundary of the Inca Sliver there. In central Peru the prolongation of the MFS is the Chonta Fault system and our observations agree with this possible limit. In southern Peru the deformation becomes more diffuse with probably the existence of an additional Altiplano block. Our sparse data set and currently on-going postseismic effects prevent any clear conclusions. More measurements are needed in the future to constraint the pattern of deformation in the eastern side of the sliver in order to better define the structures accommodating the partitioning and in order to evaluate if it is dominated by shear stress or other mechanisms. For the sub-Andean ranges in central and north Peru we propose crustal shortening rates at ~2.5mm/yr, however, a densification of GPS measurements there would help to quantify more precisely the crustal faults interaction and its associated seismic hazard.

Compared to others oblique subduction zones, we note that northern and central Peru do not have a volcanic arc. Volcanic arc may define a strip of crustal and lithospheric weakness with locally thinned crust and hot material. This weakness strip might foster the development of large strike-slip fault systems and thus favoring high partitioning. In the absence of a volcanic arc over ¾ of the length of the Peru segment, partitioning remains relatively low. Furthermore, the average elevation of the Andes is significantly larger than for mountain ranges where high partitioning is found. Possible gravitational potential energy contrast between the Andes and the Amazon basin could also add another contribution to the stress field and would contribute to the shortening perpendicular to the Andean cordillera observed in the sub-andean domain.

At the larger scale of the Andean subduction, various slivers have been reported in Chile, Ecuador and Colombia [*Trenkamp et al.*, 2002; *Brooks et al.*, 2003; *Chlieh et al.*, 2011; *Métois et al.*, 2013]. For all these slivers, the sense of the trench-parallel component is consistent with the sense of the Nazca/South America obliquity. We therefore conclude that obliquity is the driving process for the lateral motion of the slivers in the South America subduction zone. Sliver motions and active crustal

shortening in the sub-Andean region appear as the main dominant processes for the present day deformation of the Andes. Finally, the diverging motion northeastward of the North Andean sliver and southeastward of the Inca sliver explains the opening of the Gulf of Guayaquil in the northern Andes, and the converging motion southeastward of the Inca sliver and northwestward of the northern Chile Sliver seem to play a role in the development of the Altiplano plateau holding it laterally.

2. Interseismic Coupling (ISC) along the megathrust of Peru

Modeling of the GPS surface velocities show that the ISC along the subduction plate interface in Peru and Ecuador is heterogeneous at various scales. At the largest scale, we identify a ~1000-km-long segment in northern Peru and southern Ecuador (from lat. 9ºS to 2ºS) in which the ISC is weak to low, and thus where convergence is accommodated predominantly by aseismic slip. This area is among the largest aseismic subduction segment in the world, similar in length to central America [*Correa-Mora et al.*, 2009; *LaFemina et al.*, 2009; *Franco et al.*, 2012]. The very weak coupling therefore provides an explanation to the quiescence evidenced in historical earthquake catalogs during the past five centuries. Nonetheless, our modeling also indicates that some significant coupling at a scale of ~100km can be confined to the shallowest portion of the seismogenic zone. While the very low coupling makes unlikely any occurrence of great earthquakes (M≥8.5 as the observed in Japan, Sumatra or Chile in last decade) in northern Peru, the shallowest portion of the subduction interface can still host moderate size (M~7.5) tsunami-earthquake type events as in 1960 (7.5Mw) and 1996 (7.6Mw).

In central Peru our models evidence a high ISC with asperities that correlate with the rupture areas of past earthquakes. These asperities can either rupture independently trough large earthquakes (M8.0 type) as in 1940, 1966, and 1974, or in a single event producing a great earthquake and tsunami (M8.6-8.8 type) as it occurred in 1746. In southern Peru our models show two asperities that are highly coupled and that correlate with the rupture areas of the near Nazca 1913 (M~8.0) event and the extreme south rupture area of the 1868 earthquake (that was partially filled with the M8.4 23/06/2001 event). We also found that the AREQ (Arequipa) GPS sites (lat. ~16.4ºS) is presently showing the ongoing postseismic effect of the

Mw=8.4 2001 earthquake (lat. ~16.3ºS at ~200 km to the east), suggesting that either afterslip or viscoelastic deformation, or both processes are still taking place there. *Ortega*, [2013] showed that GPS coastal sites are already showing a strong interseismic loading, however the postseismic signal is still contaminating the GPS velocities over a large area as the AREQ time series shows. Our dataset for this region is not dense enough to characterize the impact and extent of the postseismic deformation, however we highlight this effect for future studies. Currently new and denser measurements are being acquired in this region by the Caltech and ISTerre teams. Future estimations of the interseismic coupling in this region will have to take the post-seismic deformation into account.

The seismic cycle behavior of southern and central Peru segments appears to be similar in the time interval between large and great earthquakes. In these zones the current rates of surface deformation are high. The Central Peru segment is currently undergoing a pre-seismic phase since mature asperities are continuously accumulating stress, and the sequence of M~8 earthquakes during the 20^{th} century only released a small fraction of the stress accumulated since the 1746 great earthquake. In terms of seismic potential the central Peru segment represents one of the most hazardous areas along South America. A third of the Peru's population is living there and our results warn for a preparation of a big earthquake and tsunami.

Aside from the implication for seismic hazard, we find a correlation between the lateral variations of the ISC and geomorphic structures on the subducting plate. The Nazca Ridge and the Mendaña Fracture Zone correlate with a considerable decreasing of the ISC. Our results therefore provide a key for future studies on the factors controlling the interseismic coupling, indicating the areas where changes in any controlling parameter(s) should be sought.

Despite the regional coverage of our geodetic network (~70 km of inter-sites distance) we are able to constrain the area of highly coupled areas. These areas could correspond to one or more neighboring local asperities. A densification of more GPS sites in the coastal ranges with an inter-site distance of ~20-30 km would enhance the mapping of such single asperities and improve the current apparent coupling. Similarly, such a densification in the sub-Andean region and around crustal faults will help to quantify the seismic hazard in the nearby cities.

3. Peculiar Slow Slip Events and Seismic Swarm in a weakly coupled subduction zone

Finally, we document novel observations of a Slow Slip Event (SSE) and synchronous seismicity that occurred in the northern Peru subduction zone. The SSE lasted 7 months and induced surface trenchward displacements of 14 mm at the Bayovar continuous GPS site (lat. 6°S). During this period a sequence of localized seismicity swarms occurred in the same area, with four significant earthquakes of moment magnitude ranging from 5.3 to 6.0, where the two first were characterized by a sequence of foreshocks/mainshock/aftershocks while the third is characterized with long source time function.

This observation is novel in several ways: it is probably the first observation of a correlation between rupture characteristics with aseismic slip occurring in a subduction zone. Our observation suggest that the mixed process of seismic and aseismic slip contribute with the same order of magnitude to the slip on the plate interface. A small pulse of creep could have triggered the sequence of foreshocks before the two first main events, bringing small asperities to the seismic rupture, followed by an aftershocks sequence. Our observation demonstrates that earthquakes rupture changed the state of stress on the plate interface, causing either afterslip or simply favoring the acceleration of the pre-existing aseismic slip. Denser continuous GPS and seismic monitoring in this segment will enable to detect this and other events and signals (i.e. tremors, vlf, etc.) and evaluate their contribution to the budget balancing the convergence. In chapter 4, we propose a model in which the anatomy of the subduction interface is made of small to moderate-size isolated patches of velocity weakening material embedded in a much larger velocity strengthening area which promotes aseismic slip or large postseismic slip once the small asperities rupture. This appears to be the behavior of the northern Peru subduction segment. Further observations in others subduction zones should tell us whether the proposed model for the Piura peninsula also holds for others weakly coupled subduction zones.

4. Anatomy of the subduction plate interface

The results obtained in this thesis finally allow me to provide inferences about the anatomy of the plate interface in terms its frictional properties at the scale of the Peru segment. I propose that the southern and central Peru segments are areas where the plate interface is composed of a background velocity strengthening material area in which there are embedded large areas of velocity weakening material that are the responsible of accumulating stress to produce large earthquakes. The typical size of velocity-weakening asperities is > 100km, as observed from the rupture of the Pisco Mw 8.0 2007 and Arequipa 2001 Mw 8.4 earthquakes. If these areas are close enough one to each other they will rupture together in a single event, but if a wide barrier such as the Nazca Ridge separates them they will rupture independently. Asperities there appear to be surrounded by velocity-strengthening areas, where afterslip and aftershocks propagate after the earthquake rupture, as it was documented for the Pisco 2007 earthquake [*Perfettini et al.*, 2010]. The northern Peru segment contrasts with this usually proposed anatomy. Our observations suggest that the subduction interface is mostly dominated by velocity strengthening material that facilitates steady creep, in which small- to moderate-size isolated patches of velocity weakening material accumulate stress leading to earthquakes of magnitude lower than ~7.5. The asperities in this environment seem to be surrounded by conditionally stable areas that may fail in tsunami-like earthquakes.

To summarize, the difference of the seismic cycle behavior reflects the response of drastically plate interfaces anatomy to the same forcing (the convergence rate does not differ by more than 10% between northern and southern Peru). The northern segment is characterized by occurrence of tsunami-earthquakes in the shallow portion of the plate interface and slow earthquakes eventually associated with seismicity swarms. The southern and central segments are characterized by the occurrence of regular large to great earthquakes. Whether slow slip events and tremors can be observed there remain as open questions.

List of Figures

List of Tables

References

Abe, K., and S. Noguchi (1983), Determination of magnitude for large shallow earthquakes 1898-1917, *Phys. Earth Planet. Inter.*, *32*, 45–59.

Barazangi, M., and B. L. Isacks (1976), Spatial distribution of earthquakes and subduction of the Nazca plate beneath South America, *Geology*, *4*, 686–692.

Barke, R., and S. Lamb (2006), Late Cenozoic uplift of the Eastern Cordillera, Bolivian Andes, *Earth Planet. Sci. Lett.*, *249*(3-4), 350–367, doi:10.1016/j.epsl.2006.07.012.

Beck, S. L., and S. P. Nishenko (1990), Variations in the mode of great earthquake rupture along the central Peru subduction zone, *Geophys. Res. Lett.*, *17*(11), 1969 – 1972.

Beck, S. L., and L. J. Ruff (1989), Great earthquakes and subduction along the Peru trench, *Phys. Earth Planet. Inter.*, *57*(3-4), 199–224, doi:10.1016/0031-9201(89)90112-X.

Bevis, M., and S. J. Martel (2001), Oblique plate convergence and interseismic strain accumulation, *Geochemistry Geophys. Geosystems*, *2*, 1–13.

Bevis, M., E. C. Kendrick, R. Smalley, T. Herring, J. Godoy, and F. Galban (1999), Crustal motion north and south of the Arica deflection: Comparing recent geodetic results from the Central Andes, *Geochemistry Geophys. Geosystems*, *1*, 1–12.

Bevis, M., E. Kendrick, B. Brooks, R. Allmendinger, B. Isacks, and R. Smalley Jr. (2001), On the strength of interplate coupling and the rate of back arc convergence in the central Andes: An analysis of the interseismic velocity field, *Geochemistry Geophys. Geosystems*, *2*(11), doi:10.1029/2001GC000198.

Bilek, S. L. (2010), Invited review paper: Seismicity along the South American subduction zone: Review of large earthquakes, tsunamis, and subduction zone complexity, *Tectonophysics*, *495*(2), 2–14, doi:10.1016/j.tecto.2009.02.037.

Bourgeois, J., C. Petroff, H. Yeh, V. Titov, C. E. Synolakis, B. Benson, J. Kuroiwa, J. Lander, and E. O. Norabuena (1999), Geologic Setting, Field Survey and Modeling of the Chimbote, Northern Peru, Tsunami of 21 February 1996, *Pure Appl. Geophys.*, *154*(February 1996), 513–540.

Brace, W. F., and J. D. Byerlee (1966), Stick-slip as a mechanism for earthquakes., *Science*, *153*(3739), 990–2, doi:10.1126/science.153.3739.990.

Brooks, B. A., M. Bevis, E. Kendrick, R. Maturana, and M. Araujo (2003), Crustal motion in the Southern Andes (26°–36°S): Do the Andes behave like a microplate?, *October*, *4*(10), 1–14, doi:10.1029/2003GC000505.

Brooks, B. A. et al. (2011), Orogenic-wedge deformation and potential for great earthquakes in the central Andean backarc, *Nat. Geosci.*, *4*(5), 1–4, doi:10.1038/ngeo1143.

Brown, L. D., R. E. Reilinger, S. R. Holdahl, and E. I. Balazs (1977), Postseismic crustal uplift near Anchorage, Alaska, *J. Geophys. Res.*, *82*(23), 3369–3378, doi:10.1029/JB082i023p03369.

Bürgmann, R., P. Segall, M. Lisowski, and J. Svarc (1997), Postseismic strain following the 1989 Loma Prieta earthquake from GPS and leveling measurements, *J. Geophys. Res.*, *102*(B3), 4933–4955.

Bürgmann, R., M. G. Kogan, V. E. Levin, C. H. Scholz, R. W. King, and G. M. Steblov (2001), Rapid aseismic moment release following the 5 December, 1997 Kronotsky, Kamchatka, earthquake, *Geophys. Res. Lett.*, *28*(7), 1331–1334.

Cahill, T., and B. L. Isacks (1992), Seismicity and shape of the subducted Nazca Plate, *J. Geophys. Res.*, *97*(B12), 17503, doi:10.1029/92JB00493.

Carlotto, V., J. Quispe, H. Acosta, R. Rodriguez, D. Romero, and Et.al (2009), Dominios geotectónicos y metalogénesis del Perú, *Bol. la Soc. Geolofgica del Peru*, *103*, 1–89.

Chemenda, A., S. Lallemand, and A. Bokun (2000), Strain partitioning and interplate friction in oblique subduction zones: Constraints provided by experimental modeling, *J. Geophys. Res.*, *105*(B3), 5567–5581.

Chlieh, M., J. B. De Chabalier, J. C. Ruegg, R. Armijo, R. Dmowska, J. Campos, and K. L. Feigl (2004), Crustal deformation and fault slip during the seismic cycle in the North Chile subduction zone , from GPS and InSAR observations, *Geophys. J. Int.*, *158*, 695–711, doi:10.1111/j.1365-246X.2004.02326.x.

Chlieh, M., H. Perfettini, H. Tavera, J.-P. Avouac, D. Remy, J.-M. Nocquet, F. Rolandone, F. Bondoux, G. Gabalda, and S. Bonvalot (2011), Interseismic coupling and seismic potential along the Central Andes subduction zone, *J. Geophys. Res.*, *116*(B12405), 1–21, doi:10.1029/2010JB008166.

Correa-Mora, F., C. DeMets, D. Alvarado, H. L. Turner, G. Mattioli, D. Hernandez, C. Pullinger, M. Rodriguez, and C. Tenorio (2009), GPS-derived coupling estimates for the Central America subduction zone and volcanic arc faults: El Salvador, Honduras and Nicaragua, *Geophys. J. Int.*, *179*(3), 1279–1291, doi:10.1111/j.1365-246X.2009.04371.x.

Dalmayrac, B. (1978), *Geologie des Andes Peruviennes*, edited by O.R.S.T.O.M., O.R.S.T.O.M., Paris, France.

Darwin, C., G. B. Sowerby, and E. Forbes (1846), *Geological observations on South America: Being the third part of the geology of the voyage of the Beagle, under the command of Capt. Fitzroy, RN during the years 1832 to 1836*, Smith, Elder and Company, 65, Cornhill.

DeMets, C. (2001), A new estimate for present-day Cocos-Caribbean Plate motion: Implications for slip along the Central American Volcanic Arc, *Geophys. Res. Lett.*, *28*(21), 4043, doi:10.1029/2001GL013518.

Devlin, S., B. L. Isacks, M. E. Pritchard, W. D. Barnhart, and R. B. Lohman (2012), Depths and focal mechanisms of crustal earthquakes in the central Andes determined from teleseismic waveform analysis and InSAR, *Tectonics*, *31*(TC2002), 1–33, doi:10.1029/2011TC002914.

Dewey, J. F., and S. H. Lamb (1992), Active tectonics of the Andes, *Tectonophysics*, *205*, 79–95, doi:10.1016/0040-1951(92)90419-7.

Dorbath, L., A. Cisternas, and C. Dorbath (1990), Assessment of the size of large and great historical earthquakes in Peru, *Bull. Seismol. Soc. Am.*, *80*(3), 551–576.

Dorbath, L., C. Dorbath, E. Jimenez, and L. Rivera (1991), Seismicity and tectonic deformation in the Eastern Cordillera and the sub-Andean zone of central Peru, *J. South Am. Earth Sci.*, *4*, 13–24.

Douglas, A., J. Beavan, L. Wallace, and J. Townend (2005), Slow slip on the northern Hikurangi subduction interface, New Zealand, *Geophys. Res. Lett.*, *32*(L16305), 1–4, doi:10.1029/2005GL023607.

Dragert, H., K. Wang, and T. S. James (2001), A Silent Slip Event on the deeper Cascadia subduction interface, *Science (80-.).*, *292*(5521), 1525–8, doi:10.1126/science.1060152.

Espinoza, J. (1992), Terremotos tsunamigenicos en el Ecuador, *Acta Ocean. del Pacifico.*, *7*(1), 1–8.

Fedotov, S. A. (1967), *The seismic cycle, quantitative seismic zoning and long-term seismic forecasting In: Seismic Zoning of the USSR*, Nauka, Moscow.

Franco, A. et al. (2012), Fault kinematics in northern Central America and coupling along the subduction interface of the Cocos Plate, from GPS data in Chiapas (Mexico), Guatemala and El Salvador, *Geophys. J. Int.*, *189*(3), 1223–1236, doi:10.1111/j.1365-246X.2012.05390.x.

Gagnon, K., C. D. Chadwell, and E. O. Norabuena (2005), Measuring the onset of locking in the Peru-Chile trench with GPS and acoustic measurements., *Nature*, *434*(7030), 205–208, doi:10.1038/nature03412.

Hasegawa, A. (2014), Seismicity, Subduction Zone, in *Encyclopedia of Solid Earth Geophysics SE - 14*, edited by H. Gupta, pp. 1305–1315, Springer Netherlands.

Hayes, G. P., D. J. Wald, and R. L. Johnson (2012), Slab1.0: A three-dimensional model of global subduction zone geometries, *J. Geophys. Res.*, *117*(B01302), 1–15, doi:10.1029/2011JB008524.

Heki, K., S. Miyazaki, and H. Tsuji (1997), Silent fault slip following an interplate thrust earthquake at the Japan Trench, *Nature*, *386*(April), 595–598.

Heuret, A., C. P. Conrad, F. Funiciello, S. Lallemand, and L. Sandri (2012), Relation between subduction megathrust earthquakes, trench sediment thickness and upper plate strain, *Geophys. Res. Lett.*, *39*(L05304), 1–6, doi:10.1029/2011GL050712.

Holtkamp, S. G., M. E. Pritchard, and R. B. Lohman (2011), Earthquake swarms in South America, *Geophys. J. Int.*, 128–146, doi:10.1111/j.1365-246X.2011.05137.x.

Von Huene, R., and S. Lallemand (1990), Tectonic erosion along the Japan and Peru convergent margins, *Geol. Soc. Am. Bull.*, *102*(June), 704–720.

Ide, S., G. C. Beroza, D. R. Shelly, and T. Uchide (2007), A scaling law for slow earthquakes., *Nature*, *447*, 76–79, doi:10.1038/nature05780.

Ihmle, P. F., J.-M. Gomez, P. Heinrich, and S. Guibourg (1998), The 1996 Peru tsunamigenic earthquake : Broadband source process, *Geophys. Res. Lett.*, *25*(14), 2691–2694, doi:10.1029/98GL01987.

Isacks, B. L. (1988), Uplift of the Central Andean Plateau and bending of the Bolivian Orocline, *J. Geophys. Res.*, *93*(B4), 3211–3231, doi:10.1029/JB093iB04p03211.

Jarrard, R. D. (1986), Terrane motion by strike-slip faulting of forearc slivers, *Geology*, *14*(September), 780–783.

Jonsson, S., P. Segall, R. Pedersen, and G. Bjornsson (2003), Post-earthquake ground movements correlated to pore-pressure transients, *Nature*, *424*(6945), 179–183.

Kaneko, Y., J.-P. Avouac, and N. Lapusta (2010), Towards inferring earthquake patterns from geodetic observations of interseismic coupling, *Nat. Geosci.*, *3*(5), 363–369, doi:10.1038/ngeo843.

Kelleher, J. A. (1972), Rupture Zones of Large South American Earthquakes and Some Predictions, *J. Geophys. Res.*, *77*(11), 2087–2103.

Kendrick, E., M. Bevis, R. Smalley Jr., and B. Brooks (2001), An integrated crustal velocity field for the central Andes, *Geochemistry Geophys. Geosystems*, *2*, 11, doi:10.1029/2001GC000191.

Kendrick, E., M. Bevis, R. Smalley, B. Brooks, R. Barriga, E. Lauria, and L. P. S. Fortes (2003), The Nazca–South America Euler vector and its rate of change, *J. South Am. Earth Sci.*, *16*(2), 125–131, doi:10.1016/S0895-9811(03)00028-2.

Krabbenhöft, A., J. Bialas, H. Kopp, N. Kukowski, and C. Hübscher (2004), Crustal structure of the Peruvian continental margin from wide-angle seismic studies, *Geophys. J. Int.*, *159*(2), 749–764, doi:10.1111/j.1365-246X.2004.02425.x.

LaFemina, P., T. H. Dixon, R. Govers, E. Norabuena, H. Turner, A. Saballos, G. Mattioli, M. Protti, and W. Strauch (2009), Fore-arc motion and Cocos Ridge collision in Central America, *Geochemistry, Geophys. Geosystems*, *10*(5), 1–21, doi:10.1029/2008GC002181.

Lockridge, P. A. (1985), *Tsunamis in Peru-Chile, Report SE-39,*, Boulder, WDC-A for Solid Earth Geophysics, 97p.

Loveless, J. P., and B. J. Meade (2010), Geodetic imaging of plate motions, slip rates, and partitioning of deformation in Japan, *J. Geophys. Res.*, *115*(B02410), 1–35, doi:10.1029/2008JB006248.

Macharé, B. J., C. H. Fenton, M. N. Machette, C. Costa, and R. L. Dart (2003), *Database and Map of Quaternary Faults and Folds in Perú and its Offshore Region FOLDS IN PERÚ AND ITS OFFSHORE REGION*.

Machare, J., and L. Ortlieb (1992), Plio-Quaternary vertical motions and the subduction of the Nazca Ridge, central coast of Peru, *Tectonophysics*, *205*, 97–108, doi:10.1016/0040-1951(92)90420-B.

Mccaffrey, R. (1992), Oblique Plate Convergence, Slip Vectors, and Forearc Deformation, *J. Geophys. Res.*, *97*(B6), 8905–8915.

Mccaffrey, R., P. C. Zwick, Y. Bock, L. Prawirodirdjo, J. F. Genrich, C. Stevens, S. S. O. Puntodewo, and C. Subarya (2000), Strain partiotioning during oblique convergence in northern Sumatra: Geodetic and seismologic constraints and numerical modeling, *J. Geophys. Res.*, *105*(B12), 28,2363–28,376.

Megard, F. (1984), The Andean orogenic period and its major structures in central and northern Peru, *J. Geol. Soc. London.*, *141*, 893–900, doi:10.1144/gsjgs.141.5.0893.

Mégard, F. (1978), *Étude géologique des Andes du Pérou Central*, Contributi., edited by ORSTOM, ORSTOM, Paris.

Melbourne, T. I., and F. H. Webb (2002), Precursory transient slip during the 2001 Mw = 8.4 Peru earthquake sequence from continuous GPS, *Geophys. Res. Lett.*, *29*(21), 1–4, doi:10.1029/2002GL015533.

Métois, M., A. Socquet, C. Vigny, D. Carrizo, S. Peyrat, A. Delorme, E. Maureira, M.-C. Valderas-Bermejo, and I. Ortega (2013), Revisiting the North Chile seismic gap segmentation using GPS-derived interseismic coupling, *Geophys. J. Int.*, *194*(3), 1283–1294, doi:10.1093/gji/ggt183.

Moreno, M., M. Rosenau, and O. Oncken (2010), 2010 Maule earthquake slip correlates with pre-seismic locking of Andean subduction zone, *Nature*, *467*(7312), 198–202, doi:10.1038/nature09349.

NGDC http://www.ngdc.noaa.gov (n.d.), NGDC-NOAA, *Natl. Geophys. Data Cent. NGDC*.

Nishenko, S. P. (1991), *Circum-Pacific Seismic Potential*, U.S. Geological Survey, National Earthquake Information Center.

Nocquet, J.-M., E. Calais, Z. Altamimi, P. Sillard, and C. Boucher (2001), Intraplate deformation in western Europe deduced from an analysis of the International Terrestrial Reference Frame 1997 (ITRF97) velocity field, *J. Geophys. Res.*, *106*(B6), 11239–11257, doi:10.1029/2000JB900410.

Nocquet, J.-M. et al. (2014), Motion of continental slivers and creeping subduction in the northern Andes, *Nat. Geosci.*, *7*(March), 287–291, doi:10.1038/NGEO2099.

Norabuena, E. O., L. Leffler-griffin, A. Mao, T. Dixon, S. Stein, I. S. Sacks, L. Ocola, and M. Ellis (1998), Space Geodetic Observations of Nazca-South America Convergence Across the Central Andes, *Science (80-.).*, *279*(5349), 358–362, doi:10.1126/science.279.5349.358.

Obara, K. (2002), Nonvolcanic Deep Tremor Associated with Subduction in Southwest Japan, *Science (80-.).*, *296*(May), 2001–2003.

Okada, Y. (1985), Surface deformation due to shear and tensile faults in a half-space, *Bull. Seismol. Soc. Am.*, *75*(4), 1135–1154, doi:10.1016/0148-9062(86)90674-1.

Okada, Y. (1992), Internal deformation due to shear and tensile faults in a half-space, *Bull. Seismol. Soc. Am.*, *82*(2), 1018–1040.

Ortega, F. (2013), Aseismic Deformation in Subduction Megathrusts: Central Andes and North-East Japan, 1–198 pp., California Institute of Technology.

Ozawa, S., M. Murakami, and T. Tada (2001), Time-dependent inversion study of the slow thrust event in the Nankai trough subduction zone, southwestern Japan, *J. Geophys. Res.*, *106*(B1), 787–802, doi:2000JB900317.

Pelayo, A. M., and D. A. Wiens (1990), The November 20, 1960 Peru Tsunami Earthquake: Souce Mechanism of a Slow Event, *Geophys. Res. Lett.*, *17*(6), 661–664, doi:10.1029/GL017i006p00661.

Peng, Z., and J. Gomberg (2010), An integrated perspective of the continuum between earthquakes and slow-slip phenomena, *Nat. Geosci.*, *3*(9), 599–607, doi:10.1038/ngeo940.

Perfettini, H., and J. Avouac (2004), Postseismic relaxation driven by brittle creep: A possible mechanism to reconcile geodetic measurements and the decay rate of aftershocks, application to the Chi-Chi earthquake,Taiwan, *J. Geophys. Res.*, *109*(B02304), 1–15, doi:10.1029/2003JB002488.

Perfettini, H., J.-P. Avouac, and J.-C. Ruegg (2005), Geodetic displacements and aftershocks following the 2001 Mw=8.4 Peru earthquake: Implications for the mechanics of the earthquake cycle along subduction zones, *J. Geophys. Res.*, *110*(B09404), 1–19, doi:10.1029/2004JB003522.

Perfettini, H. et al. (2010), Seismic and aseismic slip on the Central Peru megathrust, *Nature*, *465*(7294), 78–81, doi:10.1038/nature09062.

Pritchard, M. E., E. O. Norabuena, C. Ji, R. Boroschek, D. Comte, M. Simons, T. H. Dixon, and P. a. Rosen (2007), Geodetic, teleseismic, and strong motion constraints on slip from recent southern Peru subduction zone earthquakes, *J. Geophys. Res.*, *112*(B3), 1–24, doi:10.1029/2006JB004294.

Radiguet, M., F. Cotton, M. Vergnolle, M. Campillo, A. Walpersdorf, N. Cotte, and V. Kostoglodov (2012), Slow slip events and strain accumulation in the Guerrero gap, Mexico, *J. Geophys. Res.*, *117*(B4), 1–13, doi:10.1029/2011JB008801.

Reid, H. F. (1910), *The mechanics of the earthquake*, Carnegie institution of Washington.

Ruegg, J. C., M. Olcay, and D. Lazo (2001), Co-, Post- and Pre(?)-seismic Displacements Associated with the Mw 8.4 Southern Peru Earthquake of 23 June 2001 from Continuous GPS Measurements, *Seismol. Res. Lett.*, *72*(6), 673–678.

Ruegg, J. C., A. Rudloff, C. Vigny, R. Madariaga, J. B. de Chabalier, J. Campos, E. Kausel, S. Barrientos, and D. Dimitrov (2009), Interseismic strain accumulation measured by GPS in the seismic gap between Constitución and Concepción in Chile, *Phys. Earth Planet. Inter.*, *175*(1-2), 78–85, doi:10.1016/j.pepi.2008.02.015.

Ruff, L., and H. Kanamori (1980), Seismicity and the subduction process, *Phys. Earth Planet. Inter.*, *23*, 240–252.

Ruiz, S., M. Metois, A. Fuenzalida, J. Ruiz, F. Leyton, R. Grandin, C. Vigny, R. Madariaga, and J. Campos (2014), Intense foreshocks and a slow slip event preceded the 2014 Iquique Mw 8.1 earthquake, *Sci.* .

Salichon, J., B. Delouis, P. Lundgren, D. Giardini, M. Costantini, and P. Rosen (2003), Joint inversion of broadband teleseismic and interferometric synthetic aperture radar (InSAR) data for the slip history of the Mw = 7.7, Nazca ridge (Peru) earthquake of 12 November 1996, *J. Geophys. Res.*, *108*(B2), 1–13, doi:10.1029/2001JB000913.

Savage, J. C. (1983), A dislocation model of strain accumulation and release at a subduction zone, *J. Geophys. Res.*, *88*(B6), 4984–4996, doi:10.1029/JB088iB06p04984.

Scholz, C. H. (1998), Earthquakes and friction laws, *Nature*, *391*(January), 37–42.

Schwartz, S. Y., and J. M. Rokosky (2007), SLOW SLIP EVENTS AND SEISMIC TREMOR AT CIRCUM-PACIFIC SUBDUCTION ZONES, *Rev. Geophys.*, *45*(RG3004), 1–32, doi:10.1029/2006RG000208.1.

Seiner Lizárraga, L. (2009), *Historia de los sismos en el Perú. Catálogo: Siglos XV-XVII*, edited by F. Editorial, Universidad de Lima, Lima.

Seiner Lizárraga, L. (2011), *Historia de los Sismos en el Perú Catálogo: Siglos XVIII-XIX*, edited by Universidad de Lima, Universidad de Lima (Fondo Editorial).

Sempere, T. et al. (2004), Sistemas transcurrentes de escala litosférica en el sur del perû, *Publicación Espec. Bol. la Soc. Geológica del Perú*, *5*, 105–110.

Silgado, E. (1978), *Historia de los sismos más notables ocurridos en el Perú (1513-1974)*, Lima.

Sladen, A., H. Tavera, M. Simons, J. P. Avouac, A. O. Konca, H. Perfettini, L. Audin, E. J. Fielding, F. Ortega, and R. Cavagnoud (2010), Source model of the 2007 Mw 8.0 Pisco, Peru earthquake: Implications for seismogenic behavior of subduction megathrusts, *J. Geophys. Res.*, *115*(B22405), 1–27, doi:10.1029/2009JB006429.

Soloviev, S. L., and C. N. Go (1975), *A catalogue of tsunamis on the eastern shore of the Pacific Ocean, Moscow, "Nauka" Publishing House, 202p. English translation: Soloviev S.L., Go Ch.N. (1984). A catalogue of tsunamis on the eastern shore of the Pacific ocean, Translation by Canada Instit*, Ottawa, Canada KIA OS2.

Spiske, M., J. Piepenbreier, C. Benavente, A. Kunz, H. Bahlburg, and J. Steffahn (2013), Historical tsunami deposits in Peru: Sedimentology, inverse modeling and optically stimulated luminescence dating, *Quat. Int.*, *305*, 31–44, doi:10.1016/j.quaint.2013.02.010.

Stein, S., R. J. Geller, and M. Liu (2012), Why earthquake hazard maps often fail and what to do about it, *Tectonophysics*, *562-563*, 1–25, doi:10.1016/j.tecto.2012.06.047.

Suarez, G., P. Molnar, B. C. Burchfiel, and G. Suárez (1983), Seismicity, fault plane solutions, depth of faulting, and active tectonics of the Andes of Peru, Ecuador, and southern Colombia, *J. Geophys. Res.*, *88*(B12), 10403–10428, doi:10.1029/JB088iB12p10403.

Swenson, J. L., and S. L. Beck (1999), Source Characteristics of the 12 November 1996 M w 7.7 Peru Subduction Zone Earthquake, *Pure Appl. Geophys.*, *154*(3-4), 731–751, doi:10.1007/s000240050250.

Trenkamp, R., J. N. Kellogg, J. T. Freymueller, and H. P. Mora (2002), Wide plate margin deformation, southern Central America and northwestern South America, CASA GPS observations, *J. South Am. Earth Sci.*, *15*(2), 157–171, doi:10.1016/S0895-9811(02)00018-4.

UNAVCO Science Report (1994), *Geoscientific Research and the Global Positioning System*, Boulder, Colorado.

United Nations (2004), *World Population to 2300*, New York.

Valladares, C. E., and J. L. Chau (2012), The Low-Latitude Ionosphere Sensor Network (LISN): Initial Results, *Radio Sci.*, *47*(RS0L17), doi:doi:10.1029/2011RS004978.

Vallée, M. et al. (2013), Intense interface seismicity triggered by a shallow slow slip event in the Central Ecuador subduction zone, *J. Geophys. Res.*, *118*(6), 2965–2981, doi:10.1002/jgrb.50216.

Veloza, G., R. Styron, M. Taylor, and A. Mora (2011), Open-source archive of active faults for northwest South America, *Gsa Today*, *22*(10), 4–10, doi:10.1130/GSAT-G156A.1.

Vigny, C. et al. (2011), The 2010 Mw 8.8 Maule Megathrust Earthquake of Central Chile, Monitored by GPS, *Science (80-.).*, *332*(6036), 1417–1421, doi:10.1126/science.1204132.

Wallace, L. M., and J. Beavan (2010), Diverse slow slip behavior at the Hikurangi subduction margin , New Zealand, *J. Geophys. Res.*, *115*(B12402), doi:10.1029/2010JB007717.

Walter, J. I., S. Y. Schwartz, J. M. Protti, and V. Gonzalez (2011), Persistent tremor within the northern Costa Rica seismogenic zone, *Geophys. Res. Lett.*, *38*(1), 1–5, doi:10.1029/2010GL045586.

Wang, K., Y. Hu, M. Bevis, E. Kendrick, R. Smalley, R. Barrriga, and E. Lauria (2007), Crustal motion in the zone of the 1960 Chile earthquake: Detangling earthquake-cycle deformation and forearc-sliver translation, *Geochemistry, Geophys. Geosystems*, *8*(10), 1–14, doi:10.1029/2007GC001721.

Wang, K., Y. Hu, and J. He (2012), Deformation cycles of subduction earthquakes in a viscoelastic Earth, *Nature*, *484*(7394), 327–332, doi:10.1038/nature11032.

Wipf, M. A. (2006), Evolution of the Western Cordillera and Coastal Margin of Peru : Evidence from low-temperature Thermochronology and Geomorphology, 163 pp., Swiss Federal Institute of Technology Zürich.